ELECTRO-ANATOMICAL MODELS OF THE COCHLEAR IMPLANT

by

Darren M. Whiten

B.S., Biomedical Engineering, Boston University, 1999
M.S., E.E., Electrical Engineering and Computer Science, MIT, 2003

Submitted to the Harvard-MIT Division of Health Sciences and Technology
in partial fulfillment of the requirements for the degree of

DOCTOR OF PHILOSOPHY

at the

MASSACHUSETTS INSTITUTE OF TECHNOLOGY

February 2007

Author .....
Harvard-MIT Division of Health Sciences and Technology
November 8, 2006

Certified by .....
Donald K. Eddington, Ph.D.
Associate Professor of Otology and Laryngology, Harvard Medical School
Principal Research Scientist, Research Laboratory of Electronics, MIT
Thesis Supervisor

Accepted by .....
Martha L. Gray, Ph.D.
Edward Hood Talpin Professor of Medical and Electrical Engineering
Co-Director, Harvard-MIT Division of Health Sciences and Technology

ELECTRO-ANATOMICAL MODELS OF THE COCHLEAR IMPLANT

by
Darren M. Whiten

Submitted to the Harvard-MIT Division of Health Sciences and Technology
on November 8, 2006, in partial fulfillment of the
requirements for the degree of

DOCTOR OF PHILOSOPHY

Abstract

While cochlear implantation has become the standard of care in treating patients with severe to profound sensorineural hearing loss, the variation in benefit (communicative ability) individual patients derive from implantation remains both large and, for the most part, unexplained. One explanation for this variation is the status of the implanted ear which, when examined histopathologically, also displays substantial variation due to both the pathogenesis of hearing loss (etiology, etc.) and pathological changes initiated by implantation. For instance, across-patient variation in electrode position and insertion depth is clearly present, as are differential amounts of residual spiral ganglion survival, fibrous tissue formation and electrode encapsulation, cochlear ossification, and idiosyncratic damage to adjacent cochlear structures.

Because of the complex geometric and electrical properties of the tissues found in the implanted ear, demonstrating the impact of pathological variability on neuronal excitation, and ultimately on behavioral performance, will likely require a detailed representation of the peripheral anatomy. Our approach has been to develop detailed, three-dimensional (3D) electro-anatomical models (EAMs) of the implanted ear capable of representing the aforementioned patient-specific types of pathological variation. In response to electric stimulation, these computational models predict an estimate of (1) the 3D electric field, (2) the cochleotopic pattern of neural activation, and (3) the electrically-evoked compound action potential (ECAP) recorded from intracochlear electrodes.

This thesis focuses on three aims. First, two patient-specific EAMs are formulated from hundreds of digital images of the histologically-sectioned temporal bones of two patients, attempting to incorporate the detailed pathology of each. Second, model predictions are compared to relevant reports from the literature, data collected from a cohort of implanted research subjects, and, most importantly, to archival data collected during life from the same two patients used to derive our models. The latter comparisons to archival data (in the form of intracochlear potential recordings, psychophysical threshold measures, and ECAP recordings) collectively show a promising correspondence between model-predicted and empirically-measured data. Third, by making incremental adjustments to the anatomical representation in the model, the impact of individual attributes are investigated, mechanisms that may degrade benefit suggested, and potential interventions explored.

Thesis Supervisor:

Donald K. Eddington, Ph.D.
Associate Professor of Otology and Laryngology, Harvard Medical School
Principal Research Scientist, Research Laboratory of Electronics, MIT

Acknowledgments

Many thanks to the following for serving as members of the thesis committee:

- **Donald K. Eddington, Ph.D.**
  Associate Professor of Otology and Laryngology, Harvard Medical School
  Principal Research Scientist, Research Laboratory of Electronics, MIT
- **Charles Finley, Ph.D.**
  Associate Professor of Otolaryngology and Biomedical Engineering
  University of North Carolina at Chapel Hill
- **Joseph B. Nadol, Jr., M.D.**
  Walter Augustus Lecompte Professor & Chairman
  Department of Otology & Laryngology, Harvard Medical School
  Chief of Otolaryngology, Massachusetts Eye and Ear Infirmary
- **Christopher Shera, Ph.D.**
  Associate Professor of Otology & Laryngology and Health Sciences & Technology
  Harvard Medical School

Portions of this work were funded by:

- **National Institutes of Health**
  Training Grant 5-T32-DC00038
  Contract N01-DC-2-1001
  NRSA Fellowship F31-DC007305-01
- **The Deafness Research Foundation**
  2801 M Street NW, Washington, DC 20007
- **The Amelia Peabody Fund**
  Massachusetts Eye and Ear Infirmary
  243 Charles Street Boston, MA 02114

I sincerely thank the many people who contributed to this work:

Don Eddingon, who somehow provided a delicate mixture of encouragement and guidance, all the while maintaining a hands-off approach to mentoring, which, for those of us who reject micro-management, was especially appreciated. Don's clear thought process, integrity, and willingness to dedicate time to the endeavors of others are all greatly admired.

The members of the Cochlear Implant Research Laboratory (Margaret Lankow, Victor Noel. Joe Tierney, Maggie Whearty, and Meng Yu Zhu), for the endless series of favors I asked of them.

The Temporal Bone Registry and the members of the Otopathology Laboratory, especially Barbara Burgess and Richard Cortese for preparing and helping to photograph the histological materials used in this project.

The present/past faculty, staff, and students of the Eaton Peabody Laboratory, for providing an environment where many of one's most pressing questions could be quickly answered by an expert, who just so happened to be waiting for the elevator. Thankfully, we all have Dianna Sands, without whom those elevators, and surely EPL, would likely grind to a halt.

The friends I've made over 10 years spent in and around Boston (a list is unnecessary - you know who you are). I owe a special thanks to Drs. Guy Rachmuth and S. Terrence Ruggles, who invariably made graduate school seem like an excellent choice by pointing out that a lot of people go to college for seven years.

Lastly, and most importantly, I thank my parents and my brother, Matt, for years of encouragement, without which this work would never have reached its completion.

Darren Whiten
November 2006

---

in fond memory of Mr. & Mrs. George Whiten

and with the deepest appreciation for our research subjects,
especially the anonymous individual herein referred to
as "the Ineraid subject" whose contributions
to the field of cochlear implants
remain outstanding

This page intentionally left blank

Contents

Chapter 1

Introduction

1.1 Background and significance

Excluding the pacemaker, the cochlear implant (CI)[1] is the most widely prescribed and successful neural prosthesis in use today. Two features stand out when one considers the nearly 100,000 cochlear implant users worldwide [86]. First, is the significant improvement in communication provided to most patients. Second, is the wide range in benefit to speech reception measured across patients, even across subsets of patients each with the same device and a similar, or ostensibly identical, medical history [11].

While the efficacy of the CI for treating severe to profound sensorineural hearing loss has been well established,[2] the fundamental mechanisms underlying the wide range in benefit measured across CI patients remain unclear, presenting two clinical problems. First, for an implantee experiencing little improvement in speech reception, there is typically little or no evidence to suggest why the treatment worked poorly or what, if any, corrective action can be taken. Second, there is currently no method to identify, from among CI candidates, those likely to receive little benefit in order to spare them the risk and expense of surgery.

Demonstrating the mechanisms that limit communicative ability with a CI will impact both the research and clinical settings. First, it will provide focus to researchers working to improve the benefit provided to CI users. Second, it may allow clinicians to increase the preponderance of patients receiving outstanding benefit by (1) adjusting the current surgical techniques and/or device based on specific patient attributes, or (2) identifying poor candidates in the clinic, thereby avoiding their implantation.

Patient attributes associated with benefit have been extensively investigated us-

[1] Readers unfamiliar with auditory physiology and cochlear implants are referred to the introductory material in section 1.3 on page 16.

[2] See Nadol et al. [142] for review.

ing many approaches. Psychophysically, measures have been made to test a subject's ability to receive both cochlear place information [152, 31, 234, 207, 38, 77, 35, 78] and temporal information [27, 30, 72, 57]. In searching for a correlate to benefit, researchers have also examined cognitive measures [101, 32], evoked potential measures [17], radiologically-derived estimates of insertion depth [191], and histological preparations of the implanted ear [95]. Others have compared benefit to patient characteristics such as age or etiology of deafness [10, 11], concentrating on what Blamey, et al. [11] termed "secondary factors:" measures or characteristics that may indirectly reflect the state of the more fundamental factors likely determining the benefit an individual patient receives. For instance, because the number of surviving spiral ganglion cells (SGCs) is related to the duration of hearing impairment and etiology [158, 150, 144, 88], some have examined the relationship between performance and these two secondary factors. The study by Blamey [11] examining the largest number of subjects to date (N=808) found duration of deafness, age at onset of deafness, and etiology together accounted for only 20% of the variance in speech recognition across patients. This is about the same percentage of performance variance explained by measures of cognitive function [101], electrode threshold [10], and electrode insertion depth [120, 191].

While other weak correlations have been found (e.g., patients with a shorter duration between the onset of deafness and implantation have a tendency to receive more benefit[11, 108]) a satisfying reason for this, i.e., one grounded in pathology, etiology, anatomy, or the surgical procedure, has not. For instance, evidence for poor performance in those patients where the device dissects the cochlear duct or damages the endosteum, possibly inciting fibrous tissue growth and ultimately ossification, would be a more satisfying explanation for degraded benefit than simply duration of deafness for at least a few reasons. First, it would describe a primary mechanism influencing benefit. Second, it would give clinicians and researchers a very specific problem to address.

In the absence of strong evidence for the primary mechanisms influencing CI benefit, two trends have occurred. First, a great deal of research effort has been directed toward factors that are only presumed to influence benefit. For example, based on speculation that degeneration of the peripheral dendrites might negatively impact benefit, some researchers have begun advocating the use of neurotrophins to slow peripheral degeneration in the ears of implanted patients [229]. Second, many promising ideas have yielded only minimal improvements in benefit to the CI community; for example, recent work at this institution involving the use of high-rate desynchronizing pulse trains (DPT) to restore stochastic independence to the timing of auditory-nerve fibers [115, 116, 117]. While the DPT idea (credited to Rubinstein et al. [180]) was, and remains, an excellent suggestion, as of yet it has not delivered the astonishing improvement in benefit that it was once thought it might.

Since the pathological correlates of most forms of sensorineural deafness are found

in the inner ear, as opposed to more central pathways [145], it seems likely that, to some extent, histopathological correlates of behavioral performance with a CI ought to also exist in the implanted cochlea. Clearly, the status of the implanted ear, when examined histopathologically, displays substantial variation [146], including that due to both the pathogenesis of hearing loss (e.g., etiology), as well as pathological changes initiated by the trauma of implantation itself. For instance, across-patient variation in electrode position and insertion depth is evident, as are differential amounts of residual spiral ganglion survival, fibrous tissue formation, electrode encapsulation, cochlear ossification, and idiosyncratic damage to cochlear structures such as basilar membrane perforation and erosion of the modiolar bony wall.

However, using conventional histological techniques, a consistent correlation between these histopathological observations and objective measures of behavioral performance has not been demonstrated [145]. For instance, the histopathological analyses of cadaveric temporal bones from users of multichannel cochlear implants during life [146, 95, 43, 121, 112, 230, 155, 206, 28, 113, 92, 91] include studies that examine the degree to which variation in the peripheral anatomy accounts for variance in both psychophysical and speech reception measures. Taken together, the results of these earlier studies do not demonstrate a consistent relationship between histopathology and performance. For instance, in a recent study of 15 donated temporal bones at this institution [97], neither the segmental nor total spiral ganglion cell counts were significantly correlated with NU6 word scores. Likewise, comparing a larger number of bones across studies, Blamey [9] found no strong evidence relating spiral ganglion counts to speech recognition scores.

One interpretation of these data is that factors such as spiral ganglion survival do not influence psychophysical and speech-reception performance. Another is that the methods used were unsuitable for identifying how SGC density interacts with other features of the implanted ear to influence performance. Although these studies are clearly an appropriate first step, they suggest that to understand the extent to which SGC survival is import for benefit, one may need to account for more than just the total number of spiral ganglion cells. For instance, whether a spiral ganglion cell discharges will not only depend on the cell body's presence and its geometric distance from the stimulating electrodes, but also on the orientation of its axon (and dendrite if present) relative to the complex 3D electric field generated by the stimulating electrodes. The details of the electric field along a nerve fiber will depend on a number of patient-specific anatomical details (e.g., the longitudinal and radial location of the electrode, the details of the implanted temporal bone's 3D anatomy, the types and degree of damage to cochlear structures, and the distribution of intracochlear fibrous and bony tissues).

Accordingly, it is not surprising that a simple measure of SGC survival based on the classic two-dimensional (2D) reconstruction of the human temporal bone does not capture the overall impact of a patient's peripheral anatomy and pathology. This

view is consistent with a more recent study by this laboratory [99] using 2D reconstructions that did not find a consistent relationship between segmental SGC counts made along Rosenthal's canal and psychophysical threshold; the hypothesis being that electrodes located at cochleotopic positions with higher SGC survival ought to have lower psychophysical thresholds. Given the difficulties encountered in using classic 2D analysis to find a relation between factors such as total SGC and benefit, or a relation between segmental SGC and psychophysical threshold, it is likely a new approach is needed. The type of model described here builds on work done by Girzon [60] and others in the Cochlear Implant Research Laboratory at the Massachusetts Eye and Ear Infirmary.

Our approach to identifying the peripheral mechanisms most influencing benefit is to develop detailed 3D electro-anatomical models (EAMs) of the implanted ear capable of representing the different types of (patient-specific) peripheral anatomical and pathological variation seen in a collection of implanted temporal bones. In response to stimulation by an arbitrary set of stimulating electrodes, these models predict an estimate of (1) the 3D electric field, (2) the pattern of neural activation as a function of cochleotopic position, and (3) the evoked potentials recorded on intracochlear electrodes. By deriving these models from the histologically-processed temporal bones of individual patients, the opportunity exists to test the models' predictions against archival data collected from each patient during life. These comparisons, in the form of intracochlear potential recordings, psychophysical threshold measures, and ECAP recordings, provide an important measure of how confident one can be in the model predictions as representative of the physical situation.

Finally, given the variability seen across implanted ears, we can investigate which aspects of the peripheral anatomy ought to have the largest impact on the spike activity elicited by intracochlear stimulation. For instance, the impact of the new bone and fibrous tissue deposits that typically fill the bony duct near the cochleostomy site can be investigated by incrementally removing these tissues from the model and recalculating the predictions of intracochlear current flow, neural activation, and evoked potential waveforms. A series of EAM models that capture the variation in peripheral anatomy seen across implanted patients would enable one to investigate the influence of many relevant anatomical variations on electric hearing, and how one might adjust the stimulus parameters (e.g., the stimulating electrode configuration and waveform shape) to optimize the correspondence between electrically-generated and acoustically-elicited patterns of spike activity.

Ultimately, we expect these models to aid in the interpretation of data collected from human and animal experiments, and suggest new methods for producing spike activity patterns more similar to those present in the normal-hearing ear. For example, in Chapter 4, the model is used to describe how replacing the cochlear fluids with an adipose tissue suspension might improve the spatial selectively of neural excitation using monopolar stimulation. Ultimately, uncovering the features of the implanted

ear that most strongly influence electric hearing may allow us to (1) understand the relationship between the peripheral pathology and patient benefit, should such a relationship exist; and (2) focus future research on overcoming specific factors that limit performance.

Future applications

In addition to facilitating investigations of how different aspects of the peripheral anatomy influence the patterns of spike activity on the array of auditory-nerve fibers during intracochlear stimulation, the work in this thesis can be used to address a much wider range of issues. For example, these models can serve as a scaffold that, with further refinement, allows one to visualize in 3D whether evidence for damage (e.g., fracture of the osseous spiral lamina, or dissection of the spiral ligament) at a specific cochleotopic position correlates with either a low SGC count, dendritic degeneration, or morphological changes to constituent cells at the same cochleotopic position. Also, because the correct anatomical positioning of both the facial and vestibular nerves are incorporated, refined models could also be used to evaluate the potential for unintentional (ectopic) stimulation of other proximal nerves by a cochlear implant. In its current formulation, the model predicts the activation of the auditory nerve, but with relatively small additions predictions of facial and vestibular nerve activation elicited by intracochlear stimulation could be incorporated as well. Similarly, expanding this modeling approach to include a more detailed representation of the vestibular system, along with a single-fiber model of the vestibular nerve, would allow it to be used as a research tool in the design of a vestibular implant to differentially stimulate the branches of the vestibular nerve without exciting either the auditory or facial nerves.

1.2 Document organization

This thesis is organized into three major chapters:

Chapter 2

This chapter describes three EAMs. Two patient-specific EAMs (psEAMs) are formulated from images of the histologically-sectioned temporal bones of two patients, attempting to incorporate the detailed pathology of each. The first psEAM, with patient-specific aspects removed, is referred to as the basic model (bEAM) and is used to generate preliminary results. This chapter is subdivided into four sections that describe model formulation (section 2.2), prediction of intracochlear current flow (section 2.3), prediction of neural activation patterns (section 2.4), and prediction of

evoked potentials (section 2.5). Where appropriate, model predictions are compared to relevant reports from the literature for each.

Chapter 3

In chapter 3, model predictions are compared to archival data collected during life from the same two patients used to derive our models. Three sources of archival data were identified against which the patient-specific predictions of these models are tested: (1) intracochlear potential recordings, (2) the most recent psychophysical threshold measures made with each patient during life, and (3) ECAP measures made using various stimulating and recording electrode combinations. Additionally, a set of psychophysical predictions made using the bEAM are tested experimentally using a cohort of implanted research subjects.

Chapter 4

Lastly, incremental adjustments to the anatomical representation in the model are made to investigate the impact of individual features, suggest potential mechanisms that may degrade benefit, and explore potential interventions.

1.3 Introductory material

1.3.1 Introduction to the peripheral auditory system

The mammalian auditory system is a remarkable sound-processing instrument capable of detecting sound energies across a wide range of frequencies and intensities. The processing of sound by the peripheral auditory system is often described as occurring in three steps: collection by the external ear, transmission across the middle ear, and transduction into a neural code by the inner ear.

Sound propagating through air is collected by the external ear at the pinna and guided toward the tympanic membrane, or eardrum, which marks the boundary to the middle ear (Figure 1-1). Energy is transmitted across the middle ear into the inner ear by the bones of the ossicular chain: the malleus, incus and stapes. These effectively counter the (acoustic) impedance mismatch between the air-filled external ear and the fluid-filled inner ear. Accordingly, the middle ear overcomes the loss of transmission that typically occurs when sound propagating through air meets a fluid interface.

Transduction into a neural code occurs in the cochlea, a system of fluid-filled compartments encased in the unusually dense temporal bone. The spiralling cochlear duct is partitioned by two membranes to form three parallel chambers called the scala vestibuli, scala media, and scala tympani as shown in Figure 1-2. The scala media

and scala vestibuli are separated from the scala tympani by a fibrous divide called the basilar membrane. This serves as a basement membrane for the organ of Corti, whose motion-sensitive hair cells perform transduction.

These compartments spiral around a common bony axis, the modiolus, that encases the auditory-nerve. The cell bodies of the afferent fibers are aggregated into a spiralling ganglion, that sits in a cavity of the modiolus (Rosenthal's canal). The peripheral process of these bipolar neurons extends radially to exit the bony modiolus at the habenula perforata and synapse on the base of an individual sensory hair cell. The axonal process extends centrally through the internal auditory meatus (IAM) to terminate in the cochlear nucleus of the brainstem. In the normal human, approximately 30,000 fibers innervate hair cells over roughly 2.5 turns of the cochlear spiral [184]. Superficial fibers along the nerve trunk exterior peel off first to innervate the base of the cochlear spiral, whereas medial fibers travel further up toward the apex before fanning out to innervate the apical turns.

Sound energy is injected into the scala vestibuli through the oval window by the piston-like action of the stapes. Since the fluid of the scala vestibuli is essentially incompressible, a traveling wave displacement of the basilar membrane is initiated that propagates up the cochlear spiral. Local displacements of the basilar membrane cause the attached sensory hair cells to release neurotransmitter, initiating action potentials on the synapsed afferent fibers. Accordingly, information about the local membrane motion (i.e., its frequency and amplitude) is carried to the central nervous system (CNS) by this corresponding subset of local nerve fibers.

The elastic properties of the basilar membrane systematically vary over the length of the cochlear spiral such that the mechanical resonant frequency of the partition systematically varies from the base to the apex, allowing the structure to behave as a mechanical frequency analyzer. Disjoint frequency components of the incoming sound preferentially excite disjoint longitudinal regions of the membrane: high frequency components excite basal regions while low frequency components excite apical regions. Consequently, the power spectrum of the incoming sound is mirrored in both the displacement profile along the basilar membrane and the corresponding discharge patterns of fibers spread along the membrane. Nerve fibers, and the hair cells on which they synapse, are typically referenced by the sound frequency to which they are most sensitive - the characteristic frequency (CF). The logarithmic map of characteristic frequency to longitudinal position along the basilar membrane's 2.5 spiraling turns is referred to as the cochlear frequency axis.[3]

[3]Note in the following discussions, the terms *frequency axis* or *CF* are used to describe positions along the (spiralling) basilar membrane, while the term *cochlear axis* is used to describe the axis around which the basilar membrane spirals.

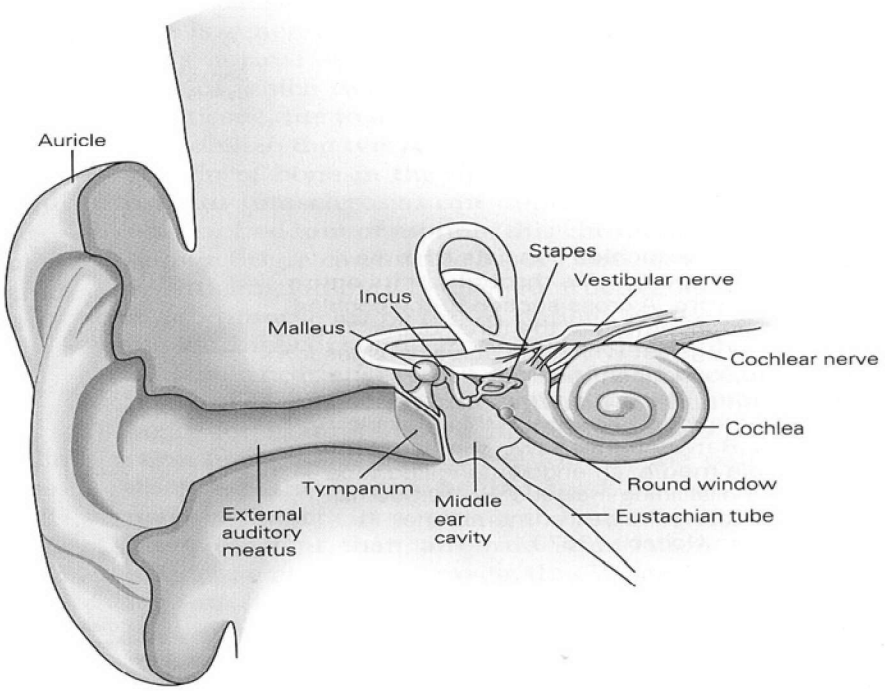

Figure 1-1: Peripheral auditory system. Shown are the structures of external ear, the middle ear (malius, incus, and stapes), and the inner ear. From this vantage point, the axis of the cochlear spiral is nearly perpendicular to the page. [Adapted from Noback, CR. 1967. *The human nervous system : basic principles of neurobiology.* New York : McGraw-Hill. Permission granted]

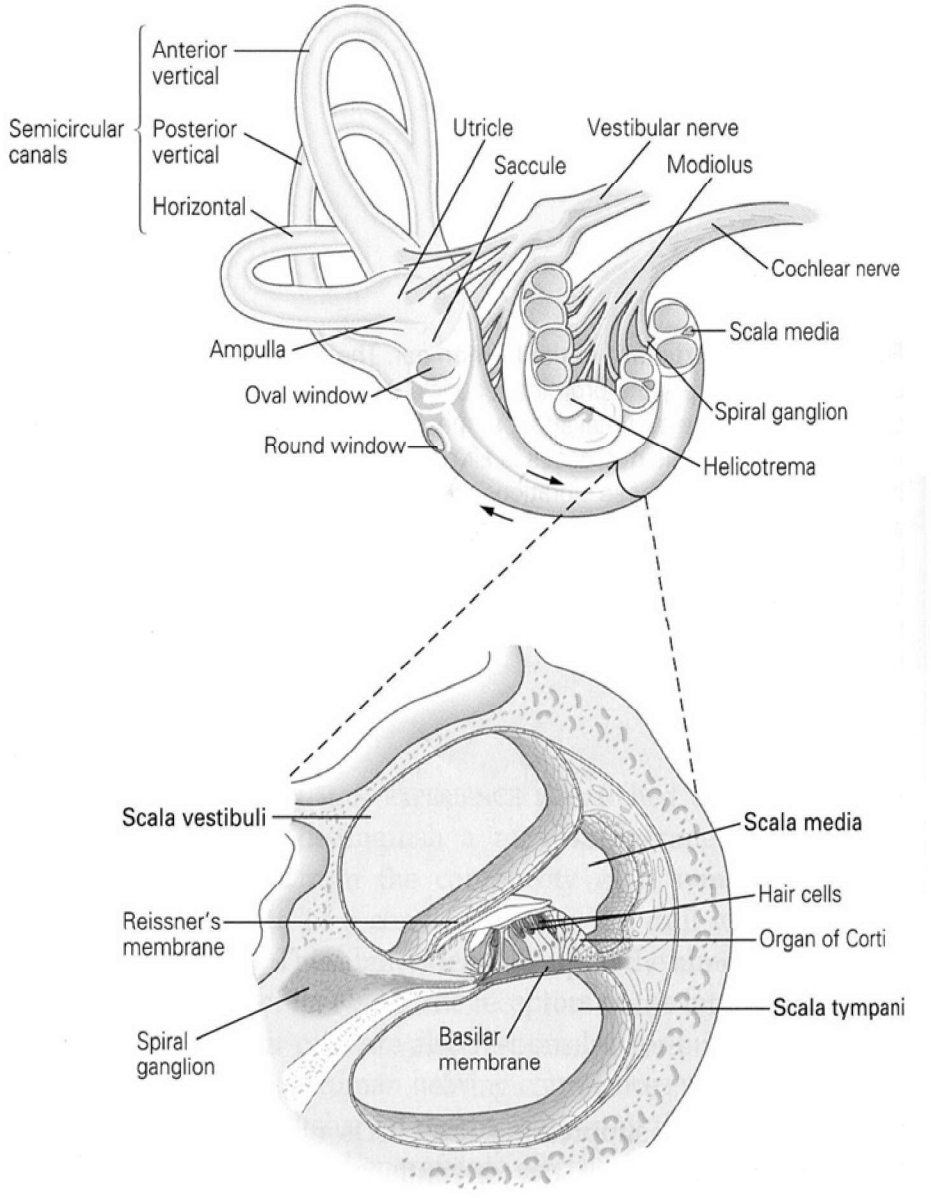

Figure 1-2: Inner ear structures. Sound energy delivered to the oval window travels up the cochlear spiral via a travelling wave displacement of the basilar membrane. The elastic properties of the membrane vary from base to apex allowing it to behave as a mechanical frequency analyzer. [Adapted from from Noback, CR. 1967. *The human nervous system : basic principles of neurobiology.* New York : McGraw-Hill. Permission granted]

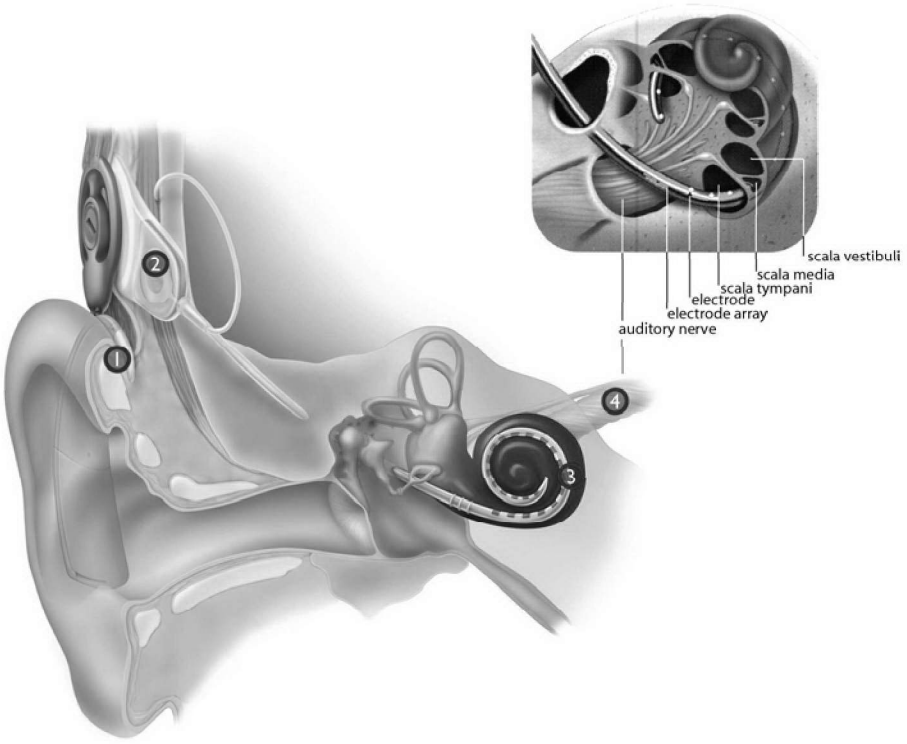

Figure 1-3: Cochlear implant schematic. Typical electrode carriers have up to 24 electrode contacts, each intended to stimulate a different subpopulation of afferent nerve-fibers. Shown are the external sound processor (1), subcutaneous implant device (2), electrode array (3), and auditory nerve (4). Figure adapted from *www.cochlearamericas.com*, Cochlear Corporation, Englewood, Colorado.

1.3.2 Introduction to cochlear implants

The cochlear implant is a neural prosthesis used to partially restore hearing in patients with specific types of profound sensorineural hearing loss. The most common forms of sensorineural deafness involve a loss of hair cell function [81], thus interfering with the transduction process even though a viable population of afferent nerve-fibers may remain. The implant attempts to bypass the external ear, middle ear, and transduction apparatus of the inner ear (hair cells) to directly stimulate afferent fibers via a surgically-implanted electrode array. Typically, arrays have up to 24 contacts spaced along an inert silastic carrier that is inserted into the scala tympani (Figure 1-3). The electrode array parallels the frequency axis of the basilar membrane, such that adjacent intracochlear contacts along the array may focally stimulate adjacent fiber populations that, in the normal ear, encode different frequencies of the incoming sound. Accordingly, the distribution of stimulation across electrodes attempts to mimic the excitation profile along the frequency axis of the basilar membrane present in the normal ear.

Stimulation of individual electrodes is typically accomplished via short biphasic

current pulses (20 to 400 μs per phase) delivered at a pulse rate of around 800 pulses per second (pps). Current pulses can be delivered to an individual electrode referenced to a far-field ground (monopolar) or between adjacent electrodes (bipolar). An externally worn sound processor employs a filter-bank to decompose the incoming sound spectrum into frequency bands, then uses the band-energy to modulate the pulse-train amplitude applied to each electrode. Accordingly, temporal changes in an electrode's pulse-train amplitude reflect temporal changes in the corresponding sound spectrum band.[4]

In one popular stimulation strategy, continuous interleaved sampling (CIS), the phase of the pulse-train delivered to each electrode is staggered such that no two electrodes are pulsed simultaneously. This helps to minimize field interactions between electrodes, however the subpopulations of nerve-fibers excited by adjacent electrodes are still likely to overlap extensively. This overlap has generally been considered a cause for poor performance, as discussed below.

Implants must be calibrated on a patient-by-patient basis. To fit individual patients, two psychophysically defined levels are recorded for each electrode in isolation: threshold and maximum comfortable level. These measures mark the lowest and highest pulse train amplitudes used by the device. Audiologists routinely use these to specify an electrode-specific function that maps a range of sound energies in the analysis band into the dynamic range of pulse train amplitudes bounded by the threshold and maximum comfortable levels.

Ideally, each contact along the electrode array would excite small, disjoint populations of afferent fibers along the cochlear spiral. This would allow for a detailed representation of the incoming sound spectrum to be encoded in the auditory-nerve while preserving the temporal information in each band. Unfortunately, this is not the case. Focal stimulation is severely limited because of interference between adjacent electrodes; the geometry, proximity, and viability of the target fibers; electrode placement; and a host of other implicated problems. While the number of disjoint bands in a device can be as high as 22, present estimates indicate that the maximum number of independent channels of information received by the implant user is typically limited to about 8 [39, 49, 83].

Besides the limitations imposed by the inability of the electrode array to focally stimulate narrow regions along the frequency axis of the cochlea, others are imposed by the population of surviving cochlear neurons. Neural survival is typically measured by the presence of perikarya in Rosenthal's canal. It is well documented that hair cells are more susceptible to injury (ototoxic or noise induced) than cochlear neurons or supporting cells. A staggering loss of hair cells may be accompanied by almost no immediate loss of cochlear neurons or supporting cells. However, the secondary

[4]The effective stimulus strength can also be modulated by adjusting the pulse phase duration. As a first-order approximation, the stimulus strength can be specified as the charge delivered during each pulse phase (i.e., the duration-amplitude product).

loss of spiral ganglion cells following hair cell degeneration typically occurs [151, 233, 148]. In histological studies of the deafened ear, the survival of spiral ganglion cells has been reported to decrease with both age and the duration of deafness, but is reportedly most influenced by the etiology of the hearing loss. Data suggest that patients who experience aminoglycoside exposure or idiopathic sudden sensorineural hearing loss have the highest survival of spiral ganglion cells, while patients who lost hearing to postnatal viral labyrinthitis, bacterial meningitis, or congenital factors have the lowest survival rates [151]. Recently, this has led researchers to search for, and find, neurotrophic factors that appear to prevent the secondary degeneration of spiral ganglion cells after an experimentally-induced sudden loss of hair cells. [232, 200, 190].

Intuitively, one might presuppose that implant users with higher spiral ganglion survival would have better speech recognition scores. While it has been reported that electric stimulation thresholds tend to be anti-correlated with spiral ganglion survival [88], no consistent correlation between spiral ganglion survival and speech scores has been reported to date.

Another variable across patients is the depth to which the electrode array can be inserted into the scala tympani during surgery. This is often limited, theoretically resulting in a mismatch between the frequency band a particular electrode is encoding, and the frequency region of the cochlea it stimulates. While one might expect better performance with a deep electrode insertion where the placement of the information band delivered by the electrode is closer to the "correct" place along the cochlea, to date there is only a limited amount of evidence to support this [191]. It is not unusual for patients with limited insertion depths to perform as well as, or even better than, patients with deep electrode insertions [118].

Various other factors have been suggested to explain implantee performance, including the medial-lateral[5] position of the electrode array, insertion trauma, changes in the tissue properties of the cochlea (e.g., ossification or fibrous tissue formation), the status of neural pathways central to the auditory nerve, and a host of cognitive and age-related factors. For most of these factors, no direct method of measuring an individual contribution to auditory performance has been identified.

[5]Medial refers to a position closer to the cochlear axis in a radial coordinate scheme.

Chapter 2

An electro-anatomical model

2.1 Introduction

A quantitative model of the implanted cochlea, capable of representing the histopathological variation seen across implanted patients, would be a useful tool in investigating the influence of the peripheral anatomy on electric hearing. In this chapter the methods used to construct an electro-anatomical model and generate predictions are discussed. This includes the techniques to: (1) formulate a patient-specific model [section 2.2], (2) predict intracochlear current flow [section 2.3], (3) predict neural activation patterns [section 2.4], and (4) predict evoked potentials recorded on inactive electrodes [section 2.5]. By capturing the peripheral anatomy of individuals, specifically those aspects of the anatomy that vary across implant patients, differences in anatomy can be viewed, quantified, and analyzed in 3D as well as probed for their relative impact on electric hearing. To our knowledge, these models are the first of their kind to meticulously use hundreds of histological images, thus enabling patient-specific anatomy to be encoded.

2.1.1 Previous modeling work

The earliest models of electric stimulation treated the cochlear spiral as a transmission line [8, 93, 202, 156] to address the issue of longitudinal current spread. In order to make rudimentary predictions of how current flows longitudinally along the length of the cochlea, these models essentially treat the unrolled cochlea as a cylindrical tube encased in bone. Present transmission line models can be made patient-specific by measuring (in individual patients) the voltage on inactive electrodes while delivering current to a single monopolar electrode, then fitting the voltage data to a discrete transmission line model, as done by Vanpoucke et al. [216]. Typically, these models make predictions such as where along the implanted array the longitudinal impedance changes, possibly due to a deposit of fibrous tissue or new bone. While this technique, referred to as electric field imaging (EFI), has the advantage that it can be done easily

on many patients, it is difficult to predict a pattern of neural excitation from this type of data, and nearly impossible to incorporate measures such as SGC count, making a rigorous patient-specific comparison difficult.

Recently, investigators have used 3D volume conduction models that estimate the potential field in the cochlea in response to intracochlear stimulation [60, 47, 124]. The work of several investigators (Finley et al. [47], Rattay et al. [170, 168], Frijns et al. [54, 56], and Hanekom [73, 74]) have coupled these calculated potential distributions with single-fiber models to render predictions of neural excitation. While these previous models have provided valuable insight into both intracochlear current flow and neural activation, they have shortcomings that this work is intended to address.

First, previous volume conductor models do not include sufficient anatomical detail to characterize individual patient differences. Previous models all are derived from a single midmodiolar histological image of a normal cochlea, meaning they are not intended to exhaustively capture an individual patient's anatomy, nor do they include local anatomical structures such as the facial nerve or vestibular labyrinth. These local structures may be important to consider, especially for monopolar stimulation since current must exit the cochlea to reach the return electrode (typically on the stimulator body or embedded in the temporalis muscle). Recent EFI work has suggested the facial nerve as a potential pathway for a significant amount of electrical current exiting the cochlea [215].

Second, with the exception of Briaire and Frijns [13], previous models have not attempted to predict the ECAP waveform recorded from intracochlear electrodes. This is a weakness because these are the measures that are most directly linked to the periphery and, therefore, most likely to be captured by a model of the periphery.

Third, and most importantly, the predictions of these models have not been extensively tested against empirical data collected from implant users. This is a critical and often overlooked step in the modeling process. Comparing our predictions with empirical data will both identify areas where the model predictions are particulary poor as well as challenge some of the assumptions of our approach.

This modeling approach builds upon the work of Girzon [60] and Frijns [54] to address all three of these issues. First, it represents the anatomy of a subject's temporal bone in much greater detail than previous approaches since it is based on a registered set of histological images representing the entire cochlea. Intracochlear bone and fibrous tissue commonly found near the electrode array are included, along with local anatomical structures such as the facial and vestibular nerves. Second, the model predicts evoked potentials recorded from intracochlear electrodes for arbitrary stimulus levels and combinations of the recording/stimulating electrodes. Should the proposed model accurately reflect changes in ECAP morphology as the stimulating and recording electrodes are varied, one feels confident in using the model to interpret other ECAP data. Third, as described in the next chapter, the models will be exten-

sively tested against empirical data by comparing patient-specific model predictions with measures made in the same subjects during life.

2.1.2 Chapter overview

Two patient-specific models are presented based on images taken from the serial-sectioned temporal bones of two implanted donors. The models incorporate the distribution of surviving spiral ganglion cells (SGCs), intracochlear new bone and fibrous tissue deposits, the presence or absence of an intact basilar membrane, the electrode type and position, the 3D shape of the cochlear spiral and surrounding anatomical structures, and any unique damage that an implant may have caused (for instance, erosion of the modiolar wall by the electrode array). The psEAMs are referred to as the Ineraid and Nucleus models because of the implant device used in each subject. The 3D reconstruction of these two temporal bones is discussed in this chapter, with attention to those aspects of the implanted ear that are not visible or quantifiable in a contemporary 2D reconstruction.

The Ineraid model fitted with a uniform compliment of surviving SGCs and all intracochlear bone and fibrous tissues removed is referred to as the basic electro-anatomical model (bEAM) and is used to generate the preliminary data presented in this chapter. Since the 3D geometry and electrode position are based on that of the Ineraid patient, this formulation remains partially patient-specific. Regardless, this model aims to give insight into how the 3D structure impacts excitation before the effects of intracochlear tissues and SGC survival are considered in later chapters.

The modeling process is broken into four conceptual steps. First, a 3D volume conduction model is formulated from a set of histological images taken from the serial sectioned temporal bone with the implanted electrode array left in situ. Surface renderings of the model allow the details of the structure to be visualized and quantified in 3D. A complement of fiber tracks is added to the model with their trajectories based on the position of the auditory nerve, Rosenthal's canal, and the osseous spiral lamina as captured in the histological images. The total number of spiral ganglion cells associated with each fiber track is based on segmental counts made along Rosenthal's canal using standard light microscopy.

Second, the pulsatile[1] electric field created by stimulating an arbitrary combination of electrodes (e.g., monopolar, bipolar, or tripolar) in the volume conduction model is computed using finite-difference techniques. This solution describes intracochlear current flow during stimulation, including current flow along each model fiber track.

Third, the time-varying response to the pulsatile electric field is computed for a model nerve fiber associated with each fiber track. Each model fiber occupies a

[1]In this chapter the stimulus waveform is always pulsatile, although an arbitrary waveform shape can be used in the model.

trajectory along, and is associated with, one fiber track. While model fibers have a different total length depending on their trajectory and cochleotopic position, they each use a common single-fiber model of the auditory nerve to predict a response to electric stimulation. By iteratively scaling the electric field created by the stimulating electrodes, a threshold is assigned to each model fiber; that is, the minimum amplitude stimulus necessary to initiate a propagating action potential.[2] The activation pattern (a plot of model-fiber threshold versus cochlear position) describes the spatial sensitivity of the model fibers to excitation by a particular stimulating waveform and electrode configuration.

Fourth, the neural activation pattern is used to predict the electrically-evoked compound action potential (ECAP) waveform recorded on inactive electrodes during a 1-ms time window following the stimulus. This is accomplished by combining the predicted spatio-temporal pattern of spike activity with a second application of the finite-difference method to compute a predicted waveform for each recording electrode.

These four steps (model generation, current flow prediction, neural activation prediction, and ECAP prediction) are presented in detail separately. A single simulation provides a collection of predictions that together quantitatively describe electric stimulation of the auditory nerve and make predictions about the familiar recordings one can make on an implanted subject (e.g., intracochlear potential recordings, psychophysical thresholds, and ECAPs). Subsequent chapters will use these predictions to both test the models against empirical data (Chapter 3) and address the question of what impact various anatomical attributes (e.g., intracochlear tissue deposits) have on the response to electric stimulation (Chapter 4).

2.2 Formulating patient-specific models

Two patient-specific electro-anatomical models (psEAMs) were formulated based on the donated temporal bones obtained from the NIDCD National Temporal Bone, Hearing and Balance Pathology Resource Registry at the Massachusetts Eye and Ear Infirmary. These patients were chosen specifically because for each there exists a record of psychophysical threshold measures made at regular intervals while using the implanted device. Since the Ineraid patient served extensively as a research subject, also available are a variety of additional measures including impedance recordings, intracochlear potentials, and evoked potentials. Relevant otologic and histologic characteristics of each patient are presented in Table 2.1.

[2]Note the electric field is generated exclusively by the stimulating electrode. Responding model fibers do not contribute to the predicted electric field during pulsatile stimulation.

Ineraid Patient	
Device	Symbion Ineraid, right ear
Age at implantation	30
Duration of deafness	10 years
Duration of device use	10 years
Most recent scores	NU6 word 70%
Otologic history	Bilateral sequential sudden hearing loss with vertigo; possible Cogan's syndrome
Histological findings	Fibrous tissue and new bone (labyrinthitis ossificans) in the basal turn; severe endolymphatic hydrops of all three cochlear turns; degeneration of the organ of Corti with loss of hair cells (inner and outer) throughout; degeneration of the spiral ganglion; scala media appears to be herniated into scala tympani in the ascending middle turn; patchy atrophy of the stria vascularis.
Nucleus Patient	
Device	Nucleus spectra 22 processor, right ear
Age at implantation	75 (first implant) 76 (re-implanted)
Duration of deafness	Progressive
Duration of device use	4 years
Most recent scores	NU6 word 16%; CNC word 16%; CNC phonemes 38 %
Otologic history	(Right, implanted) Progressive hearing loss from age 20 with significant drop at age 72 while on chemotherapy (Left) neonatal or congenital, attributed to mumps or polio.
Histological findings	Severe degeneration of the organ of Corti throughout the inner ear; no recognizable hair cells in the middle or apical turn; endolymphatic hydrops visible in the middle and apical turns; near total degeneration of the stria vascularis; extensive new bone and fibrous tissue formation along the implant; osseus spiral lamina nearly totally devoid of dendrites.

Table 2.1: Patient Characteristics. Source: Department of Otolaryngology, Massachusetts Eye and Ear Infirmary.

2.2.1 Methods

In all cases, the temporal bones were removed after death and fixed in 10% buffered formalin with the implanted electrode arrays left in situ. Decalcification was accomplished with ethylene-diamene-tetra-acetic acid (EDTA). The specimens were then post-fixed in 2% osmium tetroxide (Nucleus only), dehydrated in graded alcohols, exchanged with propylene oxide and embedded in araldite. The specimens were then serially sectioned in the horizontal (axial) plane at an average thickness of 20 μm by a technique previously described [149].

Sectioning can be problematic because contact between the cutting blade and the (typically platinum) electrodes often causes deformation of the tissue section. For this reason, a method was developed to photograph the face of the tissue block before

the microtome blade sliced off each section. This provides a digital picture of each section before cutting introduces artifacts. This procedure follows three steps for each section: (1) apply a thin layer of toluidine blue to the face of the tissue block, (2) photograph the surface using a digital camera (Canon Pro 1, 8 Mpixel) mounted above the block, (3) slice off the 20 μm section. The digital images of each section captured before being cut from the tissue block ("block images") clearly show the outline of the bony labyrinth, the undisturbed position of the electrode, as well as most cochlear structures of interest. Since the camera and tissue block are fixed in position, the series of block images are essentially registered. The technique used to obtain a series of block images was only performed on the Ineraid bone.

For the Ineraid bone, every 5th section was mounted on a glass slide, flattened, and cover-slipped. The Nucleus bone was treated in the same way but included every other section.[3] High resolution images of each mounted slide were captured at low power (1.25x) under a light microscope fitted with a high resolution camera (Olympus BX51, Olympus DP70 12.5 Mpixel). We refer to these as slide images. Accordingly, this process yielded two sets of color images for the Ineraid bone (94 slide images with 100 μm spacing and 364 block images separated by 20 μm) and a single set of 180 slide images for the Nucleus bone with 40 μm spacing.

These image sets were cropped, resampled, and registered using the Amira[4] reconstruction and modeling software package. For the Ineraid bone, the collection of block images required only a minimal amount of adjustment to produce a properly aligned 3D image. Into this set of block images, individual histological images were inserted, replacing the corresponding block image with a registered and scaled histological image of the same tissue section. This yielded a composite 3D image of $17.8 \times 17.8 \times 20 \mu m$ resolution, consisting mostly of block images, with every 5th image from a conventionally stained and mounted section. For the Nucleus bone the single set of histological images yielded a 3D image with $16.8 \times 16.8 \times 40 \mu m$ resolution.

Segmentation, 3D reconstruction, and resistivity assignment

Each voxel of the 3D image set was assigned a resistivity tag (segmentation) based on the tissue or material it represents using the Amira segmentation tool. This software allows three separate orthogonal planes, each intersecting the 3D image, to be viewed and segmented simultaneously. Identification of intracochlear bone and fibrous tissue was done using both the high resolution histological images as well as examining slides under a light microscope. Segmented regions included: (1) the electrode carrier; (2) electrode contacts; (3) modiolar bone; (4) Rosenthal's canal; (5) intracochlear fluid spaces; (6) normal bone; (7) intracochlear fibrous tissue; (8) pathological bone; (9)

[3]Decalcification, embedding, sectioning, and mounting of histological materials was performed by members of the Histopathology Laboratory at the Massachusetts Eye and Ear Infirmary.

[4]Amira is a registered trademark of Mercury Computer Systems, San Diego, CA.

internal auditory meatus; (10) auditory nerve; (11) vestibular nerve; (12) facial nerve; (13) air spaces of the middle ear, and (14) the internal carotid artery. In the Ineraid bone, the vestibular system was also segmented since the more diffuse current field expected with monopolar stimulation might be impacted by vestibular pathways. Resistivity values for the materials used in each volume conduction model are listed in Table 2.2.

Tissue	resistivity (Ωcm)	ref
bone	5000	[59] (also see [181, 103])
modiolus with nervous tissue	300	[59]
auditory/vestibular/facial nerves	300	[59]
intracochlear fluid space	50	[160]
vestibular fluid space	50	[160]
connective membrane	300	
fibrous intracochlear tissue	300	[59]
new intracochlear bone	5000	[59]
electrode carrier (Ineraid and Nucleus)	∞	
band electrode rings (Nucleus)	∞	
ball electrode contacts (Ineraid)	50	
middle ear airspace	∞	

Table 2.2: Resistivity values for model tissues. For the Ineraid model, the spherical stimulating electrode is replaced with a 1 uA point current source at its center while the electrode contact was assigned the same resistivity as intracochlear fluid. For the Nucleus model, the carrier and electrode contacts were treated as nonconductive. Voxels representing the basal and apical ring electrodes of the stimulating pair were held at $\pm$ 1 volt, respectively, while the current between them was measured so that a scaled 1 μA solution could be obtained.

To visualize the segmentation, 3D surface renderings of various structures were generated and viewed simultaneously with representative 2D histological images. Sample renderings from each bone are shown in the results section.

Specification of model fiber tracks

A set of model fiber tracks are defined in the 3D model space based on the expected path a single afferent neuron is likely to take between the habenula perforata and internal auditory meatus (see Figure 2-4). Each fiber track marks a trajectory along which the associated model fiber sits, defining which potentials are extracted to be used as inputs to the single-fiber model used in computing a response. Fiber tracks are defined in each conduction model using a collection of landmarks manually placed on visible anatomical structures at incremental longitudinal cochlear positions. For each cochleotopic position the landmarks included: (1) the tip of the osseous spiral lamina, (2) the junction of Rosenthal's canal with the spiral lamina, (3) the center of Rosenthal's canal, (4) the junction of the internal auditory meatus with the cavernous modiolar bone, and (5) remaining segments of the auditory nerve inside the internal

auditory meatus. In defining the trajectory of model fiber tracks it was assumed that afferent units follow a purely radial course between the perikaryon in Rosenthal's canal and the point of innervation along the organ of Corti. The position along each fiber track (or model fiber) is referenced to the position of the cell body in Rosenthal's canal, with peripheral and central segments having negative and positive positional values, respectively.

The peripheral termination of the 200 model fiber tracks are equally spaced along the longitudinal dimension of the cochlea[5] and indexed by the angular variable θ (degrees from the base). This angular index was specifically chosen so that the geometric relationship of fibers at different cochleotopic positions is easily interpreted. For instance, cross-turn coupling might be expected for fibers separated by 360 degrees in θ. In both models, the location of the most-basal fiber track was determined by the position of the basal-most surviving SGCs. In neither model was the basal hook region populated by model fibers.

In areas where the basilar membrane was dissected by the device, the midpoint between the tip of the osseous spiral lamina and the lateral bony wall was used as a heuristic estimate of the position of the organ of Corti. Cochlear position was converted to characteristic frequency estimates using Greenwood's formula [65].[6]

In the Nucleus bone, a basal section of Rosenthal's canal was obliterated by invasion of the implant array and soft tissue growth (see results). This section was not populated with fiber tracks. Due to substantial drilling and damage at the cochleostomy site, the hook region could not be reconstructed accurately, making an accurate estimate of cochlear position (and characteristic frequency) difficult.

Model calibration - spiral ganglion cell counts

To calibrate the number of neurons represented by each fiber track (and its associated model fiber), segmental counts of the number of spiral ganglion cells in Rosenthal's canal (RC) were made under a light microscope fitted with the Neurolucidia[7] software package. To estimate the number of ganglion cells per unit length along the longitudinal axis of RC, the ideal sampling plane would continuously rotate, remaining perpendicular to the axis of the canal as samples are taken from base to apex as shown in Figure 2-1A. Since the temporal bones were sectioned in the horizontal plane from superior to inferior (as is standard practice [184]), only midmodiolar sections tend to intersect Rosenthal's canal perpendicular to the spiraling axis of the

[5]Longitudinal cochlear position was measured along the approximate position of the organ of Corti, starting at the base.

[6]For an average human $F = A(10^{ax} - k)$ where F is the characteristic frequency (Hz); A= 165.4 (Hz) a= 2.1; x is the normalized position along the basilar membrane (0=apex,1=base); and k = 0.88. Note the constants A and a were not adjusted to the individual length as described by Ketten et al [96] as this adjustment had a negligible impact on the frequency estimates.

[7]Neurolucidia is a registered trademark of MBF Bioscience, Williston, VT.

canal as in Figure 2-1B. Other sections tend to intersect the canal tangential to its axis (Figure 2-1C), such that a much longer segment of the canal is captured than in midmodialar sections. Because a longer segment is captured, the total SGC count from such a section tends to be higher. What is needed is a method for normalizing the counts from these tangential sections to reflect a measure of the number of SGCs *per unit length along the canal.*

To address this issue of tangential sampling of the spiral ganglion, segments of the ganglion captured in tangential sections (e.g. Figure 2-1C) were partitioned spatially into disjoint zones using a coordinate grid created in Neurolucidia. For each mounted section in a series of adjacent slides, this grid allows the total cell count to be subdivided into different zones, with each zone encapsulating a segment of RC that may span several slides. For instance, the length of RC captured in Figure 2-1C can be subdivided into 8 zones. A typical histological image of the basal turn (corresponding to that of Figure 2-1C) displaying these zones is shown in Figure 2-1D. The area of the spiral ganglion is colored black, with the subspace occupying zone 5 colored gray for illustration. Using this coordinate grid, cells in zone 5 can be counted on mounted sections adjacent to the one displayed in Figure 2-1D. Accordingly, cell counts from all mounted sections containing segments of RC inside zone 5 can be added together.

This process of subdividing the tangential sections allows for the 2D reconstruction of the ganglion shown in Figure 2-1E. Dotted horizontal lines denote the mounted sections analyzed, while the outline of RC (obtained from Amira) is shown in blue. The rectangular boxes define zones inside which total SGC estimates were made. The entire length of RC was partitioned into a collection of these zones, with a SGC count assigned to each based on measures made on consecutive sections. Regions where the plane of section approaches 45 degrees to the axis of the canal are especially problematic because to be subdivided they require angled zones, which would require a finer grid then the one used here. This technique also has the drawback that the sampling interval captured along RC is nonuniform. For example, zones containing perpendicular sections capture a shorter longitudinal interval of RC than tangential regions such as zone 5.[8]

Using Amira, the number of fiber tracks having a cell body position in each rectangular zone was determined. Inside each zone, dividing the estimated SGC count by the number of fiber tracks allowed each track (and its model fiber) to be assigned a weight N_f (actual neurons per model fiber) describing the neuron survival. For example, the total cell count made on slide 326 was partitioned among 8 spatial zones.

[8]To most accurately capture the distribution of SGCs, each cell could be counted using Neurolucidia to record the spatial position of each cell. Given these coordinates in 3D space, the number of SGCs along the longitudinal axis of RC could be measured using a uniform sampling interval. This idea is currently being pursued at our institution.

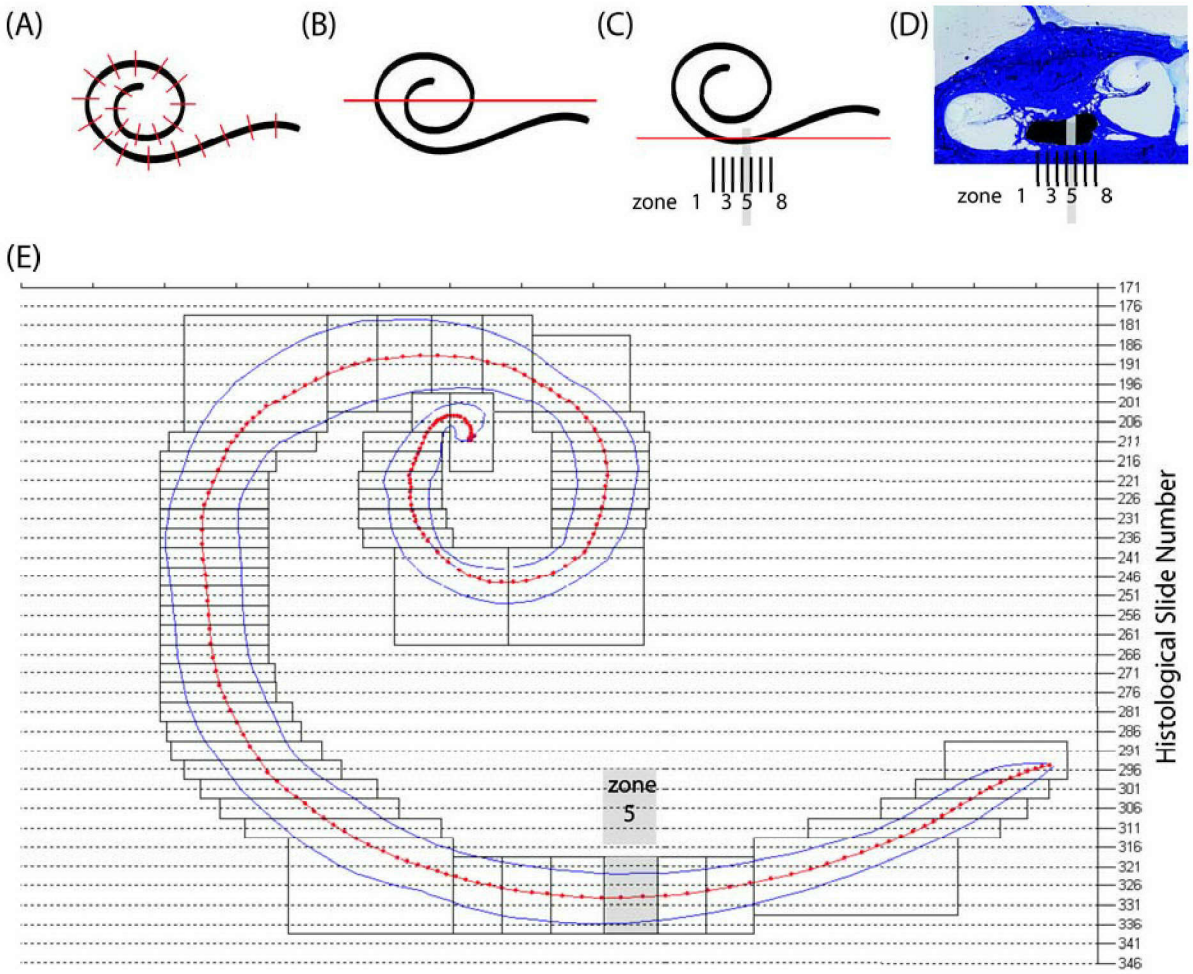

Figure 2-1: (A) Schematic of Rosenthal's canal (black) with tic marks indicating the ideal orientation of sectioning for estimating the number of SGCs per unit length along the canal. (B) A perpendicular section (C) A tangential section. (D) Representative histological section corresponding to the case of panel C showing a tangential section of the basal turn. (E) 2D reconstruction of the Ineraid bone showing the outline of RC (blue), the position of model fiber cell bodies (red filled circles), and the collection of control zones (rectangular boxes). Horizontal dashed lines represent sections for which counts were made on. For each control box, the total number of estimated SGCs divided by the number of model fibers residing in that box was used as a weight describing the number of actual neurons per model fiber.

The estimated number of cells[9] for zone 5 (shaded region in Figure 2-1E) was 132 neurons, based on partial counts taken from slides 321, 326, 331, and 336. Since this segment of RC encompasses 2 fiber tracks, each was assigned a weight (N_f) of 66 neurons per model fiber.

[9]The total SGC estimate incorporates interslide distance and a correction factor of 0.68 to account for double counting [143].

2.2.2 Results

Representative midmodiolar histological images from the Ineraid and Nucleus preparations are shown in Figure 2-2. In both cases the implant has dissected the spiral ligament, damaged the stria vascularis, and a dense layer of fibrous tissue encapsulates the array. In the Nucleus bone, fibrous tissue and new bone nearly completely fill the basal turn. In the basal areas of damage, the communication of different fluid spaces is not known. Because of the extensive disruption of the basilar membrane and Reissner's membrane by the device in both cases, we have assumed fistulae provide a communication of cochlear fluid spaces normally separated by distinct scala in the healthy ear. This is to suggest the membranous epithelium does not strictly compartmentalize the fluid spaces at cochlear positions where membrane dissection occurred.[10]

Reconstruction results for both bones are shown in Figure 2-3. For the Ineraid bone, Panel A depicts a midmodiolar segmented image. Panel B shows an Amira-generated surface rendering of various cochlear structures intersected by a histological image. Panel C includes the reconstruction of Rosenthal's canal along with the population of 200 model fiber tracks (individual red lines). Panels D and E show reconstructions of structures from the Nucleus bone.

Reconstructions of the electrode array for the Ineraid and Nucleus bones are shown in panels A and B of Figure 2-4, respectively. Surface renderings of RC along with the respective population of fiber tracks are displayed. Of particular interest is the buckling of the Nucleus electrode array; the ultimate consequence of which appears to be damage to RC in the basal turn. Careful examination revealed a small population of surviving SGCs basal to this buckling (Figure 2-4B, marker 6) separated from the surviving apical population of SGCs (marker 9) by a region where invasion of the electrode array is speculated to have obliterated a segment of RC (marker 7).

The distribution of intracochlear new bone and fibrous tissue as a function of longitudinal position from the cochleostomy site is shown in Figure 2-5 for both bones. For the Ineraid bone, shown in Panel A, new bone growth is localized primarily to the cochleostomy site and the descending basal turn, whereas in the Nucleus bone extensive new bone formation is found along the entire length of the electrode array. The local decrease in new bone seen 5 millimeters apical to the cochleostomy site in Figure 2-5B is due to electrode array buckling, which occupies a large fraction of the bony duct's volume. The insertion depth of the electrode array is approximately 4 millimeters deeper in the Ineraid bone, as shown by the triangles in 2-5.

While the organ of Corti is typically 2.5 turns, RC typically spirals only approximately 1.5 turns. The issue arises how to map the trajectory of each peripheral

[10]Irrespective of whether or not the basilar membrane is intact, data by Honrubia et al. [84] in the guinea pig suggest that the scala vestibuli and scale tympani are electrically coupled, more than one might expect given their communication at the helicotrema.

process from the cell body in Rosenthal's canal to a cochlear position at the organ of Corti. Toward the base, this mapping remains simple - fibers course radially in the osseous spiral lamina, connecting positions along the ganglion to positions along the organ of Corti. Toward the apex the mapping becomes compressive with incremental segments along RC innervating increasing lengths of the organ of Corti. Leake et al. [106] systematically investigated this mapping in the human, finding a fairly consistent relationship between the longitudinal RC position and the position at the organ of Corti when both were expressed as a percentage of total length. The mapping between the longitudinal position of the cell body in RC and its peripheral process is shown in Figure 2-6A for the 200 model fibers of the Ineraid bone.[11] This ad hoc mapping in the model was created by placing marker points along the organ of Corti and Rosenthal's canal, where the marker point became compressed at the very apex of RC. A comparison of this ad hoc mapping to that reported by Leake et al. is given in Panel B. The similarity between this mapping in the Ineraid model (gray line) and that reported by Leake (black line) suggests the heuristic used for defining model fibers is appropriate.

Characteristic frequency estimates made using Greenwood's formula were assigned to both the model fibers and electrode contacts in each model. Figure 2-7 plots these estimates versus cochlear position in degrees (θ).[12] The frequencies of the basal- and apical-most stimulating electrodes were estimated as 8,267 and 452 Hz for the Ineraid bone, 5,590 and 828 Hz for the Nucleus. Since the apical-most contact of the Ineraid bone is approximately a quarter turn apical to the most apical contact in the Nucleus bone, it is not surprising that its estimated frequency of 452 Hz is nearly half that of the Nucleus. This makes qualitative sense if one considers that since the 2.5 turns of the cochlea span 60 dB in frequency (20 Hz - 20 kHz) then, roughly speaking, each quarter turn spans roughly 6 dB or an octave in frequency. Examination of Figure 2-7 shows that, in terms of θ, each quarter turn of 90 degrees corresponds to roughly an octave span in frequency. Especially for the basal turn, this provides a useful rule of thumb for interpreting data in terms of the angular index θ.

The weights (N_f) applied to calibrate how many surviving SGCs each model fiber represents are shown in Figure 2-8. At all cochlear positions, the number of SGCs per model fiber of the Ineraid bone meets or substantially exceeds that of the Nucleus bone. The total estimated SGC counts for the two bones were 10,248 and 3,865, respectively.

[11] The position along a fiber track where it crosses the center of Rosenthal's canal is taken as the cell body location.

[12] Application of Greenwood's formula requires an estimate of total cochlear length as measured along the basilar membrane. In the Nucleus bone the hook region was obliterated by drilling and/or fibrous tissues, making an accurate measure of total cochlear length difficult. While the hook region only represents a small fraction of total length, because of these difficulties the frequency estimates for the Nucleus bone should be taken as rough estimates.

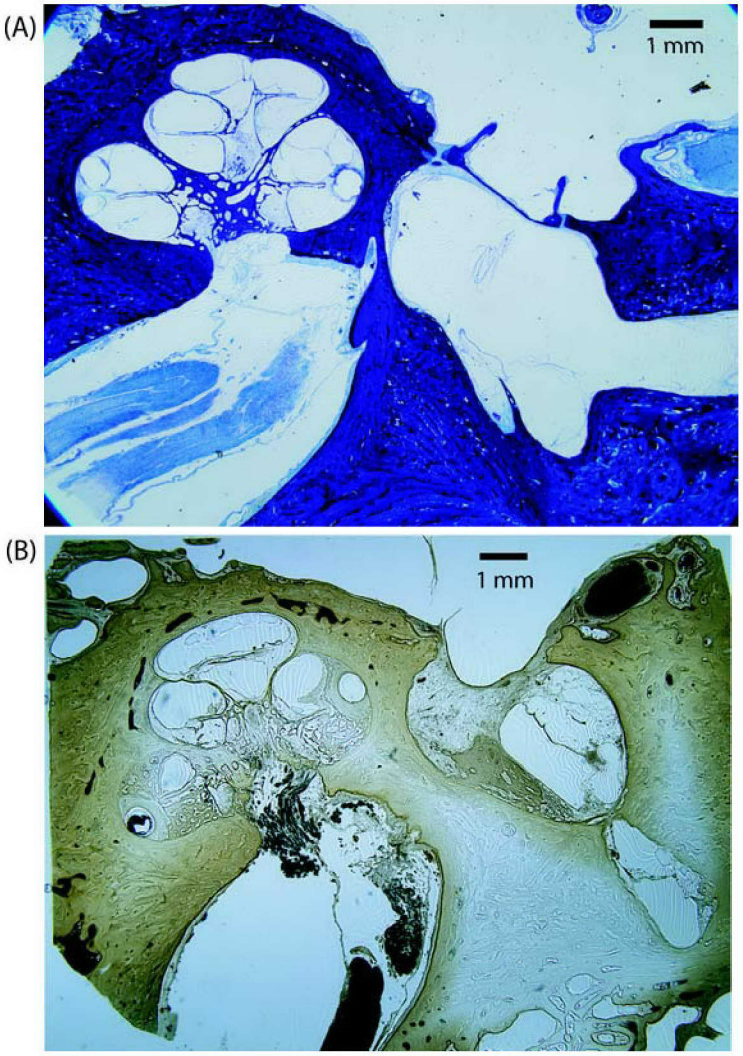

Figure 2-2: (A) Representative midmodiolar images for the Ineraid bone (A) and the Nucleus bone (B). In both cases the electrode array dissected the basilar membrane and is surrounded by a sheath of dense fibrous tissue. The damage to the Nucleus bone is clearly more severe, with new bone and fibrous tissues nearly filling the basal turn.

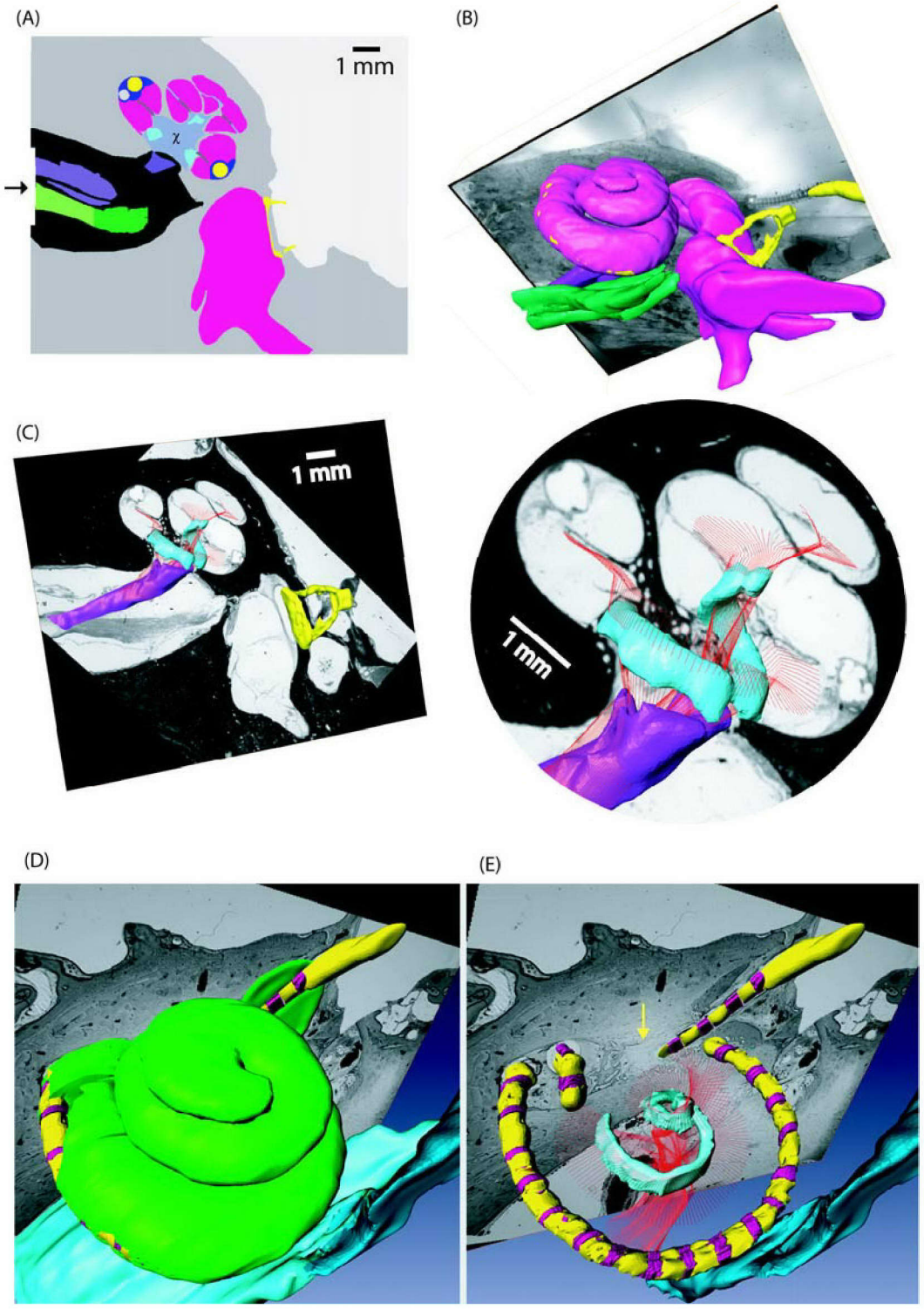

Figure 2-3: (A) Segmented midmodiolar image corresponding to Figure 2-2A. The arrow marks the disk shaped intersection of the auditory nerve with the model boundary used as a grounding plate for monopolar stimulation. (B) Surface rendering showing the wall of the bony labyrinth (pink); auditory (purple), vestibular (green) and facial (green) nerves; stapes (yellow); and implant array (yellow). The image intersecting the model is one of the block face images taken during histological sectioning. (C) Reconstruction of RC and the auditory nerve along with the population of fiber tracks (red lines), intersected by a histological image captured under the microscope. (D) Surface rendering of Nucleus bony wall intersected by a basal histological section. (E) Intracochlear structures of the Nucleus bone. The downward arrow marks a region where the electrode array has damaged and eroded RC.

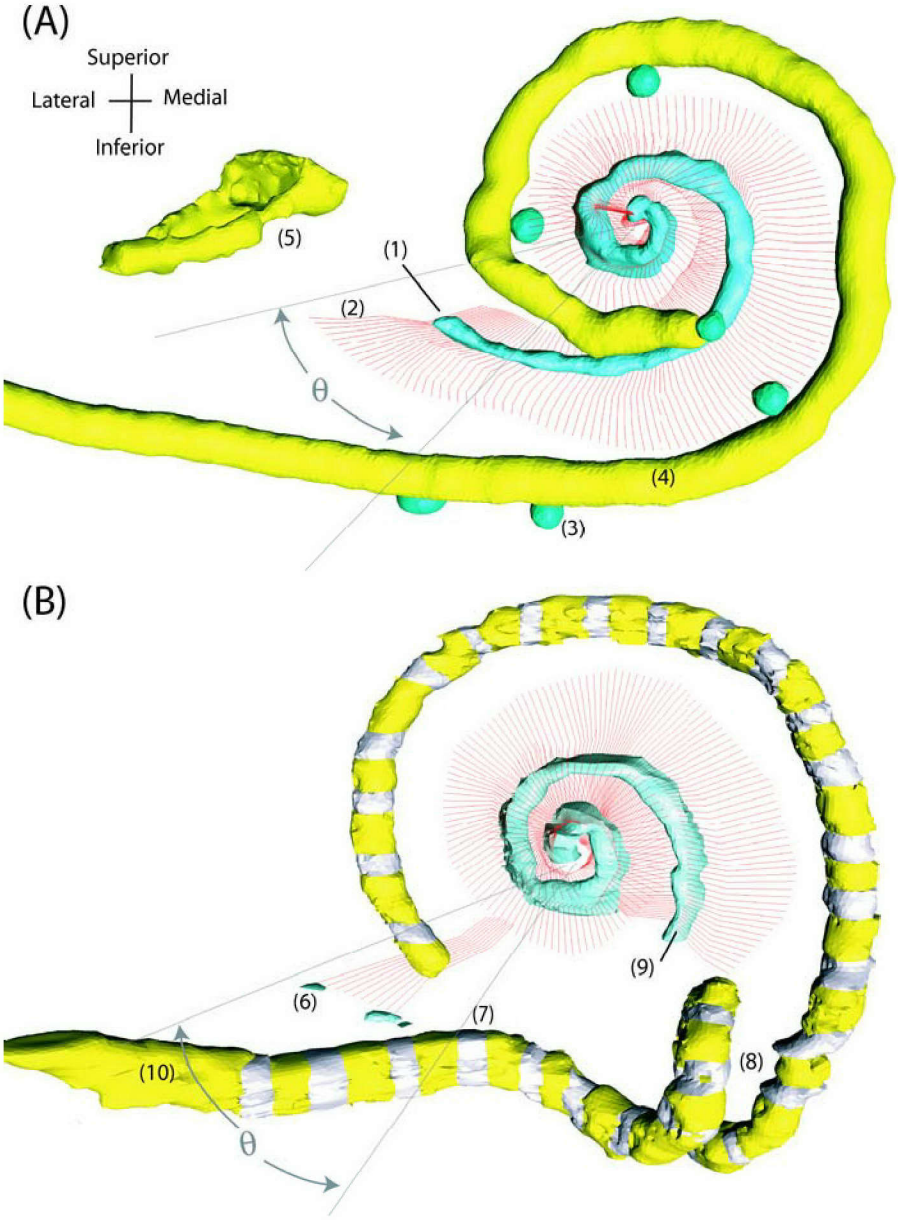

Figure 2-4: (A) Reconstruction of the Ineraid model showing Rosenthal's canal **(1)**, basal fiber tracks **(2)**, ball electrodes **(3)**, silastic carrier **(4)**, and stapes **(5)**. (B) Reconstruction of the Nucleus array showing a basal segment **(6)** and apical segment **(9)** of RC with fiber tracks, separated by an atrophic region **(7)** where the electrode array apparently eroded the modiolus. There is coiling **(8)** of the electrode carrier in the basal turn, shortening the insertion depth of the device. The Nucleus array **(10)** has 22 active banded electrodes along with **10** inactive stiffening rings at the basal end. These plots are drawn from the vantage point looking down the cochlear axis. The angular variable θ is used to index fiber tracks in degrees from base to apex.

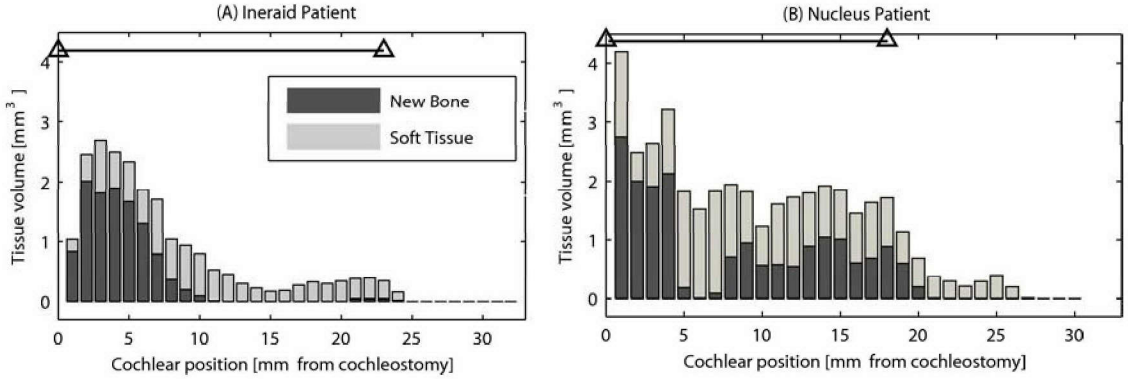

Figure 2-5: Volume of new bone and soft fibrous tissue in the bony duct as a function of longitudinal position for the Ineraid patient (A) and the Nucleus patient (B). The left and right △s mark the cochleostomy site and apical termination of the electrode array, respectively.

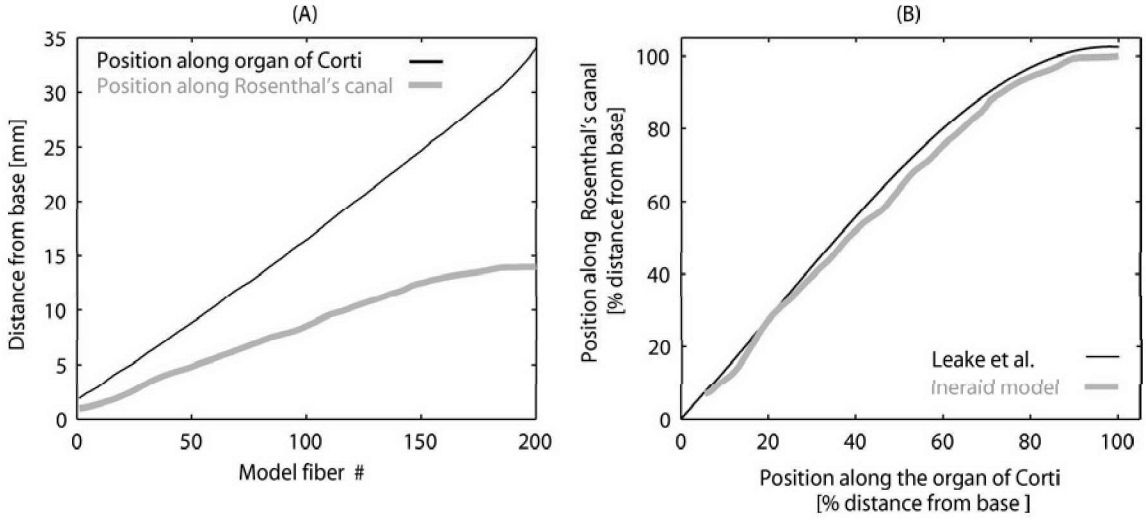

Figure 2-6: (A) Longitudinal position of the model fiber track in Rosenthal's (gray line) and at the peripheral termination along the organ of Corti (black line) plotted as a function of model fiber number. Note the most-basal fiber has a cochlear position of ≈ 2 mm because of the exclusion of the hook region. (B) Mapping between longitudinal position along Rosenthal's canal and the organ of Corti for fibers of the Ineraid model (gray) and as reported by Leake et al. [106] (black)

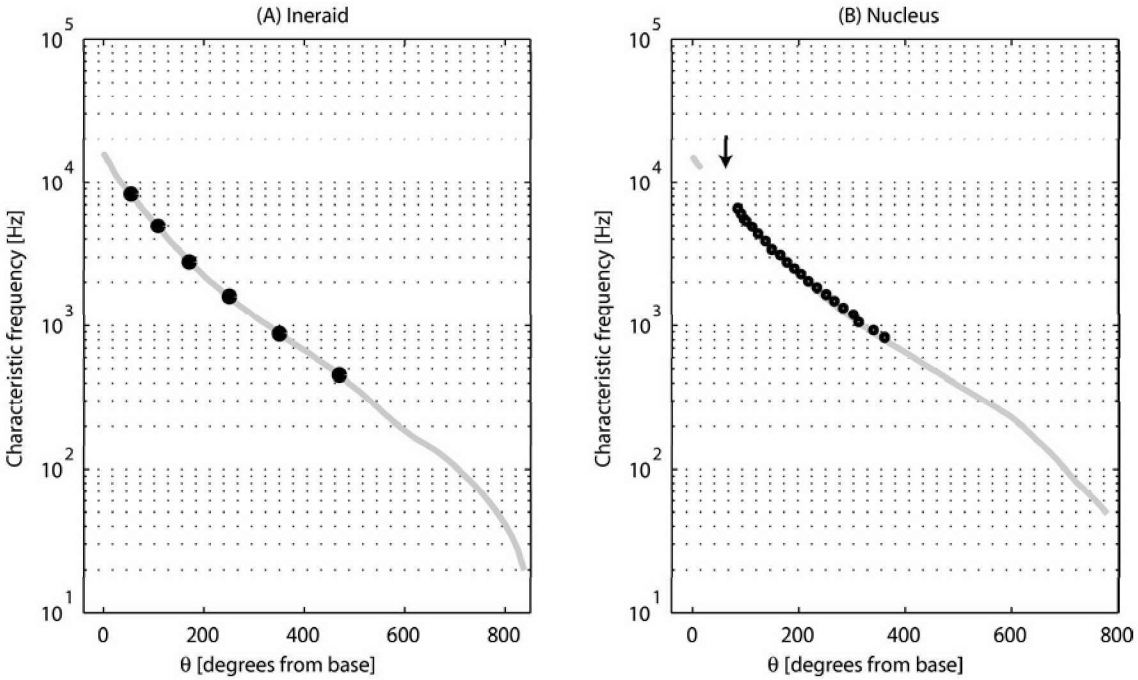

Figure 2-7: (A) Characteristic-frequency estimates for the Ineraid model fibers (line) and electrode contacts (filled circles) as a function of longitudinal cochlear position (θ) in degrees from the base. (B) As in Panel A, for the Nucleus model. Only the 22 active electrodes are plotted. Notice the gap in model fibers basal to the basal-most electrode contact due to the obliteration of RC in this region (see ↓).

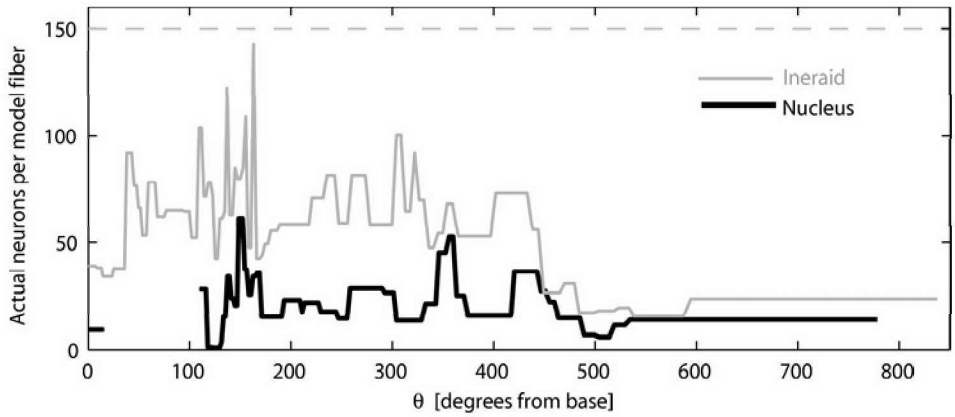

Figure 2-8: Fiber weights N_f for the Ineraid (gray) and Nucleus models (black). The dashed horizontal line represents the approximate number of SGCs each model fiber would represent given a healthy population of 30,000 SGCs uniformly distributed across cochlear length.

2.3 Prediction of current flow

After a segmented model is created using the reconstruction software and a resistivity assigned to each material, a prediction of current flow is made. The potential field created by the simulating electrode(s) in the volume conduction model is computed for an arbitrary configuration of stimulating electrodes.

Given the 3D assignment of resistivities, the position of point current sources, and a set of boundary conditions, a solution is obtained for a 1 μA unitary current[13] between stimulating electrodes. Scaling this solution as a function of time, in this case a 30 μs/phase biphasic pulse, yields the time-varying potential at all spatial positions on the model interior. The time-varying potential along each model fiber is then extracted and treated as the extracellular potential ($V_e(t)$) in the single-fiber model used to calculate a neural response. Additionally, the 3D current density field is calculated to quantify the amount of current passing through various anatomical regions of the model as the stimulus conditions are changed. Monitoring the predicted change in current flow as either the electrode position or the anatomy is modified, allows one to probe the impact of these individually.

2.3.1 Methods

The pulsatile potential field created by the simulating electrode(s) in the volume conduction model is computed using finite-difference techniques in combination with the preconditioned conjugate gradient method (see Mohr and Vanrumste [137]). Briefly, the first step of this calculation provides a discrete approximation to the elliptical boundary value problem describing current flow under electroquasistatic conditions inside the model of the implanted ear:

$$\nabla \cdot \mathbf{J} = -\sigma \nabla^2 \Phi = \left\{ \begin{array}{ll} +1\mu A & \mathbf{r} = \mathbf{r}_{source} \\ -1\mu A & \mathbf{r} = \mathbf{r}_{sink} \\ 0 & \text{otherwise} \end{array} \right\} \tag{2.1}$$

where $\mathbf{r}$ is the positional index of 3D space, $\mathbf{J}(\mathbf{r})$ is the current density field, $\sigma(\mathbf{r})$ is a scalar describing the conductivity of each region of space, $\Phi(\mathbf{r})$ is the potential field, and $\mathbf{r}_{source}$ and $\mathbf{r}_{sink}$ are the respective positions of theoretical point current sources and sinks (analogous to charge density in electrostatics [162]).

We adopt the Neumann boundary condition:

$$\mathbf{J} \cdot \mathbf{n} = 0 \tag{2.2}$$

[13] All current values and current waveforms are given as 0-peak.

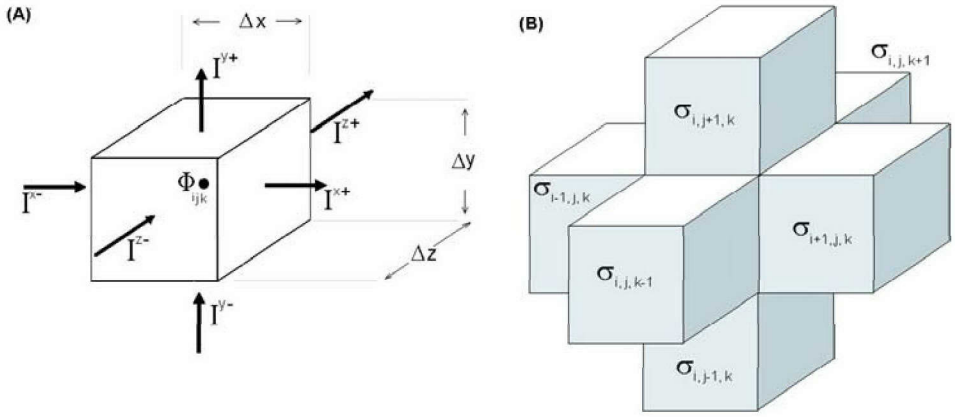

Figure 2-9: (A) A single element (voxel) of the volume conduction model. The potential $\Phi_{i,j,k}$ is measured at the center of the element with isotropic conductivity $\sigma_{i,j,k}$. (B) Six neighbor approximation. The potential and conductivities of the six neighboring elements are used to write a current conservation equation for the element centered on $\Phi_{i,j,k}$.

where **n** is an outward normal vector at the model boundary, meaning current flow is confined to the model interior. The model solves a discrete approximation to 2.1 and 2.2 to return the potential $\Phi_{i,j,k}$ at the center of each conductive element $\sigma_{i,j,k}$ in the model, indexed in 3 dimensions by i, j, and k. This is accomplished by writing a current conservation equation:

$$I^{x-} - I^{x+} + I^{y-} - I^{y+} + I^{z-} - I^{z+} = I^{s}, \tag{2.3}$$

for each element such as the one shown in Figure 2-9A where I^{x-} is the current entering the element in the x-direction and I^{s} the volumetric current source, equal to zero except for elements containing a current source or sink. The current I^{x-} is defined by the potential at the element's center $\Phi_{i,j,k}$, that of its neighbor in the negative x-direction $\Phi_{i-1,j,k}$, the conductivities of the two elements $\sigma_{i,j,k}$ and $\sigma_{i-1,j,k}$, and the element's physical dimensions as:

$$I^{x-} = \left(\frac{\sigma_{i,j,k} \cdot \sigma_{i-1,j,k}}{\sigma_{i,j,k} + \sigma_{i-1,j,k}}\right)\left(\frac{\Phi_{i-1,j,k} - \Phi_{i,j,k}}{\Delta x}\right)\Delta y \Delta z \tag{2.4}$$

Equations similar to 2.4 describe the coupling between the potential $\Phi_{i,j,k}$ and the potential of each of its 6 neighbors. Substituting these six equations into the current conservation equation of 2.3

allows a linear function of seven unknowns to be written for each element as:

$$\begin{aligned} &\alpha_1\Phi_{i,j,k} + \alpha_2\Phi_{i-1,j,k} + \alpha_3\Phi_{i+1,j,k} + \\ &\alpha_4\Phi_{i,j-1,k} + \alpha_5\Phi_{i,j+1,k} + \alpha_6\Phi_{i,j,k-1} + \alpha_7\Phi_{i,j,k+1} \;=\; I^s_{i,j,k} \end{aligned} \tag{2.5}$$

where the α coefficients are determined by the conductivity and physical dimensions of the center element and its 6 neighbors. Writing an equation such as 2.5 for each element defines a system of linear equations that can be recast in matrix form, $\mathbf{A\Phi} = \mathbf{I^s}$, where the elements of $\mathbf{\Phi}$ are the unknown potentials, $\mathbf{I^s}$ is a vector of zeros with nonzero entries only at source and sink locations, and $\mathbf{A}$ is a symmetric sparse matrix with only seven nonzero diagonals containing the values of α.

In the second step of this procedure, the potential solution $\mathbf{\Phi}$ is obtained as $(\mathbf{A}^{-1})\mathbf{I^s}$.[14] Since the number of unknowns for these systems approaches 20 million, an iterative solver is needed. Here we use the preconditioned conjugate gradient (PCG) method with symmetric successive over relaxation (SSOR) as implemented by Girzon [60].

For the Ineraid model, the monopolar stimulating electrode is replaced with a 1 μA point current source at its center. The potential of the disk-shaped intersection of the auditory nerve with the posterior aspect of the model (see $\rightarrow$ in Figure 2-3A) is held at zero,[15] forcing current to exit the model via this grounding electrode in the internal auditory meatus (5.7 mm from RC). For the Nucleus model, volume elements (voxels) representing the basal and apical ring electrodes of the bipolar stimulating pair were held at $\pm$ 1 volt respectively, while the current between them was measured. Normalizing by this current returns the spatial solution for 1 μA of current between electrodes.

The current density vector, $\mathbf{J}$, is calculated as $-\sigma\nabla\Phi$ as in equation 2.1. Since this 3D field is difficult to display in a meaningful way, two summary measures of the current density were computed as a function of cochlear position. First, the magnitude of the current density vector was measured in RC ($|J_{rc}|$) at the position of the cell body associated with each model fiber. The component of the current density vector in the direction parallel to the fiber's trajectory, J_{rc}, was also computed as $\mathbf{J} \cdot \mathbf{n_{rc}}$ where $\mathbf{n_{rc}}$ is a unit vector pointing in the direction of the model fiber (Figure 2-10). Accordingly, at each position along RC the ratio of J_{rc} to $|J_{rc}|$ describes the proportion of the current density orientated parallel the model fiber's trajectory in

[14]For a system containing only point current sources, the solution to $\mathbf{A\Phi} = \mathbf{I^s}$ is not unique, having an infinite number of solutions differing only by a constant. The solution can be made unique by fixing a single value of $\Phi_{i,j,k}$; however, we did not follow this approach since all later computations involved derivatives of Φ such that any additive constant to the solution vector does not have an effect.

[15]By fixing the solution of this disk, the Neumann boundary condition normally found at the model boundary is replaced by this Dirichlet boundary condition.

RC.

The second measure is the longitudinal current density, J_l, running along the bony duct parallel to the lateral bony wall in the apical direction. These measures were made along a curve fit to the center of the scala tympani by evaluating $\mathbf{J} \cdot \mathbf{n_l}$ at each cochlear position, where $\mathbf{n_l}$ is a unit normal vector tangential to the curve, pointing toward the apex (Figure 2-10). The magnitude of the current density at each cochlear position $|J_{cp}|$ along this curve was also measured for comparison, such that the ratio of J_l to $|J_{cp}|$ describes the proportion of the current density orientated longitudinally.

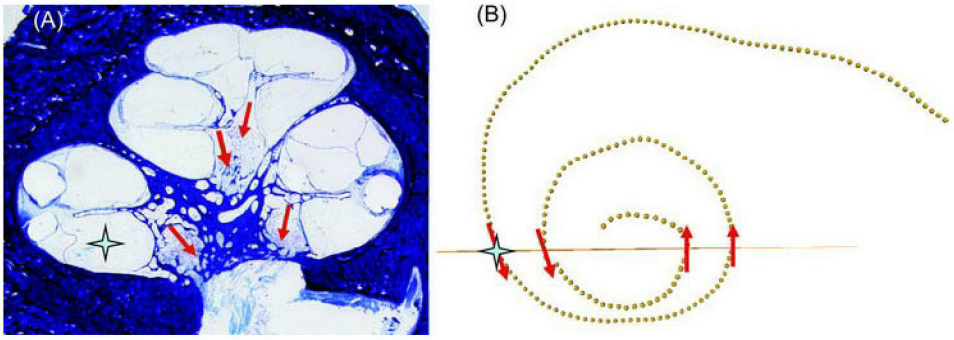

Figure 2-10: (A) Measurement of the modiolar current J_{rc}. Mid-modiolar section showing the orientation of J_{rc} (red arrows) at four different positions along RC. Each arrow shows the direction of the unit normal vector $\mathbf{n}_{rc}$ used to calculate $J_{rc} = \mathbf{J} \cdot \mathbf{n}_{rc}$. (B) Measurement of J_l. Coronal view of reconstructed sections, with the dotted line representing the center of the scala tympani at each longitudinal cochlear position. The horizontal line shows the position of the histological section on the left. The star marks the center of the scala for the same turn as in the left picture. For each cochlear position along the curve, J_l is measured as the component of current density in the direction tangential to this spiral (toward the apex). Each arrow shows the direction of the unit normal vector $\mathbf{n}_l$ used to calculate $J_l = \mathbf{J} \cdot \mathbf{n}_l$.

The distribution of J_{rc} and J_l as a function of cochlear position (θ) describe current flow for any configuration of stimulating electrodes. These were specifically chosen to mirror a transmission line analogue where J_l represents current carried in the conductor (in this case cochlear fluid inside the bony duct), while J_{rc} represents the current that exits the "conductor" into RC. Using these two measures alone, a rudimentary description of current flow in the model is obtained. Tracking changes in J_{rc} and J_l while making anatomically relevant changes to the model illustrates the influence of anatomy on current flow.

2.3.2 Results

Preliminary current flow experiments were conducted using the basic formulation of the Ineraid model (bEAM). Model predictions of the potential field and current flow created by monopolar stimulation of the most basal (EL6) and apical (EL1) electrodes are shown in the left and right column of Figure 2-11, respectively. The panels of the top row show the potential predicted at the center of the scala tympani as a function

of cochlear position. The panels of the middle row show the longitudinal current predictions (J_l and $|J_{cp}|$). The bottom panels show the currents in Rosenthal's canal (J_{rc} and $|J_{rc}|$) as a function of cochlear position (θ).[16]

For the case of basal stimulation in left column of 2-11, the potential as a function of cochlear position has several local maxima and minima, corresponding to places where the direction of longitudinal current reverses. For example, the basal-most local minima in Panel A ($\bigtriangledown$ at a cochlear position of $\approx$ 280 degrees) marks where the longitudinal current J_l changes from positive to negative in Panel C. Immediately basal to 280 degrees, the longitudinal current flows apically. For $280 < \theta < 480$ degrees current flows toward the base due to cross-turn coupling. Above $\approx$ 480 degrees, J_l is once again positive marking another change in the longitudinal current direction such that 480 degrees is a local maxima ($\bigtriangleup$) in the potential curve of Panel A. The sign of J_l also reverses at the position of the electrode (marked by $\otimes$), since the convention adopted is for positive J_l to indicate apically flowing current. Areas where the trace for J_l and $|J_{cp}|$ meet indicate areas along the scala where the current density vector is longitudinal in orientation.

Regardless of the direction of the longitudinal current, the orientation of the current in RC as measured by J_{rc} in Panel E, is always positive (flowing away from the cochlear duct into the modiolus). Furthermore, the curves for J_{rc} and $|J_{rc}|$ nearly overlap, indicating the current density vector is essentially aligned with the trajectory of the model fiber at the cell body. The bulk of the current entering RC is spread over the basal 400 degrees, indicating current spread is not confined to a single cochlear turn. Panel E shows an unexpected local minima in J_{rc} near 200 degrees, which was determined to be a result of the asymmetry created by the angle of the internal auditory meatus to the axis of the cochlear spiral, as discussed in Chapter 4.

For the case of apical stimulation in the right column 2-11, the potential as a function of cochlear position in Panel B only shows cross-turn coupling apical to the electrode, with a single local minima represented by the $\bigtriangledown$ to the right of the electrode's position. In the same regions where cross turn coupling gives rise to positive and negative values for J_l with *basal* stimulation (0-500 degrees), *apical* stimulation shows longitudinal currents that are strictly negative (current flow toward the base). As was the case for basal stimulation, the RC current for apical stimulation in Panel F is both strictly positive, and spread over multiple cochlear turns.

Comparing the distributions of J_{rc} shown in the bottom panel, it is clear that the region of the maximum of J_{rc} depends on the stimulating electrode position, but the longitudinal current spread is so extensive that at least an entire cochlear turn has significant current flow into RC. Using the heuristic from Figure 2-7, a span of 360

[16]Note for consistency RC-currents are plotted versus θ (which measures the angular position of the model fiber's peripheral element) even though the cell bodies of the most apical fibers ($\theta > \approx 600$) occupy the same position in RC. This can be seen in Figure 2-6A where the apical-most fibers all have the same position along RC.

degrees in θ translates to a frequency span of roughly 4 octaves. Clearly the neurons influenced by stimulation of either electrode span a wide range of characteristic frequencies according to this prediction. In the case of apical stimulation, the majority of the spread in J_{rc} is basal to the position of the electrode, as seen in Figure 2-11F.

Additionally, the total current that enters RC (as opposed to alternative pathways to the ground in the internal auditory meatus) is larger for apical stimulation. This result can be seen by comparing the area under the curves for J_{rc} in the bottom panels of 2-11. Even without the use of a single-fiber model, this result suggests apical electrodes will have lower psychophysical thresholds, since the geometry results in a larger proportion of the stimulus current entering RC.

Intracochlear currents in a homogeneous model

An important issue to address is to what extent a volume conduction model is even necessary. One alternative is to simply represent the anatomy of the model nerve fibers and position of the electrodes as a collection of points in 3D space, then use electrostatic theory to analytically define the potential everywhere in space assuming a uniform conductivity. This approach, henceforth referred to as the homogeneous model, has often been used as a first-order approximation for the extracellular potential along a nerve fiber. To measure the impact of representing the anatomical inhomogeneities, plots for J_l and J_{rc} were calculated for the homogeneous model[17] and compared to the predictions of the computational volume conduction model (bEAM).

The potential function measured at the center of the scala tympani is plotted in Figure 2-12A for both the volume conduction and homogenous models. Each is normalized as a percent of the maximum value.[18] Shown in panels B and C of Figure 2-12 are predictions of J_l and J_{rc}, respectively, for monopolar stimulation of electrode 3 (EL3). Comparing the homogeneous J_l (gray) with the volume conduction solution (black), it is clear the homogeneous prediction shows significantly less longitudinal spread than the volume conduction solution. The homogeneous solution for the RC-currents J_{rc} (gray) has regions where the predicted RC-current flow is both positive (headed into the modiolus) and negative (headed out of the modiolus), whereas in the volume conduction counterpart J_{rc} is consistently positive. Furthermore, the bulk of the homogeneous J_{rc} (gray) in panel C is concentrated in a region of roughly 75

[17]Replacing all cochlear tissues with a homogeneous, isotropic, conductive medium; the potential in 3D space can be solved analytically for an arbitrary collection of stimulating electrodes using superposition. For a 1 μA point current source in an infinite homogeneous medium of conductivity σ the potential Φ is described by:

$$\Phi(r) = \frac{1\mu A}{4\pi\sigma r} \tag{2.6}$$

where r is the distance from the source. The conductivity of nerve tissue $\sigma = \frac{1}{300\Omega cm}$ was used for this solution.

[18]The potential Φ is plotted as $\frac{\Phi - min(\Phi)}{(max(\Phi) - min(\Phi))}$

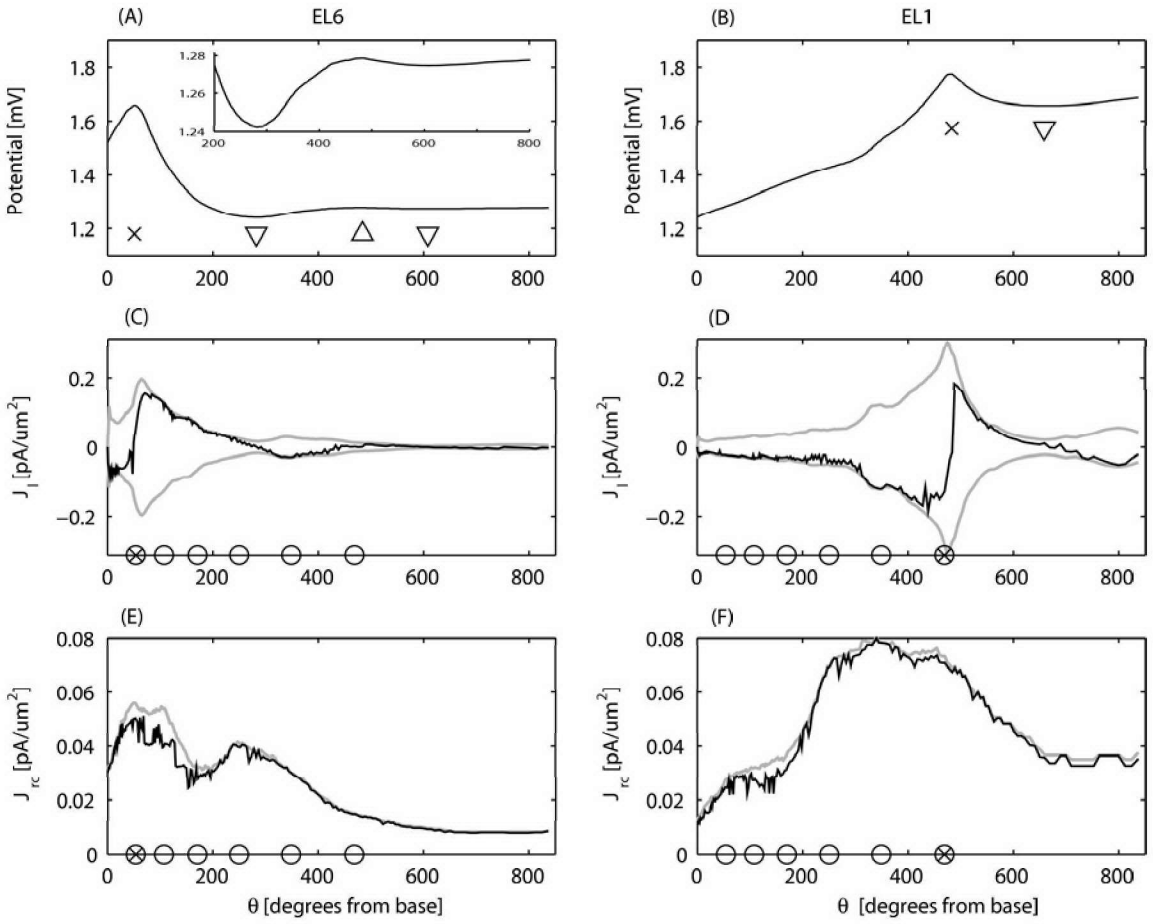

Figure 2-11: (Top Panels) Potential measured at the center of the scala tympani as a function of cochlear position (θ), measured in degrees from the base, for basal (A) and apical (B) monopolar stimulation with 1 μA. The position of the electrode is marked by $\times$. Local minima and maxima are marked by $\bigtriangledown$ and $\bigtriangleup$ respectively. These mark positions where the derivative of the potential with respect to θ is zero. **(Middle Panels)** Longitudinal current J_l versus θ for basal (C) and apical (D) stimulation with the active electrode marked by $\otimes$. J_l shown in solid black with positive values indicating apical flow. $|J_{cp}|$ and $-|J_{cp}|$ are shown in gray, where the ratio $J_l/|J_{cp}|$ is the percentage of the current vector pointing in the longitudinal direction. **(Bottom Panels)** RC-currents J_{rc} (black) and $|J_{rc}|$ (gray) versus θ for apical (E) and basal (F) simulation.

degrees, while the bEAM J_{rc} (black) is spread across a substantial percentage of the total RC length.

Collectively, the panels of Figure 2-12 show that the distribution of intracochlear currents predicted by the model have very little similarity with the familiar analytic solutions obtained with a homogeneous model. Accordingly, the use of a homogeneous model to predict spatial (cochleotopic) excitation patterns seems fairly limited, even if one represents the fiber trajectory in 3D before applying an analytic solution as was done here. The dissimilarity between the homogeneous and volume conduction solutions also suggests that the Euclidian distance between a spiral ganglion cell and

the stimulating electrode provides little information about the spatial selectivity of stimulated neurons.

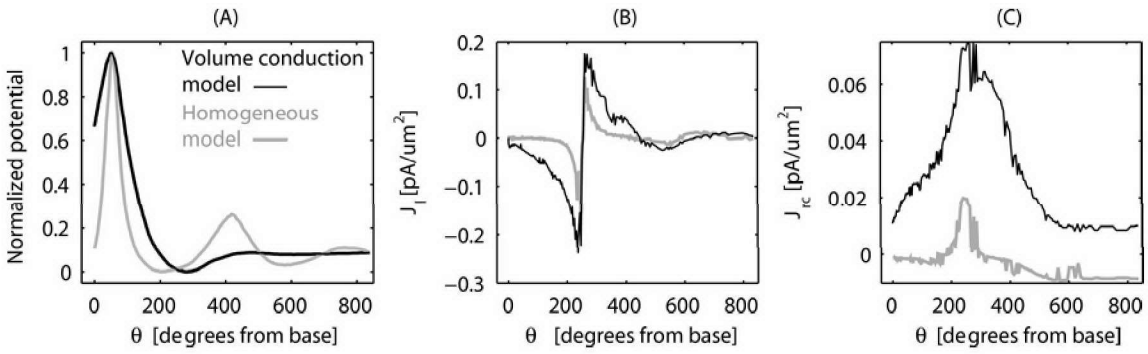

Figure 2-12: (A) Normalized potential function predicted at the center of the scala tympani for the bEAM volume conduction and homogeneous models. (B) Longitudinal current J_l versus cochlear position, predicted for stimulation of EL3 in both models. (C) J_{rc} predicted for both models. Note the applied current is 1 μA in each case.

Comparison of monopolar versus bipolar intracochlear current flow

To compare the intracochlear current patterns elicited during monopolar and bipolar stimulation, two Nucleus-style ring electrodes were added to the basic model and used to compute a bipolar solution. Two cylindrical sections of the electrode carrier, each measuring 0.3 mm long with a separation of 0.7 mm, were held at $\pm$ 1 V. The computed potential solution was then scaled such that 1 μA of current passed between the electrode pair. This provided a bipolar solution for comparison with the 1 μA solution for a monopolar electrode at a similar cochlear position in the same model. Measures of the longitudinal and RC-currents for the bipolar (gray) and monopolar (black) are compared in Figure 2-13.

For the bipolar case, the longitudinal current density J_l in Figure 2-13A has a sharp negative peak at a position between the two electrodes. Here the peak is negative since the positive apical electrode drives current toward the base. While this peak is at the target cochleotopic position (i.e., between the electrodes), it is oriented longitudinally - orthogonal to the nerve fibers - such that it is unlikely to excite those neurons. This is consistent with plots of the RC-current shown in Figure 2-13B. Here a few points are worth emphasizing. First, the monopolar J_{rc} is unimodal and approximately an order of magnitude larger than the bipolar case. This is consistent with behaviorial thresholds for monopolar stimuli typically being nearly an order of magnitude lower than bipolar stimuli. Second, for the bipolar case, the J_{rc} is biphasic and spans an appreciable length of the cochlea. This is clarified in Figure 2-13C where the monopolar and bipolar traces of J_{rc} are normalized as a percent maximum. These suggest that with bipolar stimulation the spread of current (as measured in the modiolus) can be similar to that present with monopolar stimulation.

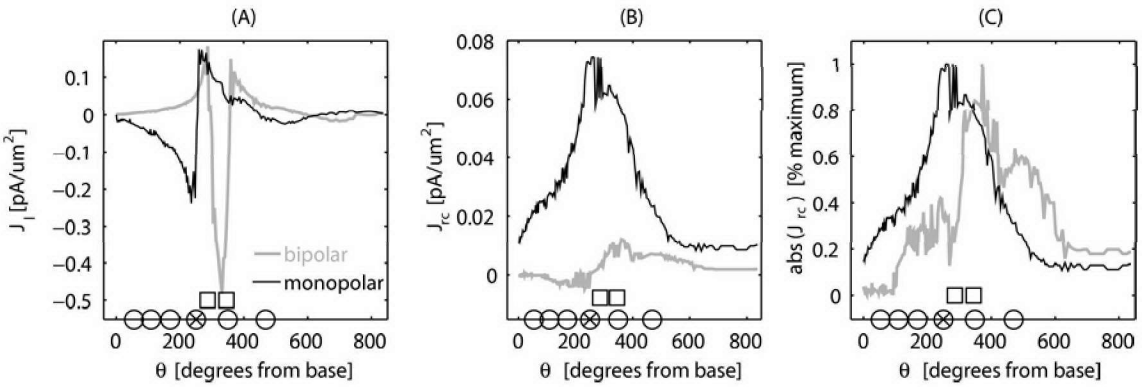

Figure 2-13: (A) Longitudinal current J_l for 1 μA monopolar stimulation with EL3 (black), and 1 μA stimulation with a Nucleus-style, bipolar pair at the same cochleotopic position (gray). The position of the active monopolar electrode is given by $\otimes$. The position of the Nucleus-style ring electrodes are marked by $\square$. (B) Modiolar currents J_{rc} for monopolar (black) and bipolar (gray) stimulation. (C) RC-current pattern after taking the absolute value of J_{rc} (bipolar case) and normalizing each curve as a percent of its maximum value.

Sensitivity of model to resistivity value assignments

To measure the influence of the resistivity assignments on the modeling results, the field solution was recomputed and the RC-current magnitude $|J_{rc}|$ recalculated as the resistivity values of bone, intracochlear fluid, and the modiolar/nerve tissue[19] were individually adjusted. Results are shown in the three columns of Figure 2-14 for three stimulus electrodes. The top, middle, and bottom rows show $|J_{rc}|$ versus cochlear position as the resistivity of bone, fluid, and nerve tissue are varied from their reference values (Table 2.2). The resistivity of each was doubled (+6 dB), and halved (-6 dB).

A few qualitative aspects of Figure 2-14 fit with intuition. Doubling the bone resistivity (+6 dB condition, top row) and halving the nerve resistivity (-6 dB condition, bottom row) have a similar effect in that both increase $|J_{rc}|$ in comparison to the reference condition. This is largely expected since either of these changes makes the modiolus a relatively lower resistance path to ground. Comparing the top and bottom rows of Figure 2-14, it is clear the overall influence of changing the resistivity of bone or nerve tissue is to scale $|J_{rc}|$ in opposite directions, while the shape of these $|J_{rc}|$ curves remains largely the same (compare the +6 dB condition of Panel A with the -6 dB condition in Panel H). This supports the idea that it is the geometry of the model and the ratio of the conductivities that determines the shape of $|J_{rc}|$ for stimulation by a monopolar electrode. This agrees with the findings of Rattay [168] who reported that in their model doubling resistivity of nerve, cochlear fluid, bone,

[19]This includes all 300 Ωcm areas of the modiolus, nerve tissue, and internal auditory meatus.

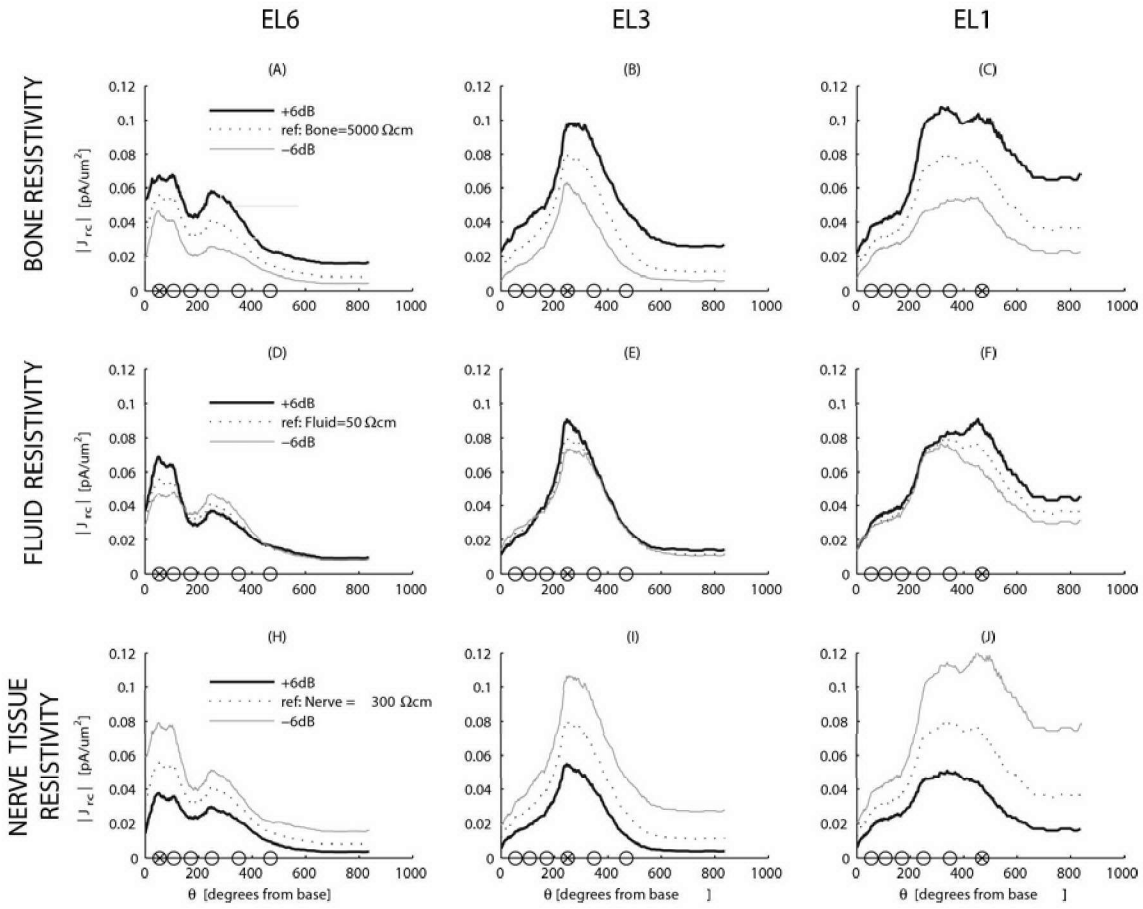

Figure 2-14: Sensitivity of $|J_{rc}|$ to resistivity value. Modiolar current is plotted versus cochlear position for monopolar stimulation by EL6 (left column), EL3 (middle column) and EL1 (right column) while the resistivity of bone (top row), fluid (middle row), or nerve tissue (bottom row) is varied. Electrode positions shown as open circles with the stimulating electrode marked as $\otimes$. **(A-C)** RC-currents predicted for bone resistivities of 10,000 Ωcm (+6 dB re reference), the standard 5,000 Ωcm (ref),and 2,500 Ωcm (-6 dB). **(D-F)** RC-currents as for three intracochlear fluid resistivities (+6 dB, ref, and -6 dB). **(H-J)** RC-currents predicted for three nerve resistivities (+6 dB, ref, and -6 dB).

the basilar membrane, or organ of Corti did not essentially change the shape of the extracellular potentials along model fibers.

Unexpectedly, changes in the fluid resistivity had a relatively small impact on both the shape and magnitude of $|J_{rc}|$. Lowering the fluid resistivity (gray, middle row) slightly broadened the distribution of current in panels D and E; however, it shifted the peak in $|J_{rc}|$ of panel F toward a cochlear position of 320 degrees even though the EL1 stimulating electrode is located at 469 degrees. Comparing the columns of Figure 2-14, it is also clear that adjusting the resistivity of any material had its largest impact for apical stimulation (right column) where the magnitude of the RC-current can vary by as much as 9 dB as the resistivity is adjusted over a range of 12 dB.

2.3.3 Discussion

While changes in the bone resistivity of ± 6 dB have a tendency to simply scale $|J_{rc}|$ by an average of roughly +/- 2.5 dB (see Figure 2-14), lowering the bone resistivity to near 600 Ωcm (a value from Suesserman [204] commonly used in other modeling studies, e.g., Frijns et al. [53] and Hanekom [73]) has an effect on both the magnitude and shape of the current distribution across cochlear position.

In Figure 2-15, $|J_{rc}|$ is plotted as a function of θ for bone resistivities in the bEAM that span nearly three orders of magnitude. Decreasing bone resistivity to 600 Ωcm moves the predicted RC-current further toward that predicted with a homogeneous model (compare the dotted and gray lines in 2-15). Beginning with the 600-Ωcm case, as the bone resistivity increases two trends are apparent: (1) more current enters the 300 Ωcm modiolus, and (2) J_{rc} becomes less localized around the stimulating electrode, as seen in panel B where each curve is normalized to its maximum value. With bone set to 50 kΩcm, current spreads across the entire spiral such that $|J_{rc}|$ is only marginally focused at the stimulating electrode.

Figure 2-15 shows current flow predicted by the bEAM to fall conceptually between two extremes: (1) the homogeneous case where current flow is not influenced by inhomogeneities in the intracochlear tissues, and (2) the transmission line case (i.e., 50 kΩcm bone) where current in the fluid spiral resembles that of a transmission line with a length constant comparable to, or greater than, the 35 millimeter total length of the cochlea, such that there is little variation in either J_{rc} or J_l across cochlear position.[20] Figure 2-15 suggests current flow predicted by the bEAM with 600 Ωcm-bone to be similar to the homogeneous model while the 5 kΩcm bEAM is closer to a transmission line model.

This agrees with the modeling results of Rattay [168] who concluded that "(i) changing the conductance of any region between a factor of 0.5 and 2 will not fundamentally influence the voltage profile [along model fibers]" and "(ii) if we follow Finley (1990)[reference to [47]], assuming a bone conductance more close to that of nerve tissue, all results concerning voltage distribution are moved toward the homogeneous field solution...."

This observation also agrees with the analysis of Girzon [60], who measured the potential on unstimulated intracochlear electrodes while stimulating with a monopolar electrode in a series of 5 subjects. Comparing these recordings to predictions made by various models, he also concluded the measured intracochlear potentials were better

[20]For a resistive transmission line with a current (I) delivered to the core conductor (cochlear fluid) at a position (z=0), the current density exiting the conductor ($\tilde{J}_{rc}$) along its length z will vary approximately as:

$$\tilde{J}_{rc} = I \cdot \phi \cdot e^{\frac{-|z|}{\lambda_c}} \tag{2.7}$$

where λ_c and ϕ are constants determined by the ratio of bone to fluid resistivity, the conductor dimensions, and the termination conditions. The length constant λ_c will increase as the ratio of bone to fluid resistivity increases.

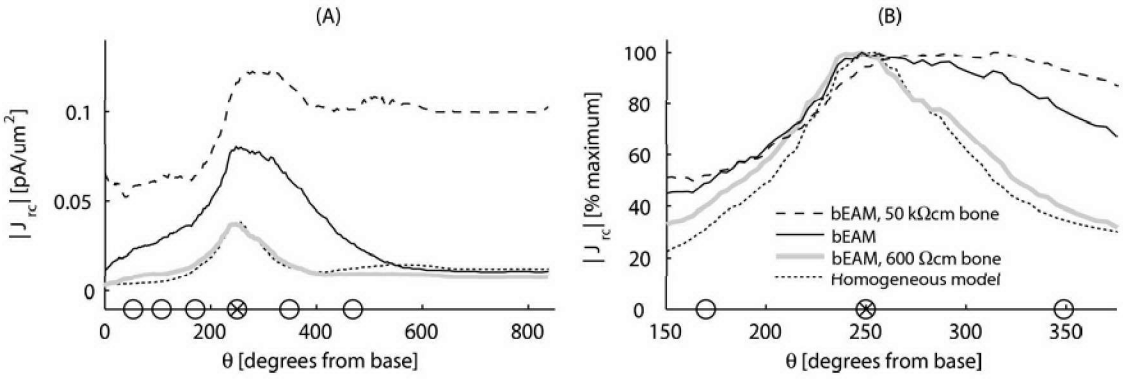

Figure 2-15: (A) RC-current versus cochlear position for stimulation by EL3 in the bEAM (black), the bEAM with 50 kΩcm-bone (broken black), the bEAM with 600-Ωcm bone (gray), and the homogeneous model (dotted). (B) As in panel A, with each curve normalized as a percent maximum. Note the magnitude $|J_{rc}|$ is plotted for clarity of presentation; the predictions are similar for J_{rc}.

fit by a transmission line model than by a homogeneous EAM. This conclusion is extended here to suggest that an EAM with 600-Ωcm bone predicts patterns of current flow similar to those of a homogenous model that are inconsistent with measurements made by Girzon. This idea is expanded on in the next chapter where the Ineraid psEAM is used to predict intracochlear recordings made while the Ineraid patient served as a research subject in Girzon's study.

As was pointed out in Figure 2-11F for the case of apical monopolar stimulation, the majority of spread in J_{rc} is basal to the position of the electrode. Additionally, the total current that enters the modiolus (as opposed to alternative pathways to the ground in the internal auditory meatus) is larger for apical stimulation. In panel A of Figure 2-16, the mean J_{rc} entering Rosenthal's canal is plotted as a function of the stimulating electrode for various bone resistivities. As the bone resistivity increases more current enters the modiolus, and more current spreads to the base where it eventually exits the cochlear spiral into the vestibular labyrinth. The latter "vestibular current" can be quantified by integrating the current density passing though a disk-shaped plane in the basal turn (depicted in Figure 2-17). This calculation yields the percentage of the total 1 μA exiting the cochlea via the vestibular labyrinth (referred to as the vestibular current), plotted in Figure 2-16B as a function of the stimulating electrode for the same resistivities of bone.[21]

As one might expect, the bEAM (2-16B, open circles) predicts that the vestibular current is greatest for basal stimulation and declines as the stimulating electrode is moved toward the apex. However, for the apical-most EL1, the vestibular current is *greater* than when its basal neighbor, EL2, is stimulated. This is likely because EL1

[21] This analysis relies on the internal auditory meatus as the primary exit pathway for a monopolar current, an assumption tested in detail in the next chapter.

stimulation results in a greater amount of current crossing the intrascalar septum into the basal turn and exiting the cochlea into the vestibular system. Increasing the resistivity of bone ($\triangle$ and $\triangleleft$) reduces this effect. In the 50-kΩcm case ($\triangleleft$), the vestibular current decreases monotonically from EL6, and the percentage of current flowing into the vestibular labyrinth from the more apically positioned electrodes increases substantially compared to when bone resistivities less than 10 kΩcm are used. This is consistent with a transmission line model where current flows toward the base, with little or no cross-turn coupling. One might also expect that the new bone and fibrous tissues typically found in the basal turn near the cochleostomy site might attenuate the vestibular current (discussed in Chapter 4).

Reducing the bone resistivity ($\triangledown$ and $\triangleright$) *increases* the difference between the EL1 and EL2 vestibular current predictions. In the 600-Ωcm case ($\triangleright$), EL3 and EL2 have a *negative* vestibular current, meaning the net current though the plane in Figure 2-17 is *entering* the cochlea. This is likely because the solution approaches that of a homogeneous medium, where the cochlea duct does not channel current flow.

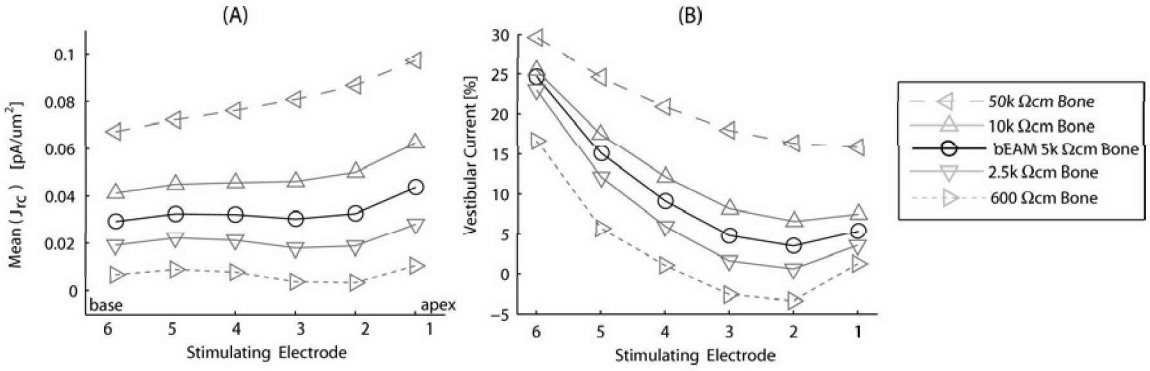

Figure 2-16: (A) Mean J_{rc} (averaged across θ) as a function of the stimulating electrode for the bEAM using various bone resistivities. (B) Current exiting the cochlea into the vestibular labyrinth as a function of the stimulating electrode for monopolar stimulation. The vestibular current (expressed as a % of the stimulating current) is positive for current exiting the cochlea.

Changes in the predicted current flow are also evident when one considers currents along the scala tympani. Shown in Figure 2-18A is a comparison of the current magnitude ($|J_{cp}|$) measured as a function of longitudinal distance from the stimulating electrode for three models: the standard bEAM (5-kΩcm -bone), the bEAM using 600-Ωcm bone, and the homogeneous model. In Figure 2-18B these measures are compared to those reported by Briaire and Frijns [15]. At a distance of 1 millimeter apical to the source, the current magnitude falls off at different rates, with the lowest rate for the bEAM and the highest rate for the homogeneous model. The 600-Ωcm model and Frijns model fall between these. This further supports the notion that the bone-to-fluid resistivity is a crucial ratio determining longitudinal spread, and benchmarks the bEAM (5-kΩcm bone, i.e., a ratio of 100) as predicting more longitudinal spread than previous models where this ratio is roughly 12 (i.e., the Frijns model) or

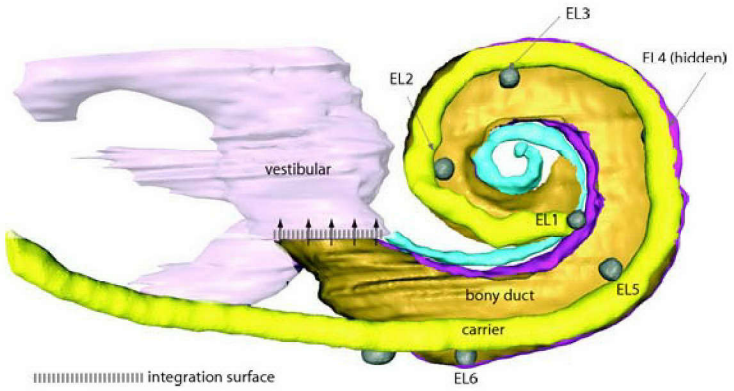

Figure 2-17: Vestibular current refers to longitudinal current exiting the bony duct of the cochlea through a horizontal plane just inferior to the stapes footplate. This current enters the vestibular duct and flows to the model ground in the IAM via the vestibular and facial nerve canals, and adjacent structures. It is measured by integrating the current density in the fluid (displayed as a collection of arrows) orthogonal to a disk-shaped plane intersecting the basal turn (dashed line shows integration surface). A positive value indicates current exiting the cochlea.

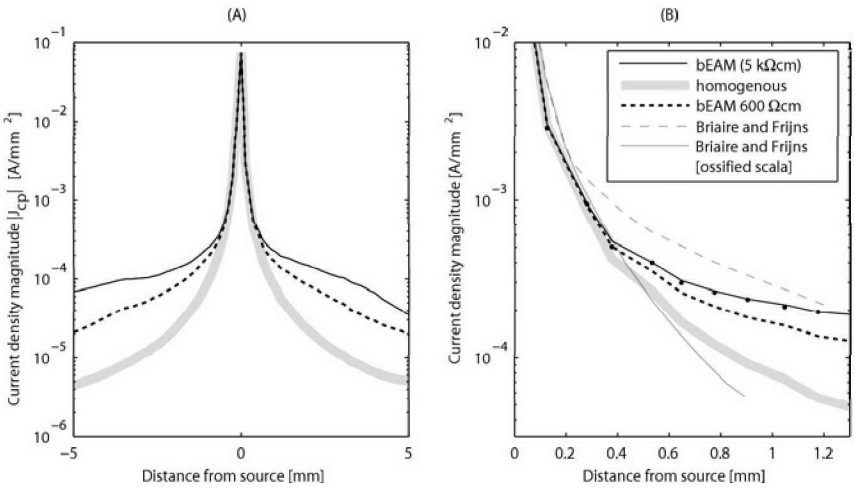

Figure 2-18: (A) Magnitude of the current density versus longitudinal distance from the stimulating electrode for the bEAM, bEAM using 600-Ωcm bone, and homogenous models. (B) Comparison to the data reported by Briaire and Frijns ([15] their figure 7A, normal scala tympani). At a distance of 1 millimeter from the source the current density falls off at different rates, with the bEAM predicting a more shallow decay than for the 600-Ωcm bEAM, the Briaire and Frijns data [15], or the homogeneous model.

unity (i.e., a homogeneous model).

2.4 Prediction of the neural activation pattern

A compartmental single-fiber model of the auditory nerve is used to compute the neural response to the electric field for each of the 200 model fibers. The input to this model is $V_{e(f,i)}(t)$, the time-varying extracellular potential extracted at positions (indexed by i) along the fiber track at each cochleotopic position (indexed by f). The model outputs are the time-varying membrane potentials, $V_{m(f,i)}(t)$, and membrane currents, $I_{m(f,i)}(t)$, associated with each model fiber. The currents $I_{m(f,i)}(t)$ are later used to compute the evoked potential recorded on each intracochlear electrode, as detailed in the next section. Collectively, this process provides a prediction of which fibers initiate an action potential as a function of cochlear position (θ) for an arbitrary stimulus configuration.

2.4.1 Background

The mathematical formulation of the time-varying membrane voltage, $V_m(x,t)$, is derived as a modified form of the cable equation. The passive cable equation for a cylindrical (unmyelinated) fiber with a linear membrane conductance, as in Figure 2-19, takes the form:

Figure 2-19:

$$\lambda^2 \frac{\partial^2 V_m}{\partial x^2} - V_m - \tau \frac{\partial V_m}{\partial t} = 0 \tag{2.8}$$

where λ and τ are space and time constants, respectively. Equation 2.8 is a second order partial differential equation (PDF) of the parabolic type where V_m is a continuous function of both space (x) and time (t), taken as the difference in potential between the outer and inner conductors ($V_m = V_i$ - V_o). The behavior of the cable is determined by the constants τ and λ,

$$\tau = \frac{c_m}{g_m} \tag{2.9}$$

$$\lambda = \frac{1}{\sqrt{(r_i + r_o) g_m}} \tag{2.10}$$

where c_m and g_m are the capacitance $[\frac{pF}{cm}]$ and conductance $[\frac{S}{cm}]$ per unit length of the

membrane. The values r_i and r_o are the resistance per unit length $[\frac{\Omega}{cm}]$ of the inner and outer conductors, respectively [224]. For a locally injected intracellular current, τ describes the temporal evolution of the disturbance to the membrane voltage from rest, while λ describes the spatial extent of the disturbance. In models of electric stimulation, it is typically assumed that the extracellular potential, $V_e(x,t)$, is fixed by the ionic currents in the biologic medium due to the stimulating electrode (i.e., the ionic currents generated by a fiber's response have a negligible impact on the external potential). When a large number of densely packed fibers are active, this assumption is likely violated [174]. For electric stimulation, equation 2.8 becomes

$$\lambda^2 \frac{\partial^2 V_m}{\partial x^2} - V_m - \tau \frac{\partial V_m}{\partial t} = - \lambda^2 \frac{\partial^2 V_e}{\partial x^2} \tag{2.11}$$

A simple but powerful result of equation 2.11 is that the rate of membrane depolarization ($\frac{\partial V_m}{\partial t}$) is related to the second spatial derivative of the external potential *along the axis* of the fiber. While equation 2.11 is valid for an unmyelinated axon, a similar equation applies for a uniform diameter myelinated fiber with periodically spaced nodes of Ranvier. Here τ and λ become periodic functions of space, making analytic solutions more complicated (see Andrietti [3], FitzHugh [50], Basser [6], Rubinstein [177]). As a first-order approximation of a myelinated fiber, the depolarization of a patch of nodal membrane is governed by the difference quotient

$$AF \equiv \frac{V_{e(x-\Delta x)} - 2V_{e(x)} + V_{e(x+\Delta x)}}{(\Delta X)^2} \tag{2.12}$$

where $V_{e(x-\Delta x)}$ and $V_{e(x)}$ are the external potentials at adjacent nodes of Ranvier separated by an internode distance ΔX. Using the terminology of Rattay [167], this "activating function" (AF) uses only the 2nd spatial difference quotient of V_e to estimate where along a myelineated fiber an action potential is likely to initiate, without considering specific fiber dimensions or nonlinear nodal kinetics. Warman's total equivalent driving function [223] furthered this idea by modeling the myelinated fiber as a passive, periodic cable and accounting for the impact of neighboring nodes. It is important to point out that even for a spatially constant electric field,[22] changes in the fiber's trajectory or termination of the fiber can cause a local membrane depolarization that initiates an action potential [174].

Incorporating nonlinear nodal membrane conductances, such as those described by Schwarz and Eikhof [185], adds significant complexity to the membrane behavior, essentially necessitating a computational solution. A typical method for solving a nonlinear PDE of this form involves a technique called the method of lines, where

[22] one for which $\frac{\partial^2 V_e}{\partial z^2} = 0$ along any straight path z.

the spatial variable (x) is discretized into N spatial regions, compartmentalizing the neuron. The spatial derivative of 2.11 is replaced by a finite difference relation, while the derivative $\frac{\partial V_m}{\partial x}$ is taken as zero within each compartment. This transforms the PDE of equation 2.11 into a system of N coupled ordinary differential equations (ODEs) where time is the only remaining independent variable. Discretizing time leaves a set of coupled, nonlinear algebraic equations [102]. In this model of the myelinated afferent auditory fiber, the spatial discretization corresponds to specifying V_m at adjacent nodes of Ranvier and internodal sections, resulting in a system of coupled ODEs which can then be solved using numerical integration.

2.4.2 Model description

The discrete cable model representation of a single nerve fiber (first described by McNeal [125]) used in this study is shown in Figure 2-20, with dimensional information in Table 2.3. Nodal kinetics are based on those described by Schwarz and Eikhof [185] as modified by Frijns [54]. Internodal segments are represented as passive leaky compartments. For a uniform diameter fiber, the *deviation* in membrane potential from rest of a single compartment, $V_{(i)}(t)$, is described below.

$$\begin{aligned} C_{m_{(i)}} \frac{dV_{(i)}}{dt} &= [G_a(V_{(i-1)} - 2V_{(i)} + V_{(i+1)})] + [G_a(V_{e_{(i-1)}} - 2V_{e_{(i)}} + V_{e_{(i+1)}})] \\ &\quad -G_{L_{(i)}}(V_{(i)} + V_{rest} - V_L) - I_{ion_{(i)}} \end{aligned} \tag{2.13}$$

using the conventions:

$V_{i_{(i)}}$	the internal potential of compartment i referenced to a far field ground
$V_{e_{(i)}}$	the external potential of compartment i referenced to a far field ground
$V_{m_{(i)}}$	$= [V_{i_{(i)}} - V_{e_{(i)}}]$ the transmembrane potential
$V_{(i)}$	$= [V_{m_{(i)}} - V_{rest}]$ the deviation of the membrane voltage from rest
V_{rest}	the resting membrane voltage as calculated using the Goldman Equation (see [54])
V_L	the leak reversal potential
$C_{m_{(i)}}$	the membrane capacitance of compartment i
$G_{a_{(k)}}$	the axial conductance of compartment k
	(note in equation 2.13 that G_a was treated as uniform)
$G_{L_{(i)}}$	the leak conductance of compartment i
$I_{ion_{(i)}}$	the active ionic current of compartment i

Equation 2.13 can be derived by balancing current at the internal node labeled $V_{i_{(i)}}$ in Figure 2-20. The values of the external potentials $V_{e_{(i)}}$ are taken from the potential field estimated along a fiber track for a unitary 1μA stimulus current on a particular electrode such that scaling $V_{e_{(i)}}$ is equivalent to scaling the electrode stimulus current. The model's nonlinear behavior is governed by the voltage-dependant sodium (G_{Na}) and potassium (G_K) conductances as described by Frijns [54]:

$$I_{Na_{(i)}} = \left[P_{Na} h_{(i)} m_{(i)}^3 \left(\frac{V_{m_{(i)}} F^2}{RT} \right) \frac{[c^o_{Na^+}] - [c^i_{Na^+}] \exp\left(\frac{V_{m_{(i)}} F}{RT} \right)}{1 - \exp\left(\frac{V_{m_{(i)}} F}{RT} \right)} \right] \cdot \pi d_{(i)} \ell_{(i)} \quad (2.14)$$

$$I_{K_{(i)}} = \left[P_K n_{(i)}^2 \left(\frac{V_{m_{(i)}} F^2}{RT} \right) \frac{[c^o_{K^+}] - [c^i_{K^+}] \exp\left(\frac{V_{m_{(i)}} F}{RT} \right)}{1 - \exp\left(\frac{V_{m_{(i)}} F}{RT} \right)} \right] \cdot \pi d_{(i)} \ell_{(i)} \quad (2.15)$$

where

P_K	potassium permeability	$n_{(i)}$,	potassium activating factor
P_{Na}	sodium permeability	$h_{(i)}$	sodium inactivating factor
$d_{(i)}$	node diameter	R	gas constant
$\ell_{(i)}$	node length	T	absolute temperature
$m_{(i)}$,	sodium activating factor	F	Faraday's constant

Here the activating factors $m_{(i)}$, $n_{(i)}$, and $h_{(i)}$ are nonlinear, time-varying, and voltage-dependant with each obeying a first-order differential equation of the form

$$\frac{dm_{(i)}}{dt} = \alpha_{m_{(i)}} + (\alpha_{m_{(i)}} + \beta_{m_{(i)}}) m_{(i)}. \quad (2.16)$$

(2.17)

The voltage dependance of $\alpha_{m_{(i)}}$ and $\beta_{m_{(i)}}$ are described in Appendix 2.7.2. Similar equations govern $n_{(i)}$ and $h_{(i)}$ as detailed below.

Dimension	**value**
peripheral diameter (d_{pr})	1 μm
cell body diameter	1.5μm
axonal diameter (d_{ax})	2 μm
peripheral node length (l_{pr})	2.5 μm
axonal node length (l_{ax})	2.5 μm
peripheral internode distance (L_{pr})	200 μm
cylindrical cell body length	2.5 μm
axonal internode distance (L_{ax})	400 μm

Table 2.3: Standard fiber dimensions adapted from [147, 199]. Note the length-to-diameter ratio was held constant for both the peripheral (L_{pr}/d_{pr}) and axonal (L_{ax}/d_{ax}) segments of the fiber. Note the cell body diameter is only 1.5 μm (see 2.4.3 for rational).

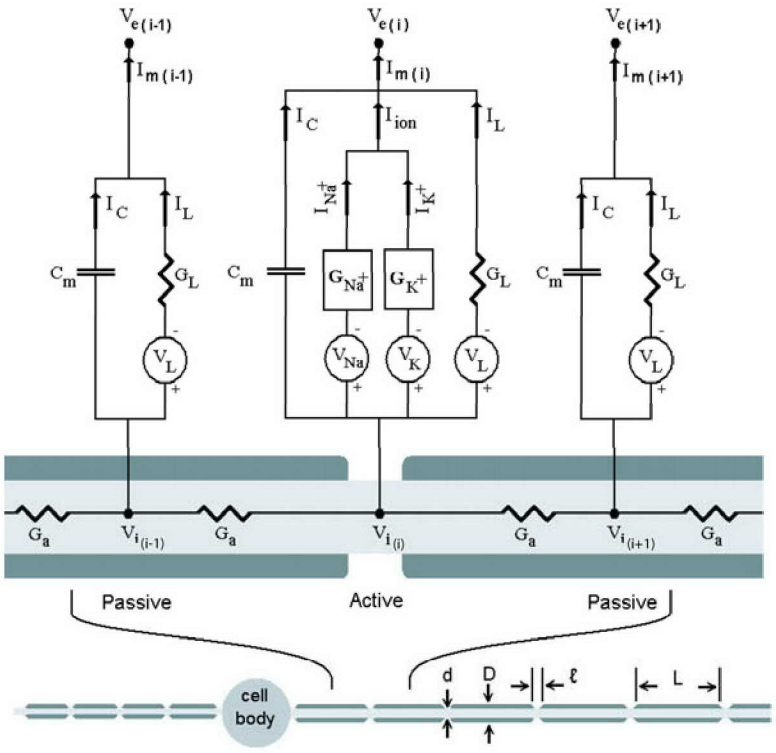

Figure 2-20: Single-fiber model. Discretized cable representation showing a single node of Ranvier flanked by two internodal compartments. Transmembrane currents at each node are composed of a capacitive current (I_c), a leak current (I_L), and an ionic current (I_{ion}). The nonlinear, voltage-dependant kinetics of the sodium (G_{Na}) and potassium conductance (G_K) are adapted from Schwarz and Eikhof [185] as in Frijns [54]. Myelinated internodes are treated as passive leaky insulators. The external potential at each position $V_{e_{(i)}}$ along a fiber track is determined by the field estimate. The length constants λ for nodal and internodal patches of membrane are 31.3 and 2,390 μm respectively. The time constants τ for nodal and internodal patches of membrane are 27.4 and 100 μs respectively. See equation 2.13 or appendix 2.7.2 for parameter conventions.

Numerical simulation

We seek a solution to the membrane voltage deviation at each node $V_{(i)}$ as a function of time to determine if a propagating action potential is observed on each model fiber f.[23] To accomplish this, $V_{(i)}$, $m_{(i)}$, $n_{(i)}$ and $h_{(i)}$ need to be simulated as a function of time, since all other model variables can be formulated from these four and the fiber dimensions. Forming column vectors from each (e.g., $\mathbf{V} = [V_{(1)}, \ldots, V_{(N)}]^T$) allows this entire system to be concisely described with the following four coupled equations (from Frijns [54]):

$$\frac{d\mathbf{V}}{dt} = \mathbf{AV} + \mathbf{BV_e} + \mathbf{C}\left(\mathbf{I_{act}} + \mathbf{I_L}\right) \tag{2.18}$$

$$\frac{d\underline{\mathbf{m}}}{dt} = \begin{vmatrix} \alpha_{m_{(1)}} \\ \vdots \\ \alpha_{m_{(N)}} \end{vmatrix} + \begin{vmatrix} (\alpha_{m_{(1)}} + \beta_{m_{(1)}}) & & 0 \\ & \ddots & \\ 0 & & (\alpha_{m_{(N)}} + \beta_{m_{(N)}}) \end{vmatrix} \underline{\mathbf{m}} \tag{2.19}$$

$$\frac{d\underline{\mathbf{h}}}{dt} = \begin{vmatrix} \alpha_{h_{(1)}} \\ \vdots \\ \alpha_{h_{(N)}} \end{vmatrix} + \begin{vmatrix} (\alpha_{h_{(1)}} + \beta_{h_{(1)}}) & & 0 \\ & \ddots & \\ 0 & & (\alpha_{h_{(N)}} + \beta_{h_{(N)}}) \end{vmatrix} \underline{\mathbf{h}} \tag{2.20}$$

$$\frac{d\underline{\mathbf{n}}}{dt} = \begin{vmatrix} \alpha_{n_{(1)}} \\ \vdots \\ \alpha_{n_{(N)}} \end{vmatrix} + \begin{vmatrix} (\alpha_{n_{(1)}} + \beta_{n_{(1)}}) & & 0 \\ & \ddots & \\ 0 & & (\alpha_{n_{(N)}} + \beta_{n_{(N)}}) \end{vmatrix} \underline{\mathbf{n}} \tag{2.21}$$

Calculation of the vectors $\mathbf{I_{act}}$ and $\mathbf{I_L}$ requires $\mathbf{V}$, $\underline{\mathbf{m}}$, $\underline{\mathbf{n}}$, and $\underline{\mathbf{h}}$. Likewise, the calculation of α and β to find $\underline{\mathbf{m}}$, $\underline{\mathbf{n}}$, and $\underline{\mathbf{h}}$ requires $\mathbf{V}$. Here $\mathbf{A}$, and $\mathbf{B}$ are tridiagonal matrices that describe the resistive coupling between compartments, and $\mathbf{C}$ is a diagonal matrix containing the nodal capacitances. The entries of $\mathbf{A}$, $\mathbf{B}$, $\mathbf{C}$, and the voltage dependency of α and β can be found in Appendix 2.7.2.

Equation 2.18 implements a sealed-end (spatial) boundary condition requiring zero axial current to the left of node 1 or to the right of the last node (node N) in Figure 2-20. This can be conceptualized as setting $G_{a_{(0)}}$ and $G_{a_{(K+1)}}$ to zero, forcing any axial current to flow only *between* compartments 1 through N. Unless otherwise specified, this system is driven by a time-varying vector of extracellular potentials, $\mathbf{V_e}(t)$, that takes the form of a biphasic pulse with 30 μs per phase:

[23] In this section the subscript f is removed for clarity, although each variable is indexed by f.

$$\mathbf{V_e}(t) = \left\{ \begin{array}{ll} 0 & 0 < t < 5\mu s \\ -S_{scale} \cdot V_{e(i)} & 5\mu s \leqslant t < 35\mu s \\ +S_{scale} \cdot V_{e(i)} & 35\mu s \leqslant t < 65\mu s \\ 0 & t \geqslant 65\mu s \end{array} \right\} \tag{2.22}$$

where S_{scale} is a scale factor applied to vary the stimulus intensity across different runs.

To obtain a simulated $\mathbf{V}(t)$, equations 2.18 - 2.21 are numerically integrated on a uniform time grid with a spacing Δt of 1μs. The fiber is initialized in its resting state with the membrane potential equal to the resting potential at all fiber nodes (i.e., $\mathbf{V} = 0$). Likewise, all elements of the vectors $\underline{\mathbf{m}}$, $\underline{\mathbf{n}}$, and $\underline{\mathbf{h}}$ are initialed in their respective resting states as m_0, n_0, and h_0 (given in appendix 2.7.2). The time derivatives of $\mathbf{V}$, $\underline{\mathbf{m}}$, $\underline{\mathbf{n}}$, and $\underline{\mathbf{h}}$ are also initialized at zero. The updated values of $\mathbf{V}(t_{n+1})$ are calculated using backward Euler because of the stiffness[24] of the coupled equations, while $\underline{\mathbf{m}}(t_{n+1})$, $\underline{\mathbf{n}}(t_{n+1})$, and $\underline{\mathbf{h}}(t_{n+1})$ were updated using forward Euler.

After integrating, the existence of a propagating action potential is determined by comparing $V_{(i)}(t)$ for the central-most node to a threshold. Next S_{scale} is changed and another run initiated. This process is iterated using a binary search algorithm until a threshold S_{scale} is found. Here threshold is defined as finding two values for S_{scale} that differ by less than 1%, the larger of which initiates an action potential, while the smaller does not. The fiber's relative threshold is taken as the larger of these values. The activation pattern describes the change in model-fiber threshold across cochlear position (i.e., a plot of fiber threshold versus θ). All calculations involving the single-fiber model were done in MATLAB.[25]

2.4.3 Rational for single-fiber model morphology

The single-fiber model does not include an accurate cell body representation. The morphology of the human spiral ganglion cell includes a dentritic diameter that is roughly half the axonal diameter (Spoendlin and Schrott [199]); and a 20-30 μm diameter perikaryon (cell body) that is unmyelinated [199, 159]. Incorporating these

[24]Stiffness measures the difficulty of solving an ODE or PDE as the ratio of the longest time scale to the shortest time scale. This is analogous to the ratio of the largest to smallest eigenvalue (i.e. condition number) in describing the difficulty of performing a matrix inversion. Explicit methods usually suffice for non-stiff problems, while implicit methods have more desirable numerical behavior for stiff problems. The stiffness of a compartmental neuron model, such as this one, increases with both the number of compartments and the degree of resistive coupling between compartments. For example, if the axial conductance G_a on both sides of a node is much smaller than the combined nodal membrane conductances ($G_L + G_K + G_{Na}$), then the nodal voltage is essentially decoupled from its neighbors, thus decreasing the stillness [102].

[25]MATLAB is a registered trademark of The Mathworks Inc., Natick, MA.

two morphological observations typically cause most McNeal-type [125] single-fiber models to fail to conduct an action potential across the cell body. An action potential (AP) initiated on the dendrite propagates to the cell body where it produces a negligible change in the membrane voltage (due to the high capacitance of a 20-30 μm diameter compartment). This failure in trans-perikaryal conduction due to the impedance mismatch created by the electrical discontinuity at the cell body has been discussed elsewhere [169, 102, 85].

Three putative mechanisms have been implicated in aiding the action potential to cross the unmyelinated cell body. First, the internode length tends to become shorter near the cell body as reported by Liberman [111] in the cat and by Brown [20] in the guinea pig. This ought to increase the axially directed currents as the AP approaches the cell body. Second, a local increase in the number of voltage-gated ion channels on each side of the cell body can provide the current needed to charge the cell body membrane. This could occur via an increased channel density or an increased nodal length for the presomatic and postsomatic sections of axon flanking the cell body.[26] Third, Ota and Kimura [157] report human perikarya to be surrounded by a single sheath of satellite cells, with neighboring cell bodies in close apposition and occasionally touching (e.g., Felder et al. [45]), effectively decreasing the capacitance between the cell body interior and the interstitial fluid.

Modeling approaches to address the failure in trans-perikaryal conduction have been to include elongated (active) unmyelinated presomitic and postsomatic compartments, along with voltage-gated ion channels on the perikarya itself. Rattay [170] incorporated a 100 μm presomatic compartment while using temperature-adjusted Hodgkin-Huxley ion kinetics [82] and an assumed 10-fold increase in channel density. Briaire and Frijns [13] also incorporated an 100 μm moderately (4 layers) myelinated presomatic compartment and cell body. While both the adjustments made by Rattay and Briaire et al. allowed for conduction past the cell body, both authors point out that small changes in the size of the peripheral or central axonal segments resulted in a loss of transmission. Given the ostensible "safety factor" in the ability of myelinated nerves to conduct an action potential (e.g., after blocking a single node of Ranvier with a neurotoxin the AP will still propagate past), it seems unlikely auditory fibers would operate in a manner teetering on conduction failure. Accordingly, we viewed alterations to our model similar in spirit to, and indeed motivated by, the Rattay and Briaire et al. models as precariously close (in the model's parameter space) to a region of transmission failure and therefore inherently unrealistic, especially considering the tendency for several aspects of saltatory conduction to be maximized (see Besser [6] for examples). Additionally, examining our institution's collection of spiral ganglion montages, each consisting of hundreds of high-power electron microscopy im-

[26] However, in the mouse cochlea, Hossain et al. [85] reported only rare increases in the density of voltage-dependant sodium channels (Nav 1.6 and Nav 1.2) on the peripheral side of the cell body, although the mouse ganglion cell body is myelinated such that these channels may not be necessary.

ages pieced together, we can not confirm the morphology used by Rattay or Briaire, specifically the existence of a 100 μm unmyelinated presomatic compartment.

The simple model we settled on does *not* incorporate the known morphology of the cell body, and arguably this is its greatest weakness. Another major weakness is discussed in section 4.2.1 of Chapter 4. Clearly, this is an area on which future work should concentrate.

2.4.4 Results

Shown in Figure 2-21 is a typical propagating action potential for the single-fiber model, after being excited by an intracellular current pulse delivered to the most-peripheral compartment. Panel A shows the deviation in membrane potential from rest ($V_{(i)}$) for two nodal compartments separated by 2400 μm. Panel B graphs the triphasic membrane current ($I_{m(i)}$) for the same two nodes.

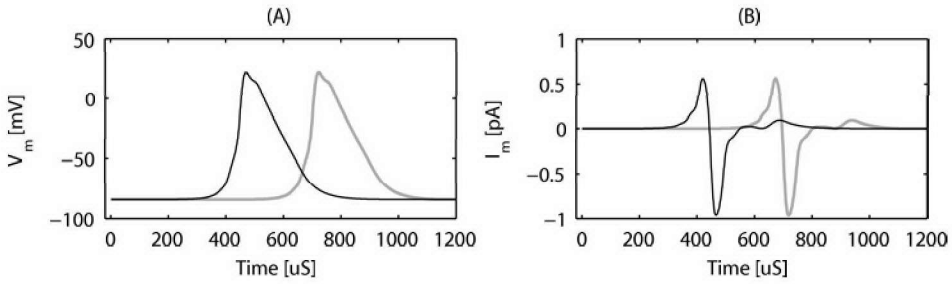

Figure 2-21: Membrane voltage (panel A) and transmembrane current (panel B) at two nodes separated by 2400 um (six internodes) after a 1 nA intracellular current injection on the peripheral-most node. The conduction velocity is 9.54 m/s.

Plots of single-fiber threshold (SFT) versus cochlear position θ (i.e., the activation pattern) are shown in panels A-F of Figure 2-22 for monopolar stimulation. The magnitudes of the predicted SFTs are above the typical values one would expect from human psychophysics (e.g., hundreds of μA), although we are primarily interested in the pattern across cochleotopic position. A scalar change to many parameters of the single-fiber model would lower the predicted SFTs into the expected magnitude range.

While the activation pattern shifts with the stimulating electrode, a strict relationship between the position of the lowest threshold fiber and that of the stimulating electrode was not found. Examining the collection of panels A-F reveals a region near 240 degrees (just basal to EL3), for which a local minimum in SFT exists in several panels. In panel A, this is most evident, while in other panels it becomes partially masked as the activation pattern shifts to overlap it. This local threshold minimum is at the same cochlear position as, and is related to, the local *maximum* in RC-current presented in Figure 2-11E. The origin of this minimum appears to be a result of the asymmetric geometry of the cochlea, as discussed further in Chapter 4.

Also of interest is stimulation of EL4 in panel C, where the lowest threshold is located near the 240 degree sensitive region, while the stimulating electrode is located at a position basal to this at 170 degrees. With the exception of EL4, there does not appear to be a symmetry in the rate with which SFT increases apical and basal to the stimulating electrode. For instance, using the minimum threshold as a reference, the EL3 thresholds increase at roughly 5.5 dB/90deg basal to, and 3 dB/90deg apical to, the position of the stimulating electrode.

The two most striking features of the SFTs in Figure 2-22 are the exceptionally broad activation patterns (referred to as activation spread), and the small range.[27] The spatial selectivity is much lower (i.e., less tuned) than those reported by other authors. The range varies from 12.5 dB on EL6 to 14.7 dB on EL4, substantially less than that predicted by other similar models such as Briaire and Frijns [14]. Both of these metrics are compared across EAMs in section 2.4.5.

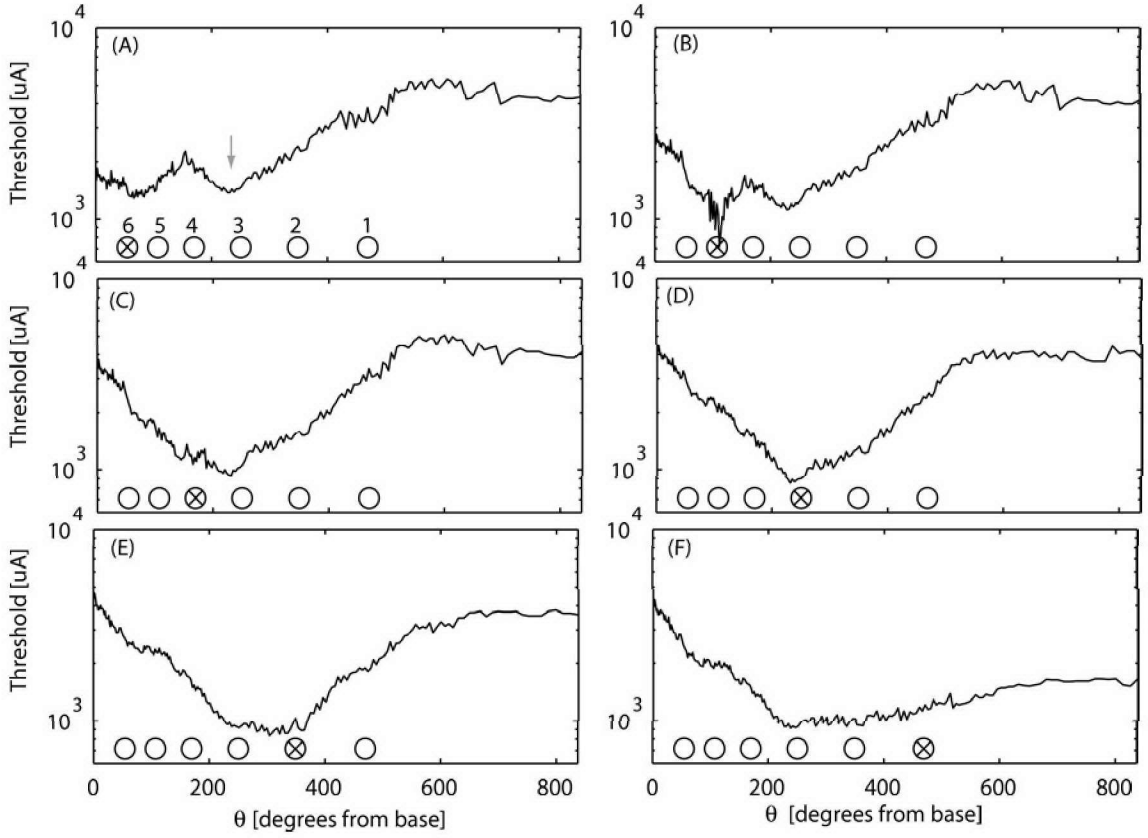

Figure 2-22: Single-fiber threshold versus cochlear position (θ) as the simulating electrode is moved from the base to the apex in Panels A-F. The position of the electrodes are shown by open circles (identified by number in panel A), with the active electrode marked by $\otimes$. Note the local minimum in fiber threshold near 240 degrees (marked by $\downarrow$) in panel A.

[27] The range is taken as the ratio of the highest to lowest threshold fiber in dB.

Monopolar versus bipolar stimulation

To compare monopolar with bipolar stimulation, two Nucleus-style ring electrodes were added to the basic model and used to compute bipolar SFTs (shown in 2-23). A few salient features stand out in this and other bipolar simulations not shown here. First is the characteristic w-shaped threshold pattern using bipolar simulation having local minima at cochlear positions adjacent to the two electrodes of the bipolar pair. A similar result has been reported in other modeling studies by Frijns [54] and Hanekom [73], and measured physiologically in the cat at both the level of the auditory nerve (see Kral et al. [104], their figure 10) and the inferior colliculus (see Rebscher et al. [172], their figure 9). Second is the increase in range from the monopolar 14.5 dB to 37.9 dB for the bipolar stimulus. Third, bipolar thresholds tend to be more than three times higher than monopolar thresholds for a stimulating electrode at a similar longitudinal position. For instance, in Figure 2-23 the minimum threshold in bipolar mode is 10 dB above the minimum threshold in monopolar mode. Similar ratios between bipolar and monopolar thresholds have been reported for: single-unit recordings made from the auditory nerve of the cat [213, 104], recordings from the inferior colliculus of the cat (+7.4 dB) [172] and guinea pig (+10 to +15 dB) [195], ECAP recordings [16], and and psychophysical measures (+7.6 dB) [7] made in human subjects.

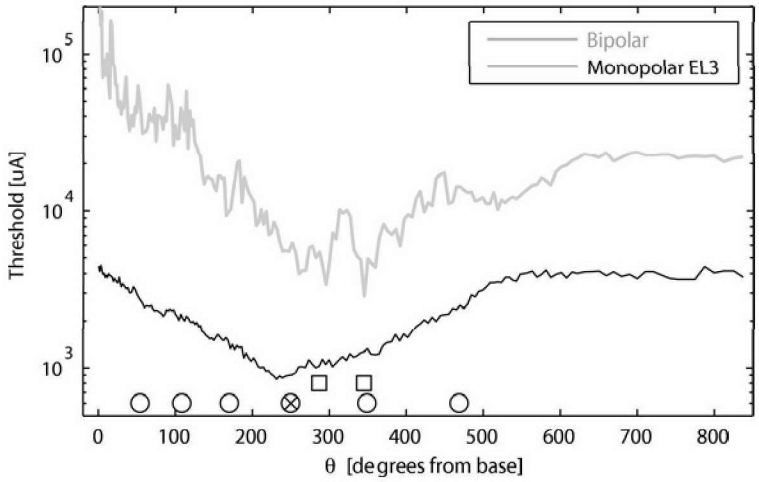

Figure 2-23: Single-fiber threshold versus cochlear position for monopolar (black) and bipolar (gray) stimulation. The position of the active monopolar electrode is given by ⊗. The position of the Nucleus-style ring electrodes are marked by □. For both monopolar and bipolar stimuli, a biphasic pulse (30 μs per phase) is used. For bipolar simulation the basal electrode is cathodic during the first phase. Measured at 6 dB above the lowest single-fiber threshold, these curves span characteristic frequencies of roughly 2.5 and 1.1 octaves for monopolar and bipolar stimuli, respectively.

Activation patterns using a homogeneous model

In order to evaluate the extent to which the nonhomogeneous structure of the EAM impacts the excitation predicted for intracochlear stimulation, the activation patterns obtained with the bEAM were compared against those obtained using the familiar analytic potential solutions in the homogeneous model. Here the model fiber tracks in 3D space are the same, but the resistivity of all tissues is assumed to be 300 Ωcm. (see section 2.3.2). Panels A-C of Figure 2-24 show predicted SFTs for monopolar stimulation of EL6, EL3, and EL1 using the volume conduction and homogeneous models. Panel D compares the SFTs obtained using the bEAM for bipolar stimulation (Nucleus-style rings) to those obtained using an analytic solution for a current dipole in the homogeneous model.

In all cases, both the spacial selectivity and range of thresholds are greater for the homogeneous model. For instance, in panel B the width of the shaded region corresponds to a 4-millimeter segment of the basilar membrane. For both the computational (bEAM) and homogeneous solutions, the vertical bar spans a range between the lowest threshold and the threshold at which a 4-millimeter length of the basilar membrane is excited. The 4-millimeter range for the bEAM is only 2.4 dB compared with 25.5 dB for the homogeneous model. This is also much less than the 12-30 dB range reported by Briaire and Frijns ([14] figure 5).

The homogeneous model stimulated with a monopolar electrode predicts an increase in cross-turn coupling, as one might expect given the geometry of the model fiber population. For instance, in panel A, two clear minima (marked by δ) separated by 361 degrees are present: one at the cochlear position of the stimulating electrode and one a full turn apical to the position of the stimulating electrode. The same phenomena is seen in panel C, where two local minima separated by nearly 360 degrees are present (also marked by δ).

In the case of bipolar stimulation (panel D), the SFTs for the homogeneous model show the same bimodal threshold pattern as for the SFTs obtained using the bEAM, with a local minima near each electrode. However, the bEAM predicts less spatial selectivity than the homogenous model. This fits with the significant current spread shown for bipolar stimulation in panel C of Figure 2-13 of the previous section.

Bipolar monophasic stimuli

For *bipolar* stimulation, the model predicts a phase dependency for *monophasic* pulses. Figure 2-25 shows SFTs for a 30 μs monophasic pulse where either the basal (dark gray) or apical (light gray) electrode is cathodic. The fiber with the lowest threshold for the basal-cathode and apical-cathode conditions, labeled α and β, are located at 295 and 344 degrees (or 1,199 and 904 Hz), respectively.

Switching the phase of the pulse from a basal to apical-cathode, increases threshold

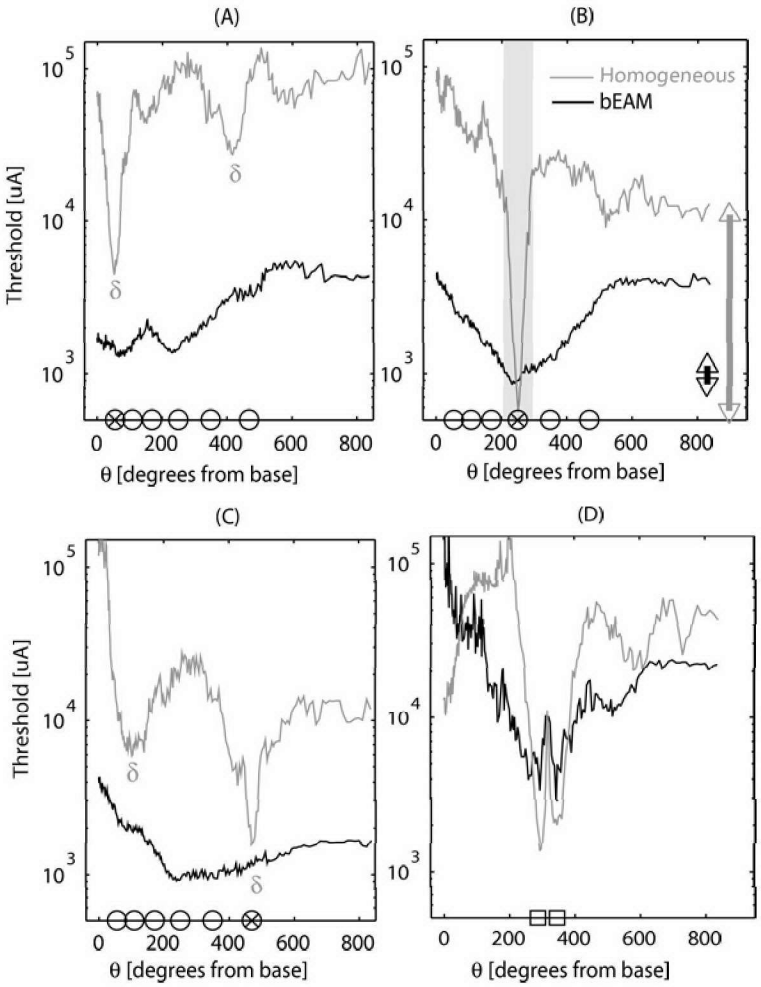

Figure 2-24: (A) Single-fiber threshold versus cochlear position (θ) predicted by the bEAM (black) and homogeneous (gray) models for stimulation of EL1. The homogeneous solution is calculated using a point electrode in an infinite 300-Ωcm isotropic medium. The position of the active monopolar electrode is given by $\otimes$. The position of the two prominent local minima in the homogeneous case (marked by δ) are separated by 361 degrees. (B) Stimulation of EL3. For both SFTs, the vertical bars span the range between the lowest ($\bigtriangledown$) and highest ($\bigtriangleup$) thresholds predicted when a 4 millimeter length (shaded region) of the basilar membrane is excited. This 4-mm range is only 2.4 dB compared with the 25.5 dB for the homogeneous model. (C) Stimulation of apical EL1. The position of the two prominent local minima in the homogenous case (marked by δ) are separated by 372 degrees. (D) Comparison of SFTs for bipolar stimulation with Nucleus style ring electrodes using the computational model (black) and an analytic homogeneous solution (gray). The position of each electrode is given by $\square$.

of the α-fiber while decreasing the threshold of the β-fiber. Note the cochlear position (θ) of the α-fiber and β-fiber are essentially the same as those of the cathodic contact of the electrode pair shown in Figure 2-25 as squares. This suggests that the most sensitive fibers for a monophasic, bipolar pulse are located near the cathodic electrode, a result that agrees with single-unit data from the cat reported by van den Honert and Stypulkowski [213], as well as earlier modeling predictions made by Finley et al.

[47]. Frijns [54] reported that for a monophasic pulse delivered to a bipolar pair of electrodes (apical cathode), fibers near the anodic electrode have thresholds 6-12 dB higher than those near the cathodic contact. Comparing the thresholds of the α and β fibers in Figure 2-25 gives a similar ratio of 9.1 dB.

These predictions imply that for a low-level monophasic pulse, i.e., one that excites only a few neurons, reversing the phase of the pulse could substantially shift the position of the activated fibers. Here the characteristic frequencies of the α and β fibers differ by 295 Hz, an amount that might be perceptually noticeable to an implant user, if monophasic pulses could be safely presented.[28] This idea is explored further in the next chapter where a psychophysical experiment designed to test this result is reported.

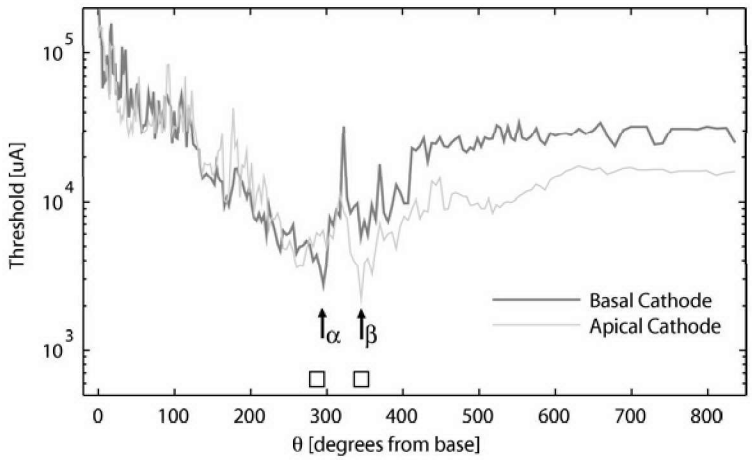

Figure 2-25: Single-fiber threshold predictions versus cochlear position (θ) for bipolar, *monophasic* stimulation. The position of the Nucleus-style ring electrodes are marked by □s. The stimulus is a 30 μs monophasic pulse. For monophasic stimulation with a basal (dark gray) and apical cathode (light gray), the most sensitive model fiber is labeled α and β, respectively. The α and β fibers are located at 295 degrees (1,199 Hz) and 344 degrees (904 Hz).

Comparisons of the threshold values obtained for monophasic and biphasic pulses are given in Table 2.4 for the α and β-fibers. For each fiber, the two biphasic thresholds (1) fall between the two monophasic thresholds, (2) are relatively close to one another, and (3) are closer to the lower of the monophasic thresholds. All of these results are consistent with the cathodic-phase electrode being primarily responsible for initiating the action potential. Examining the bottom two rows of Table 2.4 shows that for a biphasic pulse, a change in polarity does *not* shift the position of the lowest-threshold fiber (the β-fiber has the lowest threshold for both polarities). Hanekom [73] reported a similar insensitivity to polarity for the position of the most sensitive fiber, except that in that study the lowest-threshold fiber was near the basal

[28] To prevent electrolytic dissolution of the electrode contacts, changes in pH, and production of gases, charge balanced pulses are used.

electrode.

Comparing the biphasic threshold of the α-fiber (3,393 μA) with the monophasic threshold using a basal cathode (2,753 μA) gives a ratio of -1.82 dB. For the β-fiber this mono/biphasic ratio (using an apical cathode) is -1.74 dB. With *monopolar* stimulation, Rubinstein [179] used a linear analysis to predict the ratio of monophasic to biphasic thresholds reported for single-unit recordings made in the cat by Miller et al. [136] and Shepard et al. [188]. In Rubinstein's analysis the monophasic/biphasic ratio decreased from -1 to -4 dB as the pulse phase duration shortened from 100 to 40 μs, in accordance with Shepard's data. Accordingly, Rubinstein's analysis suggests a monophasic/biphasic ratio lower than the -1.82 and -1.74 dB reported here.

Stimulus configuration	**α-fiber threshold [μA]**	**β-fiber threshold [μA]**
monophasic - basal cathode	2,753	5,718
monophasic - apical cathode	6,347	2,225
biphasic - basal cathode leading	3,393	2,865
biphasic - apical cathode leading	3,658	2,718

Table 2.4: Thresholds for α-fiber and β-fiber for monophasic and biphasic pulses of 30μs per phase

Influence of fiber dimension

One important consideration is the impact of the single-fiber model's dimensions on the predictions of threshold. Recent studies have used various fiber dimensions, with variation in the fiber diameter, the internode representation (insulated or leaky), and the internode distance. Using our simplified model that neglects the cell body's impact, we systematically changed the representation of the single-fiber model's dimensions to test the sensitivity to individual changes in model fiber dimension. Five alternative fibers are shown schematically in Figure 2-26 with the corresponding dimensions given in table 2.5.

Fiber$_1$ and fiber$_2$ have a uniform diameter as opposed to the discontinuity at the cell body. Fiber$_3$ is the same as the standard fiber with perfectly insulated internodes. Fiber$_4$ and fiber$_5$ have a uniform internode spacing, with fiber$_5$ also having a uniform diameter. Activation patterns predicted using the five alternative fibers are presented in Figure 2-26 for stimulation with EL3.

All of the formulations with a discontinuity in diameter at the cell body (i.e., the standard, $fiber_3$, and $fiber_4$) tend to have a similar pattern of threshold across cochlear position. The fibers of a uniform diameter ($fiber_1$, $fiber_2$, and $fiber_5$) show a different behavior, tending to covary in Figure 2-26. Since the difference between $fiber_1$ and $fiber_2$ is a doubling of diameter, one would expect the same threshold pattern for these two fibers, with $fiber_2$ having a higher threshold because of its

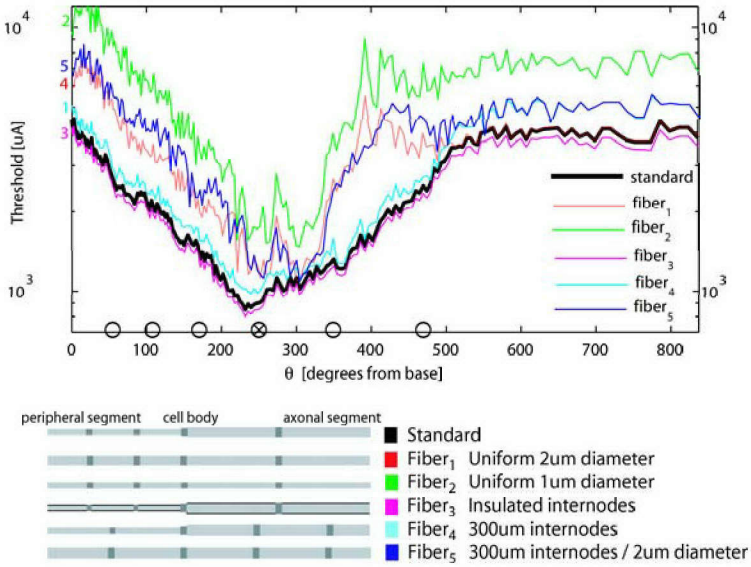

Figure 2-26: Influence of model fiber dimension. Single-fiber threshold versus cochlear position (θ) for stimulation of EL3 with six different fiber dimensions used in the single-fiber model. A schematic of the standard fiber, along with the five alternative fibers tested is given below the figure.

Dimension	**standard**	**fiber$_1$**	**fiber$_2$**	**fiber$_3$**	**fiber$_4$**	**fiber$_5$**
peripheral diameter (d_{pr}) [μm]	1	2	1	1	1	2
cell body diameter [μm]	1.5	2	1	1.5	1.5	2
axonal diameter (d_{ax}) [μm]	2	2	1	2	2	2
node length (l) [μm]	2.5	2.5	2.5	2.5	2.5	2.5
peripheral internode distance (L_{pr}) [μm]	200	200	200	200	300	300
cell body length [μm]	2.5	2.5	2.5	2.5	2.5	2.5
axonal internode distance (L_{ax}) [μm]	400	400	400	400	300	300
perfectly insulated internodes	no	no	no	yes	no	no

Table 2.5: Fiber dimensions for standard and fibers 1-5. Fiber$_1$ and fiber$_2$ have a uniform diameter as opposed to a discontinuity at the cell body. Fiber$_3$ is the standard with perfectly insulated internodes. Fiber$_4$ and fiber$_5$ have a uniform internode spacing, with fiber$_5$ also having a uniform diameter.

smaller diameter.

The impact of treating the internodes as leaky has an apparently negligible impact on the prediction of threshold (compare fiber$_3$ with the standard). Likewise, changing to a uniform internode length of 300 μm has almost no impact (compare fiber$_4$ with the standard). This is likely because both of these contain a discontinuity in diameter at the cell body that is primarily responsible for initiating an action potential.

Collectively these results point out a serious concern about this and other similar modeling projects that employ a single-fiber model. Specifically, the variation in SFT

introduced by changing the dimensions of the model fiber can be on the order of the variance in SFT seen across cochlear position. In this study the presence of a discontinuity in diameter at the cell body results in a broader activation pattern than predicted without a discontinuity.

2.4.5 Discussion

The influence of bone resistivity observed in section 2.3.2 is also seen in the neural activation patterns for monopolar stimulation. Figure 2-27 plots single-fiber thresholds (panel A) and $|J_{rc}|$ (panel B) versus cochlear position for three models: the bEAM (black line), bEAM with 600-Ωcm bone (gray line), and the homogenous model (broken line). In 2-27A there is an ordering of the predicted spatial spread across models, with the homogenous model predicting the least spatial spread and the bEAM predicting the most.

There are two reasons why the activation patterns become sharper moving from the bEAM to the homogenous model. First, J_{rc} becomes more focused at the stimulating electrode as the bone resistivity decreases, as shown in panel B of Figure 2-27 where the normalized $|J_{rc}|$ is plotted verse θ for each model. Second, for the homogenous model, the extracellular potential along model fibers immediately adjacent to the stimulating electrode have unusually steep gradients along their peripheral segments. Shown in panels C-E are the extracellular potentials along three model fiber tracks in the vicinity of the stimulating electrode: (1) the fiber track immediately adjacent to the stimulating electrode (marked by ⊗), a fiber track located basally at -25 degrees below ⊗, and (3) a fiber at +25 degrees above ⊗. In the homogeneous model (panel C), the extracellular potential for the fiber track adjacent to the electrode (⊗) has much steeper gradients along its peripheral process than those of its flanking neighbors, giving it a lower threshold. In the bEAM and 600-Ωcm bEAM (panels E and D), the traces of extracellular potential for fiber tracks adjacent to the electrode (⊗) are less steep than for the homogenous case and similar to that of its flanking neighbors.

Relationship between J_{rc} and single-fiber threshold

Shown in Figure 2-28 is a comparison of variation in SFTs to variation in J_{rc}. SFT values are normalized in dB referenced to the minimum threshold fiber, while J_{rc} values are expressed in dB referenced to the maximum J_{rc} value. Clearly, SFT and J_{rc} are inversely related across θ over nearly the same range of magnitudes. It is not surprising that a significant portion of the variation in SFT is explained by variation in the RC-currents, since the single-fiber model used has a discontinuity in diameter at the cell body.[29]

[29] Accordingly, membrane depolarization is not a strict function of only the 2nd spatial difference quotient in the extracellular potential, as it is for a uniform diameter fiber with uniformly spaced nodes of Ranvier. As noted by Reilly [174], at either a termination or a discontinuity in diameter, membrane depolarization is influenced by the first spatial derivative of extracellular potential along the fiber, which is proportional to the current density parallel to the fiber.

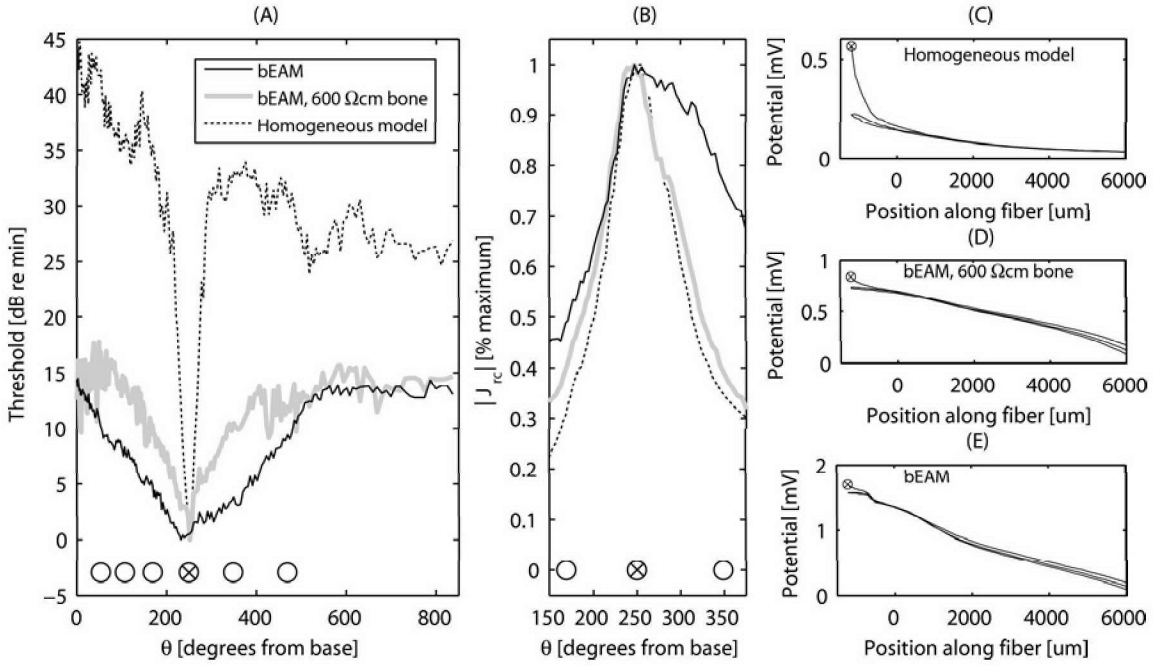

Figure 2-27: (Panel A) Single-fiber threshold versus θ for stimulation by EL3. Thresholds are expressed in dB re the minimum threshold for the bEAM (black), bEAM with 600-Ωcm bone (gray), and the homogeneous model (broken line). (Panel B) $|J_{rc}|$ versus θ for the same three cases, each normalized as a percent of the maximum. (Panels C-E) External potential along model fiber tracks near the stimulating electrode. The model fiber track closest to the stimulating electrode (marked with ⊗) and its two neighbors at ±25 degrees in θ are shown. Only in the homogeneous case of panel C is the potential along the fiber track at the simulating electrode noticeably different from the neighbors flanking it at ± 25 degrees.

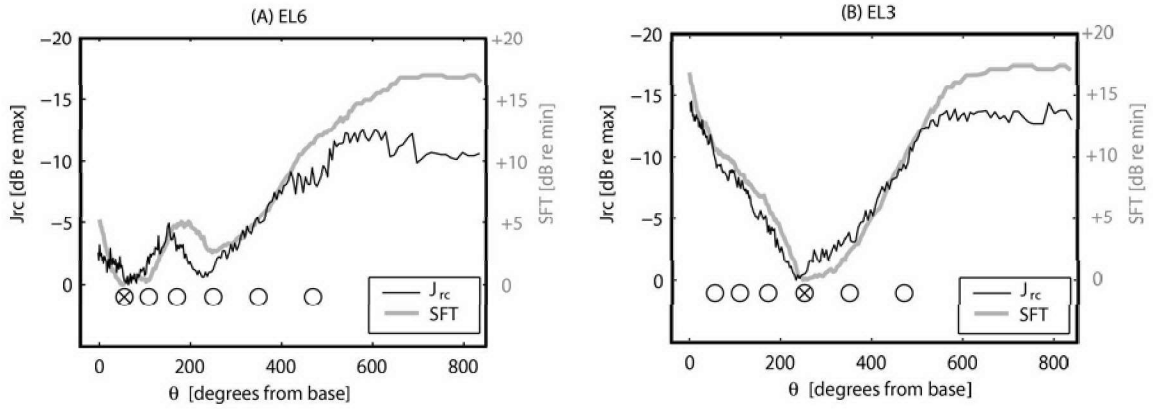

Figure 2-28: SFTs (gray) expressed as dB re the minimum threshold fiber, and J_{rc} (black) expressed in dB re the maximum, each plotted as a function of θ for stimulation by EL6 (panel A) and EL3 (panel B). Note the ordinate for J_{rc} (left axis) is reversed such that higher J_{rc} values are toward the bottom.

Spatial selectivity

Comparing the SFT patterns of the bEAM to those of other electro-anatomical models of the implanted ear, a similar dependence on bone resistivity is noticed. Shown in Table 2.6 are the resistivities of key tissues from the models of Frijns et al [54, 15, 52, 53, 55, 13], Hanekom [73], Finley [47], and Rattay [168].

The bone-to-fluid resistivity used by Frijns, Hanekom and Finley is roughly 10 while that used by the bEAM is 100. Shown in Figure 2-29 is a comparison of spatial excitation in the bEAM (gray curves) along with analogous data reported by Hanekom (left column), Frijns et al. (middle column), and Rattay et al. (right column) for monopolar stimulation (top row) and bipolar stimulation (bottom row). SFT data are normalized to the lowest threshold fiber in dB and plotted verse cochlear position relative to the stimulating electrode(s).

For both the Hanekom and Frijns models in panels A and B, the prediction for monopolar excitation (gray) are more focused than the bEAM predictions (black) likely because of the ratio of bone-to-fluid resistivities used. The same trend is seen in the comparisons to bipolar stimulation in panels D[30] and E. Again, as the ratio of bone-to-fluid resistivity increases, so does the spatial spread. The bEAM results are probably most similar to Rattay for at least two reasons. First, the single-fiber model used by Rattay includes a discontinuity in fiber diameter at the cell body. Second, the ratio of bone-to-fluid resistivity is on the order of 100, similar to in this study.

Study	**Bone [Ωcm]**	**Perilymph/Endolymph [Ωcm]**	**Nerve [Ωcm]**
bEAM	5000	50/50	300
Frijns et al [15]	641	70/60	333
Hanekom [73]	641	70/60	300
Finley [47]	630	70/60	300
Rattay [168]	6400	70/60	300

Table 2.6: Resistivity values for various models of the implanted ear.

At a stimulus level 6 dB above threshold, the bEAM predicts the recruitment of model fibers spanning 2.5 and 1.1 octaves in characteristic frequency for monopolar and bipolar stimuli, respectively. This corresponds to 11 and 4.4 millimeters, or 270 and 121 degrees in θ. To compare the spatial selectivity of the SFTs in Figure 2-29, the length of cochleotopic positions recruited is compared across models, with measures in millimeters and θ given in Table 2.7 (p.81). While the number of octaves a single electrode stimulates increases with the stimulus level, choosing 6 dB above the lowest fiber threshold allows one to make a simple comparison across models and conditions.

[30]In panel D, the Frijns data is from a region of their model centered at a cochlea position of roughly 450 degrees (electrode pair separated by 375 um)

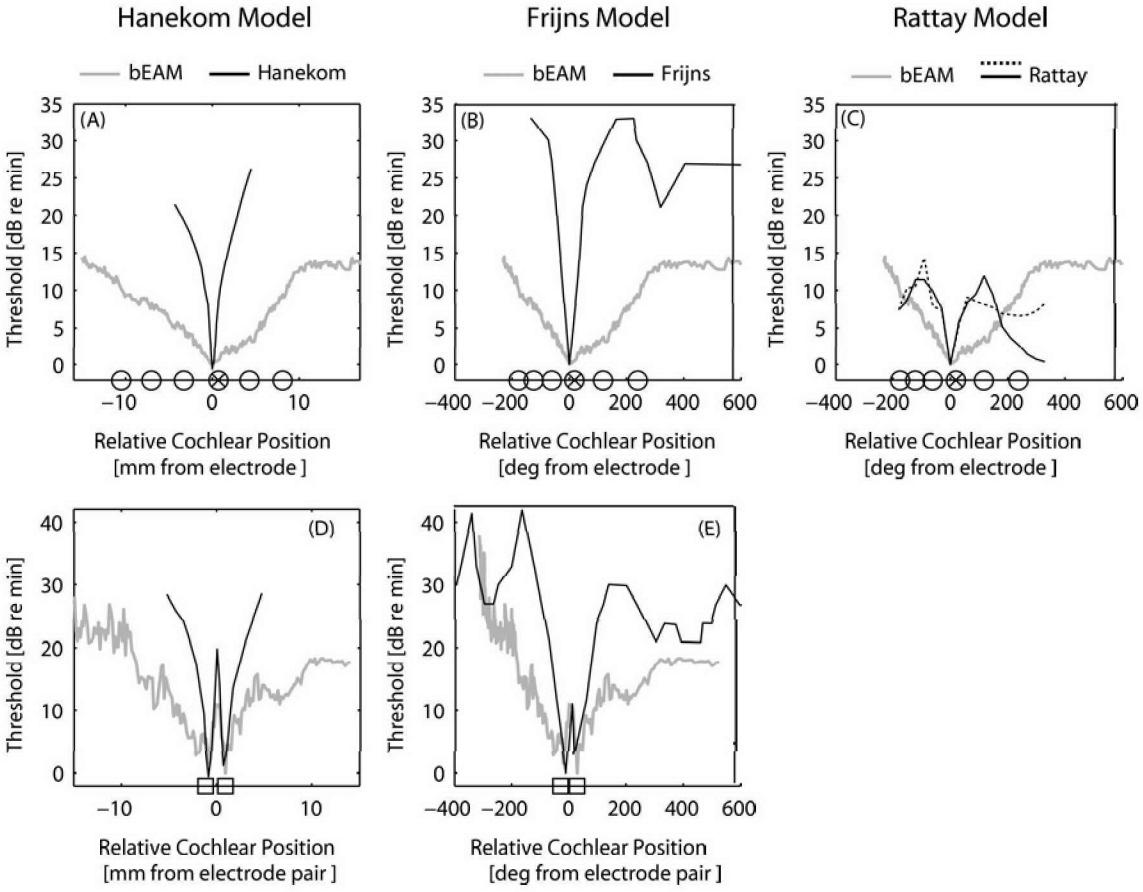

Figure 2-29: Comparison of excitation patterns predicted by the bEAM (gray) to those predicted the Hanekom (left column), Frijns et al. (middle column), and Rattay et al. (right column) models (black) for monopolar stimulation (top row) and bipolar stimulation (bottom row). The predictions are expressed in dB re the minimum threshold fiber and plotted as a function of cochlear position measured in either millimeters or degrees relative to the position of the stimulating electrode(s). In the top row, bEAM predictions for monopolar stimulation are compared with: (A) Hanekom [74] Fig 2B. (B) Briaire and Frijns [13] Fig 4A (their human model, myelinated cell body), and (C) Rattay et al. [168] (Table 2, Biphasic (-/+) condition for the standard (black) and long dendrite (dashed) case). The bottom row panels compare bEAM predictions for bipolar stimulation using Nucleus-style ring electrodes to: (D) the bipolar+1 pattern reported by Hanekom [74] (their Fig 2A), and (E) the bipolar pattern reported by Frijns [15] Fig 10B (their guinea pig model).

For monopolar stimulation, applying this heuristic 6 dB-width measure to the bEAM with 600-Ωcm bone gives 0.72 octaves. Repeating the 6 dB-width measure in Figure 2-29 of the other reported EAMs yields 0.17 octaves (Hanekom[31]), and 0.318 (Frijns[32]), and 0.64 (Rattay) for monopolar stimulation.

For the bipolar case, the pattern reported by Hanekom (Figure 2-29, panel D) yields a 6-dB width of 0.47 octaves, which is *more* than double that of monopolar stimulation. Similarly, using either the homogeneous model (Figure 2-24) or the 600-Ωcm bEAM yields predictions of SFT where the bipolar activation spread is *more* than its monopolar counterpart (see Table 2.7). Measuring at levels lower than 6 dB would tend to decrease the estimated spread in every case. We have arbitrarily chosen 6-dB level for convenience, however, the point remains that the bEAM predicts current spread and excitation spread that is much larger than previous EAMs, with a spread for monopolar stimulation that is more than double that of bipolar stimulation.

While it is difficult to make any direct comparison between these estimates of spatial spread and those measured psychophysically, for completeness we present what has been reported in the literature. For subjects using bipolar+1 stimulation with high speech recognition scores, Friesen et al. [51] estimated the number of independent channels as about seven or eight[33] in agreement with other estimates [49]. Here an "independent channel" is defined psychophysically using speech recognition tasks.

If one were to tenuously define an ad hoc "independent channel" as one in which the neural activation pattern from one electrode does not overlap with that of its neighbor, the length of cochleotopic positions corresponding to a single (mutually exclusive) independent channel can be estimated by dividing the longitudinal cochlear length of the electrode array (in frequency octaves or millimeters along the basilar membrane[34]) by the number of "independent channels" reported by Friesen et al. For instance, supposing that the typical implanted electrode array parallels cochleotopic

[31]For an average human, Greenwood's formula [65] describes the mapping between millimeters along the basilar membrane and cochleotopic frequency as $F = A(10^{ax} - k)$, where F is characteristic frequency (Hz); A= 165.4 (Hz) a= 2.1; x is the normalized position along the basilar membrane (0=apex,1=base); k = 0.88. For the basal half of the cochlear length, the log-linear function $\acute{F} = A(10^{ax})$ where k is set to zero gives a very close (< 1 dB) approximation to Greenwood's function. For this basal region of interest $\acute{F}$ has a slope of 0.2 octaves per millimeter. This approximation was used to convert the spatial spread data of Hanekom from millimeters along the basilar membrane (at 6 dB above threshold) to octaves in cochleotopic frequency.

[32]In the bEAM it was shown that for the basal half of cochlear length, 90 degrees in θ corresponds to roughly an octave in frequency. Since the 34.1 millimeter length of the Ineraid cochlea is close to the 35 millimeter average for a human described by Greenwood, this Ineraid-derived heuristic was used to convert the data of Frijns and Rattay from degrees in cochlear position to octaves in cochleotopic frequency.

[33]Friesen el al reported that "CI listeners with the highest performance level increased in performance as the number of electrodes increased up to seven, while CI listeners with low levels of speech recognition did not increase in performance as the number of electrodes was increased beyond four."

[34]In the basal turn $\acute{F}$ has a slope of 0.2 octaves per millimeter, meaning frequency octaves and millimeters in cochlea length are nearly equivalent measures.

positions between roughly 20 kHz and 1,150 Hz[35] (4.1 octaves), each of the eight independent channels corresponds to *at least* 0.51 octaves for bipolar stimulation, and likely much higher for monopolar stimulation.

Spatial selectivity: comparison to animal studies

Snyder el al. [195] measured spatial tuning curves (STCs) in the central nucleus of the inferior colliculus (IC) of the implanted guinea pig in response to electric stimulation for a variety of intracochlear electrode configurations. These measures were made using a 16-channel electrode inserted into the IC with contacts spaced approximately orthogonal to the isofrequency laminae, spanning IC depths responsive to acoustic sounds between 1 and 24 kHz. Assuming the center frequencies in the IC mirror those in the auditory nerve with minimal spectral expansion, the STC measured in the IC can be interpreted as indicative of the spatial tuning in the cochlea.

Measuring the STC width at 6 dB above threshold, Snyder el al. reported IC activation widths of 382 μm_{IC} for a pure tone, 681 μm_{IC} for bipolar simulation with 0.75 mm electrode separation, and $> 1{,}500$ μm_{IC} for monopolar stimulation. Using a similar protocol, Rebscher et al. [172] measured STCs in the IC of the implanted cat, reporting STC widths of 780 μm_{IC} for bipolar (1.1 mm electrode separation) and 1,250 μm_{IC} for monopolar stimulation. Both of these agree with the bEAM's prediction that the monopolar excitation at 6 dB above threshold is roughly twice that of bipolar. Using a protocol similar to Rebscher et al., Smith [193] recorded IC activity in the cat for monopolar and bipolar stimuli, concluding that width of the activation pattern was similar for each near threshold, while above threshold (e.g., 6 dB) monopolar stimulation yielded a slightly ($\approx 21\%$) wider activation pattern (see [193], figure 4.10). However, Smith also recorded EABR growth functions that were at least 3 times steeper in the monopolar case (see [193], figure 4.3b).

Combining the map of 764 $[\frac{\text{octaves}}{\mu m_{IC}}]$ relating best frequency to IC depth in the cat (derived from Snyder [196][36]) with the map of 0.282 $[\frac{\text{octaves}}{\text{mm}}]$ relating best frequency to

[35]Skinner et al. [191] used CT to derive estimates of total cochlear length and the cochleotopic frequency of the apical-most electrode. In 26 Nucleus 22 recipients, they reported the cochleotopic frequency of the apical electrode to range from 3674 to 308 Hz with a mean of 1147 Hz (18.9 mm insertion or 0.54 % of cochlear length). The 452 and 828 Hz estimates for the apical-most electrode of the Ineraid and Nucleus psEAM fall within this range.

[36]The data of Snyder [196] (their fig 3A) can be used to relate IC depth μm_{IC} to best frequency (converted to octaves) using a simple linear regression ($r^2 > 0.97$).

cochleotopic position (derived from Liberman [110][37]), one can estimate the Rebscher et al. measures of 780 μm_{IC} and 1,250 μm_{IC} of activation spread in the IC correspond to roughly 3.6 and 5.8 millimeters of excitation spread along the basilar membrane.[38]

Spatial selectivity: comparison to single-unit recordings

An alternative way of displaying SFT-type data is to plot the threshold for one model fiber as a function of the stimulating electrode. This reorganization is motivated by the studies of Liang et al [109], Kral et al [104], and Hartmann et al. [75], who each measured single-unit recordings in the cat auditory nerve. Since the cochlear position of the isolated units these authors were recording from were difficult or impossible to estimate, the single-unit data are typically presented as single-unit threshold versus stimulating electrode. To draw a comparison, the data from the bEAM are plotted as SFT versus stimulating electrode for a representative collection of model fibers in the panels of Figure 2-30. Moving left to right in the panels of 2-30, the cochlear position (θ) of the model fiber plotted advances as annotated at the top of the panel. The relationship between position of the fiber in and the position of the stimulating electrodes is given on the x-axis (see figure caption).

There are a few similarities between the bEAM data and the monopolar data reported from single units in the cat. First, the range of SFTs reported by these authors[39] typically do not exceed 15 dB for a single unit. This is consistent with the bEAM predictions of Figure 2-30 where a range of 3.1 to 12.5 dB is observed.

Second, Liang et al. reported three types of units[40] with 47 % for the units having "type I" behavior, where thresholds increased as the stimulating electrode moved basally. This is consistent with most of the available fibers being positioned apical to the most apical stimulating electrode and having a threshold that increases as the

[37]In the cat, Liberman [110] fit a modified form of Greenwood's formula to describe the mapping between position along the basilar membrane and cochleotopic frequency as $F = A(10^{ax} - k)$, where F is characteristic frequency (kHz); A= 0.456 (kHz); a= 2.1; x is the percentage distance along the basilar membrane (0=apex, 1=base); and k = 0.80. Over the basal half of the cochlear length ($0.5 < x < 1$), the log-linear function $\acute{F} = 0.456(10^{2.1(x)})$, where k is set to zero, gives a close (< 1 dB) approximation to Liberman's frequency map. For this basal region, $\acute{F}$ has a slope of 7 octaves per 100% cochlear length, or roughly 0.282 octaves per millimeter of cochlear length, using an average length of 24.8 millimeters for the cat cochlea.

[38]For example, given a spread of activation in the IC of 780 [μm_{IC}], the estimated length along the basilar membrane (L_{bm}) in millimeters is:

$$L_{bm}[mm] = \frac{780\ \mu m_{IC}}{764\left[\frac{\mu m_{IC}}{octave}\right] \cdot 0.282\left[\frac{octaves}{mm}\right]} = 3.6\ [mm]$$

[39]See Liang et al. [109] (Fig 4, Fig 5 and Fig 6), Kral et al. [104] (Fig 10), and Hartmann et al. [75] (Fig 4).

[40]Type I units thresholds increased as the stimulating electrode moved toward the base, type II units thresholds were very low for one or two electrodes, and type III unit thresholds included two minima typically near the ends of the array.

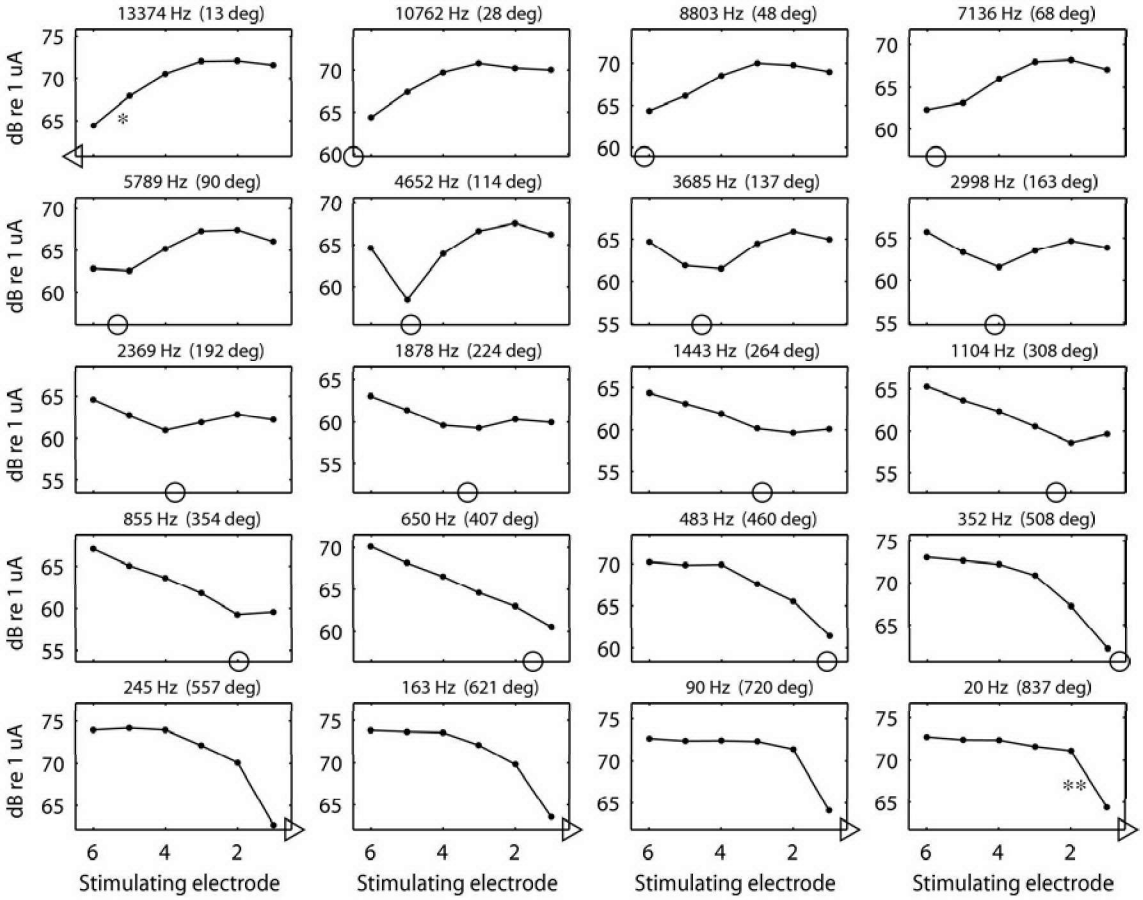

Figure 2-30: Single-fiber thresholds plotted as a function of stimulating electrode. Moving left to right in a single row, panels advance in θ for the model fiber plotted. The model fiber's position in θ and estimated characteristic frequency (Hz) are shown above each panel. The longitudinal position of the model fiber with respect to the electrodes is given by ◯. Model fibers located below and above the array's electrodes are marked by ◁ and ▷.

stimulating electrodes moves toward the base, consistent with the last two rows of Figure 2-30.

However, some aspects do not match. For the Ineraid electrode array, the x-axis of the panels in Figure 2-30 spans 6 electrodes or 20 mm. The maximal slope of these functions, normalized as threshold change (dB) per millimeter shift in the stimulating electrode, is on average 0.92 dB/mm.[41] This is lower than the reported slope of 3 dB/mm for Type I fibers, which constitute the most prevalent ones recorded from by Liang et al. Similarly, Kral et al. [104] reported an average maximal slope of 3.12 dB/mm for units with a clear minimum. Also, both Liang and Kral et al. found a few units with a very steep slope that could exceed 10 dB/mm, likely representing fibers very close to an electrode contact.

[41]For each panel in Figure 2-30, the steepest segment of the curve is used to calculate a positive slope in dB/mm. Averaging across panels gives 0.92 dB/mm.

Kral reports mean slope of 3.12 dB/mm for monopolar, 8.5 dB/mm for bipolar (0.75 mm spacing). Taking these slopes to estimate of the slope of the underlying spatial tuning curve across cochlear position, these data can be translated into 6-dB widths of 3.84 and 1.41 millimeters for monopolar and bipolar stimulation.[42]

These comparisons are somewhat tenuous, as measuring a spatial tuning curve from a single neuron while changing the stimulating electrode is not necessary the same tuning curve one will measure using a fixed stimulating electrode while measuring across neurons (SFT vs θ). These curves will only be equivalent if the SFT curves for stimulation by each electrode are nearly identical in shape.

Summary of spatial selectivity

A comparison of the spatial selectivity data presented in this section is given in Table 2.7. The bEAM model predicts the excitation spread of monopolar stimulation to be at least double that of bipolar, a result that agrees with the physiological data where monopolar-to-bipolar ratios are unanimously greater than unity. The geometric mean[43] of the monopolar-to-bipolar ratios from the physiological data listed in Table 2.7 is 1.84, below the ratio of 2.5 predicted by the bEAM. In contrast, both the homogeneous model and previous EAMs predict monopolar stimulation to be more focused than bipolar, i.e., monopolar-to-bipolar ratios less than unity.

[42]For example, in the monopolar case the width [mm] of the excitation spread can be estimated at 6 dB above threshold as:

$$2 * \left(\frac{6dB}{3.12 \frac{dB}{\text{mm}}} \right) = 3.85[mm]$$

[43]The geometric mean, μ, of N random variables x_i, with each representing a ratio measure is:

$$\mu = \left(\prod_{i=1}^{N} x_i \right)^{\frac{1}{N}} \tag{2.23}$$

Study	Cochlear length [mm]	θ [degrees]	octaves	IC depth [μm]
bEAM[a]	11.1 / 4.4	270 / 121	2.5 / 1.1	·
bEAM (600 Ωcm)[a]	3.19 / 3.3	78 / 93.4	0.72 / .77	·
Homogeneous model[a]	0.8 / 2.92	20.9 / 82.3	0.18 / 0.69	·
Frijns et al [13, 15][b,c]	·	28.6 / 58.45	0.318 / .	·
Hanekom [73][d]	0.87 / 2.39	·	0.17 / 0.47	·
Rattay [168][b]	·	57.5/	0.64/	·
Finley [47][e]	/<1.4	·	/<.28	·
Merzenich and White [130][f]	24/3	·	·	·
Snyder [195]	·	·	·	>1500/681
Rebschner [172]	5.8/3.6	·	·	1250/780
Smith [193]	·	·	·	1280/1060
Kral [104]	3.84 / 1.41	·	·	·

Table 2.7: Comparison of spatial selectivity estimated at 6 dB above threshold from various sources for monopolar and bipolar stimuli. Data are show as monopolar/bipolar. Notes: [a]Data for stimulation of EL4 used. [b]Data converted from degrees in cochlear position to octaves using 1 $[\frac{\text{octave}}{90\,\text{deg}}]$ estimate. [c]Frijns et al. [15] bipolar data are from a guinea pig model, while the monopolar data are from a human model [13]. [d]Data converted from millimeters along the basilar membrane to octaves using 0.2 $[\frac{\text{octaves}}{\text{mm}}]$. [e]Finley data estimated from [47] figure 5.13 assuming the activation function is proportional to excitation strength. Data converted to octaves using 0.2 $[\frac{\text{octaves}}{\text{mm}}]$. [f] Data converted to 6 dB measures [mm] from estimates of current attenuation of 0.5 and 4 $[\frac{dB}{\text{mm}}]$. for monopolar and bipolar stimulation as used by Bruce et al. [22]

Range of predicted thresholds

One discrepancy between the Ineraid patient psychophysics and the model is the range of single-fiber thresholds, i.e., the difference between the lowest and highest threshold for the collection of model fibers. Shown in panels A and B of Figure 2-31 are recruitment functions showing the cumulative distribution of recruited neurons[44] as a function of the stimulus level for monopolar and bipolar stimulation using the bEAM. For monopolar stimulation, the range of single-fiber thresholds (expressed in dB as the difference between the maximum and minimum single-fiber threshold) varies between only 12.5 and 17.7 dB (see Table 2.8). For the Ineraid patient, on which the bEAM is based, the range of stimulus levels separating archival behavioral threshold (T) and maximum-comfortable loudness (MCL) measures are between 14.6 and 22.5 dB as shown in Table 2.8. This is presumably a discrepancy since the Ineraid patient data suggest the range of neural thresholds span *at least* the number of decibels between MCL and T. Accordingly, the bEAM ought to account for a range of single-fiber thresholds greater than the range between T and MCL.

One factor in the model that may contribute to the underestimation of this range in predicted thresholds is that the EAM is a deterministic model, with all represented neurons of a particular cochleotopic position assigned a single threshold. While recording from single units of the auditory nerve in implanted cat preparations, van den Honert and Stypulkowski [213] estimated that the thresholds of single units with the same CF vary by as much as 12 dB. Using 12 dB as a heuristic estimate of the threshold spread at a single cochleotopic place, the recruitment functions (gray trace) in Figure 2-31 are modified such that the range of single-fiber threshold is increased by 12dB, thus allowing the model to account for the measured range of T and MCL values. Furthermore, as described in the next section "threshold" is a simplification. In implanted animals, the response of a single neuron to a single pulse of current is stochastic, with a typical range of 3-5 dB over which the discharge probability changes from near zero to unity [41, 89]. As described in the next section, incorporating this will further expand the range over which changes in level can be represented in the pattern of spikes predicted by the model.

Using the pseudo-deterministic approach of Figure 2-31, with a 12 dB heuristic as the spread of thresholds for fibers at a given cochleotopic position, the distribution of single-fiber thresholds for monopolar and bipolar stimulation are shown in the insets of panels A and B. On a log scale these distributions are nearly normally distributed, suggesting a lognormal distribution of single-fiber threshold, with the increased width of the bipolar distribution (panel B inset) reflecting a more gradual spatial spread with level as compared to the monopolar case. In the cat Miller et al. [134] also show data suggesting the population of single-unit thresholds to be nearly lognormally distributed. For a sample of 147 units in one animal, they note the range of

[44] In the bEAM each of the 200 model fibers corresponds to 150 neurons.

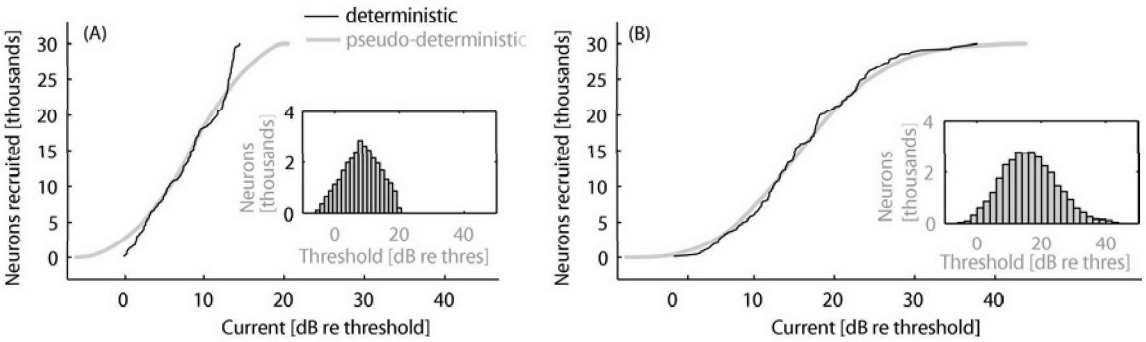

Figure 2-31: Recruitment of model neurons (black trace) as a function of stimulus intensity for monopolar stimulation by EL3 (panel A) and BP+1 simulation (panel B). Current is plotted in dB with reference to the lowest threshold predicted by the determinist bEAM. Using the heuristic that fibers at a fixed cochleotopic position have thresholds that vary by 12 dB (pseudo-deterministic model), the range of these functions is expanded (gray lines). The underlying distribution of single-fiber thresholds in the pseudo-deterministic model is shown in the inset. Note these distributions are roughly lognormally distributed.

single-unit thresholds to be about 20 dB for monopolar stimulation. Here two points should be made that will be expanded upon in the next section. First, single-unit thresholds can be modeled as lognormally distributed with the variance in the underlying distributions manifesting itself in the slope of the recruitment function (i.e., the cumulative distribution). Second, the differences between the deterministic and pseudo-deterministic models are only substantial at very high and low stimulus levels. For levels only a few dB above threshold in Figure 2-31, the slope of the recruitment functions for the deterministic (black trace) and pseudo-deterministic (gray trace) are essentially the same. As discussed in the next section, a similar conclusion can be drawn from the stochastic models of Bruce et al. [22] (their figure 4A), that predict the growth-function slopes to be similar for stochastic and deterministic models.

Electrode Configuration	EL6	EL5	EL4	EL3	EL2	EL1	BP+1
Ineraid patient (MCL-T) [dB]	14.6	20.8	22.4	22.5	20.7	19.6	
bEAM (monopolar) range [dB]	12.5	17.4	14.7	14.5	15.2	13.5	
bEAM (monopolar) range +12 [dB]	24.5	27.4	26.7	26.5	27.2	25.5	
bEAM (BP+1) range [dB]							37.9

Table 2.8: First row: range of stimulus current levels in the Ineraid patient as measured by the difference in dB between the behavioral threshold (T) and maximum-comfort level (MCL) for each monopolar electrode. Second row: range of single-fiber thresholds in the bEAM expressed as the difference in dB between the maximum and minimum single-fiber threshold for each stimulating electrode. Third row: assuming single-fiber threshold at a single cochlear position varies by 12 dB across neurons, the range of bEAM is greater that that measured in the Ineraid subject. Fourth row: range a BP+1 stimulus in the bEAM.

Influence of incorporating stochastic predictions into the bEAM

In the EAM presented thus far, a single deterministic threshold is calculated at each position in θ. Accordingly, the recruitment function describing the number of spiking neurons as a function of level is a stepwise function of level. Considering that neurons at any position in θ may differ in threshold, by as much as 12 dB [213], and the likelihood of a single neuron firing in response to a single pulse can be modeled probabilistically, a more realistic recruitment function can be constructed by statistically describing the expected number of spikes as a function of level. For example, Bruce et al. [23] fit the distribution of firing probabilities for the single-unit data of Javel et al [89] with an integrated gaussian, where the level-dependent probability of firing, $F_p(x)$, can be described by a cumulative distribution:

$$F_p(x|\mu_s, \sigma_s) = 0.5 + 0.5 \text{ erf}\left(\frac{x - \mu_s}{\sqrt{2}\sigma_s}\right) \tag{2.24}$$

The mean of the underlying distribution, μ_s, is the "threshold" level x that produces a 50 percent chance of firing, and the coefficient of variation, Θ, of the underlying distribution

$$\Theta \equiv \frac{\mu_s}{\sigma_s}, \tag{2.25}$$

is a level-independent ratio, termed the "relative spread" (RS) by Verveen [218, 219] who measured variation in excitability due to membrane noise. From data in the cat, Bruce et al. show Θ to take on values near 0.1 for short (100 μs) duration pulses, and suggest Θ does not vary with level. Using techniques similar to Bruce et al., and without resorting to large scale Monte-Carlo simulations, the deterministic predictions of SFT provided by the bEAM model can be converted to cumulative distribution functions describing the likelihood of a fiber discharging.[45] These manipulations incorporate both a ± 5 dB spread in threshold and a probabilistic model of neural discharge in response to a single pulse.

The expected total number of discharges (D_t) as a function of level is shown in Figure 2-32 for monopolar (black) and bipolar (gray) stimulation for both the

[45] The response associated with each model fiber can be made stochastic using techniques similar to those used by Bruce et al. by: (1) setting the values of $\mu_s(i)$ to the deterministic threshold predicted for fiber i, (2) assuming the thresholds for neurons at any cochlear position can vary by $\pm$ 5 dB, and (3) allowing the relative spread parameter Θ to take on a distribution of values measured in the cat. For each model fiber, the level-dependent probability of firing, $F_X(x|\mu_s)$, has an underlying probability density function, $f_X(x|\mu_s)$, that can be described as the convolution of two density functions:

$$f_X(x|\mu_s) = \quad f_{X1}(x|\mu_s) * f_{X2}(x|\mu_s) \quad 0 < x \tag{2.26}$$

$$f_{X1}(x|\mu_s) = \quad 2(\ln(10)\, x)^{-1} \quad 0.56\mu_s < x < 1.78\mu_s \tag{2.27}$$

$$0 \quad \text{otherwise}$$

$$f_{X2}(x|\mu_s) = \quad \int_\Theta f_{X2|\Theta}(x|\mu_s, \Theta) f_\Theta(\Theta) d\Theta \quad \Theta > 0 \tag{2.28}$$

stochastic case (solid lines) and the deterministic case (broken lines). For comparison, data predicted by Bruce et al. [23] for monopolar stimulation are also shown. The stochastic model tends to smooth the slope of recruitment curves and at lower levels the slopes for the monopolar and bipolar conditions become nearly identical (see inset). This is the same conclusion that Bruce et al. reached, that at very low levels the variance (or RS) of individual neurons will dominate this function. This is not the

The first function, $f_{X1}(x|\mu_s)$, describes the spread of expected thresholds at a particular cochlear position, using the heuristic that thresholds are uniformly distributed over a range of ± 5 dB around μ_s. On a dB [re 1 μA] scale, the transformed variable $Y = 20\log(X)$, takes on a uniform density defined:

$$f_Y(y|\mu_s) = \begin{array}{ll} 0.1 & 20\log(0.56\mu_s) < y < 20\log(1.78\mu_s) \\ 0 & \text{otherwise} \end{array}$$

The second function, $f_{X2}(x|\mu_s)$, is a zero-mean gaussian with a variance set according to μ_s (the model fiber's deterministic SFT) and a physiologically plausible range of values for Θ. Variation in the relative spread Θ mimics the variation in Θ for fibers of different diameters as described by Verveen [220] and modeled by Rubinstein [178]. $f_{X2}(x|\mu_s)$ describes the variation in firing probability around the 50 percent level described in equation 2.24. The relative spread parameter Θ takes on positive values from a normal distribution with a mean of 0.129 and standard deviation of 0.06 ($f_\Theta(\Theta) \sim N(0.129, 0.06^2)$ after Bruce et al. [23]), allowing $f_{X2}(x|\mu_s)$ to be obtained by integrating across Θ:

$$f_{X2}(x|\mu_s) = \int_\Theta f_{X2|\Theta}(x|\mu_s, \Theta) f_\Theta(\Theta) d\Theta \tag{2.29}$$

$$f_{X2}(x|\mu_s) = \int_0^\infty \left(\frac{1}{\sqrt{2\pi}(\Theta\mu_s)} \exp\left[\frac{-(x)^2}{2(\Theta\mu_s)^2} \right] \right) \left(\frac{1}{\sqrt{2\pi}0.06} \exp\left[\frac{-(\Theta - 0.129)^2}{2(0.06)^2} \right] \right) d\Theta \tag{2.30}$$

where $f_{X2|\Theta}$ is a zero-mean gaussian with a variance dependent on Θ and μ_s, specifically $f_{X2|\Theta} \sim N(0, \Theta^2\mu_s^2)$. Note only $\mu_{s(i)}$ is needed to calculate $f_{X2}(x|\mu_s)$.

The expected *total* number of discharges in response to a pulse of level x, $D_t(x)$, is the sum of the cumulative probability distributions $F_X(x|\mu_s)$ for each model fiber i, weighted by $N_{f(i)}$ as

$$D_t(x) = \int_0^x \sum_{i=1}^{200} N_{f(i)} F_X(x|\mu_{s(i)}) dx \tag{2.31}$$

This is essentially a Parzen window approach (see [40]) where the window function φ, or kernel, is obtained by convolving a gaussian window with a second window describing the ± 5 dB spread of fiber thresholds. Continuously lowering the variance in $f_{X1}(x)$ (e.g., choosing ± 2 dB), or lowering the values in $f_\Theta(\Theta)$ (e.g., setting $\Theta = 0.05$) will lower the variance of $f_X(x|\mu_s)$, leading to steeper $F_X(x|\mu_s)$ functions. In the limit

$$f_{X1}(x|\mu_s) = \delta(x - \mu_s) \tag{2.32}$$

$$f_{X2}(x|\mu_s) = \delta(x) \tag{2.33}$$

$f_X(x|\mu_s)$ becomes a dirac delta function and $D_t(x)$ becomes the deterministic model recruitment function. Note the simplifying assumption is made that $f_{X2}(x|\mu_s)$ is approximately the same over the ±5 dB range of x values spanned by $f_{X1}(x|\mu_s)$ for a single model fiber, that is, $f_{X2}(x|\mu_s)$ was calculated for each value of $\mu_{s(i)}$, but not adjusted for the range of values over which $f_{X1}(x|\mu_s)$ is nonzero.

case for the deterministic bEAM where the slope of monopolar recruitment is more than double that of the bipolar case.

As shown in the inset of Figure 2-32, at higher levels the slope of the stochastic functions are dominated by the underlying SFT distribution, which is steeper in the monopolar case. Accordingly, at higher levels, such as those where ECAPs are measured, the slope of the ECAP growth function is likely to reflect the underlying distribution of SFTs, a conclusion also suggested by Matsuoka et al. [122] in their model of the ECAP growth function.

Lastly, after incorporating a stochastic element into the bEAM, the spread of excitation is even broader. Shown in Figure 2-33 is the expected number of discharges per model fiber as a function of cochlear position for monopolar (panel A) and bipolar (panel B) stimulation.

Since $f_X(x|\mu_s)$ is a threshold distribution it is only valid over the range $0 < x$. This was accommodated by truncating the convolution in 2.26 to only include positive values. On a methodological level, it might be more realistic to represent the firing probability around the 50 percent level described in equation 2.24 using an integrated lognormal variable, such that the probability of firing is only nonzero for positive levels of x. Otherwise in the limit,

$$\lim_{x \to 0} D_t(x) > 0 \tag{2.34}$$

as noted by Bruce et al. (see [23] fig. 12). Using a lognormal variable, the above limit tends to zero, as we expect it to. This change to a lognormal variable was implemented (labeled stochastic* in Figure 2-32), and has the marginal effect of making $D_t(x)$ at low x a slightly steeper function, but does not change the interpretation of our results.

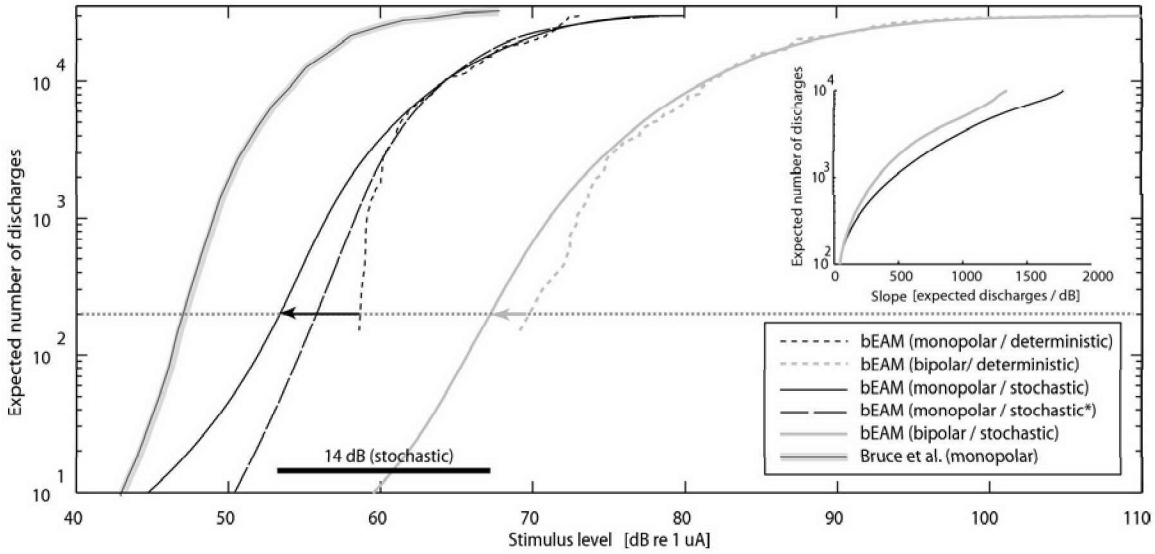

Figure 2-32: Expected number of neurons discharging as a function of level for monopolar (black) and bipolar (gray) stimulation in the deterministic (broken line) and stochastic (solid line) bEAM. Note at low levels, the slope of the monopolar and bipolar curves are dominated by a $\pm$ 5 dB spread in thresholds and the RS introduced by a probabilistic model of threshold. At a discharge of 150 expected discharges (horizontal line), the difference between deterministic and stochastic models is larger for the monopolar case (black arrow) than for the bipolar case (gray arrow). Accordingly, the levels required to reach 150 expected discharges in the stochastic case are separated by 14 dB, whereas in the deterministic model only a 10 dB difference was found. For comparison, data from Bruce el al. [23] (monopolar case, scaled to represent 30,000 total neurons) are shown with the thick gray line. Since Bruce used a heuristic for excitation spread of 0.5 $\frac{dB}{\mathrm{mm}}$ (equivalent to a 6-dB width of 24 mm), the slope of their data is steeper than that predicted by the stochastic bEAM. Note using a lognormal distribution in our derivation (labeled *stochastic**) did not influence these predictions.

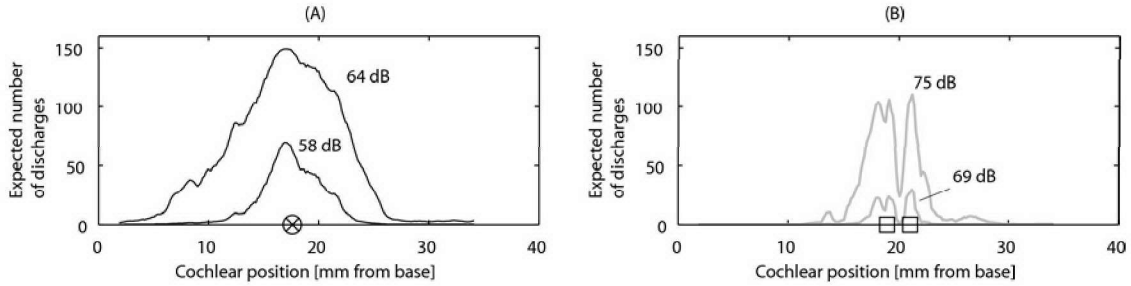

Figure 2-33: Expected number of neurons discharging for each model fiber in the stochastic bEAM as a function of cochlear position for monopolar stimulation of EL4 (panel A) and bipolar (panel B) stimulation. Two levels are shown for each: the deterministic threshold level to discharge one model fiber in the deterministic bEAM, and 6 dB above this level. Note since $N_f = 150$ for each model fiber, the maximum number of discharges each model fiber can contribute is 150.

2.5 Prediction of the electrically-evoked compound action potential

2.5.1 Methods

To predict the ECAP recorded on each intracochlear electrode in response to the collection of stimulated model fibers, a second application of the finite-difference method is used. After excitation by a biphasic pulse, the single-fiber model returns a vector of time-varying membrane voltages $V_{(f,i)}(t)$ describing the response of each compartment (indexed by i) for each model fiber (indexed by f). Some of these responses will include a propagating action potential; some will not. The transmembrane current of each compartment along each model fiber, $I_{m(f,i)}(t)$, is also predicted.

At any instant in time, the collection of membrane currents along an individual model fiber track can be conceptualized in the 3D volume conductor as being generated by a collection of point current sources, the sum of which must equal zero by the network topology of Figure 2-34. For an individual fiber, the predicted transmembrane currents are used to calculate the longitudinal currents that flow through the extracellular medium between neighboring compartments of the cable model (Figure 2-34). It is these currents that generate the ECAP recorded on the intracochlear electrodes. An example distribution of these sources is given in Figure 2-35A.

Treated as a point source, each membrane current induces a voltage on each intracochlear electrode, $\Phi_{e(r)}$, with respect to a far-field reference at $\Phi\infty$. The voltage induced by a unitary 1μA transmembrane current at compartment i of fiber f on recording electrode r is designated $W_{(r,f,i)}$. Likewise, the voltage induced by $I_{m(f,i)}$ is $W_{(r,f,i)} \cdot I_{m(f,i)}$, and the recorded ECAP is computed by summing across compartments and fibers as:

$$ECAP_{(r)}(t) = \sum_{f} \underbrace{\left(N_{f(f)} \sum_{i} W_{(r,f,i)} I_{m(f,i)}(t) \right)}_{SFAP_{(r,f)}} \tag{2.35}$$

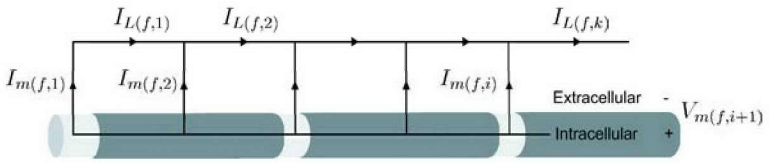

Figure 2-34: Membrane currents $I_{m(f,i)}$ and extracellular longitudinal currents $I_{L(f,k)}$. The simplifying assumption is made here that the bulk of the extracellular current flows parallel to the axis of the fiber.

where $N_{f(f)}$ is the number of neurons each model fiber represents.[46] For the bEAM with 200 model fibers, $N_{f(f)}$ is set to 150 for each f giving a total of 30,000 neurons. The contribution of an individual model fiber to the ECAP is referred to as a single-fiber action potential (SFAP) to maintain consistency with the literature.

Alternatively, from Figure 2-34 the ECAP equation (2.35) can be formulated using the longitudinal currents $I_{L(f,k)}$ instead of membrane currents $I_{m(f,i)}$.[47] Each longitudinal current $I_{L(f,k)}$ is easily calculated from the membrane current (Equation 2.36), weighted by $W^*_{(r,f,k)}$ (Equation 2.37), and added to the sum across neighboring compartment pairs k and fibers f (Equation 2.38). Here $W^*_{(r,f,k)}$ is the potential induced on electrode r by a unitary current dipole between neighboring compartments. The ECAP is calculated as a collection of current dipoles weighted by the longitudinal currents. Algebraically, equations 2.35 and 2.38 are identical, they simply express the ECAP as having been generated by a weighted collection of monopoles and dipoles, respectively.

$$I_{L(f,k)}(t) = \sum_{i=1}^{k} I_{m(f,i)}(t) \tag{2.36}$$

$$W^*_{(r,f,k)} = W_{(r,f,k)} - W_{(r,f,k+1)} \tag{2.37}$$

$$ECAP_{(r)}(t) = \sum_{f} N_{f(f)} \sum_{k} W^*_{(r,f,k)} I_{L(f,k)}(t) \tag{2.38}$$

ECAP components

To investigate how the peripheral and axonal sections of a fiber differentially contribute to the total recorded ECAP, the ECAP contribution from disjoint segments of each model fiber were calculated. For instance, a hypothetical distribution of membrane and longitudinal currents is shown in Figure 2-35A. Note the sum of $I_{m(f,i)}$ across all compartments is equal to zero. The SFAP equation for this 8-compartment fiber is given by Equation 2.39. Dividing the fiber at the 5th compartment (pointed finger) yields the two subunits of Figure 2-35B described by Equation 2.40. Note for each subunit, (1) the sum of the membrane currents remains equal to zero, and (2) the longitudinal current distribution is maintained. Essentially, this partitions the membrane current at the 5th compartment such that the longitudinal currents of the two subunits are maintained.

[46]The inner sum in equation 2.35 is essentially a discrete approximation to the continuous case, for example see equation 38 in Plonsey [162].

[47]The indices i=1...$C_{(f)}$ and k=1...$C_{(f)} - 1$ where $C_{(f)}$ is the number of compartments for fiber f. Note in the unmyelinated continuous case this alternative is equivalent to representing the membrane source as an axial dipole moment density, instead of a monopolar source density (see Plonsey [162] or Chapter 8 of [164]).

$$SFAP_{(r,f)}(t) = \sum_{i=1}^{8} W_{(r,f,i)} I_{m(f,i)}(t) \tag{2.39}$$

$$= \underbrace{\sum_{k=1}^{4} W^*_{(r,f,k)} I_{L(f,k)}(t)}_{\text{peripheral SFAP}} + \underbrace{\sum_{k=5}^{7} W^*_{(r,f,k)} I_{L(f,k)}(t)}_{\text{axonal SFAP}} \tag{2.40}$$

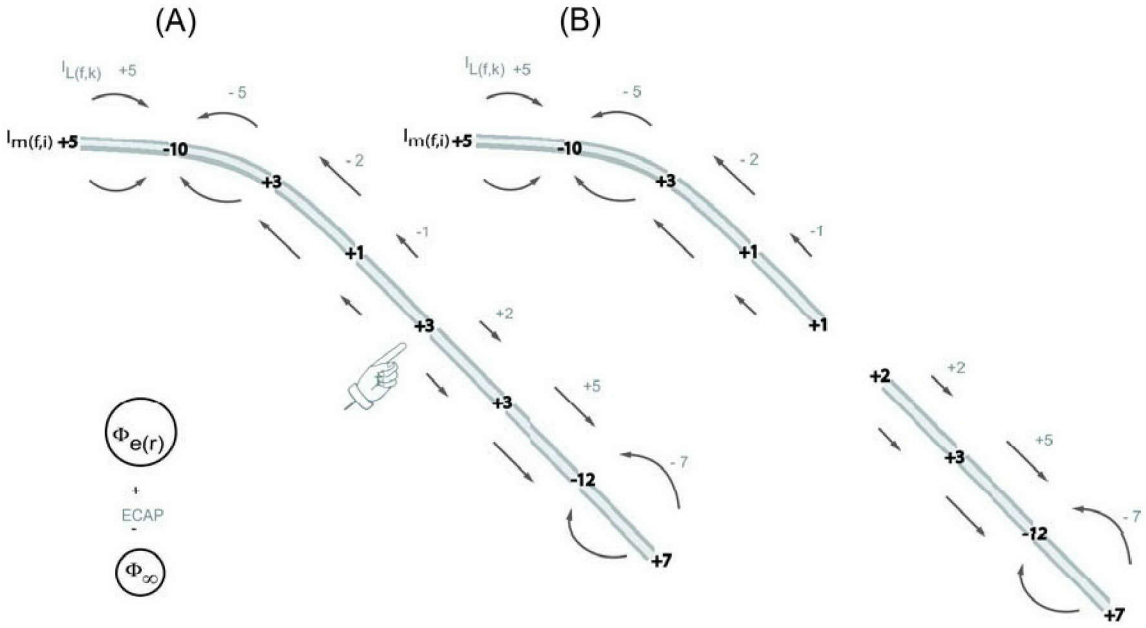

Figure 2-35: (A) Illustrative distribution of membrane current values $I_{m(f,k)}$ (black) and longitudinal current values $I_{L(f,k)}$ (gray) for an eight compartment model fiber. The ECAP is measured as the voltage between the recording electrode $\Phi_{e(r)}$ and Φ_∞ at a remote ground. (B) Same fiber as in panel A, divided into a peripheral and axonal subunit. Note for each subunit the sum of the membrane currents remains equal to zero, and the same longitudinal current distribution is maintained as in panel A.

Weight calculation

Each weight $W_{(r,f,i)}$ can be found by measuring the voltage induced on a recording electrode ($\Phi_{e(r)} - \Phi_\infty$) after placing a $1\mu A$ current source in the volume conduction model at position i of fiber f paired with a far-field return located at Φ_{rtn} (see Figure 2-36). Since Φ_e, Φ_∞, $\Phi_{(f,i)}$, and Φ_{rtn} are all nodes in a resistive network, reciprocity can be used to calculate the collection of weights simultaneously for a single recording electrode using one field solution. By the two port analogy of Figure 2-36,

$$\frac{\Phi_{e(r)} - \Phi_\infty}{i_2}|_{i_1=0} = \frac{\Phi_{(f,i)} - \Phi_{rtn}}{i_1}|_{i_2=0} \tag{2.41}$$

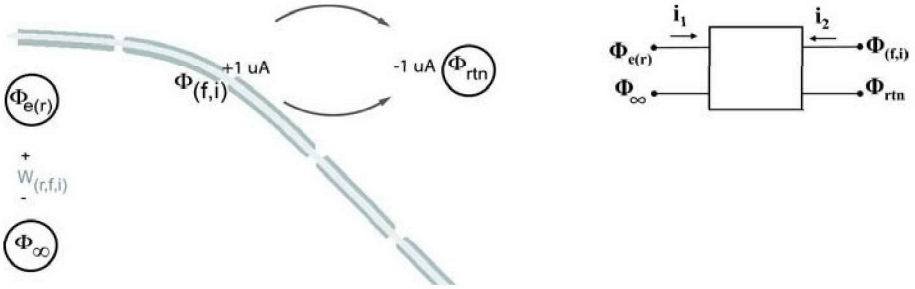

Figure 2-36: Weight calculation.

such that the voltage $\Phi_{e(r)} - \Phi_\infty$ in response to 1 μA of current between the nodes labeled $\Phi_{(f,i)}$ and Φ_{rtn}, is equivalent to the voltage $\Phi_{(f,i)} - \Phi_{rtn}$ in response to 1 μA of current between nodes labeled $\Phi_{e(r)}$ and Φ_∞ (equation 2.41). For each recording electrode, the weights are obtained by placing a $+1\mu$A source at the electrode position of $\Phi_{e(r)}$ paired with a return at Φ_∞ while recording the voltage $\Phi_{(f,i)} - \Phi_{rtn}$ for each position in the model requiring a weight. Moving the position of Φ_{rtn} in the model only shifts the entire collection of weights $W_{(r,f,i)}$ by a constant. Since the sum

$$\sum_i I_{m(f,i)}(t) = 0 \tag{2.42}$$

adding a constant to $W_{(r,f,i)}$ does not change the calculation in Equation 2.35. In other words, only differences in $W_{(r,f,i)}$ across the compartments (i) of a fiber effect the calculation. However, the predicted ECAP can be slightly sensitive to the position of Φ_∞. To measure this, $W_{(r,f,i)}$ was recalculated with the position of Φ_∞ moved to different corners of the volume conduction model.

2.5.2 Results

An example ECAP computation is shown in Figure 2-37. Here a 1,500 μA monopolar pulse (30 μs/phase, cathodic leading) is applied to EL3, initiating action potentials over a range of model fibers as shown in the plot of SFT versus θ in panel A. Fibers having a threshold to the left of the broken vertical line ($150 < \theta < 391$) will respond with an action potential.

The contribution of each SFAP to the ECAP recorded on EL4 ($ECAP_{(4)}$) is shown in panel B. The magnitude of each SFAP is plotted in grayscale (see calibration bar), forming an image where each horizontal line represents one model fiber's contribution. The cochlear positions (θ) of the simulating and recording electrodes are marked with $\otimes$ and $\odot$. Across the collection of spiking model fibers ($150 < \theta < 391$) contributing an appreciable SFAP, there is considerable variability in the timing of individual SFAPs, although they each tend to have the same basic shape characterized by a negative initial peak (N1) followed by a positive peak (P1). It is apparent in panel B that fibers at cochlear positions relatively distant from that of the recording electrode exert an appreciable SFAP. For instance, fibers near 350 degrees (marked with arrowhead in Fig 2-37B) show a contribution even though the recording electrode (EL4) is at a cochlear position of only 170 degrees.

The predicted $\text{ECAP}_{(4)}$ is shown in panel C. A scaled-template artifact rejection scheme (like that used in human recordings) is used to remove the stimulus artifact from the ECAP computations. Both the raw (gray) and artifact-rejected (black) traces are shown.

Temporal evolution of the ECAP

To further examine the temporal evolution of the predicted ECAP shown in Figure 2-37C, the SFAP for the model fiber located at 349 degrees (leftward arrowhead in Fig 2-37B) is plotted in panel A of Figure 2-38. Plotted at four instants in time in panels B-E are the membrane currents $I_{m(f,i)}$ along the model fiber.

For this fiber the action potential initiates at the cell body. At 150 μs in panel B there are four regions in the trace of I_m versus fiber position[48] showing large membrane currents (labeled 1-4). The first two (located on the peripheral process) constitute an antidromically propagating action potential, while the second pair (3-4) constitute an orthodromically propagating action potential. Initially the SFAP is dominated by negative membrane currents (labeled 2 and 3). It isn't until 450 μs that the antidromic action potential has finished propagating and the SFAP becomes positive due to the positive repolarization current (labeled 5) associated with the orthodromically propagating action potential.

[48]The position of the cell body is taken as zero, while segments peripheral to the cell body have negative values.

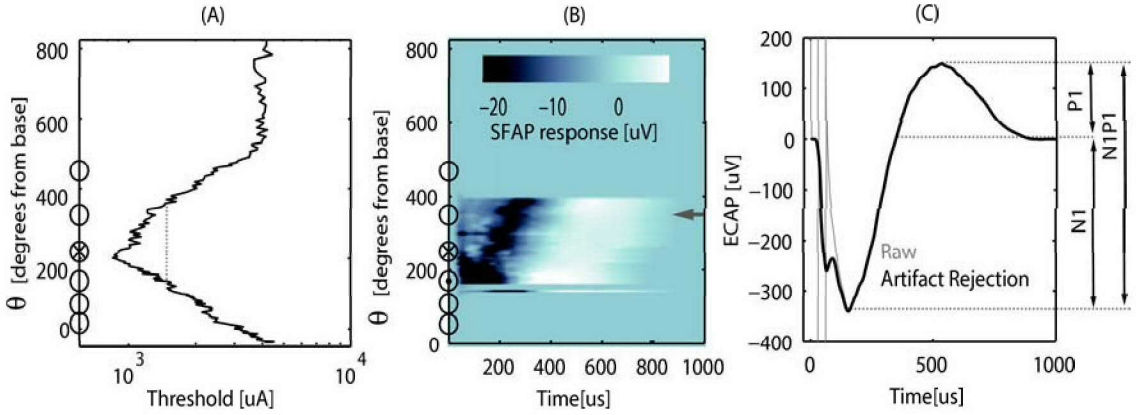

Figure 2-37: ECAP response to 1,500 μA stimulus on EL3. (A) Cochlear position of model fibers θ versus threshold (axes rotated) The vertical line marks 1,500 μA stimulus magnitude, with model fibers between 150 and 391 degrees (thresholds to the left of the line) eliciting action potentials. (B) SFAP contributions to $ECAP_{(4)}$ in response to stimulation on EL3. Each horizontal row in the image denotes a SFAP. For this simulation 100 model fibers were used such that each model fiber's SFAP represents roughly 300 neurons. The stimulating and recording electrodes are marked with $\otimes$ and $\odot$. (C) Computed $ECAP_{(4)}$ showing characteristic N1 and P1 amplitudes. The ECAP predictions before (gray), and after (black), the scaled-template artifact rejection are shown. Notice the artifact rejection does not influence the N1 measure, as the artifact component dies away roughly 30 μs after the stimulus period.

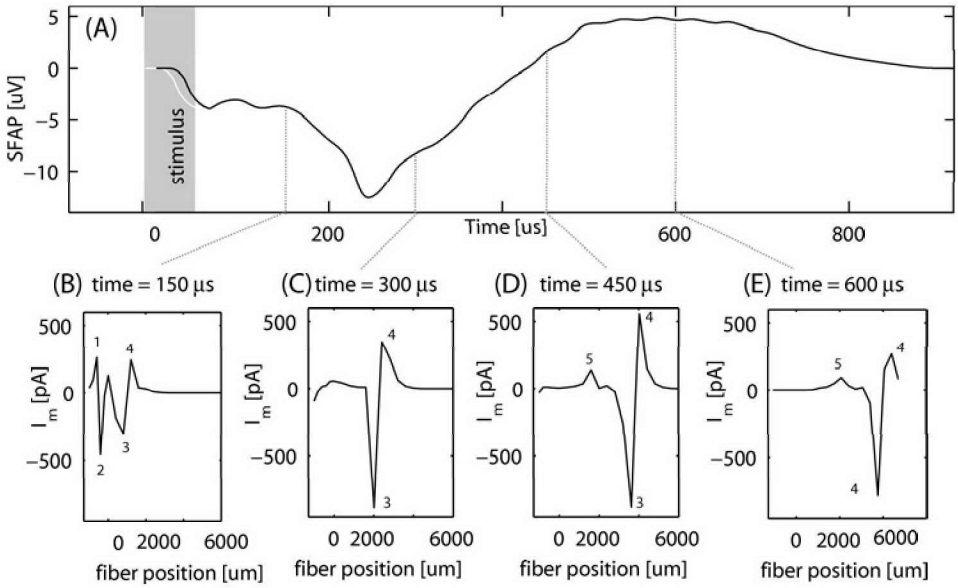

Figure 2-38: SFAP time evolution for one model fiber representing 150 neurons (N_f=150). (A) SFAP contribution to the ECAP for a single fiber located near 349 degrees, after stimulation on EL3 while recording the SFAPs on EL4, as in Figure 2-37B. The position of this fiber is marked with an arrowhead in panel B of Figure 2-37. (B-E) Nodal membrane currents versus fiber position at 150 μs, 300 μs, 450 μs, and 600 μs after the stimulus pulse onset. Here the cell body is located at a fiber position of zero. The peripheral process takes on negative position values. Only nodal currents are plotted for clarity of presentation.

Use of a volume conduction model

To investigate whether computing the weights $W_{(r,f,i)}$ using a homogeneous model results in a different ECAP prediction than computed using the heterogeneous bEAM model, a collection of homogenous weights $W^h_{(r,f,i)}$ were calculated.[49]

Using $W^h_{(r,f,i)}$ the ECAP was recalculated in response to the same stimulus as is Figure 2-37. The collection of responding fibers is the same as is the distribution of membrane currents, only the weights used in the ECAP computation change. Shown in Figure 2-39 are the SFAP contributions using $W_{(r,f,i)}$ computed using the bEAM (left column) and $W^h_{(r,f,i)}$, computed with the homogeneous model (middle column), for recording electrodes EL2 (top row), EL3 (middle row), and EL4 (bottom row). The position of the recording electrode is marked by $\odot$, while the stimulating electrode, marked by $\otimes$, remains fixed on EL3. The predicted ECAPs recorded from EL2, EL3, and EL4 using $W_{(r,f,i)}$ (black) and $W^h_{(r,f,i)}$ (gray) are shown in the right column.

Comparing panels A, D, and G of the left column, the SFAP contributions to the ECAP using $W_{(r,f,k)}$ are remarkably similar, showing an initial positive wave followed by a longer-duration negative wave. This is especially surprising considering that recording electrodes EL2 and EL4 are spatially separated by 180 degrees. Consistent with this, the ECAPs calculated using $W_{(r,f,i)}$ (black traces, right column) show little variation in either amplitude or shape as as the recording electrode is moved.

Using the homogeneous $W^h_{(r,f,i)}$, panels B, E, and and H show substantial variation in the collection of SFAPs as the recording electrode is moved. For instance, in panel B the collection of fibers localized near the recording electrode ($\odot$) show SFAP contributions that are initially positive, then negative. SFAPs from fibers apical to and basal to this collection have the opposite phase. This trend continues in panels E and H, where a narrow collection of SFAPs at a position in θ near the recording electrode have an initial positive phase followed by a negative phase.[50]

The impact of this is seen in the predicted ECAPs using $W^h_{(r,f,i)}$ in the right column of Figure 2-39. While the ECAP waveforms predicted using the bEAM weights (black) all show a clear negative N1 wave followed by a P1 wave, the ECAPs predicted using the homogeneous weights (gray) show a different behavior, such as the initial P0 wave predicted in panel I. Additionally, using $W^h_{(r,f,i)}$ the morphology of the ECAP waveform changes drastically as the recording electrode is moved, a result that does

[49] Using $\sigma = \frac{1}{300\Omega cm}$, the homogenous weights are calculated analytically as

$$W^h_{(r,f,i)} = \frac{1\mu A}{4\pi\sigma d_{(r)}} \tag{2.43}$$

where $d_{(r)}$ is the distance from position i along model fiber f to electrode r.

[50] This phenomena is similar to that reported by Briaire and Frijns [13] (their Figure 11) although they attributed it to position of the orthodromically propagating action potential along the fiber, not to the weights used in the ECAP computation.

not fit with reports from the literature nor with archival ECAP recordings made on the Ineraid patient (see sections 2.5.3 and 3.3).

Amplitude growth

Summary N1P1 amplitude statistics predicted by the bEAM for basal (EL6) and apical (EL1) stimulation are shown in the left and right columns of Figure 2-40. Panels (A) and (B) of the top row show N1P1 amplitude versus stimulus level as predicted for recording electrodes EL6, EL3 and EL1. Panels (C) and (D) show the contribution of the N1 amplitude (negative values) and the P1 amplitude (positive values) as a function of stimulus level.

To illustrate the extent to which N1P1 growth reflects a simple addition of individual SFAP amplitudes, the N1P1 amplitude is plotted versus the number of spiking model fibers in panels E and F.[51] The nearly linear shape of these functions suggests that each additional recruited fiber adds a relatively constant amount to the recorded N1P1 amplitude. This result might have been expected since we have not included any stochastic influences that would tend to increase jitter.

In panels G and H, the spatial distribution of N1P1 amplitude is plotted as a function of recording electrode. The set of curves represent a level series, with the stimulus current increasing from 1,000 to 2,000 μA in 125-μA steps. These data are replotted in panels I and J, normalized as a percent maximum. In the case of apical stimulation (right column), the N1P1 decreases monotonically as the recording electrode is moved from the apical EL1 to the basal EL6. This fits with expectation, since the recording electrode is moving further from the spike generators. The case of basal simulation is less intuitive. Here as the recording electrode is moved apical from the basal stimulating electrode, the N1P1 amplitude initially decreases, then increases for both EL2 and EL1. This is likely because of the geometry of the basal turn, as explained in the next section.

[51] In these simulations 100 model fibers were used with $N_{f(f)}$ was set to 300 neurons per model fiber.

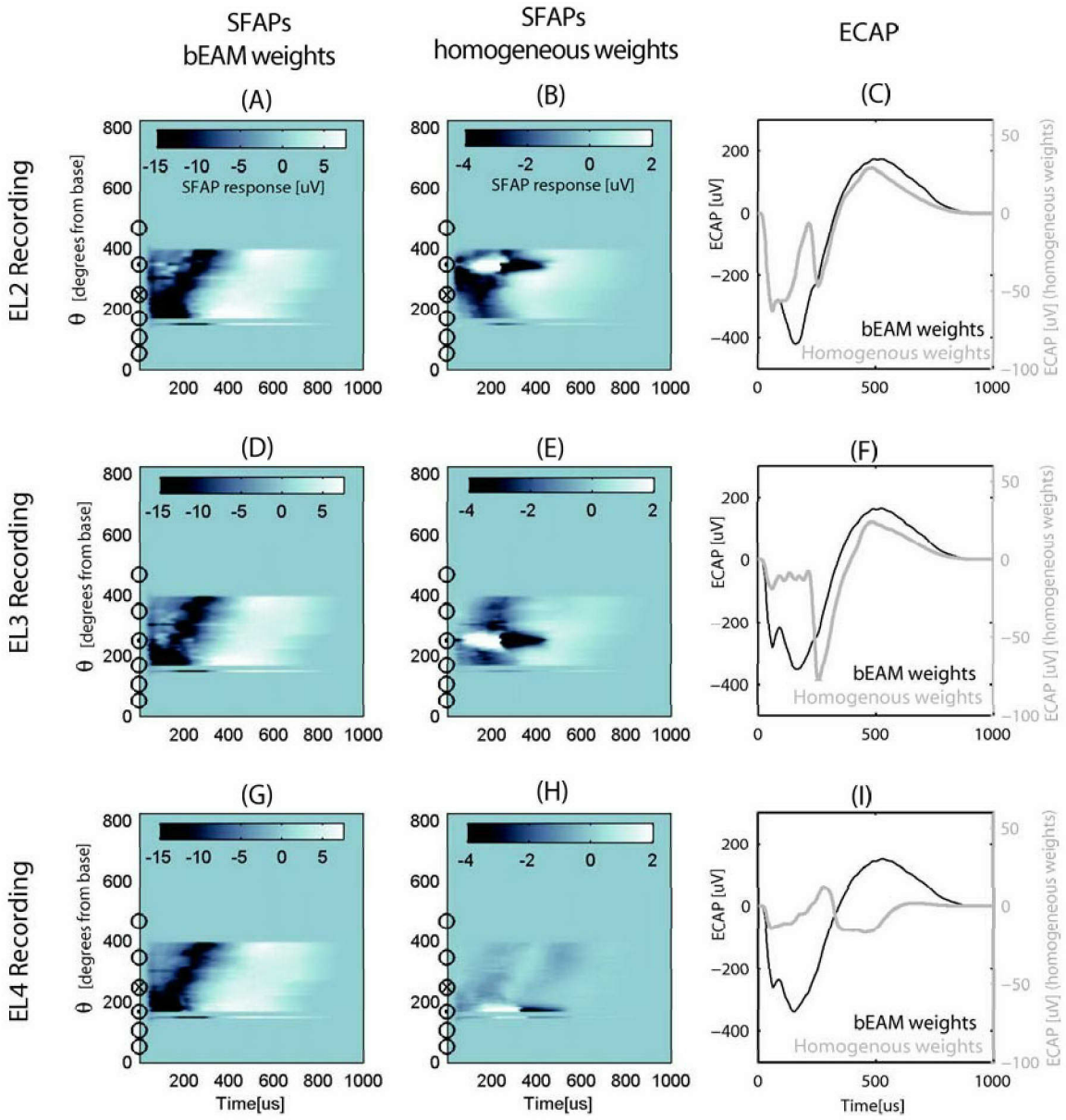

Figure 2-39: Influence of homogeneous weights $W^h_{(r,f,i)}$ on ECAP computation. Note in each panel, the collection of responding fibers and membrane currents $I_{m(f,i)}$ remain the same. **(Left Column)** SFAP contribution plotted as a function of θ and time using the computational $W_{(r,f,i)}$ for recording electrodes EL2 (top row), EL3 (middle row), and EL4 (bottom row). The positions of the simulating and recording electrodes are marked by and $\otimes$ and $\odot$. **(Middle Column)** SFAP contributions predicted using the homogeneous weights, $W^h_{(r,f,i)}$. **(Right Column)** Predicted ECAP traces using the bEAM (black) and homogeneous (gray) weights. Note the different amplitude scales for the two traces.

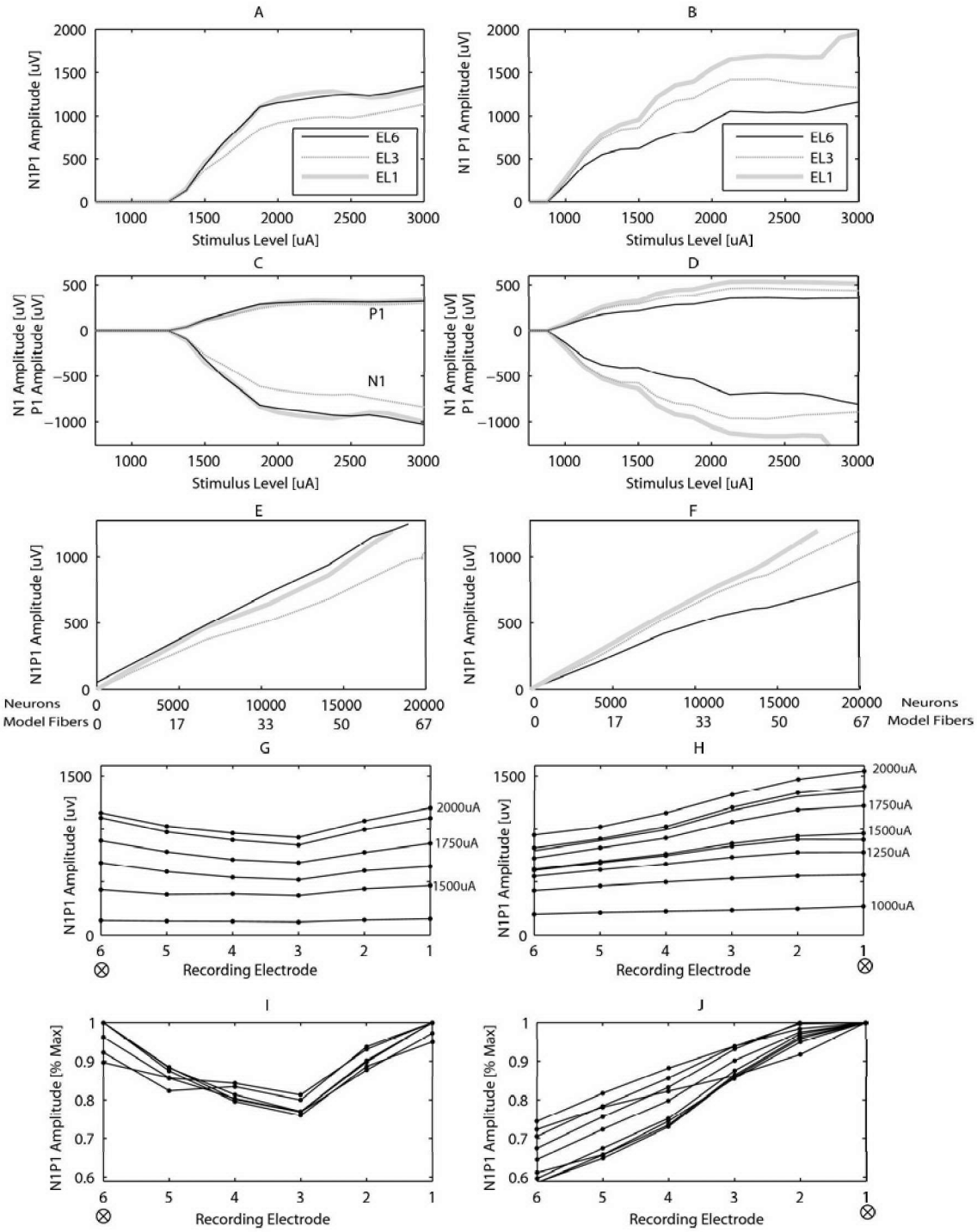

Figure 2-40: ECAP amplitude growth across stimulating and recording electrodes. Left and right columns show results for basal (EL6) and apical (EL1) stimulation. (A-B) N1P1 amplitude growth versus stimulus level as recorded on EL6, EL3 and EL1. (C-D) N1 and P1 amplitude growth versus level as recorded on EL6, EL3 and EL1. (E-F) N1P1 amplitude growth as a function of the number of contributing fibers (or neurons). Note for this simulation each of 100 model fibers represented 300 neurons ($N_{f(f)} = 300$ for all f). (G-H) N1P1 amplitude as a function of recording electrode for a series of stimulus levels. Connected curves are of increasing stimulus amplitude from 1,000-2,000 μA in 125 μA steps. (I-J) N1P1 amplitude as a function of recording electrode for various stimulus levels, as in panels G and H, but normalized by the maximum N1P1 amplitude across recording electrodes for a fixed stimulus level.

2.5.3 Discussion

The most counter-intuitive bEAM result is that model fibers distant from the recording electrode contribute a similar biphasic SFAP waveform. This is primarily due to the highly conductive cochlear fluid each of the electrodes sits in. As noted by several authors (Brown et al. [17, 16], Cafarelli-Dees et al. [24]), the ECAP morphology typically does not change significantly as the recording electrode is moved, with the overwhelming majority of recordings showing a distinct N1P1 complex. The ECAP data collected from the Ineraid subject also support this (see next chapter). As pointed out in Figure 2-39, the relative invariance of the SFAP morphology to the simulating/recording electrode configuration can not be predicted with a homogenous model, emphasizing the importance of an appropriate representation of the inhomogeneity in tissue conductivity.

Shown in Figure 2-41 is the typical contribution of a single neuron to the ECAP, averaged across cochlear position, after individually stimulating each model fiber with a monophasic, intracellular current pulse applied to the peripheral-most compartment. The averaged response is plotted for the bEAM in Figure 2-41A, and the 600-Ωcm bEAM in panel B. Also shown are typical latencies measures for the N1 ($\bigtriangledown$) and P1 ($\bigtriangleup$) waves recorded in 141 subjects by Cafarelli-Dees et al. [24].

The model-predicted waveform latencies are slightly longer than the data. This is likely due to our choice of a single-fiber model, whose conduction velocity of 9.6 m/s is relatively slow due[52] to the inclusion of leaky internodal sections. Including the influence of the cell body will also tend to delay the action potential [170]. Future renditions will incorporate somatic delay while adjusting the single-fiber model to obtain a more realistic conduction velocity.

ECAP amplitude growth

To analyze the growth of N1P1 amplitude with increasing stimulus levels (the ECAP growth function), we use the theoretical model of the evoked potential introduced by Goldstein and Kiang [62], that states auditory gross potentials can be modeled as the convolution of an elementary waveform generated by a single unit, $U(t)$, with a probability density function describing the poststimulus time distribution of elicited spikes, $PST(t)$.[53]

$$ECAP(t) = \int_{-\infty}^{t} PST(\tau)U(t-\tau)d\tau \tag{2.44}$$

[52]Moller et al. [138] report a conduction velocity in the human of 22.0 m/s.

[53]The PST distribution is the collective sum across all neurons, such that the amplitude and distribution of PST the is determined by the population of neurons included.

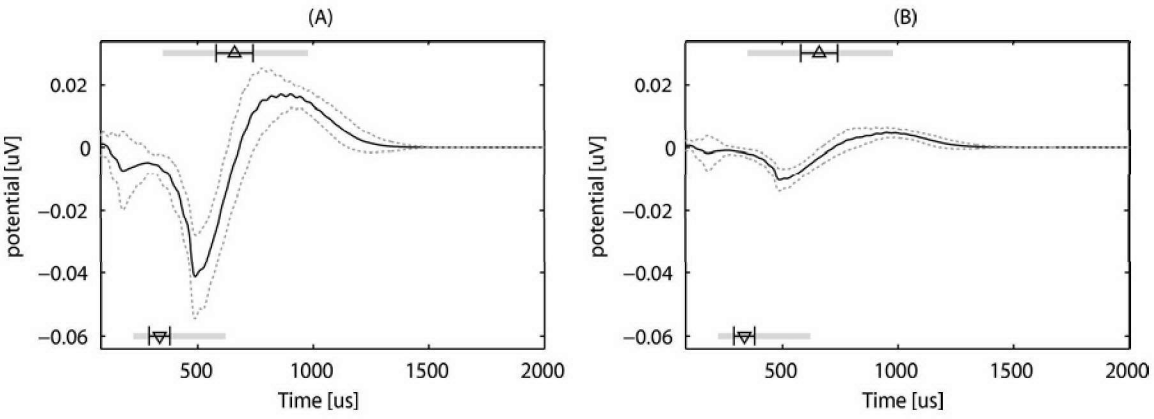

Figure 2-41: Average SFAP scaled to represent a single neuron's contribution ($N_f = 1$) to the ECAP for the bEAM (panel A) and 600-Ωcm bEAM (panel B). These estimates were obtained by initiating an action potential on each fiber's peripheral process with an intracellular current, then averaging (across θ) all SFAP waveforms predicted for EL4. The dotted line shows ± one standard deviation in the average. Mean ECAP latencies from the data of Cafarelli-Dees et al. [24] are shown for the N1 ($\bigtriangledown$) and P1 ($\bigtriangleup$) peaks. Bars around $\bigtriangledown$ and $\bigtriangleup$ mark one standard deviation, while the shaded bar designates the range of values across 585 recordings in the Cafarelli-Dees data.

In this framework, each neuron contributes an identical waveform to the gross potential regardless of cochlear position, referred to here as having a unitary amplitude δ_{SFAP}. Note δ_{SFAP} can be estimated for either an intracochlear electrode or for surface electrodes such as those used to measure the evoked auditory brainstem response (EABR). In the case of electric stimulation, we assume that the spike times are sufficiently synchronized to yield a PST distribution that approaches a Dirac delta function. This reduces the convolution in Eqn 2.44 to a summation of unit responses, where the gross potential amplitude is simply the sum of the unit potential amplitudes from the responding population of neurons. The further away from a delta function the $PST(t)$ deviates, the further the gross potential waveform is smeared in time, reducing the amplitude of the N1P1 complex.

Evidence that each unit contributes equally regardless of CF, implying little or no cancelation across synchronized units, comes from estimates of the unitary waveform made in the cat by Kiang [100] and Wang [221] using the spike-triggered averaging technique (see [100]). They found only small difference in SFAP waveforms measured for single units of different CF.[54] Similar experiments by Versnel [217] in guinea pig did not find a strong systematic relationship between the unitary potential and fiber CF.

[54]For example, Wang's estimates the unitary potential, or spike-triggered averages (STAs), where parameterized the by measuring the peak-to-peak amplitude (PPA), peak-to-peak time (PPT), and negative-peak time (NPT), or latency. No significant variation in either PPA or PPT was found across CF, however, the latency measure NPT showed shorter latencies for fibers at the base with CFs above 10k (Ch 2, Fig 8 of [221]).

Evidence for the unitary response hypothesis in the electrically excited cochlea comes from Hall [69], who measured a strong (e.g., $r^2 = 0.706$ for P1) correlation between the slope of the EABR growth function and the total number of ganglion cells surviving an otological insult; and from Smith et al. [192], who reported a near linear relationship between the percentage of surviving neurons in the cat and the slope of the EABR growth function.

The SFAPs in panels A,D, and G of Figure 2-39 also support the notions that (1) all SFAP waveforms are similar in shape, and (2) a small amount of cancelation occurs when combining SFAPs to form the predicted ECAP waveform. This trend is also apparent in panels E and F of Figure 2-40 where the N1P1 amplitude is a near-linear function of the number of neurons stimulated. While this treatment ignores both variation is single-unit thresholds (e.g., relative spread) and timing (jitter), it is a reasonable starting place, especially since Miller el al. [134] investigated the influence of including these aspects only to conclude that the distribution of fiber thresholds was the most influential in determining the growth rate of the evoked potential. As evidenced by Miller's data, adding jitter ought to make the ECAP growth curves more shallow, meaning that deterministic models such as the bEAM would be expected to slightly overestimate the ECAP growth function.

A phenomenological model of ECAP growth

Making the final assumption that neurons are, more or less, equally distributed across cochlear length, the ECAP growth function has a slope, M_{N1P1}, that can be expressed as the product of three variables in the model (units given in brackets):

$$M^s_{N1P1(r)}\left[\frac{\mu V}{\text{dB}}\right] = \delta^s_{SFAP(r)}\left[\frac{\mu V}{\text{neuron}}\right] \cdot N_f\left[\frac{\text{neurons}}{\text{model fiber}}\right] \cdot R^s\left[\frac{\text{model fibers}}{\text{dB}}\right] \tag{2.45}$$

$$= \delta^s_{SFAP(r)}\left[\frac{\mu V}{\text{neuron}}\right] \cdot N_l\left[\frac{\text{neurons}}{\text{mm}}\right] \cdot R^s_l\left[\frac{\text{mm}}{\text{dB}}\right] \tag{2.46}$$

where $\delta^s_{SFAP(r)}$ is the incremental N1P1 amplitude increase recorded on electrode r per neuron responding to stimulation by electrode s,[55] N_f is the number of neurons represented by each model fiber (150 neurons per model fiber in the bEAM), and R^s is the number of model fibers recruited per unit dB increase in the stimulus current on electrode s.

To compare estimates across models and with those in the literature, equation 2.45

[55]Here $\delta^s_{SFAP(r)}$ is taken as the average single-neuron $SFAP_{(r,f)}$ amplitude ($N_f = 1$) across responding model fibers. Strictly speaking δ_{SFAP} is a function of the recording electrode r and model fiber f. However, since the population of fibers responding changes with the stimulating electrode, the average value for δ_{SFAP} is measured as a function of r and s.

is rewritten as 2.46, where N_f is converted to N_l, the number of neurons *per millimeter of longitudinal distance* along the basilar membrane,[56] and R^s is converted to R_l^s, the recruitment of *longitudinal distance* per unit increase in stimulus level on electrode s.[57]

The conversion to stimulus level in dB (re the lowest SFT) is necessary (1) because of the different stimulus conditions used across the literature (e.g., differences in pulse width), and (2) when expressed in absolute units, ECAP thresholds (μA) and growth functions ($\mu V/\mu A$) tend to be vary inversely [16, 135, 136]. Expressing the slope of the ECAP in dB should ameliorate both of these problems. Additionally, the conversion to dB allows for a statistical interpretation of the slope ECAP of the growth function (see appendix 2.7.1).

N1P1 amplitude per neuron δ_{SFAP}

Because $\delta^s_{SFAP(r)}$ describes the average coupling between recording electrode r and a fiber stimulated by electrode s, if one stimulates at the apex while recording at the base ($\delta^1_{SFAP(6)}$), ones expects a slightly smaller value for δ_{SFAP} than if one had recorded near the apex (i.e., $\delta^1_{SFAP(2)}$). Similarly, one expects variation in $\delta^s_{SFAP(r)}$ across different recording electrodes given a fixed stimulating electrode, to mirror variation in excitation strength across electrodes (see below).

Panels A and B of Figure 2-42 show the recruitment of neurons and predicted N1P1 amplitude as a function of level for the bEAM and 600-Ωcm bEAM. Panels C and D show the same data as reported by Briaire and Frijns [13], showing lower fiber thresholds and a more gradual recruitment with level. The N1P1 amplitude is plotted in panel E for the three models as a function of the number of excited neurons, thereby removing the influence of recruitment R_l. A typical result for the bEAM is shown in black, with the range of curves marked in gray. The slope of this curve ($\delta^s_{SFAP(r)}$) averages 0.062 $\left[\frac{\mu V}{\text{neuron}}\right]$ for the bEAM, 0.021 $\left[\frac{\mu V}{\text{neuron}}\right]$ for the 600-Ωcm bEAM,[58] and 0.11 $\left[\frac{\mu V}{\text{neuron}}\right]$ for the Briaire et al. data. Since Briaire el al. used 640 Ωcm for bone, we might expect the value for δ_{SFAP} to be smaller that the bEAM, however we attribute the larger δ_{SFAP} to differences in the single-fiber model used. For instance, dimensional changes in the morphology of the SGC can lead to an increase in the magnitude of the membrane currents, thus increasing the δ_{SFAP}. Regardless, it is encouraging that the bEAM and Briaire et al. models yield

[56]In the bEAM, N_l is constant across θ, while in each psEAM N_l can vary across θ according to the pattern of surviving ganglion cells.

[57]Here "recruitment" refers to the increasing length of cochleotopic positions over which excitation occurs, assuming all neurons of a given cochleotopic position respond in unison. Since model fibers are evenly distributed across cochleotopic position, the recruitment per μA delivered to a stimulating electrode can be expressed in model fibers, degrees θ, or millimeters of cochleotopic length.

[58]Note if $\delta^s_{SFAP(r)}$ is measured as the peak-to-peak amplitude from the SFAP waveforms, mean values of 0.069 and 0.020 μV are obtained for the bEAM and 600-Ωcm bEAM.

a δ_{SFAP} of similar magnitude.

One possibility raised by 2-42 E is whether variation in ECAP growth across subjects may reflect variation in the resistivity of the bone of the otic capsule, for instance, in patients with otosclerosis [64] or Paget's disease [139] where the bone mineral density is decreased.

Variation in $\delta^s_{SFAP(r)}$ reflects the influence of the stimulating and recording electrode positions. Shown in panels F and G are plots of the measured $\delta^s_{SFAP(r)}$ as a function of the recording electrode when the simulating electrode is at the base (panel F) and at the apex (panel G). As one might expect, these mirror the plot of N1P1 amplitude across recording electrode in panels I and J of Figure 2-40. Specifically, as the recording electrode is moved away from a basal stimulating electrode (panel I, Figure 2-40), a non-monotonic decrease in the ECAP is seen, similar to the non-monotonic curve shown for $\delta^6_{SFAP(r)}$ in panel F of Figure 2-42. Longitudinally speaking, EL1 and EL2 are further from the simulating electrode (EL6), however because of cross turn coupling, these electrodes record SFAPs with higher amplitudes.

As mentioned above, for a fixed stimulating electrode one expects variation in $\delta^s_{SFAP(r)}$ across recording electrodes to mirror variation in excitation strength across the stimulating electrodes.[59] Since the spatial selectivity of the 600-Ωcm bEAM is greater than the standard bEAM (see section 2.4.5), one expects a greater variation in $\delta^s_{SFAP(r)}$ across recording electrodes for this model. This is apparent in panels H and I, where variation in $\delta^s_{SFAP(r)}$ across recording electrode is shown. Expressing the variation in $\delta^s_{SFAP(r)}$ as a coefficient of variation (CV), returns 0.15 for the bEAM, 0.31 for 600-Ωcm bEAM.

Cochleotopic spread R_l

The parameter R_l represents the spread of excitation across cochlear length with level.[60] For example, monopolar and bipolar stimuli were estimated in the last section to have 6 dB-widths of 11 and 4.4 millimeters, suggesting R_l values near 1.83 and 0.73

[59]For example, in the limit that the fluid is a perfect conductor, for a group of responding neurons each electrode will record an identical gross potential, leaving no variation in $\delta^s_{SFAP(r)}$ across recording electrodes. Likewise, varying the position of the stimulating electrode ought to have no influence on the collection of neurons excited. In the opposite case where an electrode excites a focused patch of cochlear length, one expects a large degree of variation in $\delta^s_{SFAP(r)}$ across recoding electrodes. This duality can also be understood by comparing field patterns for monopolar and bipolar electrode configurations. For the same reasons that bipolar stimulation ought to excite a narrower collection of neurons, using a bipolar pair to record the ECAP ought to have a narrower spatial selectivity than a single intracochlear electrode, which is more omnidirectional.

[60]In the implanted cochlea, two types of recruitment might be distinguished per unit increase in the stimulus level: "spatial recruitment" of neurons more distant from the electrode, and "local recruitment" of high-threshold neurons adjacent to the electrode where some neurons are already responding. While the stochastic bEAM incorporates both of these, only "spatial recruitment" occurs in the bEAM. The product $N_l\, R_l$ has units of $\left[\frac{\text{neurons}}{\text{dB}}\right]$, such that R_l is interpreted as the incremental recruitment per unit increase in stimulus level, expressed as purely "spatial" recruitment.

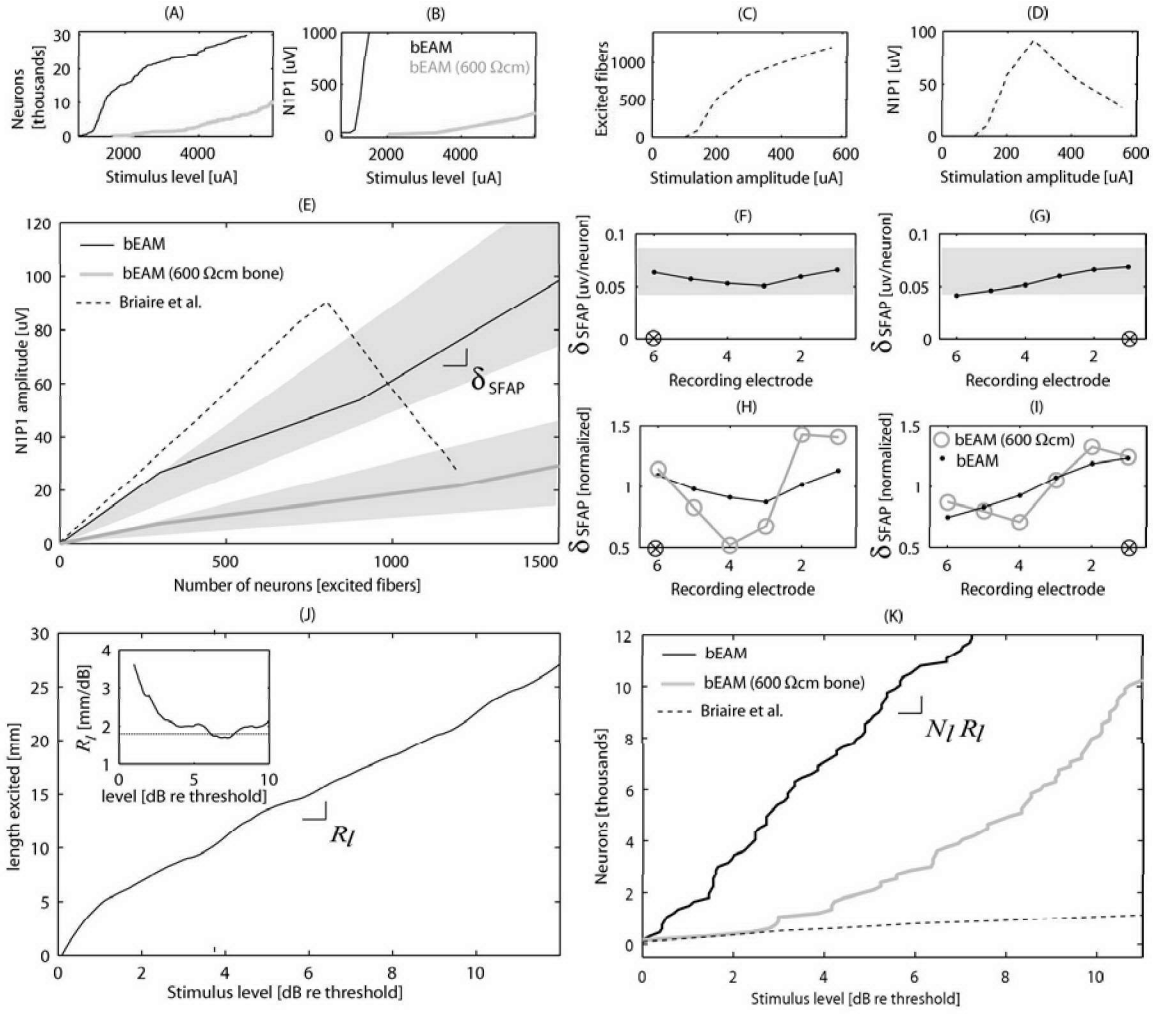

Figure 2-42: **(A-B)** Neurons recruited as a function of stimulus level for the bEAM and 600-Ωcm bEAM (panel A), with the corresponding N1P1 amplitude, recorded on EL1, shown in panel B. **(C-D)** Neural recruitment (panel C), and N1P1 amplitude growth (panel D) as reported by Briaire and Frijns [13] (their figure 10). **(E)** Data in panels A-D repotted as N1P1 amplitude as a function of the number of neurons discharging. For the bEAM and 600-Ωcm bEAM the range of curves for different stimulating-recording electrode pairs is shown in gray with corresponding δ_{SFAP} values ranging 0.041-0.088 in the bEAM, 0.009-0.032 in the 600-Ωcm bEAM. **(F-G)** Variation in $\delta^s_{SFAP(r)}$ across recording electrode shown for stimulation by EL6 (panel F) and EL1 (panel G). The entire range of δ_{SFAP} is given by the gray shading. **(H-I)** $\delta^s_{SFAP(r)}$ variation across recording electrode normalized about the mean for EL6 (panel H) and EL1 (panel I). The $\delta^s_{SFAP(r)}$ values for the 600-Ωcm bEAM show more variation than the bEAM, as seen by comparing the gray and black traces. **(J)** Average recruitment of cochlear length as a function of stimulus level, where R_l is taken as the derivative of this function evaluated at 6 dB. Notice the derivative (panel J inset) decreases to settle on a value of roughly 1.8 [mm/dB]. **(K)** Neurons recruited as a function of level (dB re threshold) comparing the bEAM, 600-Ωcm bEAM, and the model reported by Briaire et al. The slope of the Briaire et al. data suggest an $N_l\ R_l$ product $\approx 100\ \left[\frac{\text{neurons}}{\text{dB}}\right]$ and an R_l value $\approx 0.1\ \left[\frac{\text{mm}}{\text{dB}}\right]$.

$\left[\frac{\text{mm}}{\text{dB}}\right]$. Panel J of Figure 2-42 plots the recruitment function showing the increasing extent of cochleotopic positions excited as a function of the stimulus level. Strictly, speaking, the parameter R_l is taken as the slope of this function evaluated 6 dB above threshold. Comparing R_l values for the bEAM, 600-Ωcm bEAM, and homogenous models, one notices R_l decreases with increasing activation spread (see right column of Table 2.9).

The product $N_l R_l \left[\frac{\text{neurons}}{\text{dB}}\right]$ represents the recruitment of neurons with increasing level. Plotting the number or neurons recruited versus stimulus level in dB (panel K of Figure 2-42), the product $N_l R_l \left[\frac{\text{neurons}}{\text{dB}}\right]$ can be compared to the 600-Ωcm bEAM and the Briaire et al. [13] model. Given a reported value of 1,000 $\left[\frac{\text{neurons}}{\text{mm}}\right]$ for N_l in the Briaire model, the corresponding value of R_l estimated from panel K is roughly 0.1 $\left[\frac{\text{mm}}{\text{dB}}\right]$,[61] an order of magnitude smaller than the 1.83 $\left[\frac{\text{mm}}{\text{dB}}\right]$ bEAM prediction for R_l.

ECAP amplitude growth M_{N1P1}

Finally, weighting the product $N_l R_l$ with the average N1P1 contribution of each neuron (δ_{SFAP}) gives the slope of the ECAP growth function, M_{N1P1}. Typical values for M_{N1P1} are 135±25 $\left[\frac{\text{neurons}}{\text{dB}}\right]$ for the bEAM, 13±5 $\left[\frac{\text{neurons}}{\text{dB}}\right]$ for the 600-Ωcm bEAM, and ≈ 11 $\left[\frac{\text{neurons}}{\text{dB}}\right]$ for the Briaire et al. [13] model, as tabulated at the end of this section in Table 2.9. In the following sections we seek to draw comparisons between model predictions and various estimates from the literature of the parameters M_{N1P1}, δ_{SFAP}, N_f, and R_l.

Parametric estimates from the literature

In the implanted ear of a particular patient, the ECAP growth function is expected to be determined by the longitudinal spread of current with increasing stimulus levels (R_l), the neural survival at those longitudinal cochlear positions (N_l), and the electrical coupling between the responding fibers and the electrode (δ_{SFAP}). Accordingly, it is difficult to interpret differences in the slope of the ECAP amplitude function measured across patients (or across electrodes in the same patient) because it is impossible to isolate which of these three influences is being realized. However, a few points can be made. First, in a given subject, changing the stimulus condition (for instance monopolar to bipolar) while holding the recording electrode fixed, should only change M_{N1P1} by changing R_l, because δ_{SFAP} and N_l are invariant to the stimulus configuration.[62] Similarly, changes in M_{N1P1} with varying recording electrode

[61] Alternatively, one notices the 6-dB width (measured in θ) in Table 2.7 is roughly 12% that of the bEAM, giving an R_l estimate of 0.21 $\left[\frac{\text{mm}}{\text{dB}}\right]$ for the Briaire et al model.

[62] Assuming the place of stimulation is not changed, δ_{SFAP} should not change drastically. If the stimulus is moved from the base to apex, δ_{SFAP} or N_l may influence the ECAP growth function.

position (for a fixed simulating electrode) are due only to $\delta^s_{SFAP(r)}$, because the neural survival, N_l, and the recruitment, R^s_l, are invariant to the recording electrode position.

In estimating δ_{SFAP}, two limits ($\check{\delta}_{SFAP}$ and $\hat{\delta}_{SFAP}$) can be used in this phenomenological model. Under conditions where each neuron's unitary waveform is identical in amplitude and synchronized in time ($PST(t)$ is a Dirac delta function), δ_{SFAP} ought to be chosen to equal the average peak-to-peak amplitude of the unitary potential, such as the 0.24 μV reported in cat [221] or the 0.21 μV reported in guinea pig [217]. We label this estimate $\hat{\delta}_{SFAP}$. Alternatively, if one considers that some degree of canceling is likely to occur because of latency differences across neurons (i.e., $PST(t)$ deviates from a delta function), then the *effective* contribution of a single neuron to the N1P1 amplitude ought to be only a percentage of $\hat{\delta}_{SFAP}$. An approximation of this lower estimate, $\check{\delta}_{SFAP}$, can be made by dividing the maximum elicited N1P1 at high stimulus levels by the maximum number of neurons that possibly contribute to it. According, $\hat{\delta}_{SFAP}$ and $\check{\delta}_{SFAP}$ likely overestimate and underestimate the most appropriate δ_{SFAP}. $\hat{\delta}_{SFAP}$ overestimates δ_{SFAP} because some latency differences will smear the waveform reducing the N1P1 amplitude from that predicted by simply multiplying $\hat{\delta}_{SFAP}$ by the number of active neurons.[63] Similarly, $\check{\delta}_{SFAP}$ underestimated δ_{SFAP} because the maximum elicited N1P1 may not represent a case where every neuron is discharging. In the following analysis, where applicable, we report the range of recruitment values, R_l, calculated where δ_{SFAP} spans a range of estimates, that is $\check{\delta}_{SFAP} < \delta_{SFAP} < \hat{\delta}_{SFAP}$.

Note that the total cochlear length (in millimeters) divided by the range of fiber thresholds (in dB) puts an upper limit on what R_l ought to take in this phenomenological model. For instance, in the cat data, single-fiber thresholds span at least 20 dB [134], and the total cochlear length is 24 mm, meaning strictly speaking one would not expect an estimate of R_l above 1.2 $\left[\frac{\text{mm}}{\text{dB}}\right]$.

Surveying the literature allows several *rough* estimates to be made for R_l and δ_{SFAP}. From the distribution of single-unit thresholds in the cat measured by Miller et al. [134], the product $N_l\ R_l$ can be estimated as 5,483 $\left[\frac{\text{neurons}}{\text{dB}}\right]$[64] and used to predict R_l. Assuming in the cat that roughly 51,000 neurons [46] are evenly distributed along an average cochlear length of 24 mm [105], N_l is roughly 2,125 $\left[\frac{\text{neurons}}{\text{mm}}\right]$ and R_l can be estimated as:

[63] In using unitary potential waveforms to predict the total CAP measured at the round window, Wang [221] notes his synthesized CAPs have N1P1 amplitudes larger than those measured empirically.

[64] Miller et el. report a distribution of 230 fiber thresholds (their figure 13) to be fit by a modified lognormal distribution. Taking the cumulative distribution of Miller's data to represent 51,000 neurons gives a slope of roughly 5,483 $\left[\frac{\text{neurons}}{\text{dB}}\right]$.

$$R_l = \frac{(N_l\, R_l\,)}{N_l} = 2.58 \left[\frac{\text{mm}}{\text{dB}}\right]. \tag{2.47}$$

Alternatively, the parameters M_{N1P1} and $\check{\delta}_{SFAP}$ can be estimated for the cat from the intracochlear ECAP data in Miller el al. [132] as 916[65] $\left[\frac{\mu V}{\text{dB}}\right]$ and 0.21[66] $\left[\frac{\mu V}{\text{neuron}}\right]$, respectively. Note this value of $\check{\delta}_{SFAP}$ is consistent with the 0.24 μV value for $\hat{\delta}_{SFAP}$ Wang [221] estimated in the cat using the spike-triggered averaging technique. Combining these with the estimate of N_l derived above for the cat above (2,125 $\left[\frac{\text{neurons}}{\text{mm}}\right]$), R_l is estimated as

$$R_l = \frac{M_{N1P1}}{(\check{\delta}_{SFAP} \rightarrow \hat{\delta}_{SFAP}\,) \cdot N_l} = 2.05 \rightarrow 1.80 \left[\frac{\text{mm}}{\text{dB}}\right] \tag{2.48}$$

where $\rightarrow$ denotes the range of values δ_{SFAP} or R_l spans.

Charlet de Sauvage et al. [36] stimulated and recorded ECAPs from a round window electrode in the guinea pig. The authors' data (their figure 9) suggest growth rates M_{N1P1} of 152 $\left[\frac{\mu V}{\text{dB}}\right]$ and maximum N1P1 amplitudes of > 2000 μA. If the guinea pig cochlea has 24,000 neurons [46], then 0.083 $\left[\frac{\mu V}{\text{neuron}}\right]$ is a plausible value for $\check{\delta}_{SFAP}$, as compared with the $\hat{\delta}_{SFAP}$ value of 0.21 measured by Versnel et al. [217]. Supposing the guinea pig N_l to be 1200 $\left[\frac{\text{neurons}}{\text{mm}}\right]$ (24,000 neurons spread over 20 mm in cochlear length [46]), the range for R_l becomes:

$$R_l = \frac{M_{N1P1}}{(\check{\delta}_{SFAP} \rightarrow \hat{\delta}_{SFAP}\,) \cdot N_l} = 1.53 \rightarrow 0.60 \left[\frac{\text{mm}}{\text{dB}}\right]. \tag{2.49}$$

For a recording electrode placed inside the IAM in contact with the auditory nerve, M_{N1P1} and δ_{SFAP} can be estimated from Miller et al. [135] for both the cat and guinea pig. Taking 3.8 and 2.2 mV as the maximum amplitude of the N1P1 complex, and 51,000 [46] and 24,000 [46] as the number of total neurons, gives IAC-derived $\check{\delta}_{SFAP}$ values of 0.075 and 0.091 $\left[\frac{\mu V}{\text{neuron}}\right]$ for the cat and guinea pig, respectively. In agreement with Miller el al. [132], δ_{SFAP} values are smaller for ECAPs measured in the IAM rather than those measured with an intracochlear electrode. The estimates

[65] Miller el al. [132] (their figure 8B, subject D14) plot intracochlear N1P1 amplitudes as a function of stimulus level in dB to have a slope of roughly 916 $\left[\frac{\mu V}{\text{dB}}\right]$ for cathodic pulses delivered to an apical electrode.

[66] Taking the maximum value of the N1P1 amplitude (10,800 μV) as being generated by the summation of unitary potentials, without cancelation, from a population of 51,000 neurons in the cat, gives a $\check{\delta}_{SFAP}$ estimate of 0.21 $\left[\frac{\mu V}{\text{neuron}}\right]$

of M_{N1P1} are approximately 275 and 316 $\left[\frac{\mu V}{\text{dB}}\right]$.[67] As above, taking the guinea pig N_l to be 1200 $\left[\frac{\text{neurons}}{\text{mm}}\right]$ and the cat N_l above of 2,125 $\left[\frac{\text{neurons}}{\text{mm}}\right]$, the estimates for R_l become:

$$R_l = \frac{275}{0.075 \cdot 2125} = 1.72 \left[\frac{\text{mm}}{\text{dB}}\right] \quad cat \tag{2.50}$$

$$R_l = \frac{316}{0.091 \cdot 1200} = 2.89 \left[\frac{\text{mm}}{\text{dB}}\right] \quad guinea\ pig \tag{2.51}$$

$$\tag{2.52}$$

Recording the EABR from an electrode embedded in the skull of the rat, Hall [69] measured a strong (e.g., $r^2 = 0.706$) correlation between the slope of EABR growth function and the total number of ganglion cells surviving an otological insult. Since Hall measured maximum elicited P1 wave of the EABR as a function of the number of surviving neurons, his data can be used to estimate $\check{\delta}_{SFAP}$ for the P1 wave of the EABR as 0.0025 $\left[\frac{\mu V}{\text{neuron}}\right]$.[68] Note this value for $\check{\delta}_{SFAP}$, measured in the EABR, is an order of magnitude smaller than, for instance, the $\check{\delta}_{SFAP}$ measures at the round window in the cat or guinea pig. One might expect such a difference since the potential is being recorded at the brainstem. The ratio $(M_{P1}/\ N_l)$ can also be estimated from Hall's data as 0.0012 $\left[\frac{\mu V \cdot \text{mm}}{\text{dB} \cdot \text{neurons}}\right]$,[69] allowing R_l to be estimated

$$R_l = \frac{(M_{P1}/N_l)}{\delta_{SFAP}} = 0.48 \left[\frac{\text{mm}}{\text{dB}}\right] \tag{2.53}$$

In the human literature, estimates of M_{N1P1} can be used to compare stimulation configurations. As an example, Brown et al. [16] (their figure 3) report ECAP slopes $\left[\frac{\mu V}{mA}\right]$ and thresholds [mA] for monopolar and bipolar stimulation in a group of Ineraid subjects. Expressing the mean ECAP growth in dB gives 106 $\left[\frac{\mu V}{\text{dB}}\right]$ and 52 $\left[\frac{\mu V}{\text{dB}}\right]$ as M_{N1P1} estimates for monopolar and bipolar stimuli. Assuming N_l and δ_{SFAP} are essentially invariant to the stimulus parameters, one can deduce the ratio of R_l for monopolar and bipolar stimuli,

[67] Cats have 64% higher thresholds than guinea pigs, while guinea pigs have 71% steeper sloping growth functions. Normalizing the growth functions as $\left[\frac{\mu V}{\text{dB}}\right]$ these effects cancel, giving both animals similar estimates of M_{N1P1} .

[68] Hall (figure 3) reports a maximum elicited P1 wave $[\mu V]$ of the EABR as a function of the number of surviving neurons. Assuming all SFAPs add together without cancelation, the slope of this graph gives 40 μV for a population of 16000 neurons, or 0.0025 $\left[\frac{\mu V}{\text{neuron}}\right]$ as an empirical estimate of $\check{\delta}_{SFAP}$ for the EABR.

[69] Hall (his figure 9) reports the slope of the P1 growth function $\left[\frac{\mu V}{\mu A}\right]$ versus the number of spiral ganglion cells [neurons]. Converting the y-axis from $\left[\frac{\mu V}{\mu A}\right]$ to $\left[\frac{\mu V}{\text{dB}}\right]$, and converting the x-axis from [neurons] to $\left[\frac{\text{neurons}}{\text{mm}}\right]$ assuming a total length of 8 mm in the rat [141]; the slope of 0.0012 $\left[\frac{\mu V \cdot \text{mm}}{\text{dB} \cdot \text{neuron}}\right]$ is as estimate of the ratio (M_{P1}/N_l).

$$\frac{R_l{}^{monopolar}}{R_l{}^{bipolar}} = \frac{M_{N1P1}{}^{monopolar}}{M_{N1P1}{}^{bipolar}} = 2.04 \tag{2.54}$$

$$\tag{2.55}$$

This ratio agrees with the comparisons of monopolar and bipolar stimulation made in section 2.4.5, where the 6-dB widths for monopolar and bipolar stimuli were measured in the bEAM to be 11 and 4.4 millimeters, a ratio of 2.5. A similar analysis can be preformed on Abbas el al. [1] (their figure 10) for measures of EABR, yielding 0.115 and 0.06 $\left[\frac{\mu V}{\mathrm{dB}}\right]$ in response to monopolar and bipolar stimuli, giving a ratio of R_l of 1.6. Since in these data sets R_l, N_l, and δ_{SFAP} are all free parameters, the analysis stops there. In the next Chapter, where the parameter N_l is known for the Ineraid patient, a further analysis is given.

Measuring 585 ECAP growth functions from a total of 141 users of the Nucleus 24 implant, Cafarelli-Dees et al. [24] report a mean growth rate of 11.56 $\left[\frac{\mu V}{CU}\right]$ measured at a level 10 clinical units (CU) above the ECAP threshold. Since the 256 clinical units are logarithmically spaced in terms of current delivered with 0.17 $\left[\frac{\mathrm{dB}}{CU}\right]$, the data can be converted to estimates of M_{N1P1} with a mean ($\pm$ SD) of 66.0 ($\pm$ 53.4) $\left[\frac{\mu V}{\mathrm{dB}}\right]$. The estimate 106 $\left[\frac{\mu V}{\mathrm{dB}}\right]$ for M_{N1P1} from Brown et al [16] falls in this range.

All estimates for M_{N1P1} and R_l are shown in Table 2.9 for comparison with the various EAMs discussed in previous sections. Considering all species and experimental protocols, the mean of the physiological estimates of R_l for monopolar recruitment is 1.50 $\left[\frac{\mathrm{mm}}{\mathrm{dB}}\right]$ (1.6250 median), not dissimilar to the 1.8 $\left[\frac{\mathrm{mm}}{\mathrm{dB}}\right]$ predicted by the bEAM, but far from the < 0.2 $\left[\frac{\mathrm{mm}}{\mathrm{dB}}\right]$ estimates returned by the homogeneous bEAM, Frijns et al., and Hanekom models. In summary, the bEAM predictions of both ECAP growth M_{N1P1} (135 $\left[\frac{\mu V}{\mathrm{dB}}\right]$) and activation spread R_l (1.8 $\left[\frac{\mathrm{mm}}{\mathrm{dB}}\right]$) appear to be closer than previous models to the corresponding (albeit rough) estimates taken from the literature in Table 2.9.

source	species	M_{N1P1} $\left[\frac{\mu V}{\text{dB}}\right]$	$\check{\delta}_{SFAP}$ $\left[\frac{\mu V}{\text{neuron}}\right]$	$\hat{\delta}_{SFAP}$ $\left[\frac{\mu V}{\text{neuron}}\right]$	N_l $\left[\frac{\text{neurons}}{\text{mm}}\right]$	R_l $\left[\frac{\text{mm}}{\text{dB}}\right]$
EAM models						
bEAM	human	135±25	0.062	.	950	1.8
bEAM (600 Ωcm)	human	13±6	0.021	.	950	0.57
bEAM (homogeneous)	human	.	.	.	.	0.134
Hanekom model [73]	human	.	.	.	.	0.1450
Briaire and Frijns [13]	human	11	0.11	.	1,000	0.1
Intracochlear/RW gross potentials						
Miller et al. [134]	cat	.		.	2,125	2.58[a]
Miller et al. [132]	cat	916	0.21	0.24	2,125	2.05 → 1.80
Charlet de Sauvage [36]	guinea pig	152	0.083	0.21	1,200	1.53 → 0.60
Internal auditory meatus gross potentials						
Miller et al. [135]	guinea pig	316	0.091	.	1,200	2.89→
Miller et al. [135]	cat	275	0.075	.	2,125	1.72→
Litvak [114] (p.60)	cat	384	.	.	.	.
EABR potentials						
Hall [69]	rat	.	0.0025		.	0.48[b]
Smith [192]	cat	4.3	.		.	.
Single-unit recordings from the auditory nerve						
Kral [104]	cat	.	.	.	.	0.64[c]
Liang [109]	cat	.	.	.	.	0.67[d]
human intracochlear ECAP potentials						
Brown [16]	human	106	.	.	.	.
Cafarelli-Dees [24]	human	66.0 (± 53.4)	.	.	.	.

Table 2.9: Estimates of longitudinal recruitment, R_l , from modeling studies and estimates derived from physiological studies (see text). Notes: [a]Parameter estimated was the product ($\delta_{SFAP} R_l$). [b]Parameter estimated was the ratio (M_{P1}/N_l). [c]See section 2.4.5. Kral reports a changes in single-unit threshold for different simulating electrodes as 3.12 $\frac{\text{dB}}{\text{mm}}$, corresponding to a 6-dB width of 3.84 mm and an R_l of 0.64. [d]See section 2.4.5. Similar to Kral, Liang reports a changes in single-unit threshold for different simulating electrodes as 3 $\frac{\text{dB}}{\text{mm}}$, corresponding to a 6-dB width of 4 mm and an R_l of 0.67.

2.6 Chapter synopsis

The implanted cochlea is a complex tissue structure filled with conductive inhomogeneities that have a profound effect on intracochlear current flow. Collectively, the data presented in Chapter 2 show that detailed electro-anatomical modeling is a feasible approach to studying the implanted ear, yielding a rich collection of predictions for intracochlear current flow, the neural activation pattern, and the ECAP waveform.

The critical determinants of current flow are the 3D anatomical structure and the ratio of bone-to-fluid resistivity. Although small (±6 dB) parametric variations in tissue resistivity tend to have little impact, when the aforementioned ratio is changed from unity (i.e., a homogenous model) to near 10 (that used by previous EAMs) to 100 (that used by the bEAM), the differences are substantial. The bEAM, which represents the bone of the otic capsule as 5 kΩcm, predicts longitudinal current spread that spans across multiple cochlear turns where the maximum current density entering Rosenthal's canal is not always at a cochleotopic position corresponding to that of the stimulating electrode. Predictions of current spread made using 600-Ωcm bone (similar to that used in previous EAMs) are more similar to those obtained with a homogenous model. Accordingly, we separate this model from its predecessors, and define one crucial aspect of this type of modeling that needs to be tested and possibly refined (see next chapter). We conclude that an appropriate representation of *both* the detailed 3D anatomy of the cochlea, and the conductivity of its constituent tissues and fluids, is necessary to accurately predict current spread in the implanted ear.

Compared with previous EAMs, the neural activation patterns predicted using the bEAM show a greater degree of excitation spread for both monopolar and bipolar stimuli, consistent with the predicted longitudinal spread of current flow. Comparing excitation spread for different electrode configurations, the bEAM predicts a monopolar-to-bipolar ratio of 2.5, closer to the physiological estimates (1.2-2.7) than previous EAMs or a homogenous model, both of which suggest a ratio less than unity (implying that monopolar stimulation is more focused than bipolar).

The ECAP predictions made using the bEAM suggest that the inhomogeneous conductivities of the implanted ear also need to be appropriately represented in order to predict realistic ECAP waveforms with a morphology independent of the position of the recording electrode, as observed with empirically recorded ECAPs. Furthermore, measures of the unitary contribution of a single neuron to the ECAP agree with the model prediction that even fibers extensively removed from the recording electrode will unanimously exert a characteristic biphasic (N1P1) response. Finally, the predicted ECAP growth functions can be analyzed using a simple phenomenological model, yielding estimates for ECAP growth ($M_{N1P1} \approx 135 \left[\frac{\mu V}{\text{dB}}\right]$) and excitation spread ($R_l \approx 1.8 \left[\frac{\text{mm}}{\text{dB}}\right]$) that are both closer than previous models to estimates taken from the literature.

2.7 Appendix: Chapter 2

2.7.1 A probabilistic interpretation of M_{N1P1}

The M_{N1P1} measure is motivated by a probabilistic interpretation of the underlying distribution of single-unit thresholds being approximately lognormal. This approximation allows us to give a mathematical framework for analyzing ECAP growth data. There is both empirical evidence and theoretical reasons that suggest thresholds take on a lognormal distribution where the variance increases with the mean.[70] Miller et al. [134] reported the threshold distribution of 147 single units in the auditory nerve of the cat to be well-fit by a lognormal distribution. Theoretically, if the many factors that determine a single neuron's threshold (represented by the random variable X) combine in a multiplicative manner, then the distribution of single-unit thresholds, $f_X(x)$, is likely to take on a lognormal distribution where the variance in single-fiber thresholds increases with the mean.

If single-fiber thresholds are lognormally distributed with density $f_X(x)$, and cumulative density $F_X(x)$, then the log-transformed variable, $Y = 20\log(X)$, has a den-

[70] A few properties of the lognormal dist are:

$$f_X(x|\mu_{ln},\sigma_{ln}) = \left(\frac{1}{\sqrt{2\pi}x\sigma_{ln}} exp\left[\frac{-(\ln(x)-\mu_{ln})^2}{2\sigma_{ln}^2}\right]\right) \quad 0 < x,\ \sigma_{ln},\ \mu_{ln} \tag{2.56}$$

$$F_X(x|\mu_{ln},\sigma_{ln}) = \frac{1}{2} + \frac{1}{2}ERF\left[\frac{\ln(x)-\mu_{ln}}{2\sigma_{ln}}\right] \tag{2.57}$$

$$\text{mean} = e^{[\mu_{ln}+0.5\sigma_{ln}^2]} \tag{2.58}$$

$$\text{median} = e^{[\mu_{ln}]} \tag{2.59}$$

$$\text{variance} = (e^{[\sigma_{ln}^2]}-1)(e^{[2\mu_{ln}+\sigma_{ln}^2]}) \tag{2.60}$$

$$\text{CV} = \sqrt{e^{[\sigma_{ln}^2]}-1} \tag{2.61}$$

Note the coefficient of variation (CV) or "relative spread" (RS) of the lognormal distribution is independent of the mean parameter μ_{ln}. For $RS << 1$ the parameter $RS \approx \sigma_{ln}$.

Given a normally distributed variable with a mean (μ_Z) and relative spread (RS_Z), the lognormal distribution $f_X(x|\mu_{ln},\sigma_{ln})$ with $\sigma_{ln} = \sqrt{\ln(RS_Z^2+1)}$ and $\mu_{ln} = \ln(\mu_Z) - 0.5\sigma_{ln}^2$ is a very close approximation over a few standard deviations from the mean.

Considering a fiber's threshold is likely the product of several independent factors (e.g., its diameter and position relative to the simulating electrode), it would not be surprising for single-fiber thresholds to take on a lognormal distribution. A random variable whose value is determined by the product of many influences is likely to have lognormal distribution, for the same reasons a random variable whose value is determined by the sum of many influences is likely to have a normal distribution (because of the central limit theorem [37]).

A second reason for the lognormal distribution is that it simplifies the analysis of the relative spread (RS) of the ECAP due to the RS of individual fibers. As noted by Matsuoka et al. [122], the RS of the ECAPs will reflect both the distribution of underlying SFTs and the probabilistic RS of individual neurons firing. As pointed out in section 2.4.5, at levels where the ECAP is measured, the slope of the growth function is likely determined by the underlying distribution of SFTs, not by the RS of individual fibers in a probabilistic sense.

sity function $f_Y(Y)$ that is normally distributed with mean, $\frac{20}{\ln(10)}\mu_{ln}$, and standard deviation $\frac{20}{\ln(10)}\sigma_{ln}$, where μ_{ln} and σ_{ln} are the parameters of the lognormal distribution [165].

Modeling the ECAP growth function as generated by a collection of neurons with lognormal thresholds, the sigmoidal ECAP growth function, plotted on a decibel abscissa and normalized to vary between 0 and 1, is an integrated gaussian density $F_Y(y)$. The maximum slope occurs at $F_Y(y = \mu_{ln})$, having a value of

$$\max\left[\frac{\partial F_Y(y)}{\partial y}\right] = f_Y\left(y = \frac{20\mu_{ln}}{\ln(10)}\right) = \frac{1}{\sqrt{2\pi}\left(\frac{20\sigma_{ln}}{\ln(10)}\right)} \tag{2.62}$$

which *depends only on* σ_{ln}. For the untransformed variable, X, the maximum slope of the model ECAP growth function $F_X(x)$ on an absolute scale (μA) depends on *both parameters* μ_{ln} and σ_{ln}:

$$\max\left[\frac{\partial F_X(x)}{\partial x}\right] = f_X(x = \mu_{ln}) = \frac{1}{\sqrt{2\pi}\sigma_{ln}\exp(\mu_{ln})} \tag{2.63}$$

such that changes in slope can be the result of either parameter.

If single-unit thresholds are lognormally distributed, and we measure the slope (i.e., M_{N1P1}) on a dB axis, then then M_{N1P1} is inversely proportional to the parameter σ_{ln}.[71] M_{N1P1} can not be estimated on a linear scale because differences in threshold manifest themselves as differences in the slope of the cumulative distribution function. A simple example of this is given in Figure 2-43. Consider three otherwise identical implanted ears, or three electrodes in a single ear, each with lognormally distributed single-fiber thresholds spanning a range of 20 dB (similar to that reported by Miller el al. [134] figure 3). The distributions in panel A fit this description, having median thresholds of 400, 600, and 800 μA. The distribution of thresholds across ears are the same except for a 6-dB translation, as in panel B.

With other factors (i.e., N_l and δ_{SFAP}) the same, the N1P1 growth functions plotted on a linear axis (panel C) show steeper slopes and lower thresholds, the same trends reported by Brown et al. [16] and Miller et al. [135]. With level expressed in μA, this tendency for ECAP thresholds and growth functions to be inversely related is also observed the next chapter for the ECAP data of the Ineraid subject (see Figure 3-16) where ECAP threshold accounts for 49% of the variance in the slope of the ECAP growth function.

In panel C, the slope (at 50 percent of its maximum) will vary by a factor of two. Plotting all growth functions on a decibel scale (panel D), the slope of the growth functions (M_{N1P1}) are identical, illustrating that to the extent thresholds are

[71] Smaller values for M_{N1P1} will be obtained by evaluating the slope at different points along the sigmoid, although here we assume that by measuring the slope of ECAP growth functions we a coming close to the maximum slope (in fact, we are underestimating it.)

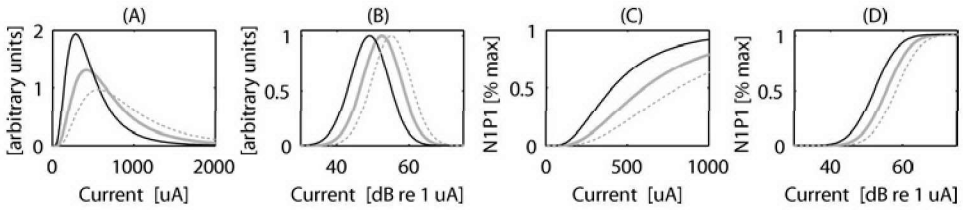

Figure 2-43: Three lognormal distributions of single-unit threshold spanning a range of 20 dB (similar to that reported by Miller el al. [134] figure 3). The distributions, having medium thresholds of 400, 600, and 800 μA, are plotted on a linear axis in panel A, on a dB axis in panel B. As seen in panel C, and on a linear axis the slope of the cumulative distribution, evaluated at 50 percent of its maximum, will vary by a factor of two, mirroring the distributions in panel A. Expressing all growth functions on a decibel scale (panel D), the slope of the growth functions (M_{N1P1}) are identical.

lognormally distributed, the slope of the growth function on a dB scale, M_{N1P1} , faithfully represents the variance of the underlying distribution, irrespective of sensitivity differences.

In this framework, the parameters μ_{ln} and σ_{ln} have different physical interpretations. Shifts in μ_{ln} across electrode or patient represent multiplicative changes in threshold, for instance, if all thresholds are increased by 5 dB. Changes in σ_{ln} represent changes in the variance of the underlying threshold distribution, for instance, the difference between monopolar and bipolar stimulation. Given similar values for δ_{SFAP} and N_l , changes in excitation spread (R_l) due the difference between monopolar and bipolar stimulation, will be reflected the ECAP growth function as changes in M_{N1P1} .

M_{N1P1} is related to the parameter σ_{ln} as

$$M_{N1P1}\left(\sigma_{ln}\right) = \frac{\delta_{SFAP}\ N_l\ L}{\sqrt{2\pi}\left(\frac{20\sigma_{ln}}{\ln(10)}\right)} \tag{2.64}$$

where L is the total cochleotopic length such that ($\delta_{SFAP}N_l$L) is the maximum response of all neurons discharging. The point being that M_{N1P1} is inversely proportional to σ_{ln}. Additionally, on a linear level axis the maximum slope of the ECAP growth function, $F_X(x)$, and its "threshold", that is, the level that it achieves a criterion value (e.g., 10% of the maximum), are inversely related in a predictable fashion. The threshold for the ECAP to reach 10 % of its maximum value (T_{ECAP}) is

$$T_{ECAP} = \exp\left[\sqrt{2\pi}\mathtt{erf}^{-1}(.8)\sigma_{ln} + \mu_{ln}\right]. \tag{2.65}$$

Comparing the ECAP slope (Eqn 2.63) and ECAP threshold (Eqn 2.65) on a linear axis, one notes the two are inversely related in such a way that their product

$$\left(\frac{1}{\sqrt{2\pi}\sigma_{ln}\exp(\mu_{ln})}\right)\left(\exp\left[\sqrt{2\pi}\mathtt{erf}^{-1}(.8)\sigma_{ln}+\mu_{ln}\right]\right) \tag{2.66}$$

depends only on σ_{ln}. Accordingly, if one were to multiply the ECAP slope by the threshold (both measured on a linear axis), as Miller ([136], table 1) did, then using this probabilistic model one would expect a result that does not depend on the sensitivity parameter μ_{ln}. This agrees with Miller's data.

We suggest that estimating the slope σ_{ln} and sensitivity μ_{ln} parameters on a log-transformed axis may be a more appropriate way of analyzing ECAP data. For example, Abbas and Brown [16] found a poor correlation between the slope of the ECAP function and measures of intensity discrimination, a result that could be due to both the analysis on a linear scale, or failure of the assumption that the total spike count is the psychological correlate of loudness as suggest by Relkin and Doucet [175].

2.7.2 Single-fiber model computation

As described by Frijns [54], the vector form of equation 2.13 is

$$\frac{d\mathbf{V}}{dt} = \mathbf{AV}+\mathbf{BV_e}+\mathbf{C}\left(\mathbf{I_{act}}+\mathbf{I_L}\right) \tag{2.67}$$

where

$$\mathbf{V} = [(V_{m_{(1)}}-V_{rest}),\ldots,(V_{m_{(N)}}-V_{rest})]^T \tag{2.68}$$
$$\mathbf{V_e} = [V_{e_{(1)}},\ldots,V_{e_{(N)}}]^T \tag{2.69}$$
$$\mathbf{I_{act}} = [I_{act_{(1)}},\ldots,I_{act_{(N)}}]^T \tag{2.70}$$
$$\mathbf{I_L} = (V_{rest}-V_L)[-G_{L_{(1)}},\ldots,-G_{L_{(N)}}]^T. \tag{2.71}$$

The resistive coupling between nodes along with the sealed end (spatial) boundary condition are incorporated in **A**,**B**, and **C** as

$$\mathbf{A} = \begin{vmatrix} \frac{-(G_{A_{(1)}}+G_{L_{(1)}})}{C_{m_{(1)}}} & \frac{G_{a_{(1)}}}{C_{m_{(1)}}} & & & 0 \\ \frac{G_{a_{(1)}}}{C_{m_{(2)}}} & \frac{-(G_{a_{(1)}}+G_{a_{(2)}}+G_{L_{(2)}})}{C_{m_{(2)}}} & \frac{G_{a_{(2)}}}{C_{m_{(2)}}} & & \\ & & \ddots & & \\ & & \frac{G_{a_{(K-1)}}}{C_{m_{(N-1)}}} & \frac{-(G_{a_{(K-1)}}+G_{a_{(K)}}+G_{L_{(N-1)}})}{C_{m_{(N-1)}}} & \frac{G_{a_{(K)}}}{C_{m_{(N-1)}}} \\ 0 & & & \frac{G_{a_{(K)}}}{C_{m_{(N)}}} & \frac{-(G_{a_{(K)}}+G_{L_{(N)}})}{C_{m_{(N)}}} \end{vmatrix}$$

$$\mathbf{B} = \begin{vmatrix} \frac{-(G_{a_{(1)}})}{C_{m_{(1)}}} & \frac{G_{a_{(1)}}}{C_{m_{(1)}}} & & & 0 \\ \frac{G_{a_{(1)}}}{C_{m_{(2)}}} & \frac{-(G_{a_{(1)}}+G_{a_{(2)}})}{C_{m_{(2)}}} & \frac{G_{a_{(2)}}}{C_{m_{(2)}}} & & \\ & & \ddots & & \\ & & \frac{G_{a_{(K-1)}}}{C_{m_{(N-1)}}} & \frac{-(G_{a_{(K-1)}}+G_{a_{(K)}})}{C_{m_{(N-1)}}} & \frac{G_{a_{(K)}}}{C_{m_{(N-1)}}} \\ 0 & & & \frac{G_{a_{(K)}}}{C_{m_{(N)}}} & \frac{-(G_{a_{(K)}})}{C_{m_{(N)}}} \end{vmatrix}$$

$$\mathbf{C} = \begin{vmatrix} \frac{1}{C_{m_{(1)}}} & & & 0 \\ & \frac{1}{C_{m_{(2)}}} & & \\ & & \ddots & \\ & & \frac{1}{C_{m_{(N-1)}}} & \\ 0 & & & \frac{1}{C_{m_{(N)}}}. \end{vmatrix}$$

The compartmental conductances and capacitances are calculated using the fiber geometry as:

$$G_{L_{(i)}} = g_L \pi d_{(i)} l_{(i)} \tag{2.72}$$

$$C_{m_{(i)}} = c_m \pi d_{(i)} l_{(i)} \tag{2.73}$$

$$G_{a_{(k)}} = \left(0.5 \frac{\rho_a l_{(i)}}{\pi (0.5 d_{(i)})^2} + 0.5 \frac{\rho_a l_{(i+1)}}{\pi (0.5 d_{(i+1)})^2} \right)^{-1} \tag{2.74}$$

where g_L, c_m, $d_{(i)}$, and $l_{(i)}$ can take on nodal or internodal values.

The voltage-dependant α's and β's that determine the activation factors $m_{(i)}$, $n_{(i)}$, and $h_{(i)}$ are given by:

$$\alpha_{m_{(i)}} = \left[\frac{A_{\alpha m}(V_{(i)} - \beta_{\alpha m})}{1 - \exp\left(\frac{\beta_{\alpha m} - V_{(i)}}{C_{\alpha m}} \right)} \right] \cdot \left[Q_{10\alpha m}^{\left(\frac{T - T_0}{10} \right)} \right] \tag{2.75}$$

$$\alpha_{h_{(i)}} = \left[\frac{A_{\alpha h}(\beta_{\alpha h} - V_{(i)})}{1 - \exp\left(\frac{V_{(i)} - \beta_{\alpha h}}{C_{\alpha h}} \right)} \right] \cdot \left[Q_{10\alpha h}^{\left(\frac{T - T_0}{10} \right)} \right] \tag{2.76}$$

$$\alpha_{n_{(i)}} = \left[\frac{A_{\alpha n}(V_{(i)} - \beta_{\alpha n})}{1 - \exp\left(\frac{\beta_{\alpha n} - V_{(i)}}{C_{\alpha n}} \right)} \right] \cdot \left[Q_{10\alpha n}^{\left(\frac{T - T_0}{10} \right)} \right] \tag{2.77}$$

$$\beta_{m_{(i)}} = \left[\frac{A_{\beta m}(\beta_{\beta m} - V_{(i)})}{1 - \exp\left(\frac{V_{(i)} - \beta_{\beta m}}{C_{\beta m}}\right)}\right] \cdot \left[Q_{10\beta m}^{\left(\frac{T-T_0}{10}\right)}\right] \tag{2.78}$$

$$\beta_{h_{(i)}} = \left[\frac{A_{\beta h}}{1 - \exp\left(\frac{\beta_{\beta h} - V_{(i)}}{C_{\beta h}}\right)}\right] \cdot \left[Q_{10\beta h}^{\left(\frac{T-T_0}{10}\right)}\right] \tag{2.79}$$

$$\beta_{n_{(i)}} = \left[\frac{A_{\beta n}(\beta_{\beta n} - V_{(i)})}{1 - \exp\left(\frac{V_{(i)} - \beta_{\beta n}}{C_{\beta n}}\right)}\right] \cdot \left[Q_{10\beta n}^{\left(\frac{T-T_0}{10}\right)}\right]. \tag{2.80}$$

$$\alpha_{m_{(i)}} = \left[\frac{A_{\alpha m}(V_{(i)} - \beta_{\alpha m})}{1 - \exp\left(\frac{\beta_{\alpha m} - V_{(i)}}{C_{\alpha m}}\right)}\right] \cdot \left[Q_{10\alpha m}^{\left(\frac{T-T_0}{10}\right)}\right] \tag{2.81}$$

$$\alpha_{h_{(i)}} = \left[\frac{A_{\alpha h}(\beta_{\alpha h} - V_{(i)})}{1 - \exp\left(\frac{V_{(i)} - \beta_{\alpha h}}{C_{\alpha h}}\right)}\right] \cdot \left[Q_{10\alpha h}^{\left(\frac{T-T_0}{10}\right)}\right] \tag{2.82}$$

$$\alpha_{n_{(i)}} = \left[\frac{A_{\alpha n}(V_{(i)} - \beta_{\alpha n})}{1 - \exp\left(\frac{\beta_{\alpha n} - V_{(i)}}{C_{\alpha n}}\right)}\right] \cdot \left[Q_{10\alpha n}^{\left(\frac{T-T_0}{10}\right)}\right] \tag{2.83}$$

$$\beta_{m_{(i)}} = \left[\frac{A_{\beta m}(\beta_{\beta m} - V_{(i)})}{1 - \exp\left(\frac{V_{(i)} - \beta_{\beta m}}{C_{\beta m}}\right)}\right] \cdot \left[Q_{10\beta m}^{\left(\frac{T-T_0}{10}\right)}\right] \tag{2.84}$$

$$\beta_{h_{(i)}} = \left[\frac{A_{\beta h}}{1 - \exp\left(\frac{\beta_{\beta h} - V_{(i)}}{C_{\beta h}}\right)}\right] \cdot \left[Q_{10\beta h}^{\left(\frac{T-T_0}{10}\right)}\right] \tag{2.85}$$

$$\beta_{n_{(i)}} = \left[\frac{A_{\beta n}(\beta_{\beta n} - V_{(i)})}{1 - \exp\left(\frac{V_{(i)} - \beta_{\beta n}}{C_{\beta n}}\right)}\right] \cdot \left[Q_{10\beta n}^{\left(\frac{T-T_0}{10}\right)}\right] \tag{2.86}$$

Parameters

symbol	value	units	description
$V_{i_{(i)}}$		V	the internal potential referenced to a far field ground
$V_{e_{(i)}}$		V	the external potential referenced to a far field ground
$V_{m_{(i)}}$		V	$=[V_{i_{(i)}} - V_{e_{(i)}}]$ the transmembrane potential
$V_{(i)}$		V	$=[V_{m_{(i)}} - V_{rest}]$ the deviation of the membrane voltage from its resting potential
V_{rest}	-0.0846	V	the resting membrane voltage as calculated using the Goldman Equation as in [54]
$C_{m_{(i)}}$		F	the membrane capacitance at compartment i
$G_{a_{(k)}}$		Ω^{-1}	the axial conductance between compartments i and $i+1$
$G_{L_{(i)}}$		Ω^{-1}	the membrane leak conductance at compartment i
V_L	-0.0846	V	the leak reversal potential
$\ell_{(i)}$		μm	compartment i length (nodal or internodal)
$d_{(i)}$		μm	compartment i diameter (nodal or internodal)
P_K	$2.04e^{-}6$	$m \times s^{-}1$	potassium permeability
P_{Na}	$51.5e^{-}6$	$m \times s^{-}1$	sodium permeability
ρ_a	0.70	$\Omega \times m$	axioplasmic resistivity
g_L	728	$\Omega^{-1} \times m^{-2}$	unit area leak conductance (nodal region)
	0.125	$\Omega^{-1} \times m^{-2}$	unit area leak conductance (internodal region)
c_m	0.02	$F \times m^{-2}$	unit area membrane capacitance (nodal region)
	$0.125e^{-4}$	$F \times m^{-2}$	unit area membrane capacitance (internodal region)
r_m	0.0014	$\Omega \times m^2$	unit area resistance (nodal region)
T	301.16	K	corrected absolute temperature
T_0	293.15	K	absolute temperature
F	96485	$C \times mol^{-}1$	Faraday's constant
R	8.314	$mol^{-}1 \times K^{-}1$	gas constant
$[c^o_{Na+}]$	142.0	$mol \times m^{-}3$	Na concentration outside
$[c^i_{Na+}]$	10.0	$mol \times m^{-}3$	Na concentration inside
$[c^o_{K+}]$	4.2	$mol \times m^{-}3$	K concentration outside
$[c^i_{K+}]$	141.0	$mol \times m^{-}3$	K concentration inside
m_0	0.0077	·	initialization value
h_0	0.0267	·	initialization value
n_0	0.76	·	initialization value
$q10_{\alpha m}$	2.2	·	temperature dependant parameter
$q10_{\beta m}$	2.2	·	temperature dependant parameter
$q10_{\alpha h}$	2.9	·	temperature dependant parameter
$q10_{\beta h}$	2.9	·	temperature dependant parameter
$q10_{\alpha n}$	3.0	·	temperature dependant parameter
$q10_{\beta n}$	3.0	·	temperature dependant parameter

symbol	**value**	**units**	**description**
$A_{\alpha m}$	0.49	·	α_m constant
$B_{\alpha m}$	25.41	·	α_m constant
$C_{\alpha m}$	6.06	·	α_m constant
$A_{\beta m}$	1.04	·	α_m constant
$B_{\beta m}$	21.0	·	α_m constant
$C_{\beta m}$	9.41	·	α_m constant
$A_{\alpha h}$	0.9	·	α_h constant
$B_{\alpha h}$	27.74	·	α_h constant
$C_{\alpha h}$	9.06	·	α_h constant
$A_{\beta h}$	3.7	·	α_h constant
$B_{\beta h}$	56.0	·	α_h constant
$C_{\beta h}$	12.5	·	α_h constant
$A_{\alpha n}$	0.02	·	α_n constant
$B_{\alpha n}$	35.0	·	α_n constant
$C_{\alpha n}$	10	·	α_n constant
$A_{\beta n}$	0.05	·	α_n constant
$B_{\beta n}$	10.0	·	α_n constant
$C_{\beta n}$	10.0	·	α_n constant

Chapter 3

Comparisons between model-predicted and empirically-measured data

3.1 Introduction

While cochlear implantation has become the standard of care in treating patients with severe to profound sensorineural hearing loss, the variation in benefit individual patients derive from implantation remains both large and, for the most part, unexplained. One possible explanation for the wide range of benefit in CI patients is the pathology and anatomy of the implanted ear, which, when examined histologically in donated temporal bones, also displays a substantial amount of variation [146].

Across patients, it is entirely possible that differences in neuronal survival, fibrous tissue and new bone formation, damage induced by the electrode insertion, electrode insertion depth, and the position of the electrode may account for substantial variation in benefit. Our approach toward uncovering the peripheral mechanisms most likely to impact benefit has been to develop detailed three dimensional (3D) electro-anatomical models (EAMs) of the implanted ear capable of representing the different types of (patient-specific) anatomical and pathological variation seen in a collection of implanted temporal bones. In response to stimulation by an arbitrary set of electrodes, these models predict an estimate of (1) the 3D electric field (2) the pattern of neural activation as a function of cochleotopic position, and (3) the evoked potentials recorded from inactive intracochlear electrodes.

This type of modeling has the potential to be a valuable tool for interpreting the impact of the peripheral anatomy on the spike patterns elicited by electric stimulation, and ultimately on benefit. In addition to helping to identify the mechanisms limiting benefit, it can also be employed (as similar models have been in the past) as a tool in designing and interpreting experiments, testing proposed modifications to the implant

device, and quantitatively evaluating new methods of stimulation.

A major limitation of previous modeling studies [54, 73, 47, 168], is the lack of systematic testing of modeling predictions. This lack of testing remains troubling for at least several reasons. First, some researchers will dismiss the modeling results without lending successful ones the consideration they deserve. Others may place unfounded and inappropriate confidence in predictions and, motivated by spurious modeling results, embark on unproductive research paths. Without systematic testing, the weakest parts of the modeling process are never identified and refined.

By deriving models from the histologically-processed temporal bones of individual patients, the opportunity exists to test the models' predictions against (archival) empirical data collected from those same patients during life. Given the anatomical and pathologic variability seen across implanted ears, we can then work to identify those attributes that have the largest impact on electric stimulation and ultimately understand the relationship between the peripheral pathology and patient benefit, should such a relationship exist.

Past models have been tested by making across-species comparisons. For example, the earlier work of Frijns [54] compared thresholds and growth functions predicted by their guinea pig model to analogous data reported by Shepherd [187] in cat. In this study we compare measurements collected from individual patients with predictions generated from models formulated using the donated temporal bones of those same individuals.

Chapter 2 describes the formulation of three electro-anatomical models (EAMs) of the implanted ear. One is intended to represent the basic geometry of the implanted ear. This basic electro-anatomical model (bEAM) predicts intracochlear current flow, neural activation patterns, and the electrically-evoked compound action potentials (ECAPs) recorded on intracochlear electrodes. Since the bEAM is based on the temporal bone geometry and electrode position of an Ineraid patient, it is in many respects already a patient-specific model. However, incorporating additional histopathological details (e.g., new bone and fibrous tissue deposits, and the distribution of residual spiral ganglion cells) yields a version which we refer to as the Ineraid patient-specific EAM (psEAM). The third model is psEAM based on the temporal bone of a Nucleus implant user. It also includes individualized temporal bone geometry, electrode placement, neural population and intracochlear tissue deposits.

Using these three models, the objective of this chapter is to test the extent to which various model prediction correspond to empirical data. By analyzing the model predictions we expect to identify those parts of the modeling process that are most and least reliable. Finding the least reliable predictions will be especially important, since this allows one to focus future efforts on those specific areas that require the most refinement.

Alternatively, one needs to concede the possibility that nearly all the model predictions will bear almost no similarity to the measured data, in which case the model

should either be retired, or a new approach taken. Additionally, since we have previously compared our modeling results to those of other authors (see chapter 2) this testing may help benchmark those models as well. The following four sources of empirical data were used to test model predictions.

(I) *Intracochlear potentials (IP).*
For the Ineraid patient, intracochlear potential recordings were made while the patient was actively using the device and serving as a research subject. These recordings measure the voltage signature on the inactive electrodes while stimulating a single electrode with a low-level (subthreshold) monopolar probe signal. Analogous predictions are made using the Ineraid psEAM. Measured IP *data* and model *predictions* are referred to as IP_d and IP_p.

(II) *Psychophysical thresholds (T).*
For both the Nucleus and Ineraid donors, there exists a chronological record of psychophysical threshold measures made using each electrode of the implant device. Using the respective psEAM, a model-predicted psychophysical threshold is computed for each electrode by assuming threshold occurs in the model when a requisite number of neurons ψ (e.g., $\psi = 25$) are excited by the stimulating electrode. The pattern of threshold across electrodes for the measured and model-predicted cases (referred to as T_d and T_p) can then be compared.

(III) *Electrically-evoked compound action potentials (ECAPs).*
For the Ineraid patient, a collection of ECAPs were recorded from the intracochlear contacts using different stimulus configurations. These data show a systematic change in the N1P1[1] amplitude as the stimulating and recording electrodes vary. Using the Ineraid psEAM, the ECAPs can be predicted for the same set of stimulus configurations to see whether the same systematic pattern exists in the model N1P1 data. Measured data and model-predicted ECAPs are referred to as $ECAP_d$ and $ECAP_p$.

(IV) *Psychophysical data from current implant users.*
Psychophysical experiments can be designed to test specific predictions made by the model. Some model predictions are not strongly influenced by the types of anatomical differences seen across patients and tend to be relatively insensitive to whether the bEAM or either psEAM is used. These "generalizable" predictions might be expected to occur in a group of current implant users. Accordingly, a novel stimulus waveform was developed for which the models predict a pitch shift when the waveform is inverted. This prediction is tested in a group of current Clarion users from the subject pool at our research institution.

[1]ECAPs are often characterized by their amplitude, specifically the difference between the first negative phase of the waveform (N1) and the first positive phase of the waveform (P1).

There are several different reasons the models may fail to predict the measured data, especially psychophysical data. First, the model's representation of the anatomy, or calculation of a neural response, may be intrinsically flawed such that it cannot predict intracochlear spike-patterns without further refinement. Alternatively, the model may be capable of accurately predicting intracochlear spike-patterns, but the model linkage between spike-patterns and the psychophysical response may be inappropriate.

Accordingly, the comparison between $ECAP_d$ and $ECAP_p$ measures are the most meaningful, as the predicted and archived waveforms can be compared directly without having to rely on any heuristic linkage between a spike-pattern and a psychophysical percept. Additionally, because they require each stage of the model to be working in a way that is at least marginally representative of the physical situation, a correspondence between $ECAP_d$ and $ECAP_p$ will certainly be noteworthy, especially considering we are using a purely deterministic single-fiber model with a simplified morphology.

The comparisons between IP_d and IP_p measures are also direct, not relying on any heuristic linkage to a psychophysical percept, however it tests only the first stage of the modeling process where intracochlear potentials are estimated using the volume conduction model.

Finally, since the comparisons of T_d and T_p (test III) and the "general" psychophysical prediction (test IV) both rely on an assumed relationship between the predicted spike pattern and a psychophysical precept, these comparisons are less direct and harder to interpret. Regardless, we applied all four tests to see how our models performed.

3.2 Methods

3.2.1 Electro-anatomical models

Two patient-specific electro-anatomical models (psEAMs) were formulated from temporal bones in our archival collection.[2] The donor patients were specifically chosen because for each there exists a record of psychophysical threshold measures made at regular intervals while using the device. Since the Ineraid patient served extensively as a research subject, also available are a variety of additional measures including measures of impedance, intracochlear potentials, and evoked potentials. Relevant otologic and histologic characteristics of each patient are presented in Table 2.1 of the preceding chapter.

The modeling process is broken into four conceptual steps, described in detail elsewhere (see Chapter 2). First, a 3D volume conduction model is formulated from a set of histological images taken from the serial-sectioned temporal bone with the implanted electrode array left in situ. A collection of model fiber tracks is added to each psEAM with trajectories based on the position of the auditory nerve, Rosenthal's canal, and the osseous spiral lamina as captured in the histological images. The total number and distribution of neurons added to the model are based on segmental counts of spiral ganglion cells (SGCs) made along Rosenthal's canal using standard light microscopy (see p.32). The longitudinal cochlear positions of model fibers and electrodes are specified by the angular variable θ, which increases in degrees from the base to the apex. Also represented are the position of the electrode array, intracochlear fibrous tissue and ossification, and idiosyncratic damage to cochlear structures.

Second, the pulsatile electric field created by the stimulating electrode(s) in the volume conduction model is computed using finite-difference techniques. This solution describes intracochlear current flow during stimulation, including current flow along each model fiber track, for an arbitrary combination of active electrodes. For monopolar stimuli, the intersection of the auditory nerve trunk with the model boundary serves as a stimulus current return.

Third, the time-varying response to the pulsatile electric field is computed for a model nerve fiber associated with each fiber track. By iteratively scaling the electric field created by the stimulus electrode, a threshold is computed for each model fiber; that is, the minimum stimulus amplitude necessary to initiate a propagating action potential. Plotting each model fiber's threshold versus cochlear position predicts the spatial sensitivity of the fiber population to excitation by a particular stimulating waveform and electrode configuration.

Fourth, the neural activation pattern is used to predict the electrically-evoked compound action potential (ECAP) waveform recorded on inactive electrodes during

[2]NIDCD National Temporal Bone, Hearing and Balance Pathology Resource Registry, Massachusetts Eye and Ear Infirmary.

a 1-ms time window following the stimulus. This is accomplished by combining the predicted spatio-temporal pattern of spike activity with a second application of the finite-difference method to compute a predicted waveform for each recording electrode.

3.2.2 Testing model predictions

(I) *Intracochlear potentials.*
As part of an earlier research protocol, intracochlear potential recordings were made on the Ineraid subject by stimulating a monopolar electrode with a 20 μA_{rms}, 20 Hz sinusoid. The potential difference between measuring electrode m using reference electrode r while stimulating on electrode s is denoted as $\mathrm{IP}^{s}_{(m,r)}$. The configuration in Figure 3-1 is written as $\mathrm{IP}^{6}_{(2,3)}$. For a purely resistive system, the pattern across measurement electrodes while using different reference electrodes (i.e., $\mathrm{IP}^{6}_{(\cdot,5)}$, $\mathrm{IP}^{6}_{(\cdot,4)}$, $\mathrm{IP}^{6}_{(\cdot,2)}$...) will have exactly the same shape, differing only by a constant. The pattern for IP_d was computed by averaging the patterns obtained with different reference electrodes as:

$$IP^{s}_{d(m)} = \frac{1}{5}\sum_{r\neq s} IP^{s}_{d(m,r)} \tag{3.1}$$

The IP_d values were scaled by 0.05 to correspond to a 1-μA_{rms} input. Analogous predictions were made in the Ineraid psEAM (IP_p) by placing a 1-μA monopolar stimulus at each electrode position while recording the potential at the center of the inactive electrode positions.

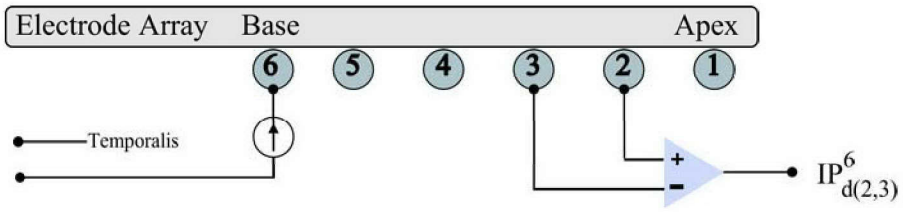

Figure 3-1: Recording setup for $\mathrm{IP}^{6}_{d(2,3)}$ made on the Ineraid subject. The return for the monopolar stimulating electrode is located in the temporalis muscle.

(II) *Psychophysical thresholds (T).*
In both psEAMs, each model fiber (indexed by i) is assigned a weight $N_{f(i)}$ describing the actual number of neurons represented. These weights were obtained by counting SGCs along longitudinal segments of Rosenthal's canal using traditional light microscopy. For a stimulus on a single electrode, the number of expected responding *neurons* can be calculated by summing $N_{f(i)}$ across all spiking model fibers. Accordingly, for each electrode, the lowest stimulus level that recruits a minimum criterion

number of neurons (e.g., 25) is taken as an estimate of psychophysical threshold (T_p^s) for electrode s. Repeating this for each electrode provides a predicted pattern of T_p across electrodes.

The model-predicted patterns (T_p) are compared with measured threshold patterns (T_d) obtained from archival patient data records. For the Ineraid patient, T_d measures were made in our laboratory using 300 ms pulse trains (250 μs per phase, 200 pps). For the Nucleus patient, the most recent T_d measures were taken from audiological reports from a different institution. The reliability of the psychophysical measures were assessed by comparing T_d values made over several years. Both patients' T_d measures showed a stationary pattern for the duration of time for which these measures were available.

(III) *Electrically-evoked compound action potentials (ECAPs).*
The Ineraid user served as research subject at Research Triangle Institute[3] where ECAP recordings were made for a variety of stimulating and recording electrode configurations. Stimuli were alternating polarity monopolar pulses (33 μs per phase, 0-800 μA) referenced to an electrode in the temporalis muscle.[4] Evoked potential recordings were made differentially between an intracochlear electrode and the ipsilateral mastoid. Stimulus artifact was attenuated by averaging 100 alternating polarity stimuli. N1P1 amplitudes were measured manually using MATLAB[5] to display and record user defined points. The ECAP measured on electrode m while simulating on electrode s is denoted as $ECAP_{d(m)}^s$.

The Ineraid psEAM was used to predict recordings ($ECAP_p$) for the same collection of stimulating and recording configurations. N1P1 amplitudes were measured automatically using custom software in MATLAB.

(IV) *Psychophysical data from current Clarion users.*
Using the bEAM, a set of bipolar stimuli were designed for which the model predicts a shift in pitch based on the polarity of the stimulus. Comparing the two waveforms (referred to as waveform A and waveform B), the model predicts waveform A to elicit a sensation of higher pitch than B, even though the latter is simply an inverted version of the former (see results section for waveforms and modeling results).

Enumerating the Clarion electrodes from apex to base, waveform A applied to the apical-most bipolar+1 pair of electrodes (3 and 1) is referred to as $[A_{31}]$. Not only does the model predict $[A_{31}]$ to have a higher pitch than waveform B applied to the same electrode $[B_{31}]$, it also predicts $[A_{31}]$ will elicit a pitch *higher* than waveform B applied to a more *basally* located electrode pair, $[B_{42}]$. This is counter-intuitive since typically as a stimulus is shifted basally, the pitch increases. Considering the

[3]RTI International, Research Triangle Park, NC 27709-2194
[4]A subset of these data are presented in Finley et al. [48].
[5]MATLAB is a trademark of MathWorks, Inc., Natick, MA.

four possible stimuli, the model predicts the pitch will steadily decrease across the following order of configurations: $[A_{42}]$, $[A_{31}]$, $[B_{42}]$, and $[B_{31}]$ (see results section).

To test this model prediction, these stimuli were presented to five users of the Clarion[6] implant system using a research interface and the BEDCS[7] research software. Presentations were controlled with MATLAB interfaced to BEDCS via an active-X connection.

Waveform B applied to the apical-most bipolar+1 electrode pair $[B_{31}]$ served as a loudness reference. The level of $[B_{31}^{ref}]$ was adjusted until the subject reported a "comfortably soft" loudness, roughly 2 on a scale of 1-10. All other stimuli were loudness balanced against this $[B_{31}^{ref}]$ stimulus to find a level that was just noticeably louder (e.g., $[B_{42}^{+}]$) and just noticeably softer (e.g., $[B_{42}^{-}]$). Loudness balancing procedures followed the adaptive procedures of Jesteadt [90]. Here stimuli based on two decision rules are interleaved such that one set of stimuli asymptotes to a level judged *louder* than the reference 70.7 % of the time, the other to a level judged *softer* 70.7 % of the time. For the louder and softer decision rules, the mean of the last eight reversal points was taken as the 70.7 % estimate. The reliability of the louder and softer estimates was tested by fitting the entire data set with a psychometric function (integrated gaussian) that returned confidence limits for points along the function. This was done to ensure the louder and softer stimuli (e.g., $[B_{42}^{+}]$ and $[B_{42}^{-}]$) were indeed above and below the point of subjective equality with $[B_{31}^{ref}]$. Errant ("bad") runs were identified and rejected by calculating the deviance[8] for the run and comparing it to boot-strap estimates (after Wichmann and Hill [226, 227]). Fewer than 5 percent of all runs were rejected.

Pitch comparisons were made pairwise, for example $[A_{31}]$ vs. $[B_{42}]$. Presentations were made in a 3-interval, 2-alternative forced-choice (2AFC) paradigm where the subject was asked to select whether the 2^{nd} or 3^{rd} interval had a higher pitch in a series of three, 500 ms duration bursts separated by 100 ms; for instance $[A_{31}^{-}][B_{42}^{+}][A_{31}^{-}]$. The first interval was used as a dummy interval and always contained the same token as either the 2^{nd} or 3^{rd} interval.

Pitch judgements based on loudness were avoided by presenting an equal number of louder and softer tokens in each pairwise comparison. For example, 40 trials of $[A_{31}^{+}]$ vs $[B_{42}^{-}]$ and 40 trials of $[A_{31}^{-}]$ vs $[B_{42}^{+}]$ were presented, such that if loudness were

[6]Clarion implant is a trademark of the Advanced Bionics Corporation, Sylmar, California.

[7]Bionic Ear Data Collection System v1.15, courtesy Leonid Litvak, Advanced Bionics Corporation, Sylmar, California.

[8]The deviance, or log-likelihood ratio, is a measure of the fit of the empirical data to the psychometric function model. Results which there is almost no residual error between the data and the model prediction (i.e., a perfect fit) will have unusually low deviance scores. Alternatively, empirical data that are an especially poor fit to the psychometric function model will have inordinately high deviance scores. Accordingly, Monte Carlo simulation can be used to designate a range of appropriate deviance values (i.e., the 95 % confidence interval), in order to reject runs outside this range where the fit is either inordinately good (no residual error) or poor (high residual error). [226]

used exclusively by the subject to make a pitch judgment, the test statistics reflect no pitch discrimination.[9]

Each comparison utilized 80 trials. Additionally, the order of the tokens was randomized with, for example, an equal number of $[A_{31}]$ or $[B_{42}]$ tokens appearing in the 2nd and 3rd positions. This was done to eliminate a pitch bias based on the presentation interval. Finally, tokens were randomized with an equal frequency of the louder interval in the 2nd and 3rd positions.

Pitch comparisons of the same stimulus at different levels (e.g., $[A_{31}^{-}]$ vs $[A_{31}^{+}]$) were also included in the presentation queue to determine the degree to which level influenced the pitch judgement.

3.3 Results

(I) *Intracochlear potentials.*
To measure how the model predictions change as the level of anatomical detail increases, several alternative models were used to calculate IP_p values. The lowest-detail model consists of the bEAM with all tissues and materials replaced by 300 Ω-cm tissue. Here the trajectory of the model's nerve fibers are still represented, but the volume conduction model is replaced by an infinite homogenous medium without boundary conditions. The potential solution is obtained analytically using point current sources in an infinite homogenous medium (referred to as the homogeneous model). The next level of detail is the bEAM which represents the geometry of the Ineraid cochlea, followed by the complete Ineraid psEAM. Previous work has shown that the model results are sensitive to the resistivity of bone when changes over an order of magnitude are made (see p.51). Since other models [12, 13, 73] have used approximately 600 Ωcm for the resistivity of bone (as opposed to the 5 kΩcm used in the bEAM and psEAMs), a version of the bEAM using 600-Ωcm bone was also used to predict IP_p.

Comparisons of IP_d (gray) with IP_p (black) are shown in Figure 3-2 using four models to generate IP_p data: the Ineraid psEAM (○), bEAM (△), bEAM with 600-Ωcm bone (▽), and the homogenous 300-Ωcm model (◇). Note the subtle non-monotonicity in the IP_d data in panel A where the apical $IP_{d(1)}^{6}$ is slightly higher than its basal neighbor $IP_{d(2)}^{6}$. In this and other subjects, Girzon [60] also found this type on non-monotonic behavior for basal stimulation (see [60] Table 7.2, page 114).

Especially for apical stimulation using the psEAM in the top row of panel C, the IP_p fit to the data is promising. The bEAM appears to fit the data better than the psEAM for basal stimulation (compare rows 1 and 2 of panel A). However, overall the psEAM and bEAM predict the data better than a homogenous model or a model

[9] In other words, if the subject simply chooses the louder interval in the $[A_{31}]$ vs $[B_{42}]$ pitch comparison, half of those chosen as higher in pitch would be $[A_{31}]$, half would be $[B_{42}]$.

where 600-Ωcm bone is used. Not surprisingly, there are similarities between IP_p predictions obtained using the 600-Ωcm bEAM ($\bigtriangledown$), and the homogenous 300-Ωcm model ($\diamondsuit$). For instance, for apical stimulation both of these show a characteristic local maximum at $IP^1_{p(5)}$, likely because the position of the apical EL1 is geometrically close to EL5, separated only by the bony intrascalar septum, making their electrical potentials tightly coupled (see p.37). In the psEAM and bEAM, the resistivity of this septum is an order of magnitude higher, reducing the cross-turn current flow and making the potential of these two electrodes less tightly coupled.

This suggests the ratio of bone-to-fluid resistivity is an important parameter. For the bEAM using 600-Ωcm bone, this ratio is only 12 as compared to a ratio of 100 in the psEAM. To the extent this ratio is high, one expects a minimal amount of cross turn coupling, with the fluid spiral behaving more like a transmission line.

Thus far, monopolar results have been obtained using a current return positioned at the intersection of the model boundary with the auditory nerve in the internal auditory meatus (IAM). To test the influence of this assumption in the psEAM (that the majority of the current exits the bony labyrinth through the IAM), IP_p estimates were computed using several alternative returns. First, the vestibule and the carotid canal were individually grounded. Here the intersection of the model boundary with the vestibule (or the carotid canal) was used as a return. Next, a round-window ground was added to the model either in isolation or in addition to the IAM ground (referred to as the dual-ground condition).

A comparison of IP_p predictions using these alternatives with the measured IP_d are shown in Figure 3-3. With the exception of the dual-ground condition for basal stimulation (IP^6_p) in the bottom row of panel A, these alternative grounds tend to decrease the overall fit, as shown in Table 3.1 where RMS error values[10] are listed for each model rendition tested. The round-window grounding condition yielded the worst overall fit, as seen in the last entry. However, as shown in Figure 3-4 either adding a round window ground or switching from the psEAM to the bEAM, where the intracochlear tissues occupying the basal turn are absent, tended to reduce the potential gradients during basal stimulation thus bettering the fit. A best fit to the data can likely be obtained using a weighted average of IP_p solutions obtained with different ground positions (i.e., a percentage of current exits the model via each ground). Because it provided the best fit to the data, the single IAM ground was selected for subsequent experiments.

In summary, the psEAM tends to best predict the data for apical stimulation,

[10]To calculate RMS error, zero mean estimates of IP_d and IP_p are compared as

$$Error_{RMS} = \sqrt{\frac{1}{15}\sum_{s=[6,3,1]}\sum_{m\neq s}\left([IP^s_{d(m)} - < IP^s_d >] - [IP^s_{p(m)} - < IP^s_p >]\right)^2} \qquad (3.2)$$

where <> indicates the sample mean operator.

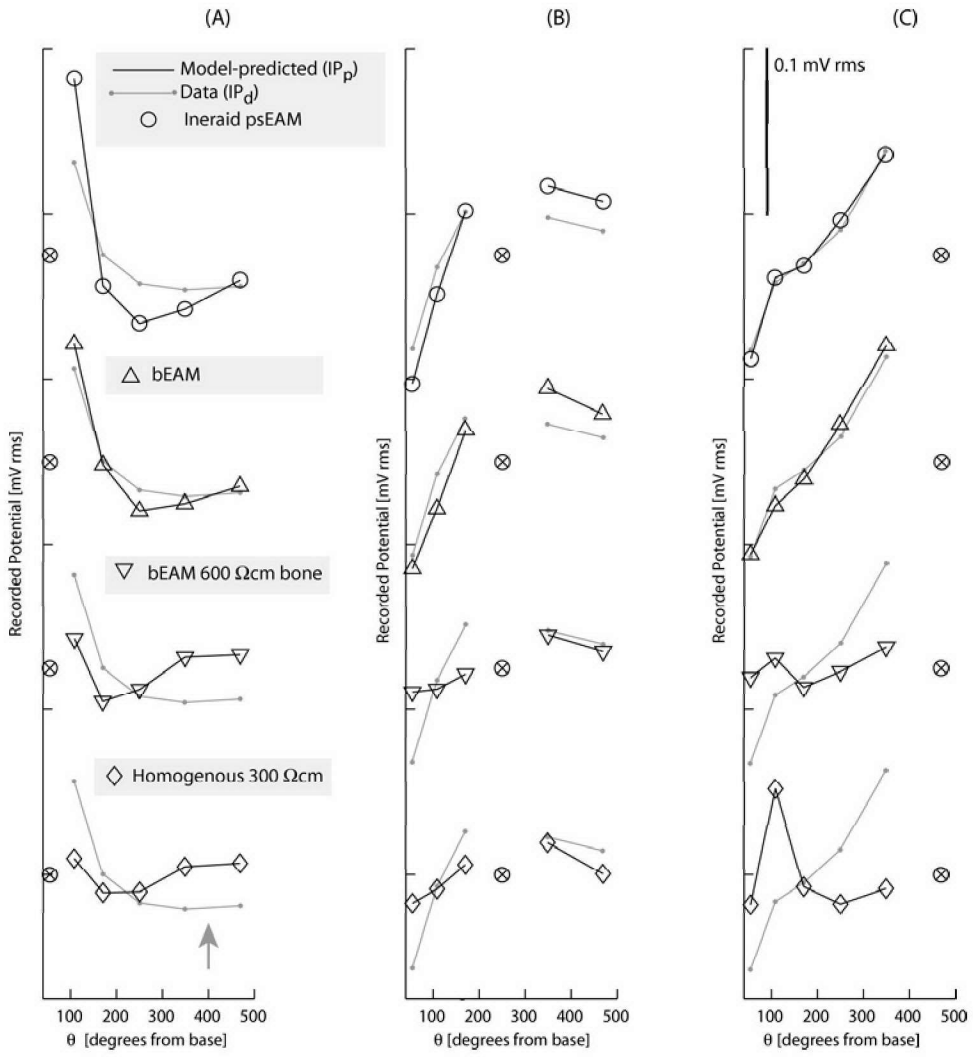

Figure 3-2: Plots of IP_d (gray) and IP_p (black) as a function of recording electrode position for stimulation of EL6 (panel A), EL3 (panel B), and EL1 (panel C). Four models are used to generate IP_p: the Ineraid psEAM (○), bEAM (△), bEAM with 600-Ωcm bone (▽), and homogenous 300-Ωcm model (◇). The position of the stimulating electrode is given by ⊗. Note the non-monotonicity in the IP_d data in panel A ($IP^6_{d(1)}$ is slightly higher than its basal neighbor $IP^6_{d(2)}$ (gray arrowhead)).

and the assumption that current exits the otic capsule primarily via the IAM seems plausible, especially for apical stimulation (see discussion section). Representing the peripheral anatomy as a homogeneous medium provides little ability to predict the IP_d measures.

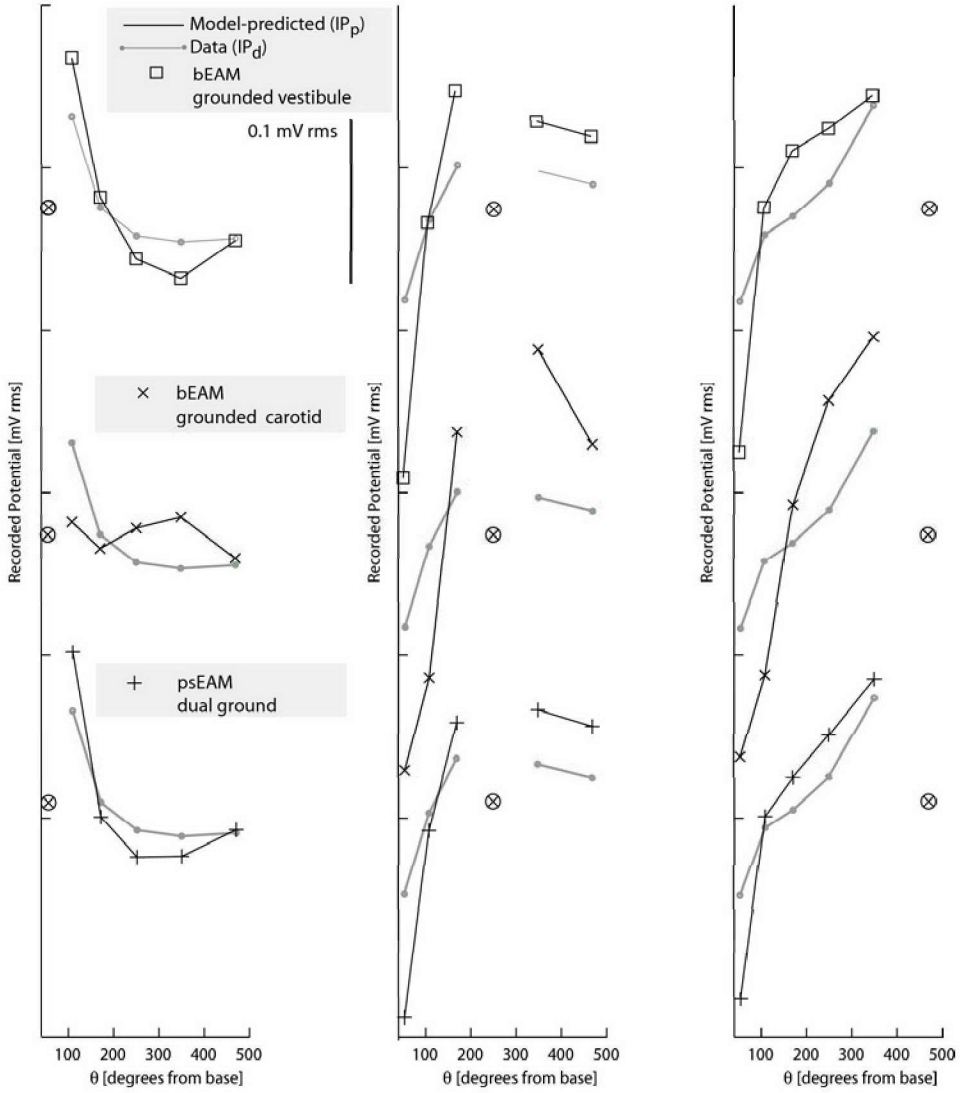

Figure 3-3: Comparison of IP_d (gray) with IP_p (black) for stimulation of EL6 (panel A), EL3 (panel B), and EL1 (panel C) using three alternative grounds: grounded vestibular (□), carotid canal (×), and a dual ground (+) where both the IAM and round window were grounded.

Model	**RMS Error [mV]**
psEAM	0.1428
bEAM	0.0872
bEAM w/ 600 Ωcm bone	0.2213
homogenous	0.2572
psEAM (vestibular ground)	0.3435
psEAM (carotid ground)	0.4431
psEAM (dual ground)	0.2507
psEAM (round window ground)	0.6823

Table 3.1: RMS error calculation for each model version tested.

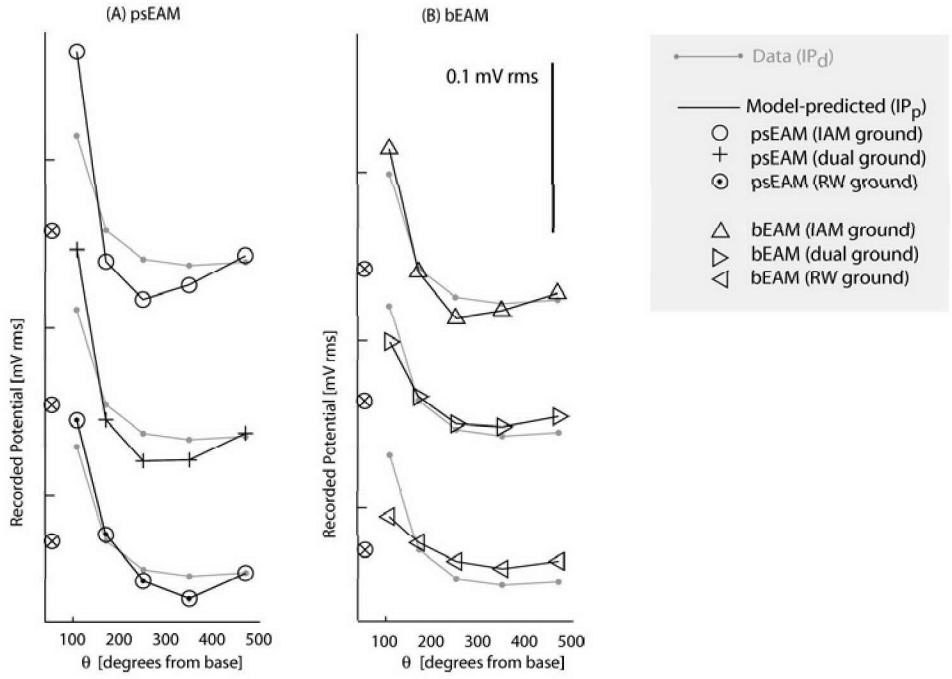

Figure 3-4: Comparison of IP_d^6 (gray) with IP_p^6 (black) for basal stimulation of EL6 in the psEAM (panel A) and bEAM (panel B) using the default IAM ground, dual grounds in the IAM and at the round window, and a single round window (RW) ground.

(II) *Psychophysical thresholds (T)*

Model-predicted (T_p) and measured (T_d) threshold patterns are compared in Figure 3-5 for the Ineraid and Nucleus subjects, using the criterion that psychophysical threshold occurs when 150 neurons are excited (ψ=150). For each subject, predictions are shown for the psEAM, and a version of the psEAM with intracochlear new bone and soft tissue deposits replaced by fluid. In addition, predictions of T_p are shown for the bEAM which has a uniform distribution of surviving neurons. Although absolute T_p values tend to be significantly higher than T_d, here we are interested in the pattern across stimulating electrodes.

In both psEAMs the inclusion of new bone and soft tissue deposits tended to *lower* single-fiber thresholds, consequently lowering the T_p predictions, especially for basally located electrodes in the Ineraid psEAM. Reasons for this prediction are discussed in the next chapter.

Additionally, the pattern of surviving neurons across cochlear position, $N_{f(i)}$, seems to have little influence on the prediction of T_p. This suggests even a few neurons sparsely spread across θ will show a similar pattern for T_d, a result due to the extensive longitudinal spread of current detailed in previous sections. For example, in panel A the Ineraid psEAM (10,248 neurons) without intracochlear tissues ($\bigtriangledown$) has essentially the same T_p values as the bEAM ($\bigtriangleup$) which has 30,000 uniformly distributed neurons. More explicitly, shown in panel B is the variation in T_p predictions for the Ineraid psEAM ($\circ$) as the neuronal survival vector $N_{f(i)}$ is manipulated. For several alterations to $N_f(i)$, the variation in psEAM T_d (gray shading) is minimal. Likewise in panel B, changing the criterion ψ imparts only a minimal amount of variation (gray shading) to the bEAM T_d predictions ($\bigtriangleup$).

While T_p predictions were not found to be sensitive to different values of ψ less than 1,000, they were found to be sensitive to the morphology of the single-fiber model used. Using the five alternative-fiber morphologies described in section 2.4.4 (p.69), a range of T_p estimates are obtained for the Ineraid psEAM, as shown by the gray shading in 3-5A. This does not support the model's ability to predict T_d , as changes to the model used introduce variance into the T_p estimates equal to, or greater than, the variance in the measured T_d.

For both subjects, T_d values tend to increase toward the base, a feature present in the T_p estimates obtained from both versions of the Nucleus psEAM, but only in the Ineraid version without intracochlear tissues. This may be an artifact of a hypothesized grounding pathway located in the base that shunts current away from the excitable tissues during basal monopolar stimulation, as detailed in the discussion section. Alternatively, the decreased T_p values at the base predicted by the Ineraid psEAM could be a result of overestimating the resistivity of intracochlear new bone (5 kΩcm). It is possible that the relatively porous intracochlear bone has a lower resistivity, which would tend to move the T_p estimates in Figure 3-5 toward those of

the bEAM (compare ∘ with △).

In the present formulation, the T_p data do not suggest a robust ability of the psEAMs to predict patterns of psychophysical threshold across the entire implanted electrode array. One noteworthy exception is at the basal end of the Nucleus model where the electrode array is coiled (see p. 37). According to Nucleus patient records, the second-most basal electrode pair (EP19, denoted with ∅ in Figure 3-5) was turned off. This was likely due to an extremely high T_d value (corresponding to 94 nC per phase) listed in the patient's chart, although we can not verify this to be an accurate threshold measure. It is likely the threshold for EP19 was at least 94 nC per phase, if not greater. This departure of EP19 from the other electrodes pairs appears to be captured by the Nucleus psEAM, where in both formulations T_d estimates for EP19 are higher than any electrode. This appears to be due to the both the unusual orientation of this pair in the coiled region of the array and the lack of any surviving neurons nearby, as discussed in the next chapter.

Overall, correlations between T_d and T_p were only significant for the Nucleus psEAM as shown in the inset of Figure 3-5, with T_p accounting for up to 84 percent of the variation in T_d mainly due the increased values toward the base. Removing EP19 from the analysis drastically lowers the percentage of variation the model predictions can account for (see Figure 3-5 caption). While it is impressive the model accounts for variation in T_d for the basal half of the Nucleus array, it does not perform nearly as well over the apical half. Other attempts made by our laboratory to predict psychophysical thresholds using the same method were also only marginally successful [225]. Potential reasons for this are given in the discussion.

Notice in Figure 3-5 that only the Ineraid T_d data have error bars, as the psychophysical threshold measures made in our laboratory were done using standard psychophysical procedures, while these measures were not available from the Nucleus subject's archival reports. However, variation in T_d across the array of the Nucleus subject spans 47 clinical units,[11] which is larger that the typical test-retest variation anecdotally reported for similar audiological testing done at our institution [70].

As of yet we have not made T_p comparisons between patients, as the Nucleus thresholds were obtained at a different pulse rate than the Ineraid data and it is known that higher pulse rates tend to elicit lower psychophysical thresholds [186]. In all likelihood, the pulse rate used by the Nucleus subject's Spectra 22 processor was substantially higher than the 200 pps rate used in making the Ineraid T_d measures.

[11] A "clinical unit" is the nomenclature used to describe the current amplitude steps used by the Nucleus device. An increase in stimulus level of one clinical unit corresponds to approximately a 0.176 dB increase in the charge delivered per phase of the stimulating pulse.

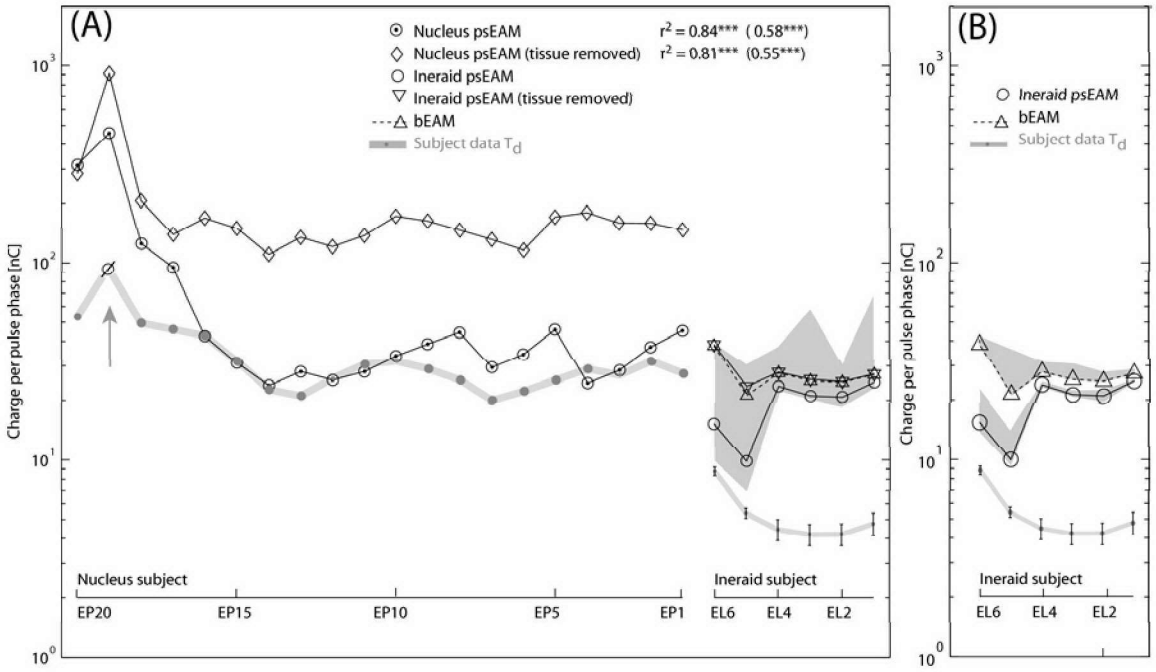

Figure 3-5: (A) Measured T_d patterns as a function of stimulating electrode for the Ineraid and Nucleus subjects (gray). Model-predicted T_p patterns for the Ineraid ($\circ, \bigtriangledown$) and Nucleus ($\diamond, \odot$) subjects are shown using the threshold criterion ψ =150 neurons excited. Note both T_d and T_p measures have been converted to the charge delivered per phase [nC] of the stimulating pulse in order to account for the different pulse durations used. T_p predictions are shown for both the psEAM, and the psEAM with intracochlear new bone and soft tissue removed. Estimates of T_p from the bEAM are also shown ($\bigtriangleup$). Correlations between T_d and T_p are given in the legend with the level of statistical significance indicated by asterisks: $(p < 0.05)^*, (p < 0.01)^{**}, (p < 0.001)^{***}$. Removing EP19 ø from the Nucleus data set drastically reduces the r^2 values as indicated by the values in parentheses. **(B)** T_p versus stimulating electrode for the bEAM ($\bigtriangleup$) using $\psi = 150$ neurons excited, as replicated from panel A. Changing the criterion ψ between 30 and 2000 neurons imparts only a minimal amount of variation to the bEAM T_p estimate (shown by shading). Also shown are T_d estimates for the psEAM ($\circ$) as replicated from panel A. These T_d estimates use the patient-specific distribution of the residual neural survival, where each entry in the vector $N_{f(i)}$ denotes the number of neurons represented by model fiber i. Modifying the neuronal survival vector, $N_{f(i)}$, while holding $\psi = 150$, also has little impact on the psEAMs T_p predictions (shown by shading). Here the patient-specific $N_{f(i)}$ vector was either multiplied by 3 (giving over 30,000 neurons), divided by 3, replaced with a uniform distribution ($N_{f(i)} = 150$ for all i), or replaced with a diminished uniform distribution ($N_{f(i)} = 30$ for all i).

(III) *Electrically-evoked compound action potentials (ECAPs).*

Shown in panels A and B of Figure 3-6 are $ECAP_d$ and $ECAP_p$ recordings in response to a stimulus pulse on EL3. For all recording electrodes, the measured $ECAP_d$ waveforms show a characteristic negative phase followed by a positive phase (N1P1). As reported by others [16, 17], except for variation in amplitude, the ECAP morphology does not change drastically as the recording electrode is moved. These characteristics are also seen in the model-predicted $ECAP_p$ and measured $ECAP_d$ traces for a wide range of stimulating and recording configurations.

One explanation for this in the case of $ECAP_d$ is that electric stimulation activates neurons over nearly the entire range of cochlear positions such that any chosen recording electrode will be near a few firing neurons. The model suggests this is not the case, since even low-level stimuli that activate only a single model fiber show a characteristic negative-positive morphology for each choice of recording electrode.

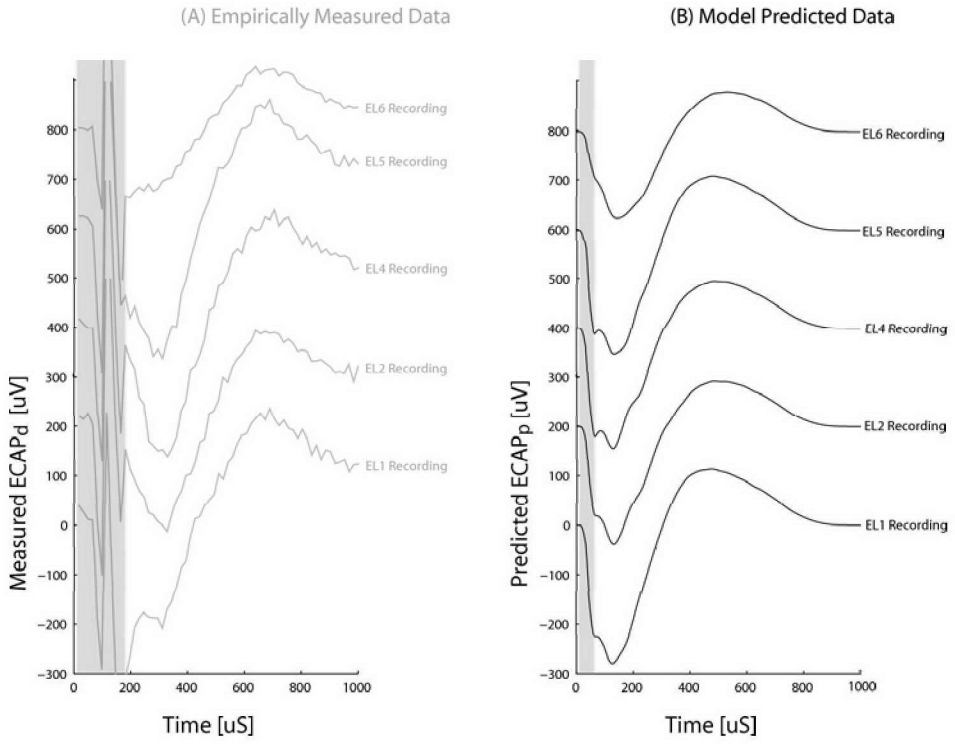

Figure 3-6: $ECAP_d$ (panel A) and $ECAP_p$ (panel B) recordings for stimulation by EL3. Regions contaminated with stimulus artifact are shaded in gray. Individual traces are offset by 200 μA for clarity of presentation. Note both the magnitude and latency of the predicted $ECAP_d$ are similar to the empirical data.

Shown in the panels of the top row of Figure 3-7 are $ECAP_d$ measures of N1P1 amplitude across recording electrode for stimulation by EL6, EL5, EL3 and EL1. Within each panel, lines connect measures made at the same stimulus level, with stimulus levels increasing from 279 to 800 μA. Analogous N1P1 measures made on

a collection of $ECAP_p$ waveforms using the Ineraid psEAM are shown in the panels of the bottom row. Since the largest-amplitude physiological $ECAP_d$ recordings are the most reliable, comparisons between $ECAP_d$ and $ECAP_p$ are made for the highest amplitude $ECAP_d$ measures (thick lines in panels A-D of Figure 3-7).

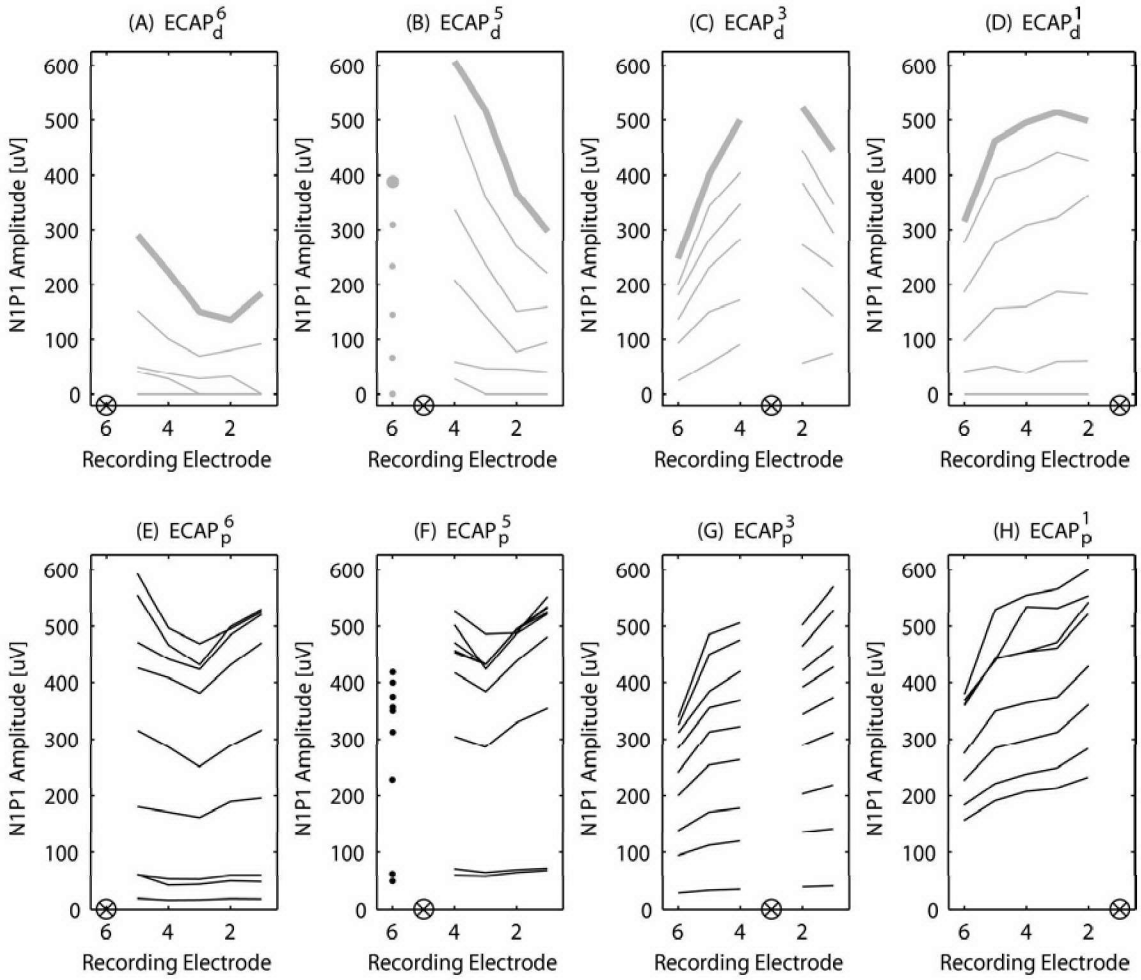

Figure 3-7: N1P1 amplitude measures from $ECAP_d$ (top row) and $ECAP_p$ (bottom row) as a function of stimulating and recording electrode. (Panels A-D) Ineraid patient N1P1 amplitudes across recording electrode for $ECAP_d^6$, $ECAP_d^5$,$ECAP_d^3$, and $ECAP_d^1$. Connected lines within each panel show an amplitude series with the position of the stimulating electrode marked by $\otimes$. $ECAP_d$ recorded in response to monopolar stimulation (279.2, 344, 424.8, 524.8, 648, and 800 μA pulses, 33 μs per phase biphasic pulse) relative to a return embedded in the temporalis muscle. Recordings were made differentially between the measurement electrode and the ipsilateral mastoid by averaging 100 alternating polarity stimuli. (Panels E-H) psEAM-predicted N1P1 amplitude measures in response to biphasic pulses increasing in amplitude from 750 μA to 2750 μA in 250 μA increments. This range of levels was chosen because of the typical 9 dB range of levels across which a response is noticed in the $ECAP_d$ data.

One aspect not captured by the model is the difference in N1P1 amplitude *across stimulating electrodes* at higher current levels. Specifically, in response to stimulation by EL6 the $ECAP_d^6$ measures in panel A of Figure 3-7, are substantially smaller

than those obtained by stimulation of the other electrodes in panels B-D ($ECAP_d^5$, $ECAP_d^3$, and $ECAP_d^1$). The corresponding model data does not show this overall difference in N1P1 amplitude between EL6 stimulation in panel E and the other stimulating electrodes in panels F-H. Such a disparity could be due to either the threshold or slope of the ECAP growth function (see discussion section).

The $ECAP_d$ and $ECAP_p$ data can be compared either (1) across recording electrodes for a fixed simulating electrode or (2) across stimulating electrodes for a fixed recording electrode. We focus on the former here, while a discussion of ECAP amplitude growth is given in the discussion section. The comparison between $ECAP_d$ and $ECAP_p$ is most straight-forward across recording electrodes for a fixed stimulating electrode because the only variable is the position of the recording contact, as opposed to comparisons across stimulating electrodes where the collection of responding neurons also varies. To aid in this comparison, N1P1 amplitudes for both $ECAP_p$ and $ECAP_d$ (highest stimulating amplitude) are plotted together as zero-mean vectors in Figure 3-8.

Taken as a series (combining these zero-mean vectors across the 4 stimulating electrodes) there is a significant correlation between $ECAP_d$ and $ECAP_p$ measures (r^2=0.38, p<0.01). Note this implies the model predicts variation across the recording electrodes,[12] but, as mentioned earlier, it does not strictly account for variation in N1P1 amplitudes across stimulating electrodes. This correlation was not observed (r^2=0.019 p=0.56) when the bEAM was used to predict $ECAP_p$ measures as shown in the panels of Figure 3-9.

Most impressive in Figure 3-8 is that for $ECAP^6$ (panel A) the model accounts for a non-monotonic change in N1P1 amplitude as the recording electrode is moved apically from a basal stimulating electrode. This is likely because the geometric distance between EL6 and EL1 is closer than between EL6 and, for instance, EL4 because of the spiraling configuration of the array (see p. 37). The major feature for which the model does not account is the monotonically decreasing N1P1 amplitude from $ECAP_{d(3)}^5$ to $ECAP_{d(1)}^5$ in panel B, and from $ECAP_{d(2)}^3$ to $ECAP_{d(1)}^3$ in panel C.[13]

As the calculation of $ECAP_p$ relies on several stages of the model running in succession, a reduced model was formulated to assess the influence of each stage on the $ECAP_p$ prediction. The sequence of computational steps are: (1) calculating the intracochlear potential and current distributions using the volume conduction model, (2) computing the response of each model fiber to yield estimates of extracellular current flow along each fiber, and (3) using the volume conduction model to calculate

[12]Variation in N1P1 amplitude can be parsed into two factors: that due to changes in the recording electrode (σ_r) and that due to changes in the stimulating electrode (σ_s). The latter variance (σ_s) is removed by subtracting the mean for each stimulating electrode series (ie. $ECAP_p^6$ - $< ECAP_d^6 >$) since the model does appear to account for variance introduced by changing the stimulating electrode.

[13]Increasing the bone resistivity to 10 kΩcm did not alleviate this disagreement.

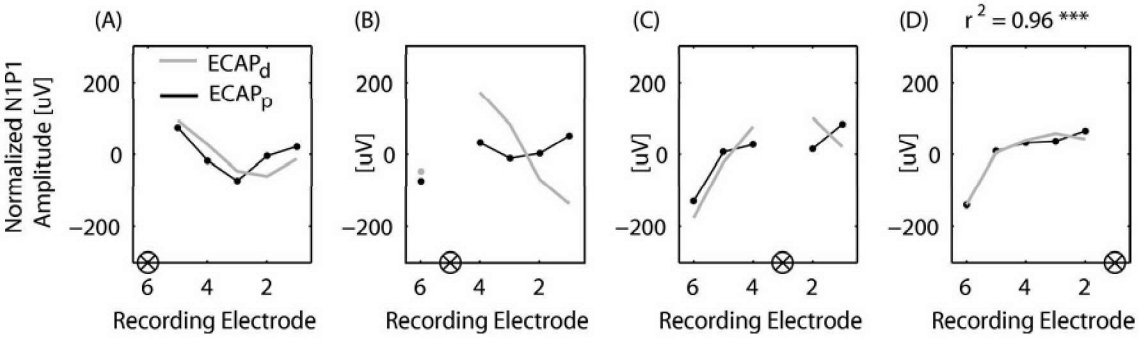

Figure 3-8: N1P1 measures from $ECAP_d$ (gray) and $ECAP_p$ (black) data normalized as zero-mean vectors. $ECAP_d$ measures were made at 800 μA (highest stimulation amplitude). $ECAP_p$ data generated using the psEAM at an (arbitrarily chosen) level of 2625 μA. Taken as a series (combining these zero-mean vectors for the 4 stimulating electrodes) there is a significant correlation between $ECAP_d$ and $ECAP_p$ measures ($r^2 = 0.38, p < 0.01$). Taken individually the only significant correlation is seen for the comparison between $ECAP_d^1$ and $ECAP_p^1$. In this and subsequent figures, statistical significance is indicated with asterisks: $(p < 0.05)^*, (p < 0.01)^{**}, (p < 0.001)^{***}$.

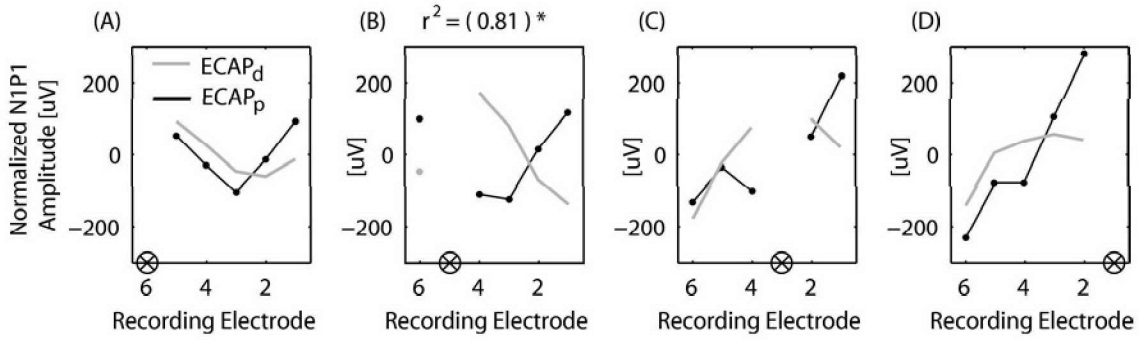

Figure 3-9: Normalized N1P1 measures from $ECAP_d$ (gray) and $ECAP_p$ (black) made using the bEAM with a uniform collection of nerve fibers (i.e., N_f=300 neurons for each model fiber) at 2625 μA . Note the fits are worse than when the psEAM is used. Taken as a series there is no significant correlation between $ECAP_d$ and $ECAP_p$ measures. Taken individually only $ECAP_d^5$ and $ECAP_p^5$ show a significant *negative* correlation (indicated by parentheses).

the voltage signature on each electrode induced by the collection of extracellular currents generated by the model fibers.

Focusing on the third step of the process, the unitary contribution of each model fiber to the $ECAP_p$ was estimated by artificially initiating an action potential on the peripheral-most compartment of each fiber with an intracellular current. This provides a collection of unitary extracellular currents[14] that, when combined with the volume conduction model, return the voltage signature for each single-fiber action potential (SFAP). Using the collection of unitary SFAPs (uSFAP), the $ECAP_p$ can be easily computed by adding together the uSFAPs for an arbitrary collection of

[14]Note since the dimensions of all model fibers differ only in total length, and the same intracellular current was used for each fiber, these unitary extracellular currents will all be similar.

fibers. For instance, the $ECAP_p$ waveform recorded on EL1 in response to all model fibers in the first cochlear turn spiking simultaneously is calculated by combining the uSFAPs for fibers with $0 < \theta < 360$.

A simple heuristic to link the position of the stimulating electrode with that of the responding fibers was to assume all fibers within ± 45 degrees (in θ) of the active electrode were activated. Using both the psEAM and bEAM, $ECAP_p$ data sets were computed using ± 45 and ± 100 degrees as the heuristic distance to the stimulating electrode. As the results using ± 45 and ± 100 degrees were similar, only the ± 100 estimates are shown in Figure 3-10. To the extent variation in the uSFAP-derived N1P1 amplitude matches that observed using the full modeling process, this variation is likely determined by the geometric and electric relationship of the fibers with the intracochlear electrodes (i.e., the third step), and not on an artifact of the first or second modeling steps. The correlation between $ECAP_d$ and $ECAP_p$ are tabulated in Figure 3-11 for each model formulation tested.

In summary, correspondence between the psEAM-predicted and measured ECAPs is strongest for apical stimulation, as was the case for predicting IP_d data with the psEAM. This correspondence is seen in both the psEAM model, and the psEAM model using unitary SFAPs, suggesting it is a feature of the 3D electrical relationship of the electrodes to the excitable neurons, not an artifact of the single-fiber model or stimulus conditions.

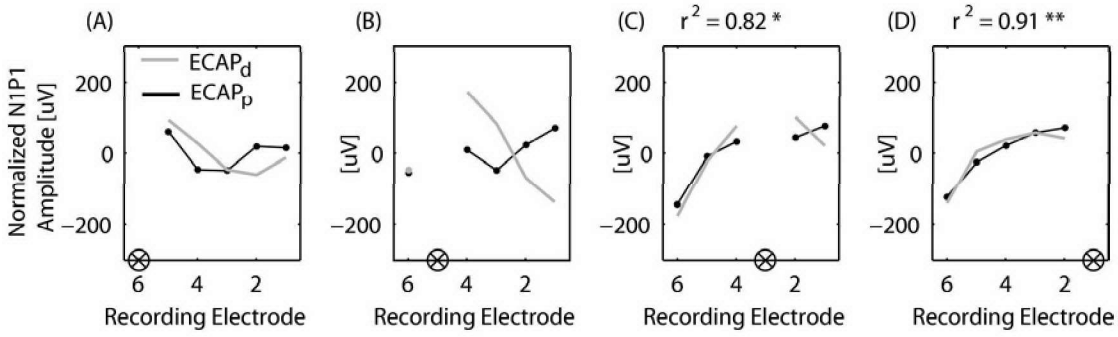

Figure 3-10: uSFAP-derived, normalized N1P1 amplitudes using the psEAM volume conduction model (solid black) with a uniform complement of 30,000 surviving neurons (i.e., $N_f = 150$). These data are computed using ± 100 degrees in θ as the heuristic distance, relative to the stimulating electrode, over which fibers spike.

		low level (1875 uA or +/-45 deg)					high level (2625 uA or +/-100 deg)				
model	$N_f(i)$	r_{EL6}	r_{EL5}	r_{EL3}	r_{EL1}	r_{total}^2	r_{EL6}	r_{EL6}	r_{EL6}	r_{EL6}	r_{total}^2
psEAM	ps	0.35	-0.29	0.70	0.89*	0.08	0.73	0.04	0.82	0.98***	0.38***
psEAM	300	0.35	-0.29	0.70	0.85	0.12	0.79	0.04	0.83	0.81	0.34***
bEAM	300	0.03	-0.74	0.55	0.74	0.01	0.45	-0.9*	0.42	0.73	.02
unitary psEAM	ps	0.52	-0.12	0.89*	0.99***	0.11	0.53	-0.25	0.90*	0.99***	0.20*
unitary psEAM	300	0.53	-0.12	0.89*	0.99**	0.17	-0.46	0.43	0.90*	0.95**	0.25*
unitary bEAM	300	0.82	-0.68	0.62	0.94**	0.05	0.68	-0.71	0.72	0.87	.06
unitary bEAM 600 ohm-cm bone	300	-0.30	-0.83	0.57	0.61	(0.03)	-0.4	-0.92*	0.47	0.53	(0.05)
							***p<0.01		**p<0.025		*p<0.05

Figure 3-11: Tabulated correlation coefficient between N1P1 amplitudes from $ECAP_p$ and $ECAP_p$ for each stimulating electrode for each model rendition used to generate $ECAP_p$. The fiber weighting $N_{f(i)}$ is either patient specific (ps) or a uniform distribution (i.e., 30,000). Low and high levels correspond to μA for the first three rows. Low and high levels correspond to ± 45 and ± 100 degrees for the unitary models of the last three rows. Note that negative correlations were measured when stimulating with EL5. For each model, the coefficient of determination (r^2) is shown, as these were always based on positive correlations, except in the last row where parentheses indicate an r^2 based on negative correlation. Correlations tended to be better for both the higher level and for the psEAM.

(IV) *Psychophysical data from current Clarion users.*

As a final test, the bEAM was used to make a set of predictions for bipolar stimuli. This model includes a uniform population of SGCs that respond to arbitrary stimuli applied to a bipolar pair of electrodes. Shown in Figure 3-12 are model predictions of single-fiber threshold as a function of cochlear position (θ) in response to *bipolar* stimulation by a *monophasic* pulse with a cathodic basal electrode (panel A), and a *monophasic* pulse with a cathodic apical electrode (panel B). The lowest-threshold fibers for these two stimuli are located at two longitudinally distinct cochlear positions, near 1199 Hz and 904 Hz, as shown by the leftward-pointing arrows. This suggests that two mutually-exclusive populations can each be excited by low-level presentations of these two monophasic stimuli, where fibers near the cathodic contact of the electrode pair tend to produce spikes.

Since charge-balanced stimuli are required for safety considerations, we used these model results to design two novel stimulus waveforms that could be safely used in psychophysical experiments. These waveforms (referred to as waveforms [A] and [B]) are shown in panels C and D, with the model-predicted responses presented in the dot-raster plots of panels E and F, respectively. Waveform [A] consists of a 3200 Hz biphasic pulse train, with only the upper envelope modulated by an 800 Hz modulator, such that pair-wise pulses are not charge balanced, but over one cycle of the modulator charge balance is maintained.

For [A], the model predicts the *basal* subset of fibers (those near 1199 Hz) will respond to the modulation peaks in the waveform (panel E). For [B], the model predicts the *apical* subset of fibers (those near 904 Hz) will respond to the modulation peaks in this waveform (panel F). Panels G and H show the number of total spikes in response to a 12.5 msec presentation of [A] and [B] as a function of cochleotopic position and stimulus level. At low-levels, there is a phase dependent shift in activation between [A] and [B] following the position of the electrodes (marked by squares). As level increases, the asymmetric nature of the response decreases with fibers at both cochleotopic positions being activated.

Additional model predictions are shown in panel B of Figure 3-13 for presentations of [A] and [B] on neighboring pairs of bipolar+1 electrodes. For instance, waveform [A] applied to electrode pair 4-2 is denoted [A_{42}]. Collectively, the model makes three predictions for stimuli like [A] and [B]: (1) a human subject will be able to discriminate low-level presentations of [A] from [B] even though these stimuli are spectrally identical and applied to the same bipolar electrode pair. (2) the discrimination will be based on a place cue such that waveform [A] elicits a sensation of higher pitch than that elicited by waveform [B], and (3) comparing presentations on neighboring bipolar+1 pairs of electrodes, as in panels A and B of Figure 3-13, the pitch should

decrease across $[A_{42}]$, $[A_{31}]$, $[B_{42}]$, and $[B_{31}]$.[15]

Results from pitch ranking experiments with four subjects[16] are shown in panel C alongside the corresponding model predictions. Combining across subjects, significantly[17] more (68%, 434/640) presentations of [A] were chosen as higher in pitch than [B] for stimuli presented to the same electrode pair. Had we presented loudness balanced stimuli (e.g., $[A_{31}^{ref}]$ vs $[B_{31}^{ref}]$) in our pitch comparison tests, it is conceivable this percentage might be larger. The most counter-intuitive model prediction, that $[A_{31}]$ would be chosen as higher in pitch than $[B_{42}]$, was not found to be the case as this occurred in only 37% (119/320) of trials after combining data from four subjects.

The bottom three rows serve as a control. Assuming the subject can discriminate the pitch of neighboring bipolar+1 pairs, one expects the pitch of a loudness-balanced stimulus to increase as the electrode pair is shifted basally (e.g., $[A_{31}]$ to $[A_{42}]$). The bottom three rows indicate each subject could discriminate the pitch of these stimuli and, as expected, the pitch increases as the electrode pair shifts basally.

For comparisons examining the influence of level on pitch judgements (e.g., $[A_{42}^{+}]$ vs $[A_{42}^{-}]$), only two presentations showed a significant effect of level on pitch. The first of these was subject one, who chose $[A_{42}^{+}]$ as higher in pitch than $[A_{42}^{-}]$. The second of these was subject four, who chose the lower-level $[A_{31}^{-}]$ as *higher* in pitch than the higher-level $[A_{31}^{+}]$. This is counter-intuitive since typically subjects report the pitch of a higher-level stimulus above that of a lower-level stimulus when asked to make a pitch judgement between two stimuli that differ only in level [42]. Curiously, this subject was the only one of the four to not consistently chose [A] as higher in pitch than [B] when presented on the same electrode pair.

No consistent pattern was found to suggest [A] or [B] elicited a louder sensation when presented at the same level to the same electrode. For instance, it was not the case that the loudness-balanced level of $[A_{31}]$ was always above $[B_{31}^{ref}]$. A complete set of all data is presented in Figure 3-18 of the Appendix.

[15]Enumerating the Clarion electrodes from apex to base, waveform A applied as the apical-most bipolar+1 pair of electrodes (3 and 1) is referred to as $[A_{31}]$.

[16]One subject was eliminated from the analysis because they were unable to discriminate the pitch of stimuli on neighboring electrodes (e.g., $[A_{31}]$ vs $[A_{42}]$). Interestingly, this subject made all pitch comparisons based on level, consistently choosing the *lower* level token as higher in pitch.

[17]Binomial sign test [189], $p << 0.01$.

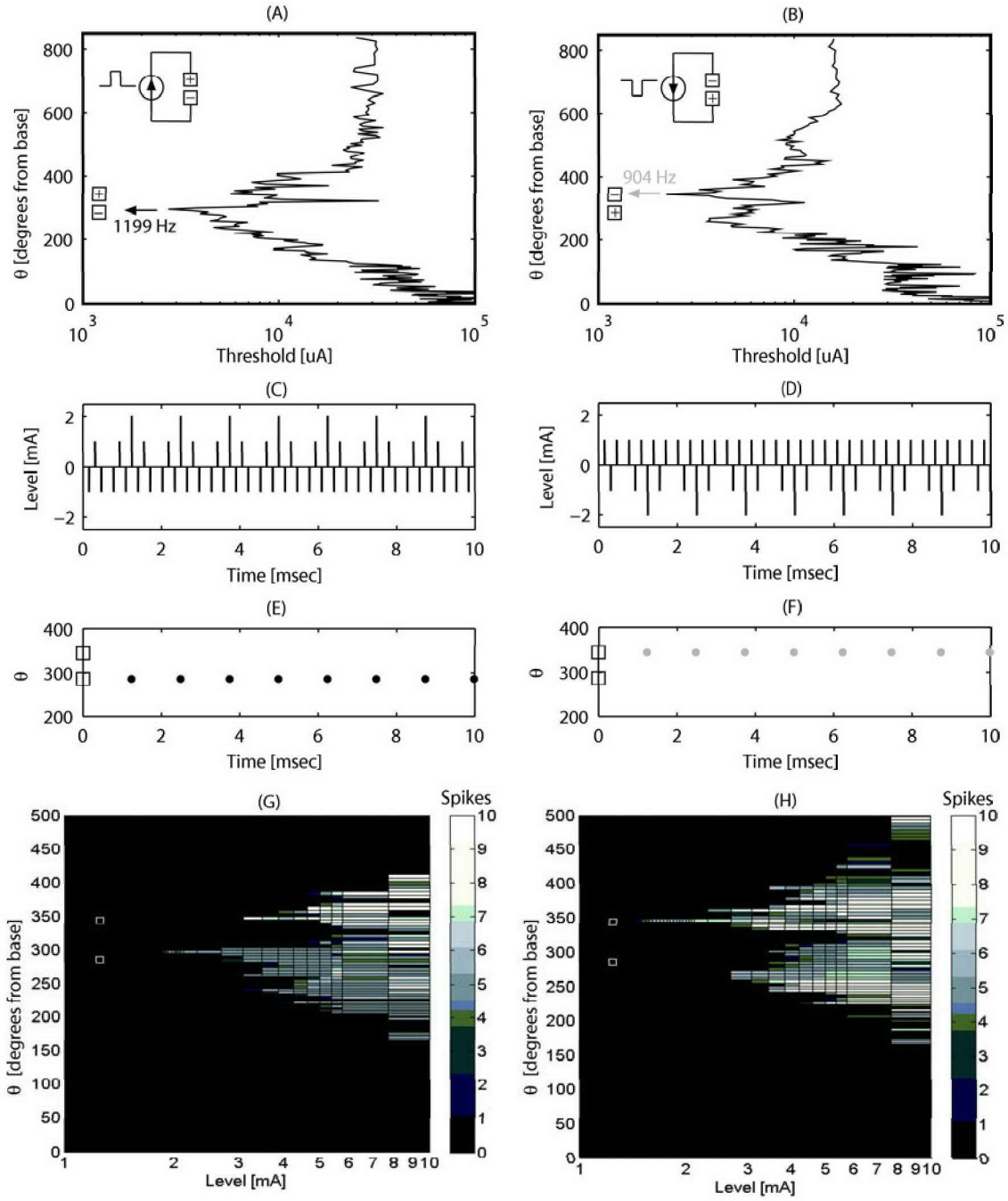

Figure 3-12: Single-fiber threshold as a function of cochlear position (θ) in response to *bipolar* stimulation by: (panel A) a *monophasic* pulse with a cathodic basal electrode, and (panel B) a *monophasic* pulse with a cathodic apical electrode. Note the axis is rotated such that cochlear position appears on the y-axis. Leftward arrows mark lowest-threshold fibers for these two stimuli which are located at two separate cochlear positions, near 1199 Hz (black arrow) and 904 Hz (gray arrow). (Panel C) Waveform [A]. (Panel D) Waveform [B]. (Panel E) Dot-raster prediction of response to [A]. (Panel F) Dot-raster prediction of response to [B]. (Panel G) Total spikes in response to a 12.5 millisecond presentation of [A] as a function of cochleotopic position and level. A level of 1 μA is shown in panel C. (Panel H) Total spikes in response to presentation of waveform [B].

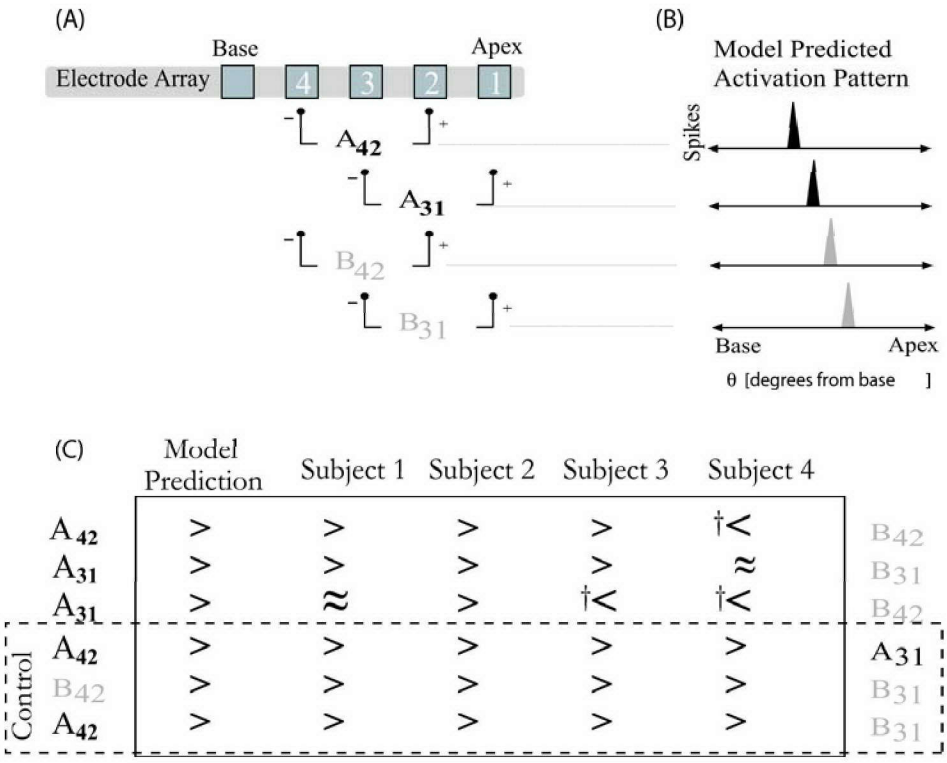

Figure 3-13: (A) Electrode configuration for $[A_{42}]$, $[A_{31}]$, $[B_{42}]$, and $[B_{31}]$. (B) Schematized activation patterns for $[A_{42}]$, $[A_{31}]$, $[B_{42}]$, and $[B_{31}]$ as predicted by the model. Notice these predictions suggest a rank ordering of pitch with $[A_{42}]$ having the highest pitch. Predictions where the basal fiber population responds are colored black, while predictions where the apical fiber population responds are colored gray. (C) Pitch judgements from 4 subjects along with the corresponding model prediction. Entries where the pitch of the left column configuration is judged greater than that of the right column configuration (binomial sign test [189] $p<0.025$) are indicated with $>$. Results that disagree with the model prediction are marked by †. The bottom three rows served as a control, since shifting the same stimulus toward the base ought to increase the pitch.

3.4 Discussion

(I) *Intracochlear potentials and current flow in the inner ear.*
There are several potential pathways for a monopolar current to exit the cochlea, bearing in mind that most current is believed to be carried by interstitial fluids, with only a small percentage crossing cellular membranes [174]. On a macroscopic level, the bony labyrinth is bordered laterally by the middle ear spaces, and posteriorly by the mastoid air spaces, both of which represent high impedance boundaries to any substantial current flow. Additionally, given the relatively large diameter of the bony duct filled with low-impedance perilymph, it is seems unlikely an appreciable amount of intracochlear current crosses into the vasculature to be carried out of the labyrinth by the cochlear artery or (anterior and posterior) spiral veins. Alternatively, the large diameter of the internal carotid artery and internal jugular vein (possibly via the posterior canal) could serve as a local pathway for substantial current.

Using the same terminology as Mens et al. [127], it is useful to divide the exit pathways for a monopolar current into three mutually exclusive categories: (i) that exiting through the internal auditory meatus (IAM) via either the modiolus or vestibular cribrose areas,[18] (ii) that exiting via a nonspecific "basal pathway" described by Kiang [100] and others, and (iii) that exiting by flowing diffusely through the bony otic capsule into adjacent structures. While the last of these (iii) has been considered a high impedance pathway, the finding by Zehnder et al. [231] that the endosteal bone of the human otic capsule contains an extensive network of interconnected canaliculi which communicate with the perilymphatic space makes one curious as to whether this pathway is more viable than originally thought. This discussion will focus on (i) and (ii).

To explain evoked potential recordings made at the round window, Kiang et al. [100] suggested the primary exit for current in the inner ear is located at the base, through the cochlear aqueduct connecting the basal turn to the subarachnoid space, the endolymphatic duct, or through the cochlear windows connecting to the middle ear mucosa. Since the blood supplies of the cochlear windows, middle ear, and temporalis muscle (in which the monopolar return is located) all primarily arise from branchings of the external carotid artery[184], one might hypothesize a low impedance connection via the interstitial fluid spaces connecting these tissues.

Evidence for such a low impedance pathway in the basal turn of the implanted ear does exist. Kasper et al. [94] - whose protocol for measuring intracochlear potentials is essentially identical to ours - showed larger potential gradients[19] for apical than basal stimulation, suggesting both increased longitudinal current flow for an apically stimulated electrode and a basally located current exit. Data from Honrubia et al.

[18]Near their peripheral terminations, all nerve fibers of the inner ear sense organs pass through holes in the bony labyrinth called cribrose or cribriform areas [184].

[19]The difference in potential across recording electrodes.

[84] (their fig 3, p.27) made in the guinea pig also support a basally-located grounding pathway for intracochlear currents flowing to a remote body ground.[20]

The experiments of Mens et al. [128] also support this pathway. Measuring the voltage signature between the ipsilateral (+) and contralateral mastoid (-) of Nucleus users, they presented bipolar pulses using an anodic[21] electrode fixed at the base, and a cathodic electrode that was advanced from the base to apex. To the extent the cochlear spiral behaves as a near-perfectly insulated tube, open to extracochlear fluid only at the basal end, this potential difference ought to be strictly positive and monotonically increasing. To the extent the cochlear spiral behaves as if encased in an electrically-porous material, this potential difference ought to be non-monotonic, oscillating to reflect the rotating axis of the dipole moment created by the advancing cathodic electrode. In non-otosclerotic patients, Mens et al. noted that the inter-mastoid potential difference was both exclusively positive and increased monotonically as the cathode advanced toward the apex (data replicated in panel A of Figure 3-14). This suggests a low impedance electric coupling between the cochlear base and the ipsilateral mastoid, specifically via the "basal pathway" mentioned above. In the two patients with otosclerosis, the inter-mastoid potential difference was non-monotonic as the cathodic electrode was advanced (data replicated in panel C of Figure 3-14). The authors postulated the non-monotonicity indicates considerable current exiting through the otic capsule.

In the psEAM, current exits the model exclusively through the medial aspect of the internal auditory meatus (IAM), (ii) above. The rational behind this choice lies in the supposition that the fenestrated bone of the modiolus bathed in perilymph, together with the internal auditory canal, provides a low impedance pathway for current to exit the otic capsule. Empirical evidence in support of this also exists. In the guinea pig, Spellman et al. [198] reported the magnitude of the impedance between an intracochlear and IAM electrode to be less than 1.5 times higher than the impedance between an apical and basal intracochlear electrode. Likewise, using samples of fixed human cochlear bone, Ifukube et al. [87] measured the resistance of a modiolar sample to be 2 orders of magnitude lower than of an interscalar septum sample.

This pathway is supported by the fluid communication between the scala tympani and modiolar structures. For example, Schuknecht et al. [183] describe small openings, canaliculi perforantes, in the tympanic rim of the osseous spiral lamina of the cat, allowing continuity of perilymph with the fluid spaces of the organ of Corti. More recently, Glueckert et al [61] described the ultrastructure of the human spiral ganglion, harvested from normal hearing patients undergoing surgery for life-threatening petroclival meningioma. Using scanning electron microscopy, they found

[20] Although the bulla of guinea pig protrudes into the middle ear space, making this comparison more tenuous because the apical turns of the otic capsule are surrounded by air.

[21] Here polarity refers to the first phase of the biphasic pulse.

Rosenthal's canal to have a thin bony wall separated from the scala tympani by a fragile network of highly-trabeculated endosteal bone, and a thin (< 1 μm) layer of mesothelial cells that line the perilymphatic space. Also reported were perforations in these mesothelial sheets (in earlier studies thought to be processing artifact) that allow a communication route between scala tympani and modiolar fluid spaces.

Especially in ears where the electrode appears to penetrate the basilar membrane providing a communication for electric current between the fluids of separate scala, the continuity of the perilymphatic space[22] from the scala vestibuli into the vestibule and semicircular canals suggests current may exit the bony labyrinth via the vestibular apparatus. At least theoretically, a monopolar current introduced inside the bony labyrinth may enter the internal auditory meatus via either the cochlear modiolus, or the cribrose areas through which the branches of the vestibular nerve communicate with the vestibular labyrinth.

The close fit of the psEAM intracochlear potentials for apical stimulation in panel C of Figure 3-2, suggests the IAM grounding pathway is a reasonable first approximation, at least for stimulation with an apical electrode. Using the IAM ground, the observation that the fit is more dissimilar for basal stimulation suggests another lower impedance path in the base for which we have not accounted. As shown in Figure 3-4, adding a round window ground to the psEAM tends to better the fit by lowering the gradients generated by a basally stimulated electrode (EL6).

Bone resistivity of the optic capsule.

Recently, Micco [131] used the four-electrode reflection-coefficient method described by Suesserman [203] to report that the resistivity of the modiolus was lower from 427 Ωcm in the normal gerbil cochlea to 288 Ωcm after substantial neural degeneration had occurred. Several lines of evidence suggest the endosteal bone of the otic capsule has a bulk resistivity higher than the roughly 600-Ωcm value used in previous models, making it a high impedance to intrascalar current.

First is the comparison of the otic capsule to the morphology of other bone. Bone is essentially a collagen matrix in which calcium crystals (hydroxyapatite) are deposited, typically characterized in other parts of the body as either compact (cortical) or cancellous (trabecular), for both of which dielectric properties have been measured. Saha et al. [181] measured wet cancellous and cortical bone in human specimens, finding cancellous bone to have resistivities near 500 Ωcm while cortical bone had resistivities between 1.5 and 10 kΩcm depending on the specimen orientation. In other experiments, the conductivity of bone has been found to be less than 1 % of the suspension solution [103], even though the fluid phase occupies 15-20% of the volume,

[22]Note also the lacuno-canalicular system described by Zehnder [231] supports a low impedance electrical coupling between the scala tympani and scala vestibuli, without considering the connection of these at the helicotrema.

implying the spongy composition of the bone architecture significantly decreases it's effective conductivity. Moving away from the wall of the scala, the bone of the otic capsule is comprised of the endosteal, enchondral, and periosteal layers. Given that the resistivity of bone is thought to be determined mostly by the fluid phase [103], and the petrous bone housing the otic capsule is among the hardest bones in the body (having bone mineral density comparable to that of cortical bone[139]), before any measure is made it seems unlikely that resistivity would be near that of cancellous bone.

Second, our IP_p experiments suggest a 1:100 ratio of fluid-to-bone resistivity is needed to account for intracochlear potentials (see Figure 3-2). In modeling the data of their inter-mastoid potential recordings using a boundary element model, Mens el al. [127] came to precisely the same conclusion, namely that the "model using a high resistivity ratio (1:100) between the bony and the other compartments [of the inner ear] was the only one that produced outcomes similar to the potentials observed in non-otosclerosis patients."

Using the bEAM, we can reproduce the experiments of Mens et al. [128, 129] if we assume the potential of the contralateral mastoid is near zero, that is, the same as the rest of the body, and that the potential of the ipsilateral mastoid is closely coupled to that of the cochlear windows by the inner ear mucosa. Shown in the right column of Figure 3-14 are potentials predicted by the bEAM at the stapes footplate while apically advancing a cathodic electrode paired with a basal anode fixed at EL6. Analogous data to the Mens et al. "advancing cathode" experiment are shown using the standard bEAM with 5-kΩcm bone in panel B, and the bEAM with 600-Ωcm bone in panel D. The similarity to the Mens el al. data is apparent in both, with the 600-Ωcm model representing the oscillations seen in otosclerotic[23] and possibly pagetic [24] ears.

[23]Grayeli [64] et al. found significantly lower bone mineral densities (BMDs) around the bony labyrinth in otosclerosis patients than in a control population using CT scanning.

[24]A similar porous bone model might be considered for the temporal bone in patient's with Paget's disease. For instance, using CT scanning Monsell et al. [139] measured decreased bone mineral densities in the pagetic ears, suggesting a lower resistivity.

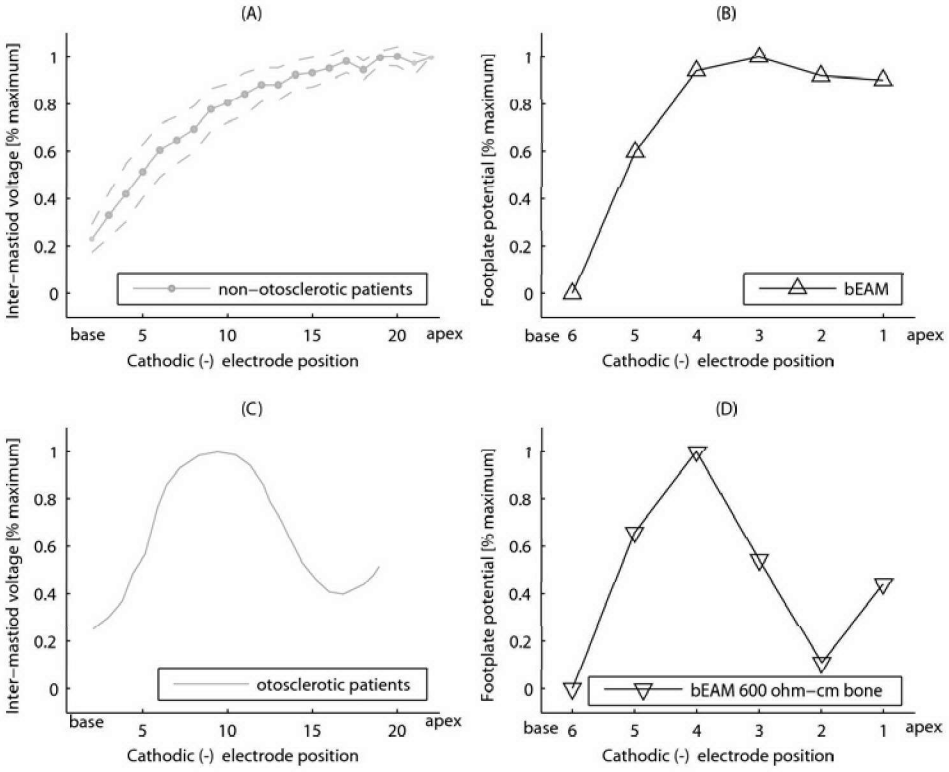

Figure 3-14: (A) Data from Mens et al. ([129], figure 3B) showing the voltage signature between the ipsilateral (+) and contralateral mastoid (-) of non-otosclerotic Nucleus users, while presenting bipolar pulses using an anodic (here polarity refers the first phase of the biphasic pulse) electrode fixed at the base (electrode 1), and a cathodic electrode that was advanced from basal electrode 2 to apical electrode 22. Dashed lines represent plus and minus one standard deviation across 21 patients. To the extent the cochlear spiral behaves as a near-perfectly insulted tube, open to extracochlear fluid only at the basal end, this potential difference ought to be strictly positive and monotonically increasing. (C) Data from Mens et al. ([127] their figure 1A) showing the voltage signature between the ipsilateral (+) and contralateral mastoid (-) of a Nucleus user with otosclerosis. (B) Potential measured in the bEAM at the stapes footplate while apically advancing a cathodic electrode paired with a basal anode fixed at EL6. By definition this potential is zero for the cathode at the basal EL6 position. (D) Potential at the footplate using a bEAM with 600-Ωcm bone.

Psychophysical thresholds

As mentioned in the introduction, there are serval reasons the model may fail to predict the measured psychophysical data, including (1) the model's representation of the anatomy, or calculation of a neural response, may be intrinsically flawed, and (2) the model may accurately predict intracochlear spike-patterns, but the model linkage between the spike-pattern and psychophysical response may be inappropriate.

Since the model was modestly successful at predicting both IP_d and $ECAP_d$ data, it seems likely that the linkage used to couple spike-patterns with psychophysical thresholds (2 above) needs refinement. The criterion to define behavioral threshold (ψ) relies on an assumption that sensation level is related to the sum of the spikes produced in the auditory nerve, a common assumption Relkin and Doucet [175] termed the "spike-count hypothesis." The aforementioned later presented evidence against the spike-count hypothesis, at least for the wide span of loudness intensities in acoustic-hearing animals.

Using our ψ criterion also implies that the spatial distribution of recruited neurons is irrelevant to the perceptual detection task, a concept that is thought to be false in the normal ear. With normal hearing subjects, psychophysical threshold and loudness percepts are often explained in the framework of an auditory filter-bank (see [140] for review). Near threshold, it has been suggested that sound energy within an auditory filter is completely integrated, while sound energy within adjacent filters is not. Consequently, the threshold level for detecting a narrowly spaced tone-complex falling in a single auditory filter will be lower than that of a similar tone-complex with widely spaced frequency components falling in adjacent auditory filters [58, 80]. If the concept of an auditory filter is applied to the psychophysics of electric hearing, then we expect the recruitment of ψ closely spaced model fibers to induce a different psychophysical percept than the recruitment of ψ model fibers dispersed over a wide range of cochleotopic positions.

Lastly, we did not take into account the stochastic nature of neural discharges, nor morphological variations across the residual ganglion population. For instance, to the extent that diameter variation in the constituent fibers at any cochleotopic position exists, one also expects variation in single-fiber threshold. Considering the data of Nadol et al. [147] suggests variation in the diameter of human afferent fibers on the order of 31 percent of the mean diameter[25]), and Rubinstein's [177] derivation that threshold is inversely proportional to the square of fiber diameter for myelinated nerves, a range of greater than 5 dB in threshold spread is predicted by the Nadol diameter data. Similarly, Van den Hornert et al. [213] used a version of the McNeal

[25]Nadol et al. ([147] their Table II) measured the diameters of the axonal and peripheral segments in man. Calculating the average coefficient of variation (standard deviation divided by the mean) for the Nadol data, one estimates a variation in diameter of 28.9 and 34.8 percent of the mean for the axonal and dendritic sections, respectively.

model [125] to suggest that a 2:1 ratio of fiber diameters would account for a spread of thresholds between 8.3 and 12 dB depending on the distance to the electrode. While these are approximations, the point remains that diameter variation may have a substantial impact on the variance in SFT at any cochleotopic position.

To address the impact of stochastic effects on the psEAMs T_d predictions, we utilized a model similar to Bruce et al., [21, 23, 22] who studied the expected number of discharges in a stochastic model of the auditory nerve. In the psEAM, the function describing the total number of spiking neurons, $S_t(x)$, is a piecewise constant function of level x with incremental increases of $N_{f(i)}$ when fiber i is recruited (see Figure 3-15). At levels below the lowest SFT, the function

$$S_t(x) = \int_0^x \sum_i N_{f(i)} \delta(x - \mu_{s(i)}) dx \tag{3.3}$$

abruptly goes to zero, where $\mu_{s(i)}$ is the single-fiber threshold of model fiber i and δ is the Dirac delta function. Using our ψ criterion, T_p was taken as the minimum level x that satisfies $S_t(x) > \psi$.

If we instead treat each spike occurrence as stochastic, the firing efficiency, which describes the probability that a neuron discharges in response to a single pulse, changes from near zero to unity as the stimulus level increases over a few dB range from below to above the neurons's "threshold" - which is typically taken as the level that elicits a firing efficiency of 0.5 [41, 178]. This description is rooted in the observations of membrane noise first described by Verveen [219, 220, 218], and modeled by Clay and DeFelice [29] and later by Rubenstein [178]. The sigmoidal-shaped firing efficiency function is fit with a cumulative distribution function $F_X(x) = Pr(X < x)$, typically an integrated gaussian, where $f_X(x)$ is the underlying normal probability density function.

$F_{X|\mu_s}(x|\mu_{s(i)})$ describes the probability of model fiber i discharging at level x, where the parameter $\mu_{s(i)}$ is the SFT predicted by the deterministic model. Further assuming a range of thresholds for fibers at a common θ,[26] the function $F_{X|\mu_s}(x|\mu_{s(i)})$ is further smoothed, that is, made more shallow, exhibiting a higher degree of relative spread. The total expected number of discharges,[27] $D_t(x)$, becomes

$$D_t(x) = \int_0^x \sum_i N_{f(i)} f_{X|\mu_s}(x|\mu_{s(i)}) dx \tag{3.4}$$

[26]For instance, due to diameter differences where threshold varies inversely with fiber diameter [125, 224, 2]

[27]Here we intentionally adopt the terminology "discharge" to denote the number of *expected* neurons conducting an action potential in a probabilistic sense, while we use the term "spikes" to denote the *deterministic* number of neurons conducting an action potential in the psEAM. Accordingly, as a function of level x, the total expected discharges $D_t(x)$ is a smooth function, while the number of spikes $S_t(x)$ is a stepwise continuous function incrementally increasing by $N_f(i)$ after each model fiber i is recruited.

where the density function $f_X(x|\mu_{s(i)})$ was described earlier in Chapter 2.[28]

Comparisons of the stochastic $D_t(x)$ (solid lines) and deterministic $S_t(x)$ (broken lines) obtained using the Ineraid psEAM are shown in Figure 3-15 for stimulation by EL6, EL4 and EL2. At low levels the expected total activity is strikingly similar for the stochastic. As pointed out by Bruce et al. [23], this suggests that at very low levels, the function describing the increase in the expected number of discharges with level is dominated by the relative spread contributed by a small number of neurons.

The ψ criterion of 150 spikes/discharges is illustrated in Figure 3-15 with the shading such that T_p is illustrated as the level that either $D_t(x)$ or $S_t(x)$ rises above the horizontal edge of shaded area. The T_p values for the deterministic EL6 (black $\downarrow$) and EL2 (red $\downarrow$) are separated by more than 4 dB while, for the same ψ criteria the stochastic T_p values for EL6 (black $\uparrow$) and EL2 (red $\uparrow$) are separated by less than 0.7 dB. At lower ψ criteria, e.g., 10 discharges, the separation between the stochastic T_p values for different electrodes shrinks to less than half a decibel. While it is difficult to specify what, if any criterion ψ number of spikes/discharges might elicit a detectable psychophysical percept, studies done on tactile perception have found perceptual threshold to occur after stimulating only a single tactile afferent fiber [212], suggesting ψ to be relatively small.

The behavior described in Figure 3-15 is due to the observation that at low levels the slope of $D_t(x)$ is dominated by the slope of $F_{X|\mu_s}(x|\mu_{s(i)})$ in equation 3.4, as opposed to at higher levels where the slope is dominated by the distribution of single-fiber thresholds as in the deterministic $S_t(x)$.[29] This suggests the psEAM may be more likely to predict data at stimulus levels higher than those of psychophysical thresholds, for instance, the level at which the ECAP is first recorded. These typically fall closer to a patient's maximum comfortable level (MCL) than threshold level [24].

[28]Briefly, the deterministic SFT for fiber i can be interpreted probabilistically as $\delta(x - \mu_{s(i)})$, a density function with zero variance centered on $\mu_{s(i)}$. Convolving this with an appropriate Parzen window, or kernel, allows us to simulate the stochastic model described by Bruce et al. [23] (see, p.84).

[29]This agrees with the interpretation of Bruce et al., who suggested that at very low levels, the function describing the increasing expected number of discharges with level is dominated by the relative spread (RS) contributed by a small number of neurons as opposed to the distribution of fiber thresholds.

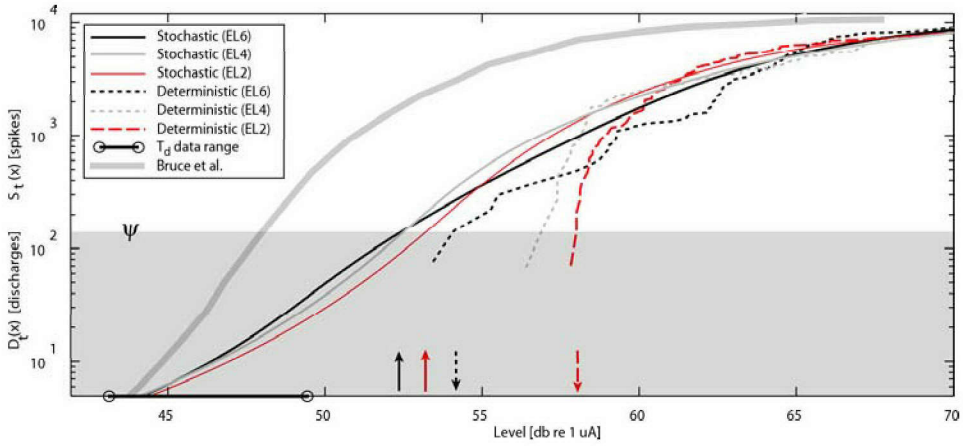

Figure 3-15: Stochastic $D_t(x)$ (solid lines) and deterministic $S_t(x)$ (broken lines) as a function of level x obtained using the Ineraid psEAM for stimulation by EL6 (black), EL4 (gray) and EL2 (red). A ψ criterion of 150 neurons is illustrated with the shading, such that psychophysical threshold T_p is illustrated as the level that either $D_t(x)$ or $S_t(x)$ rises above the shading. The T_p values for the deterministic EL6 (black $\downarrow$) and EL2 (red $\downarrow$) are separated by more than 4 dB while, using the same ψ criteria, the T_p values for the stochastic EL6 (black $\uparrow$) and EL2 (red $\uparrow$) are separated by less than 0.7 dB. At lower ψ criteria, e.g., 10 discharges, the separation between the stochastic T_p values shrinks to less than 0.5 dB. For comparison, the range of archival T_d from the Ineraid patient is shown by the black horizontal line on the x-axis after converting from nC of charge per phase to the current level of a 30 μs pulse delivering the same charge per phase.

(III) *Electrically-evoked compound action potentials (ECAPs).*

The most counter-intuitive model result is that fibers located at cochlear positions spatially removed from that of the stimulating electrode will contribute a similar characteristic biphasic (N1P1) waveform to the ECAP. In the model, this results in similar waveform morphologies across recording electrodes, such as those in Figure 3-6. As mentioned in the last chapter, if the psEAM volume conduction model is replaced with a homogenous model, erratic differences in waveform morphology will be predicted for different recording electrodes. This finding that the biphasic morphology of the N1P1 response is independent of recording electrode is not new, and fits with the earlier model proposed by Kiang et al.[100] to describe single-unit contributions to the round window potential obtained by spike triggered averaging.[30] In our simulations, because the pattern of activated neurons is spread along a wide length of cochleotopic positions, and because fibers contribute a similar morphology to the ECAP, the detailed distribution of surviving neurons across θ makes little difference, while the total number of surviving neurons does.

Comparing our ECAP predictions to those reported by Briaire and Frijns [13], we note that we did not find non-monotonic ECAP growth functions, and that the latency of the N1 and P1 peaks appear more consistent with the measured data, irrespective of the fact that we used a simplified morphology to represent the auditory nerve fiber in our formulation of the single-fiber model (see section 2.4). After addressing the remaining issues in the volume conduction model (i.e., which set of grounding conditions to use) to better the fit between the IP_d and IP_p, we plan to turn our attention to incorporating a more realistic neural model to account for the influence of morphology as suggested by Rattay [170] and others.

Finally, to analyze the ECAP growth functions across different stimulating electrodes, we use the phenomenological model introduced in the last chapter describing N1P1 growth M_{N1P1} as,

$$M_{N1P1}\left[\frac{\mu V}{\text{dB}}\right] = \delta_{SFAP}\left[\frac{\mu V}{\text{neuron}}\right] \cdot N_l\left[\frac{\text{neurons}}{\text{mm}}\right] \cdot R_l\left[\frac{\text{mm}}{\text{dB}}\right] \tag{3.5}$$

where δ_{SFAP} is the increase in N1P1 per neuron, N_l is the average number of neurons per millimeter of cochleotopic length, and R_l is the longitudinal spread of fiber recruitment per dB increase in the stimulus above threshold. Measuring N1P1 growth, M_{N1P1}, on a decibel scale $\left[\frac{\mu V}{\text{dB}}\right]$ is designed to remove differences in the slope of the ECAP growth function due to sensitivity differences across stimulating electrodes. The motivation for this is to use measures of M_{N1P1} to estimate R_l, via equation 3.5.

[30] Here the contribution of a single fiber to the gross potential recorded at the round window is estimated by averaging thousands of epochs centered in time around the arrival of a spontaneous spike in an isolated fiber of the auditory-nerve (see [100, 221]).

This cannot be done unless variations in M_{N1P1} due to differences in threshold are removed.

When expressed as a function of absolute current $[\mu A]$, the ECAP threshold $[\mu A]$ and the slope of the growth function $\left[\frac{\mu V}{\mu A}\right]$ have been suggested in the literature to be anti-correlated [16, 135]. This trend is also seen in the Ineraid data set, as shown in panel A of Figure 3-16, where typical $ECAP_d$ growth functions are plotted as a function of absolute level. The $ECAP_d$ threshold, arbitrarily taken as the level to elicit a 100 μV response, accounts for 46 percent of the variance in the slope of ECAP growth (panel B). Converting to a decibel scale tends to remove this correlation (panel C).[31]

On a decibel scale, comparing the $ECAP_d$ threshold and slope (M_{N1P1}) values to those predicted by the psEAM, one finds a strong correlation between the threshold measures (panel D), and a weak correlation for the M_{N1P1} slope measures (panel E).[32] Note that the correlation between the measured and model-predicted ECAP thresholds in panel C is the result of one stimulating electrode (EL6 $\diamondsuit$) having an elevated threshold. As one might expect, this electrode (EL6) also had the highest measured psychophysical value (T_d), in agreement with the reported correlation between ECAP and the psychophysical threshold levels [18, 19].

While the correlation between the M_{N1P1} slope measures is not outstanding across all stimulating electrodes, it is impressive that the model-predicted M_{N1P1} values fall in the correct range. Replotted as a function of recording electrode in Figure 3-17 are psEAM-predicted M_{N1P1} values, bEAM-predicted M_{N1P1} values, and the M_{N1P1} values taken from the Ineraid data set. Also shown is the 66.0 $\pm$ 53.4 $\left[\frac{\mu V}{\mathrm{dB}}\right]$ range of M_{N1P1} estimated from the 141 subjects of the Cafarelli-Dees study [24].

Note the M_{N1P1} values from both the $ECAP_d$ data set and the psEAM-predicted $ECAP_p$ fall within the Cafarelli-Dees range, while the bEAM, which has a full complement of 30,000 neurons, predicts M_{N1P1} values *above* this range. Averaging across all stimulating and recording electrodes, the mean M_{N1P1} value is 52.0 $\left[\frac{\mu V}{\mathrm{dB}}\right]$ for the measured $ECAP_d$ data, 50.5 $\left[\frac{\mu V}{\mathrm{dB}}\right]$ for the psEAM prediction,[33] both of which fall just below the mean of 66 $\left[\frac{\mu V}{\mathrm{dB}}\right]$ of the Cafarelli-Dees range. The total spiral ganglion count of 10,248 in the Ineraid psEAM also falls close to the mean SGC count of 8,705 reported in studies of the implanted temporal bones at our institution [98], although

[31] This is consistent with the supposition that (1) the distribution of single-unit thresholds determines the ECAP growth, and this distribution takes on a roughly lognormal distribution such that (on an absolute scale) ECAP threshold and slope are inversely related.

[32] Alternatively, we could fit both the model and empirical ECAP growth functions with sigmoids derived from the lognormal distribution, then compare the lognormal parameters μ_{ln} and σ_{ln} which would represent the threshold and slope respectively.

[33] However, caution must be used in interpreting this result, since in this phenomenological framework an accurate estimate can be made of the product $(\delta_{SFAP} \cdot R_l)$ using two inaccurate estimates of δ_{SFAP} and R_l. For instance, simultaneously underestimating δ_{SFAP} while overestimating R_l will still return an estimate of M_{N1P1} that matches that measured from the Ineraid data.

any relationship between these two observations remains, at this point, speculative. However, it is conceivable that SGC count could account for a large percentage of variation in ECAP slope seen by Caferelli-Dees and others.

Using equation 3.5, an estimate for the longitudinal recruitment with level, R_l, can be made using a psEAM-derived estimate for N_l $\left[\frac{\text{neurons}}{\text{mm}}\right]$ and parameter estimates for δ_{SFAP} $\left[\frac{\mu V}{\text{neuron}}\right]$ taken from the previous chapter. Over the basal 25 millimeters of the Ineraid psEAM the average number of neurons per millimeter, N_l, is approximately 399 $\left[\frac{neurons}{\text{mm}}\right]$.[34] In the last chapter, δ_{SFAP} was estimated from various animal physiological studies to fall in the range 0.083 - 0.24.[35] The estimated range of recruitment becomes

$$R_l = \frac{M_{N1P1}}{\delta_{SFAP} \cdot N_l} = \frac{52}{(0.083 \rightarrow 0.24) \cdot 399} = 1.57 \rightarrow 0.54 \left[\frac{\text{mm}}{\text{dB}}\right]. \qquad (3.6)$$

This agrees with the range of R_l reported in the last chapter.

[34] Averaging over the entire cochlear length gives an estimate of N_l of 300 $\left[\frac{\text{neurons}}{\text{mm}}\right]$

[35] The bEAM predicts a value of 0.062, $\left[\frac{\mu V}{\text{neuron}}\right]$, see Table 2.9. Note the maximum elicited N1P1 in the Ineraid data set was 630 μV, suggesting that if this represents all neurons responding with minimal cancelation, then each neuron would contribute at least 0.0615 μV. Using the terminology of the last chapter, this suggests $\check{\delta}_{SFAP}$ =0.0615 [μV/neuron].

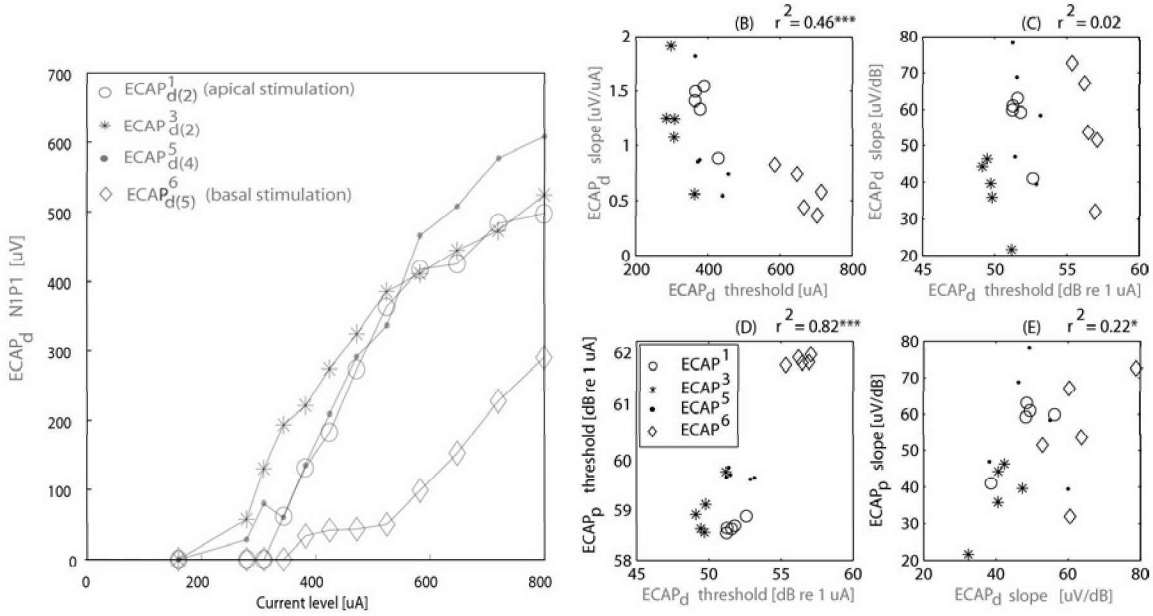

Figure 3-16: (A) $ECAP_d$ growth as a function of level for four typical stimulating/recording configurations. Note stimulating with EL6 (♢) has the highest threshold and the shallowest slope. (B) Plotting the $ECAP_d$ slope measured in $[\mu V/\mu A]$ (averaged above the threshold level) versus $ECAP_d$ threshold (the level to elicit a 100 μV response) shows that up to 46 percent of the variance in slope is explained by the threshold measures. (C) Replotting the $ECAP_d$ threshold and growth function slope M_{N1P1} on a relative scale [dB re 1 μA] shows the correlation is removed. (D) Comparison of $ECAP_d$ and $ECAP_p$ threshold levels. (E) Comparison of $ECAP_d$ and $ECAP_p$ estimates of M_{N1P1}. In all panels, statistical significance of the r^2 value is indicated above the panel with asterisks: $p < 0.05^*, p < 0.01^{**}, p < 0.001^{***}$.

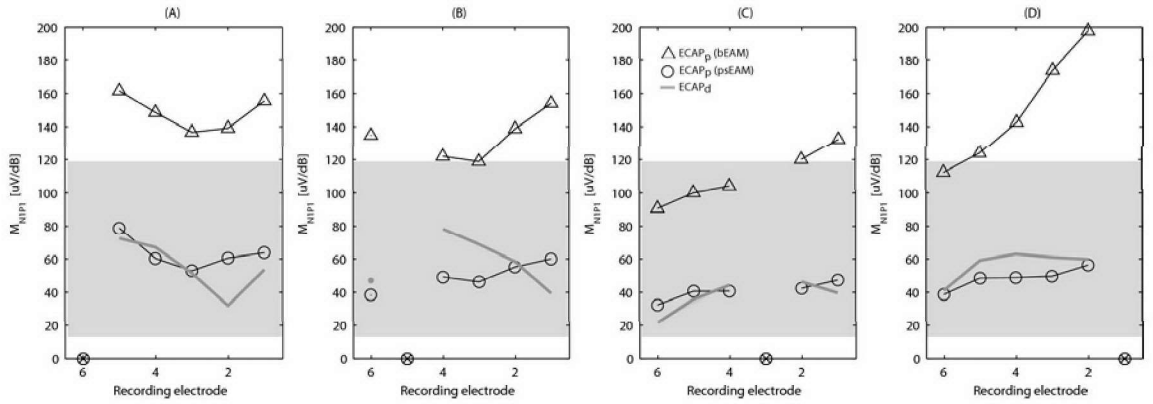

Figure 3-17: Estimate of the ECAP growth M_{N1P1} taken from the Ineraid data $ECAP_d$ (gray), the psEAM-predicted $ECAP_p$ (open circles), and the bEAM-predicted $ECAP_p$ (triangles). The range of M_{N1P1} derived from Cafarelli-Dees [24] in the last chapter is shown by the shading.

(IV) *Psychophysical data from current Clarion users.*

Our interpretation of the collected psychophysical data is that the two electrodes used as a bipolar pair recruit two groups of neurons that, to some marginal extent, do not overlap in cochleotopic position and therefore should elicit a different pitch if stimulated individually. It appears this effect is present, albeit not salient enough for our subjects to easily use it as a cue. This emphasizes the utility of a quantitative EAM capable of predictions that would not be made otherwise. While it is clear that implants provide both a place and temporal cue, both of which influence pitch perception [42, 123], we have assumed the difference in $[A]$ and $[B]$ was purely a place cue. While it is theoretically possible that the two waveforms elicit different temporal cues, although this seems unlikely since the waveforms differ only in polarity and are thus spectrally identical.

Comparing presentations where the same stimulus waveform was presented (i.e., $[A_{42}]$ vs $[A_{31}\ ]$ and $[B_{42}]$ vs $[B_{31}]$, Figure 3-13 bottom rows), in 92 % of all trials the more basal electrode pair (4-2) was consistently selected as higher in pitch, as one would expect. However, when $[B_{42}]$ vs $[A_{31}]$ was presented, this percentage was lowered significantly[36] to 68%, suggesting the waveform cue ($[B]$ *vs* $[A]$) may have partially canceled the place cue due the electrode position (4-2 vs 3-1).

Had we tested loudness balanced pairs (e.g., $[A_{42}^{ref}]$ vs $[B_{42}^{ref}]$) instead of a pair of stimuli above and below the level of subjective loudness (e.g., $[A_{42}^{-}]$ versus $[B_{42}^{+}]$) the waveform effect might have been more noticeable, although this would had obscured the interpretation of our results since it would allow for a subtle imbalance of the loudness procedure to influence the pitch judgements. For instance, no matter how carefully $[A_{31}^{ref}]$ was loudness balanced to $[B_{31}^{ref}]$, small differences in loudness could be reported as a pitch difference. It is also possible the "comfortably soft level" at which our subjects performed the discrimination task was above the level at which the model-predicted asymmetry in Figure 3-12 is significant.

We did not investigate whether the detection threshold to either waveform [A] or [B] was lower than the corresponding unmodulated pulse train of the same amplitude and pulse rate, although using asymmetric pseudo-monophasic pulses, Macherey el al. [119] showed psychophysical thresholds deceased by as much as 10 dB presumably due to the delay in charge recovery. Considering our results, one might question whether the delayed pseudo-monophasic waveform[37] used by Macherey might elicit a different pitch percept when the polarity of the waveform applied to a bipolar electrode pair is inverted.

[36] $\chi^2 test, p < 0.001$

[37] The delayed pseudo-monophasic waveform is composed of a short, high-amplitude pulse followed, after a delay, by a longer (e.g. 8x) duration pulse with a lower (e.g. 1/8) amplitude.

3.5 Chapter synopsis

Intracochlear current flow

In this chapter a collection of patient-specific model predictions are tested against empirical data to verify which aspects of the modeling process provide reliable predictions and which aspects need refinement.

The predictions of intracochlear potentials (IP_d) show a promising correspondence to measured intracochlear recordings (IP_d), suggesting the model is capable of representing the key electrical and dimensional aspects of the tissue structures that govern current flow in the implanted ear. While some issues remain; for instance, the proportion of a monopolar current that exits the cochlear labyrinth via the round and oval windows versus the internal auditory meatus, overall the model predicts the data to an extent we feel comfortable using it to further investigate the peripheral anatomy's impact on intracochlear current flow (see Chapter 4).

ECAP prediction

Another powerful result in support of the model's ability to predict current flow is the prediction of realistic ECAP waveforms whose amplitudes change as the recording electrode is moved, while the basic N1P1 morphology remains the same. For instance, in the previous chapter it was shown that a homogenous model will predict an ECAP morphology dependent on the position of the recording electrode. Even more supportive of the model's predictive capability is that for half the stimulating electrodes tested (EL6 and EL1), the psEAM-derived ECAPs were able to predict empirically-measured variations in the N1P1 amplitude across recording electrodes.

The magnitude and growth of the psEAM-predicted $ECAP_p$ waveforms agree with both archival data recorded from the Ineraid patient, as well as reports of ECAP growth in the literature. It is noteworthy that the bEAM (with its full complement of 30,000 neurons) predicts ECAP growth (M_{N1P1}) *above* the range found in the literature for human subjects. One might expect this since nearly all implanted patients have a below-normal number of residual spiral ganglion cells.

These ECAP results are especially striking considering the simplified morphology (see p.57) used in the formulation of the single-fiber model. Not only does the single-fiber model neglect to represent the cell body, it relies on a list of assumptions, several of which are likely to be violated.[38] For an ECAP waveform to be successfully predicted, several sequential computations must work in concert, with errors in any stage likely to give spurious waveforms unlikely to match the measured $ECAP_d$ data.

[38]See Section 4.2.1 of the next chapter, or for examples see Plonsey [162], Plonsey and Barr [5], Barr and Plonsey [4], and Trayanova et al. [209, 208].

Psychophysical predictions

In terms of predicting psychophysical data, the models were, in general, less successful. One notable exception is found in the predictions of psychophysical threshold in the Nucleus model, where one electrode pair (EP19) is predicted to have a T_p value nearly twice that of the other electrodes, in accordance with the archival behavioral data.

Of the subject data available, the psychophysical data is the furthest removed from the patterns of current flow and auditory-nerve activity the model is designed to predict. However, because behavioral data such as threshold are available for most of the temporal bones, these data represent a potentially important comparison to test the psEAM predictions of relative sensitivity across stimulating electrodes. There are several possible explanations for the relatively poor correspondence between T_p and T_d data. First is that the simple heuristic relating the predicted spike pattern to a psychophysical percept (i.e., the ψ criterion) is inappropriate. For example, if perceptual detection occurs with the activation of only a few neurons, it may be that stochastic influences dominate and therefore need to be incorporated in a model in order to predict T_d data. It is also possible that the aspects of the peripheral anatomy modeled may not be major factors influencing the variation in behaviorial threshold across stimulating electrodes.

Of the archival data currently available, the intracochlear potentials IP_d and $ECAP_d$ are the most strongly linked to the periphery. Accordingly, a model that successfully predicts IP_d and $ECAP_d$ data is likely to correctly predict the spike pattern elicited by electrical stimulation, even though it may fail to predict psychophysical data due to, for instance, an inappropriate linkage between a spike pattern and the psychophysical percept it elicits. Accordingly, future testing and refinement should focus on the ability of the Ineraid psEAM to predict IP_d and $ECAP_d$ types of data, as well as other archival ECAP data collected from the Ineraid patient such as ECAP masking and recovery.

Collectively, the results suggest the model is appropriate for predicting the influence of the tissue structure and conductive inhomogeneity on intracochlear current flow in the implanted ear. In the next chapter we use this modeling approach to make predictions regarding which anatomical attributes have a significant impact on the predicted current flow, and are thus likely to impact the neural activation elicited by a cochlear implant.

3.6 Appendix: Chapter 3

(A) SUBJECT [#]		(B) TOKEN 2 [%] A[4 2]	(C) A[3 1]	(D) B[4 2]	(E) LEVEL [%]	(F) TOKEN(+) [uA]	(G) TOKEN (-) [uA]
1	A[4 2]				0.8*	538	520
	A[3 1]	.9*			0.65	472	455
	B[4 2]	.98*	0.56		0.5	596	558
	B[3 1]	.96*	.83*	.9*	0.4	528	500
2	A[4 2]				0.65	730	713
	A[3 1]	0.65*			0.5	766	740
	B[4 2]	0.79*	0.89*		0.7	703	680
	B[3 1]	1*	1*	0.95*	0.5	639	563
3	A[4 2]				0.7	636	522
	A[3 1]	0.988*			0.3	543	471
	B[4 2]	0.635*	0.025*		0.55	655	521
	B[3 1]	0.988*	0.644*	1*	0.5	515	481
4	A[4 2]				0.3	116	90
	A[3 1]	1*			0.4	145	128
	B[4 2]	0.025*	0.012*		0.15*	116	86
	B[3 1]	1*	0.525	1*	0.5	153	147
5	A[4 2]				0.2*	526	385
	A[3 1]	0.53			0.05*	563	371
	B[4 2]	0.51	0.35*		0.2*	489	376
	B[3 1]	0.53	0.47	0.65*	0.05*	572	376

TOKEN 1

Figure 3-18: **(A)** Subject number. **(B-D)** Fraction of presentations in which token 2 was chosen as higher in pitch than token 1. For example, the first .9* entry in column B signifies subject 1 chose $[A_{42}]$ as higher in pitch than $[A_{31}]$ on 90% of the presentations. Asterisk indicates statistical significance ($p < 0.025$). **(E)** Fraction of trials in which the louder presentation of token 1 was chosen as higher in pitch. For example, the first entry of 0.8* indicates subject 1 chose $[A^{+}_{42}]$ as higher in pitch than $[A^{-}_{42}]$ on 80% of the trials. **(F)** Level of louder token 1 in μA. First entry of 538 signifies $[A^{+}_{42}]$. **(G)** Level of softer token 1 in μA. First entry of 520 signifies $[A^{-}_{42}]$.

Chapter 4

The influence of the peripheral anatomy on electric stimulation

4.1 Introduction

In this chapter we take a first step in investigating how individual attributes of the human peripheral anatomy impact intracochlear current flow and, thus, the neural activation pattern elicited by a cochlear implant. The motivation for this is to identify those attributes of the peripheral anatomy that have a relatively large impact and consequently may account for variation in performance across patients.

In the previous chapter EAM predictions were compared with empirical data to provide a measure of the degree to which the predictions are likely to mirror the physical situation. For stimulation with a monopolar apical electrode, predictions of intracochlear potentials (related to intracochlear current flow) were found to be the most similar to the measured data. Additionally, ECAP predictions showed a striking similarity to the measured data. We therefore concentrate on changes in intracochlear current flow to identify anatomical features that are likely to influence the patterns of neural excitation.

In addition, we use EAM techniques to (1) suggest methods to influence the activation pattern (e.g., increase spatial selectivity) by controlling intracochlear current flow, and (2) provide examples where errant patterns of current flow may create confusing cues for an implant user; specifically situations where the cochleotopic position of neural activation does not coincide with the position of the stimulating electrode (henceforth referred to as ectopic stimulation). As detailed in the following sections, an EAM model makes many such ectopic predictions, the most valuable of which are entirely counter-intuitive.

Chapter overview

The approach taken in this chapter is to investigate the impact of individual features present in the implanted ear. Some features (e.g., the unmyelinated human SGC perikaryon) are explored to determine whether they need to be incorporated in a model that accurately predicts human data. For others we make incremental modifications to the anatomy of a basic model of the implanted ear and measure the impact on intracochlear current flow, the neural activation pattern, and the predicted ECAP. For instance, the formation of new bone that is typically found in the basal turn near the cochleostomy site can be removed and the impact calculated. Alternatively, intracochlear current flow can be measured before and after the facial nerve canal or vestibular labyrinth is ossified, or after a segment of the bony duct is filled with fibrous tissue.

We focus attention on a collection of relevant features and use the Ineraid psEAM and bEAM to probe the impact of each. While we initially set out to directly compare Ineraid and Nucleus psEAMs, the ideas in this chapter are conveyed mostly using the Ineraid psEAM. We focus our initial efforts on the Ineraid model since it was more extensively tested in the last chapter. Future efforts will utilize the Nucleus psEAM to a greater extent. This chapter is organized as a survey of anatomical attributes investigated:

4.2.1 The unmyelinated human spiral ganglion cell
4.2.2 The influence of peripheral dendrites on ECAP recordings
4.2.3 The asymmetric relationship between the cochlea and internal auditory meatus
4.2.4 Distribution of surviving spiral ganglion cells
4.2.5 Influence of longitudinal impedance
4.2.6 Influence of new bone and fibrous tissue
4.2.7 Influence of the facial nerve canal and vestibular system
4.2.8 Increasing spatial selectivity

4.2 Results

4.2.1 The unmyelinated human spiral ganglion cell

In auditory science, one perplexing observation separating man from other mammals is the relatively small number (fewer than 5%) of SGCs with myelinated perikarya [157]. Especially in the case of monopolar stimulation where the model predictions of previous chapters suggest current flows into the modiolus essentially parallel to the fiber's axis, the rather large, unmyelinated SGC (diameter $\approx 30\mu m$ [147]) may impact the response to electric simulation.

In this section we detail membrane voltages that develop due to the transient polarization of the unmyelinated cell body by the exogenous electric field created by the stimulating electrodes, an effect not accounted for in previous cable models of the auditory nerve fiber. Because these membrane voltages are predicted to be on the order of a few millivolts, and occur rapidly on a sub-microsecond time scale, it is conceivable they influence the initiation of action potentials (e.g., [107]), although further modeling studies will be needed to fully investigate this effect.

Background

The discretized cable model used in the single-fiber model, based originally on the McNeal [125] model of a myelinated nerve-fiber, relies on a set of assumptions often overlooked. Among these are: (A) the principal electromotive forces driving current across the cellular membrane are in the radial direction only, while intracellular and extracellular currents are in the axial direction only, (B) the extracellular space is expansive, such that after the stimulus pulse the extracellular medium is an isopotential, and (C) the membrane dynamics of a single neuron are not influenced by the extracellular potentials in the interstitial space generated by the membrane currents of neighboring fibers conducting an action potential. Each of these assumptions is likely to be violated to some extent.[1]

Since the predictions for monopolar stimulation show a substantial current density flowing nearly parallel to the axis of the fiber near the cell body, an appreciable membrane voltage may develop at the unmyelinated cell body, a phenomenon not represented in a one-dimensional single-fiber model like that used in the EAMs discussed thus far. Approximating the SGC as a spherical shell of unmyelinated nodal membrane, isolated from its peripheral and central extensions, the steady-state mem-

[1]See Plonsey [162], Plonsey and Barr [5], Barr and Plonsey [4], and Trayanova et al. [209, 208]. For example, examining a cross-section of the densely packed neurons in a nerve trunk shows that the extracellular space allotted per neuron can be so small as to present a non-negligible resistance. As pointed out by Barr and Plonsey [5], the assumptions of the McNeal-type single-fiber model [125] (see equation 2.13, p.56), are only valid for an isolated fiber in an expansive extracellular medium where the extracellular resistivity is negligibly small, such that the extracellular space can be treated as an isopotential after the stimulus pulse.

brane voltage, V_m, in response to an externally-applied electric field can be derived analytically. The membrane voltage of a passive spherical cell with radius r in a uniform electric field of strength E_0 (e.g., $\Phi(\varphi, r) = E_0 r \cos\varphi$) can be approximated as

$$V_m \cong -1.5\ r\ (E_0) \cos\varphi, \tag{4.1}$$

where φ is the angle of the spherical coordinate system centered on the cell (see Plonsey and Altman [163]). Substituting the quantity J_{rc}/σ_e as an estimate of E_0, where σ_e is the extracellular conductivity, one can estimate the voltage across the spherical cell membrane (per unit current on the stimulating electrode) as a function of φ.

Preliminary modeling

This same conduction problem can be solved computationally by encoding a single bipolar SGC (with its peripheral and central axons included) in a simple volume conduction model (VCM), then subjecting it to a uniform field parallel to the cell's axis as shown in Figure 4-1A. Here an 800 μm length of a bipolar SGC is represented inside an $800 \times 100 \times 100\mu$m insulated box with parallel plate electrodes that deliver a uniform field of magnitude E_0. The SGC has a 30-μm diameter spherical cell body with internal conductivity σ_i equal to that of the axioplasm, an external conductivity σ_e equal to that of nervous tissue, and a 3 μm thick unmyelinated membrane of appropriate resistivity.[2] The membrane voltage $V_m(\varphi)$ on the unmyelinated perikaryon is measured as a function of the angle φ between the incident field, E_0, and cell's axis as shown in Figure 4-1B. This prediction is repeated using: (1) an isolated spherical SGC cell, and (2) four additional bipolar SGCs added to the $800 \times 100 \times 100\mu$m model space, as in panel C, such that the five cell bodies occupy 50% of the cross-sectional area.

In panel D the membrane voltage $V_m(\varphi)$ is shown as predicted analytically using equation 4.1 (gray), as well as predicted using the VCM with a single bipolar cell (black line), a single spherical cell (dotted), and with 5 bipolar SGCs (broken line). Each shows the expected cosine(φ) dependance, with a maximum positive excursion (depolarization) near 180 degrees at the axon hillock. Note the close fit between the membrane voltage, $V_m(\varphi)$, of the spherical cell calculated analytically and using the volume conduction model (compare gray and dotted traces). From equation 4.1, one notices that the membrane voltage developed by this "spherical-cell charging" is proportional to the cell radius,[3] implying that variation in SGC diameter would translate into variation in spherical cell charging, and potentially, variation in threshold.

[2] A 3 μm-thick membrane of resistivity 46,000 Ωcm is used. This ensures that the overall membrane resistance per unit area is $\approx 14\ \Omega cm^2$, which is equivalent to the passive nodal resistance $1/g_L$ in the single-fiber model.

[3] More specifically, it is dependent on the length the cell spans parallel to *Eo*, such that an oblong cell, elongated along the fiber's axis, would develop larger membrane voltage deviations.

A plot of the potential field is shown in panel E for the single bipolar SGC case. It is apparent that (1) the interior of the cell is nearly an isopotential, (2) consistent with panel D, the membrane voltage V_m is zero at φ=90 and φ=270, and (3) the cell's presence distorts the applied field.[4] The data in Figure 4-1D are calculated per 1 μA of the stimulus current, suggesting that at 500 μA the maximum membrane depolarization is on the order of 3 mV, which may contribute to the initiation of an action potential. Furthermore, as the cell packing is increased above the 5 cells in panel C that occupy only 50% of the cross-sectional area, the equivalent extracellular conductance σ_e will decrease drastically, such that for a patch of very densely packed SGCs, even higher membrane depolarization can be expected.

Lastly, the 0.645 μs time constant of spherical-cell charging[5] is much shorter than the minimum $\approx$ 28 μs time constant expected for a myelinated nerve fiber,[6] showing the membrane voltage due to spherical cell charging occurs on a sub-microsecond time scale (as observed experimentally [79]) well before nodal patches of membrane are either hyperpolarized or depolarized.

For a detailed physical explanation of this see the Discussion section of [26]. Briefly, to charge (depolarize) the entire cell body membrane, a relatively large net

[4]To the extent the membrane behaves as a perfect insulator, no current crosses the membrane, making the potential-field lines at the membrane interface orthogonal to the cell surface (i.e., current density is orthogonal to the field lines).

[5]Cartee and Plonsey [26] give the time-dependant solution for a spherical cell of radius r with axioplasmic conductivity σ_i, external conductivity σ_e, and membrane resistance per unit area r_m as

$$V_m(\varphi,t) = -\frac{3\sigma_i\sigma_e r_m r E_0 \cos\varphi}{\sigma_i r + 2\sigma_e r + 2\sigma_i\sigma_e r_m}\left(1-e^{-t/\tau_s}\right)u(t) \tag{4.2}$$

$$\approx -1.5\, r E_0 \cos\varphi \left(1-e^{-t/\tau_s}\right)u(t) \quad \text{(high } r_m \text{ limit)} \tag{4.3}$$

Under conditions where r_m is large, this simplifies to the approximation given in equation 4.1 for the steady-state. Using equation 9 of Cartee and Plonsey [26], and the parameters of the single-fiber model (page 117), the spherical-cell time constant (τ_s) is

$$\tau_s = \left(\frac{1}{r_m c_m} + \frac{2\sigma_e\sigma_i}{r c_m(\sigma_i+2\sigma_e)}\right)^{-1} = 0.645\ \mu s. \tag{4.4}$$

[6]The time constant for a myelinated fiber (τ_m) represented as a periodic cable is the weighted average of the nodal (τ_1) and internodal (τ_2) time constants,

$$\tau_m = \left(\frac{l\lambda_2^2\tau_1 + L\lambda_1^2\tau_2}{l\lambda_2^2 + L\lambda_1^2}\right) \tag{4.5}$$

where λ_1 and λ_2 are the space constants of the nodal and internodal sections, and l and L are the nodal and internodal lengths [177]. Thus, the time constant for the myelinated fiber τ_m is significantly *longer* than the time constant for a nodal patch of membrane τ_1,

$$\tau_m > \left(\frac{1}{r_m c_m}\right)^{-1} = 28\ \mu s. \tag{4.6}$$

charge must be delivered to the cell interior. For the polarization mechanism described here, the total charge on the spherical membrane is always the same, it is simply redistributed by the incident field.

Collectively, these results suggest a weakness of the one-dimensional single-fiber model used in this and previous studies to predict the impact of axially directed currents when a large diameter, unmyelinated cell body is present. Since the single-fiber model used in this study includes a discontinuity at the node representing the cell body, depolarization tends to occur at the junction of the 2 μm and 1 μm diameter segments at the cell body, possibly mimicking the effect of the cell body, although this is more fortuitous than by design. Among other reasons, since the anatomy of the human SGC does not appear to be represented well by any one-dimensional single-fiber model, in the following sections we tend to focus on J_{rc} as the metric for changes in activation in response to changes in the anatomical representation.

Predictions regarding the polarization of the cell body should be investigated in future EAMs, as a substantial portion of the current density is predicted to be parallel to the fiber axis in Rosenthal's canal. In regions of Rosenthal's canal where cell packing becomes dense, the effective extracellular resistance is increased by the presence of the spiral ganglion cell body, increasing the potential gradients across individual cell bodies. This also suggests the possibility that a cluster of closely packed cell bodies, with apposed membranes, might experience greater polarization than a single isolated SGC.

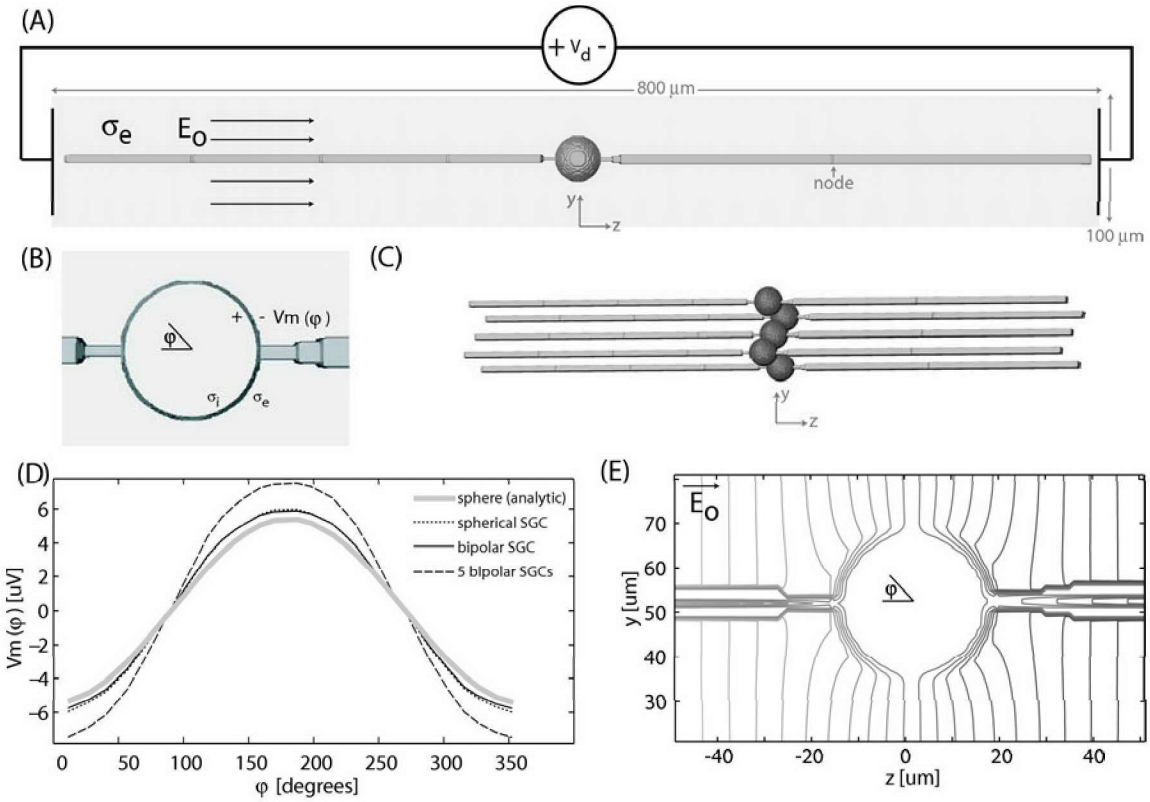

Figure 4-1: (A) Volume conduction model (VCM) for predicting $V_m(\varphi)$, the membrane voltage for a SGC with a spherical cell body exposed to an externally applied electric field of strength E_0. Here an 800 μm length of a bipolar SGC is represented in a VCM using 1-μm cubic voxels. A single 30-μm diameter unmyelinated cell body is composed of a 3-μm thick membrane of 46,600 Ωcm resistivity, such that the membrane has a per-unit-area resistance (r_m) of 14 Ωcm^2. Myelinated internodal membrane is represented as a perfect insulator, separating nodal patches of membrane with the same 14 Ωcm^2 as the cell body. The voltage across the model boundaries (V_d) is set to maintain a field strength of $E_0 = J_{rc}/\sigma_e$, where J_{rc} is chosen as the maximum RC-current in response to a 1 μA monopolar current on EL4 in the bEAM. (B) Convention for measuring $V_m(\varphi)$. (C) Several bipolar SGCs can be added to the 800 × 100 × 100μm model space. Here the 5 cell bodies occupy 50 percent of the cross-sectional area midway between the end plates (z=0). (D) $V_m(\varphi)$ predicted using analytic theory (eqn 4.1), the VCM with a spherical SGC, the VCM with a bipolar SGC, and the VCM with a bipolar SGC surrounded by 4 neighbors as in panel C. (E) Contour plot of the equipotential lines that exist during steady-state conduction for the single bipolar SGC case.

4.2.2 The influence of peripheral dendrites on ECAP recordings

Considering the results of the previous section, a new single-fiber model approach is likely necessary to predict where along a SGC an action potential (AP) initiates. In the case where the AP does initiate on the cell body, there will likely be both an orthodromic AP propagating toward the cochlear nucleus, and an antidromic AP propagating toward the neuron's peripheral termination. In this situation the bEAM predicts the presence of the peripheral dendrites will have a unique impact on the ECAP.

In section 2.5 of Chapter 2, a methodology was given for dividing a model fiber's predicted SFAP into two components: that due to membrane currents on the model fiber's dendrite and that due to currents on the model fiber's central axon. Accordingly, each SFAP from an excited model fiber can be divided into a dendritic and axonal component, as can the predicted ECAP.

Shown in panel A of Figure 4-2 is a typical ECAP prediction divided into the dendritic component (*ecapD*) due to the antidromic AP and the axonal component (*ecapA*) due to the orthodromic AP. Over roughly the first 400 μs, *ecapD* tends to be of the opposite phase of *ecapA*, lowering the amplitude of the total ECAP. The decomposition of a single SFAP into its dendritic (*sfapD*) and axonal (*sfapA*) components is shown in panel D for a model fiber at a position in θ near EL3, which for simplicity serves as both the stimulating and recording electrode. Vertical lines mark 90 and 265 μs after the pulse. The membrane voltage along the fiber in panels B (90 μs) and C (265 μs) show the antidromic and orthodromic action potentials moving away from each other. The corresponding membrane currents in panels E and F explain the phase difference between *sfapD* and *sfapA*.

At 90 μs (panel E), *sfapD* is carried mainly by the outward (positive) and inward (negative) membrane currents labeled i_1 and i_2 that resemble a dipole with its *positive* pole (i_1) orientated closer to the recording electrode.[7] At the same time, *sfapA* is carried in the opposite direction primarily by inward and outward currents labeled i_3 and i_4 that resemble a dipole with its *negative* pole (i_3) orientated closer to the recording electrode. Accordingly, at 90 μs *sfapD* exerts a positive potential on the recording electrode, while *sfapA* exerts a negative potential.

At 265 μs *sfapD* has reached the peripheral termination, leaving only a weak inward i_2 balanced by spatially diffuse outward currents, resembling a dipole with its *negative* pole orientated closer to the recording electrode. Meanwhile *sfapA* has

[7]Here we make an analogy between electrostatic dipoles and the theoretical dipoles created by point current sources in the volume conduction problem. In this electrostatics analogy, the potential on a recording electrode due to one fiber can be conceptualized as that due to a collection of line charges distributed along a fiber track, where the spatio-temporal arrangements of these line charges mirror the spatio-temporal membrane currents for a single model fiber.

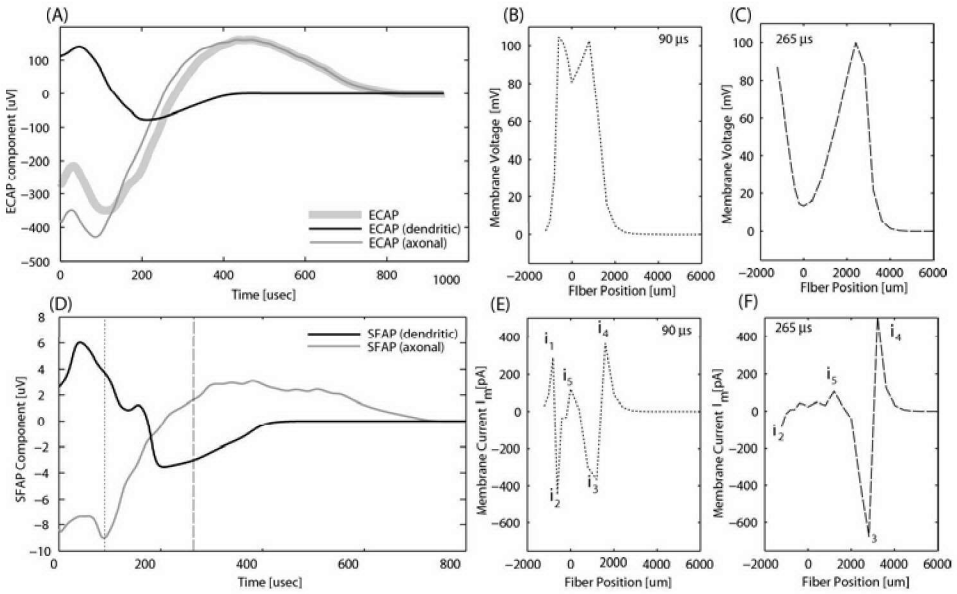

Figure 4-2: (A) Contribution of peripheral dendrites (black) and central axon (gray) to the total ECAP waveform (thick gray). EL3 is both the simulating and recording electrode. (D) Dendrite component (black) and axonal component (gray) to the SFAP waveform for one model fiber representing 150 neurons ($N_f = 150$) . Note the stimulating electrode (EL3), recording electrode (EL3), and model fiber are located at the same position in θ near 250 degrees. Dotted and dashed vertical lines mark 90 and 265 μs after the stimulus pulse. (B/C) Membrane voltage along the model fiber as a function of distance from the cell body position at 90 and 265 μs. (E) Membrane current I_m along the model fiber as a function of distance from the cell body position at 90 μs. Membrane currents labeled i_1 and i_2 represent an antidromically propagating action potential while i_3 and i_4 represent an orthodromic AP. (F) Membrane current along the model fiber at 265 μs.

propagated further down the fiber. The i_3-i_4 complex is further away from the electrode, decreasing its impact, while the repolarization current labeled i_5 imparts a positive potential to the recording electrode. The i_5-i_3-i_4 complex can be conceptualized as an quadrupole, composed of two asymmetric dipoles, that imparts a net positive potential to the electrode. It is this complex that gives rise to the typical triphasic potential waveform recorded extracellularly from a single myelinated fiber as an action potential propagates past.

For the model fiber in Figure 4-2, the stimulating/recording electrode (EL3) and the model fiber are all located at θ near 250 degrees, such that the antidromically propagating AP is moving in a trajectory headed straight toward the EL3 recording electrode. In this case the influence of the i_1-i_2 complex constituting *ecapD* exerts a maximal voltage signature on the recording electrode.

Across model fibers the same pattern for *sfapD* will not hold as the recording electrode is moved. Shown in panels A and B of Figure 4-3 are traces of *sfapD* and *sfapA* for a different model fiber located near EL4 (basal to the EL3 stimulating electrode $\otimes$) as the position of the recording electrode is varied. As the recording

electrode is moved, the magnitude and phase of *sfapD* tends to vary substantially (panel A), while the magnitude and phase of *sfapA* (panel B) remain the same. As one would expect, the maximum amplitude *sfapD* is recorded by EL4, since the model fiber generating the *sfapD* is closest to EL4. For electrodes distant from this model fiber, the recorded *sfapD* trace has a much lower amplitude and inverted phase (compare the *sfapD* for EL6 and EL4 in panel A), while the *sfapA* traces in panel B tend to have a similar amplitude and morphology across recording electrodes.

As a consequence of these differences between *sfapD* and *sfapA*, the total *ecapD* and *ecapA* show a similar pattern in panels C and D. The amplitude of *ecapD* tends to vary drastically across recording electrodes, with a maximum amplitude near the EL3 stimulating electrode, while the amplitude of *ecapA* remains similar.

An example of the geometric relationship associated with the differences between *sfapD* and *sfapA* is given in the schematic of panel E. Consider the simplified geometry where three electrodes (EL3-EL5) lie in a plane, while the model fibers form a radially-symmetric bundle resembling a funnel. Just after the pulse offset (90 μs in the previous figure) both antidromic and orthodromic action potentials exist along each stimulated model fibers.

The antidromic AP currents (white circles) can be conceptualized as a dipole with its positive pole (i_1) orientated toward the lateral wall, while the orthodromic AP currents (black circles) can be conceptualized as a dipole with the negative pole (i_3) orientated toward the electrodes. Accordingly for the $\alpha-$fiber, when recording on EL4 *sfapD* is positive while *sfapA* is negative at this instant in time. For other recording electrodes (EL3 and EL5), the *sfapD* generated by the $\alpha-$fiber will be negative due to the orientation of the i_1-i_2 dipole relative to the recording contact. Similarly, the *sfapD* due to the β_1-fiber will be positive when recorded on EL3, while negative for EL4 and EL5. This explains the *sfapD* polarity and amplitude differences shown in panel A.

Conversely, at this instant in time *sfapA* will always be negative regardless of which electrode it is recorded from or which fiber (α, β_1, or β_2) generated it, due to the common orientation of orthodromic i_3-i_4 complex (black circles) relative to all of the recording contacts. Given these predictions, the magnitude of *ecapD* will depend on the relationship between model fiber and recording electrode, while *ecapA* will show little variation across recording electrode as observed in panels C and D. The model predicts *ecapA* will dominate *ecapD*, such that the total predicted ECAPs tend to follow *ecapA*, having a common N1P1 morphology regardless of the recording electrode position, as observed experimentally.

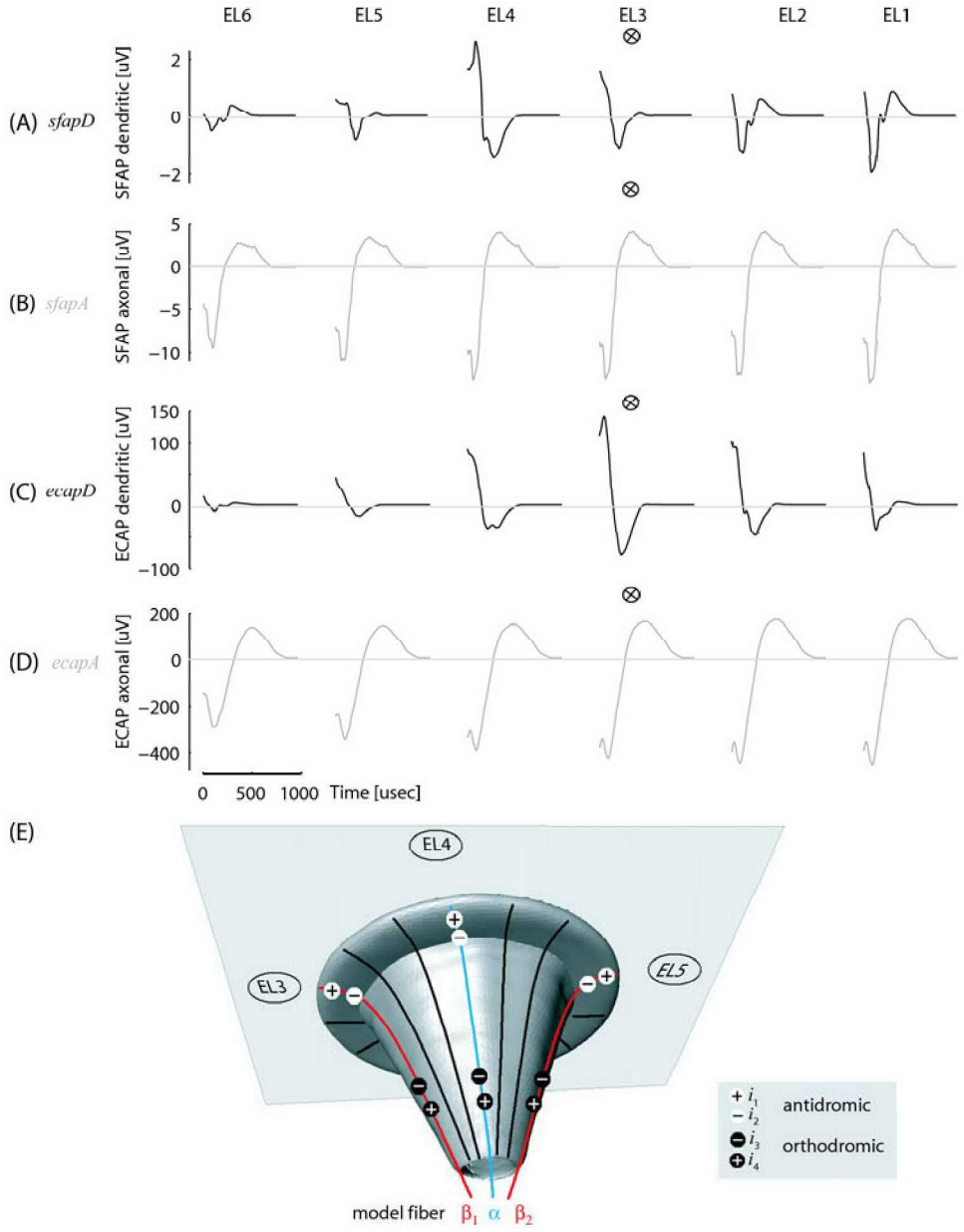

Figure 4-3: (A) Dendritic contribution (*sfapD*) to recorded potentials for a model fiber at θ close to that of EL4, just basal to the EL3 stimulating electrode (marked by $\otimes$), in response to a 1,500 μA pulse. Responses are given for one model fiber representing 150 neurons (i.e., $N_f = 150$). Moving left to right the position of the recording electrode moves from base to apex. As one would expect, the maximum amplitude for *sfapD* is recorded by EL4, since the model fiber generating the *sfapD* is closest to this electrode. (B) Axonal contribution (*sfapA*) for the same model fiber near EL4. Note scale differences as *sfapA* tends to be larger because the central nodes are twice the diameter of the peripheral nodes. (C) Dendritic contribution to total ECAP (*ecapD*) in response to the same stimulating pulse. (D) Axonal contribution to total ECAP (*ecapA*). (E) Schematic describing a geometric explanation for the waveform differences between *sfapD* and *sfapA* at $\approx 90\mu$s after the stimulus pulse. See text for explanation.

4.2.3 The asymmetric relationship between the cochlea and internal auditory meatus

As mentioned in the second chapter, one counter-intuitive prediction of the bEAM is a non-monotonic decrease in the current density entering the modiolus (J_{rc}) for regions of θ apical to a basal stimulating electrode (replicated in Figure 4-4A, black trace). Basal stimulation (EL6) shows a local maximum in $|J_{rc}|$ near 240 degrees, as do plots for stimulation by EL5 and EL4, suggesting this maximum is caused by the anatomy rather than a function of the stimulating electrode position. This unusual prediction remained (i) for different positions of the EAM return, (ii) with and without new bone and fibrous tissues at the base, (iii) with the dual-ground condition described in Chapter 3 where a second round window ground was added, (iv) with an ossified facial nerve canal or vestibular labyrinth, and (v) with segments of Rosenthal's canal apical to the basal turn ossified.

After several other modifications, the local maximum in $|J_{rc}|$ was attributed to the asymmetric nature of the cochlear spiral, specifically the orientation of the internal auditory meatus with the basal turn. Shown in Figure 4-4B are $|J_{rc}|$ predictions for stimulation by the same three electrodes (EL6-EL4) after modifying the thickness of bone separating the basal turn from the internal auditory meatus (IAM), as described below. After the modification, the behavior is monotonic, with the position of the peak in $|J_{rc}|$ corresponding to the position of the stimulating electrode.

Shown in Figure 4-5A is an image generated using the Amira software showing a midmodiolar section along with a surface rendering of the internal auditory meatus (blue). There is clear geometric asymmetry between the fluid of the basal turn and the IAM that serves as the return path for monopolar current. Two cochleotopic positions in the basal turn are labeled α and β in panel A. The impedance between β and the return in the IAM is relatively high due to both the thickness of the trabeculated bone housing Rosenthal's canal, and the thick section of adjacent bone (labeled $\oplus$). Conversely, the impedance between α and the IAM is relatively low due to both the relatively thin Rosenthal's canal, and the thin adjacent bone (labeled $\ominus$). Consequently, for monopolar current delivered to positions along the basal turn, the lowest impedance path into the IAM is via a cochleotopic position of roughly 240 degrees (vertical broken line in Figure 4-4A), regardless of the precise electrode position.

This prediction is counter-intuitive, since in Figure 4-5 one notices that the Euclidian distance from β to the return is shorter than from α. Replacing the bone adjacent to β ($\oplus$) with 300-Ωcm nerve tissue (panel B), gives the monotonic $|J_{rc}|$ behavior for basal stimulation shown in gray in panel C. Alternatively, replacing portions of the 300-Ωcm IAM near 240 degrees with bone has the opposite effect for both basal and apical stimulation (panels D and E), transforming the local maximum in $|J_{rc}|$ in the bEAM (black) to a local minimum (gray). Performing both these modifi-

cations (panel E) tends to increase $|J_{rc}|$ for θ below 230 degrees while simultaneously decreasing $|J_{rc}|$ for θ above 230 degrees.

Changing the resistivity of bone used in the model modified this tendency for current to enter the modiolus near 240 degrees. Figure 4-6 shows that for both apical and basal stimulation, the local increase in $|J_{rc}|$ near 240 degrees ($\uparrow$) is exaggerated when the bone resistivity is increased to 50 kΩcm (broken line), and vanishes when the bone resistivity is decreased to 600 Ωcm (gray line).

In summary, we conclude that compared to other modifications made (e.g., see (i)-(v) above) the predictions of intracochlear current flow, as measured by $|J_{rc}|$, are very sensitive to changes made near the intersection of the IAM with the modiolus. This prediction is rooted in the asymmetric relationship between the cochlear spiral and adjacent structures. The sensitivity of current flow to such asymmetries is significant when the ratio of bone-to-fluid resistivity is significantly higher than 10, as it is in the bEAM.

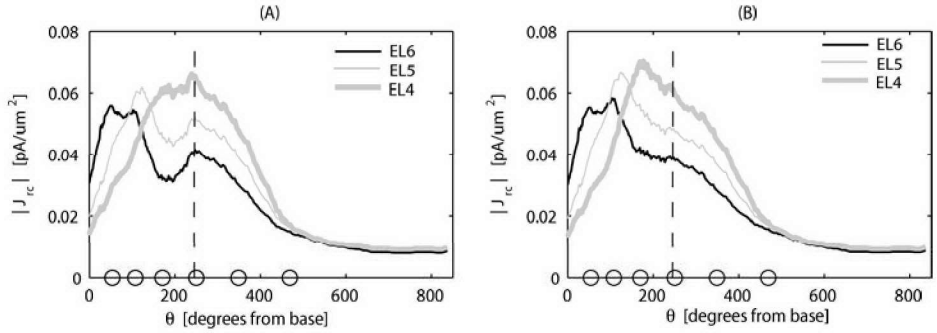

Figure 4-4: $|J_{rc}|$ versus θ for stimulation of EL6, EL5 and EL4 before (panel A) and after (panel B) a modification was made to the bEAM to counter the local maximum near 240 degrees (vertical line).

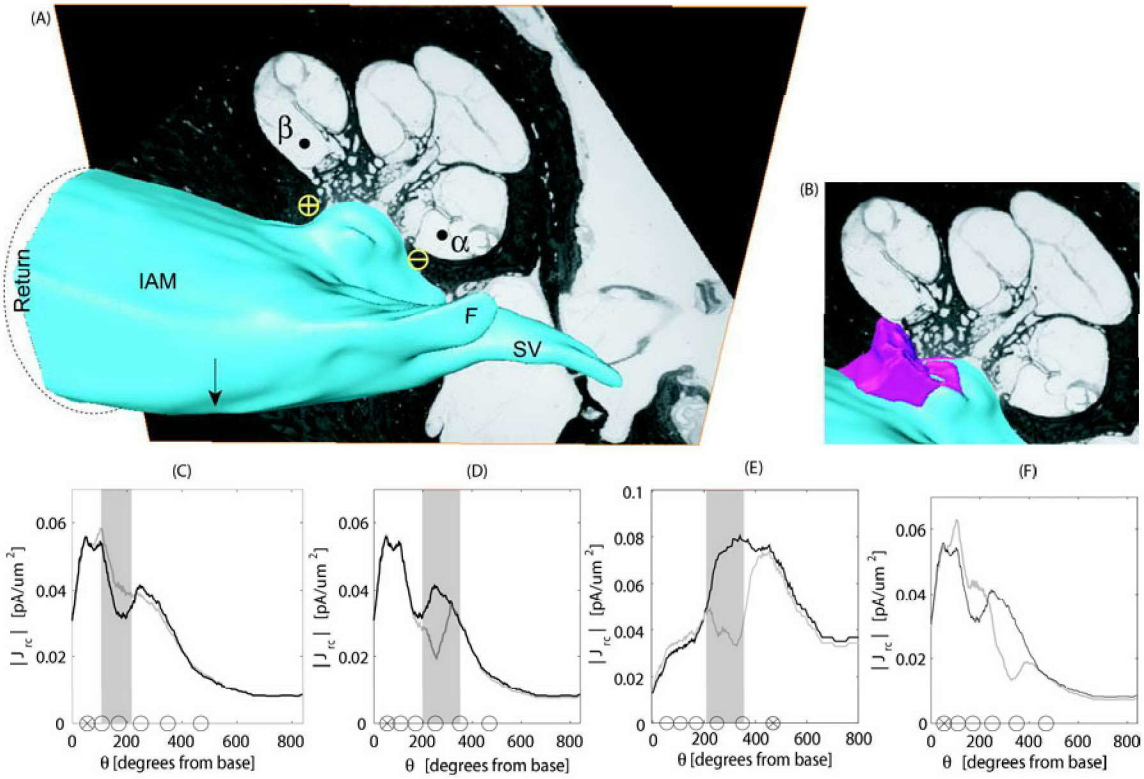

Figure 4-5: (A) Midmodiolar image with superimposed surface rendering of the internal auditory meatus (IAM, blue) and branching canals for the facial (F) and superior vestibular (SV) nerves. The monopolar return surface is located at the intersection of the proximal IAM and the model boundary. Points labeled α and β are located at cochleotopic positions with relatively low and high impedance paths into the tissues of the IAM due to the thinness of the bone labeled $\ominus$ compared to the thickness of that labeled $\oplus$. (B) Replacing bone near $\oplus$ with 300 Ωcm IAM nerve tissue, as shown in purple, lowers the impedance from β to the IAM ground. (C) $|J_{rc}|$ versus θ for basal stimulation of EL6 in the bEAM before (black) and after (gray) the modification described in panel B. Note $|J_{rc}|$ is now monotonic, with the shaded vertical bar denoting regions in θ where bone is replaced by nervous tissue. Moving the return electrode (panel A, dotted line) to the posterior wall of the IAM (labeled $\downarrow$) had virtually no effect on the prediction of $|J_{rc}|$. (D) $|J_{rc}|$ versus θ for basal stimulation of EL6 in the bEAM before (black) and after (gray) regions of the IAM near ($\ominus$) were replaced by bone. Vertical shaded bar denotes regions in θ where bone was added. (E) $|J_{rc}|$ versus θ for apical stimulation of EL1 before (black) and after (gray) regions of the IAM near $\ominus$ were replaced by bone. (F) $|J_{rc}|$ for basal stimulation of EL6 in the bEAM before (black) and after (gray) both modifications described in panels C and D were made.

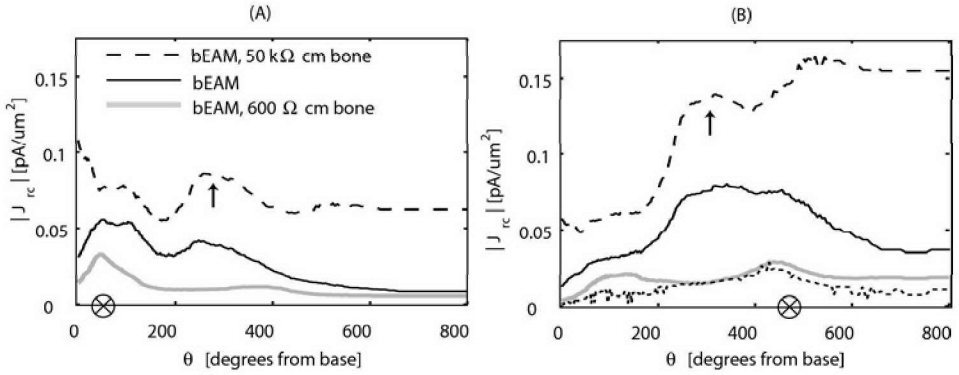

Figure 4-6: $|J_{rc}|$ versus θ in the bEAM for apical (panel A) and basal (panel B) stimulation when the bone resistivity is increased to 50 kΩcm (broken line) or decreased to 600 Ωcm (gray line). Note since plots of $|J_{rc}|$ and J_{rc} versus θ typically overlap, $|J_{rc}|$ is usually plotted for illustrative convenience. In panel B an exception is found where a second maximum is seen in $|J_{rc}|$ for the 600-Ωcm case near 100 degrees. This secondary maximum (369 degrees basal to EL1) is likely due to cross turn coupling and is not present in the plot of J_{rc} (dotted line), indicating the current density magnitude is increased, but not in the direction parallel to the fiber track.

4.2.4 Distribution of surviving spiral ganglion cells

In the last chapter it was shown that variations in the patient-specific distribution of surviving neurons, represented in the model by the vector $N_{f(i)}$, had little impact on the deterministic model's prediction of behavioral threshold (T_p). Especially for the broad patterns of current spread predicted for monopolar stimulation, this suggests that even a few hundred neurons spread across the entire cochlear length could result in relatively normal behavioral thresholds. An exception to this occurs in the Nucleus psEAM. As described in Chapter 2 (p.37), the Nucleus cochlea shows an atrophic region ($5 < \theta < 110$) just basal to where the electrode array coils around itself where no surviving SGCs were found histologically. This large region devoid of neurons is predicted to impact measures such as psychophysical threshold.

Replotted in panel A of Figure 4-7 are archival behavioral thresholds (T_d) for the Nucleus patient. Electrode pair 19 (marked by ø) was turned off in the processor map,[8] likely due to the high T_d value (94 nC per phase) listed in the patient's chart. In panels B-K are predictions of J_{rc} versus θ as the simulating electrode pair is moved basally from EP11 (panel B) to EP20 (panel K). In each panel the atrophic region devoid of SGCs is denoted by the vertical shaded bar. As the bipolar electrode pair (EP) moves basally from EP11 toward this region the peak J_{rc} amplitude (positive or negative) tends to increase over EP11-EP13 (panels B-D), decrease over EP13-EP19 (panels D-J), and then increase again from EP19 to EP20 (panels J-K). Exactly the opposite trend is seen in the behavioral threshold measures of panel A, where T_d value (labeled by the letter of the corresponding panel) *decreases* from B-D, *increases* steadily from D-J, and *decreases* from J-K. As described in the next section, this inverse correspondence suggests the amplitude of J_{rc} can be used to derive an alternative psychophysical threshold estimate (T_p^*).

The decrease in the amplitude of J_{rc} from EP13 to EP18 (panels D-I) corresponds to a transition of the position of the simulating pair into the atrophic region. The corresponding increase in behavioral T_d suggests the net impact of the atrophic region, attributed to damage done by the electrode kink at the basal end, was to increase behavioral thresholds near the base. The electrode pair with the highest behavioral T_d, EP19, corresponds to an electrode pair whose contacts reside in the basal coil of the array (see Figure 2-4, p. 37) in an unusual orientation almost orthogonal to the basilar membrane.

[8] In the archived Nucleus data EP19 has both a threshold and maximum comfortable level of 91 nC per phase, much higher than the 20-53 nC per phase range of the other active electrodes. From this observation one might speculate that during fitting the level on EL19 was raised until at 91 nC the Nucleus subject first reported both the sensation of sound and discomfort [70].

Behavioral thresholds revisited

The inverse relationship between the relative magnitude of J_{rc} and behaviorial T_d in Figure 4-7 suggests the current in Rosenthal's canal can be used to predict behavioral thresholds without either a single-fiber model or a weighting describing the number of surviving SGCs per model fiber ($N_{f(i)}$). For each stimulating electrode e, an alternate estimate for threshold can be described as

$$T_p^* = \frac{1}{\max(abs(J_{rc}(\theta)))} \tag{4.7}$$

where higher peaks (or valleys) in J_{rc} lead to lower T_p^* estimates. This is consistent with modeling results in Chapter 2, where J_{rc} and single-fiber thresholds were shown to be inversely related using the bEAM (Figure 2-28).

Predicted T_p^* and measured T_d patterns are shown in Figure 4-8 for both Nucleus and Ineraid patients, with each pattern expressed as a dimensionless variable by subtracting the mean and dividing by the standard deviation. For the Nucleus psEAM, predicted T_p^* are shown with (panel A, black line) and without (panel B, broken line) new bone and fibrous tissues included in the model. Panels C and D show the Ineraid predictions with and without intracochlear tissues. Using this simplified approach to predict behavioral thresholds, there is a significant correlation between T_p^* and the measured T_d for both Nucleus psEAM versions (panels A and B) and the Nucleus psEAM with new bone and fibrous tissue removed (panel D).

Three aspects of the measured Nucleus T_d data captured by the predicted T_p^* in panel A are worth emphasizing. First, the relatively high T_p^* for EP19, which is responsible for the high r^2 values.[9] Second, is the increasing trend in T_d as the electrode pair is moved toward the base. Third, is the local maximum in T_d near EP10, present only in T_p^* when new bone and soft tissue are included (compare panels A and B).

For the Ineraid T_d data, the model without new bone provides a better T_p^* estimate than the psEAM T_p^*, as was the case in the previous chapter where the psEAM was used to predict T_p. In both cases this is because the psEAM values tend to be too low toward the base, possibly due to the new bone forcing a higher percentage of the current delivered to the basal electrode to exit the cochlea via pathways other than the modiolus (see discussion section).

[9] As was the case using the full Nucleus psEAM, the correlation between T_p^* and T_d is driven mostly by the prediction of a high threshold for EP19 (see Figure 4-8 caption).

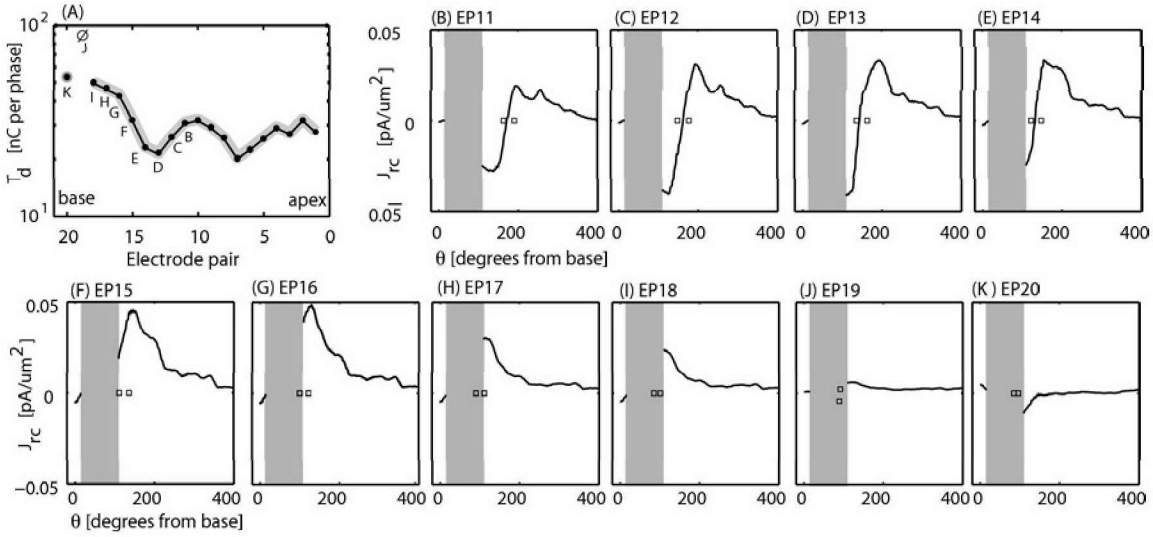

Figure 4-7: (A) Behaviorally-measured thresholds (T_d) for the Nucleus patient. EP19 (ø) was shut off apparently due to a high threshold value. (B-K) J_{rc} versus θ for electrode pairs 11-20, as labeled in panel A. In panels B-K the position of the stimulating electrodes are given by □s, while the vertical shaded bar denotes the basal atrophic region between 5 and 105 degrees in the Nucleus psEAM that does not contain SGCs or model fibers.

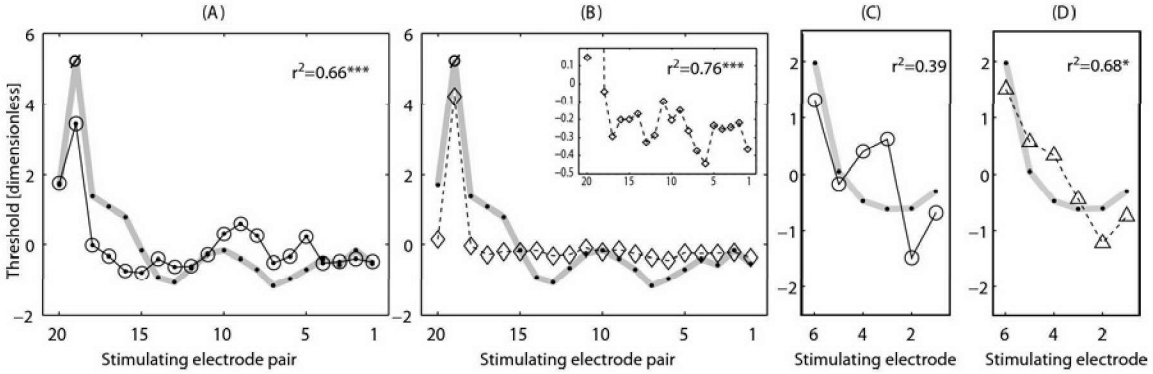

Figure 4-8: Model-predicted T_p^* (black) and measured T_d (gray) threshold patterns. Each pattern is expressed as a dimensionless variable by subtracting the mean then dividing by the standard deviation. Statistical significance is given by asterisks next to the r^2 value: $^*(p < 0.05)$, $^{**}(p < 0.01)$, $^{***}(p < 0.001)$. (A) T_p^* predicted by the Nucleus psEAM versus stimulating electrode pair. EP19 (ø) was shut off apparently due to a high threshold value. Note if EP19 is removed from the analysis the correlation becomes insignificant, $r^2 = 0.20$. (B) T_p^* predicted by the Nucleus psEAM without new bone or soft tissue included. Insert shows expanded y-axis. Note if EP19 is removed from the analysis, $r^2 = 0.49^{***}$. (C) T_p^* predicted by the Ineraid psEAM. (D) T_p^* predicted by the bEAM.

4.2.5 Influence of longitudinal impedance

To investigate the impact of a localized decrease in conductivity (for instance a deposit of new bone) a 3.5 mm segment of the cochlear duct encapsulating EL4 was completely filled with tissue as shown in Figure 4-9A. Plotted in panels B-D is the change in $|J_{rc}|$ after including the tissue (5 kΩcm or 300 Ωcm), for stimulation of EL5 basal to the impacted region (panel B), EL4 within the impacted region (panel C), and EL3 apical to the impacted region (panel D). Positive values indicate an increase in $|J_{rc}|$. For example, regions basal to the impacted region when stimulating basally (panel B), or regions apical to the impacted region when stimulating apically (panel D). A more interesting behavior is seen in panel C, where the stimulating electrode is centered inside the impacted material. At cochleotopic positions both above and below the impacted region $|J_{rc}|$ is reduced, while near the position of the electrode $|J_{rc}|$ is actually *increased.*

This increase is seen for the 300-Ωcm tissue deposit and marginally for 5-kΩcm tissue, suggesting the influence of the impacted tissue is to focus $|J_{rc}|$ at the stimulating electrode. This effect is interpreted as the tissue increasing the longitudinal impedance apical and basal to the simulating electrode to an extent that the impedance into the modiolus becomes a relatively low impedance path to the IAM ground. As described below, this result relies on the IAM as the major conduit for current exiting the cochlear labyrinth. To the extent current exits via an alternative path, such as a basal ground at the cochlear windows, this prediction will likely change (described below).

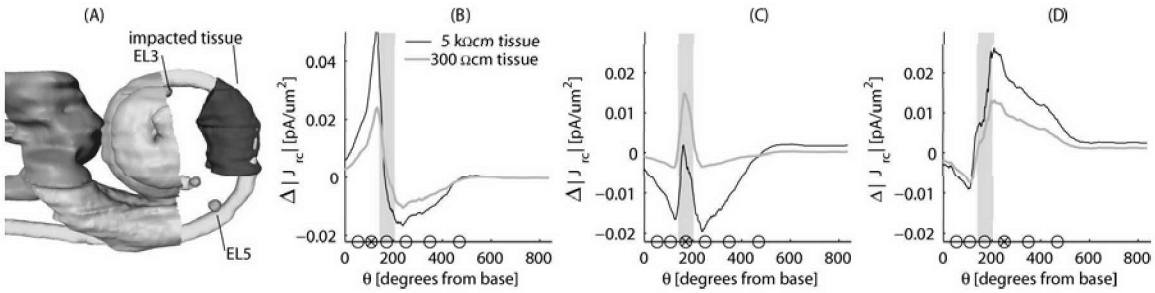

Figure 4-9: (A) 3D rendering of the bony labyrinth with half the bony duct cut away exposing a section of the electrode array near EL4, which is impacted. (B) Change in $|J_{rc}|$ versus θ for simulation of EL5 basal to the impacted region. Positive values indicate an increase in RC-current with the additional impacted tissue. In each plot $\otimes$ marks the stimulating electrode while the shaded vertical region denotes the range of impacted θ. (C) Change in $|J_{rc}|$ for stimulation of EL4 inside the impacted region. (D) Change in $|J_{rc}|$ for simulation of EL3 apical the impacted region.

4.2.6 Influence of new bone and fibrous tissue

Fibrous tissue

The foreign body immune response results in a fibrous tissue encapsuling the electrode array.[10] Grill et al. [67] estimated the resistivity of this encapsulation tissue to be 627 ± 108 Ωcm . For simplicity, in the psEAM we treated fibrous tissue as a 300 Ωcm homogenous material. It is conceivable that to the extent the encapsulation tissue forms stratified laminae, current may flow in the interstitial fluid sheets parallel to the surface of the implanted array. This depends on the nature of the fibrous tissue encapsulating the electrode, specifically the arrangement and frequency of tight junctions. Consistent with the 640-Ωcm measures of Grill et al., these tissues appear fibrous in nature, not showing signs of the tight junctions that characterize high impedance epithelia such as Reissner's membrane [154].

Simulations using the psEAM suggest the influence of thin fibrous encapsulation tissue on intracochlear current flow is minimal, unless the fibrous tissue occupies a significant proportion of the bony duct's cross-sectional area or fills in areas of trabeculated new bone growth to create an fibro-osseous occlusion of the cochlear duct.

New bone

Depending on the porosity and detailed structure of the new bone (i.e., the percentage occupied by the perilymphatic fluid phase) the bulk resistivity of the bony tissue inside the cochlear duct could vary between that of cortical bone and that of perilymph. A simple example of this is shown in Figure 4-10. Here the bulk resistivity of a material composed of fluid saturated bone is plotted as a function of the percentage of bone. When half the space is occupied by bone, the bulk resistivity roughly doubles, such that even if 80% of the space is bone, the bulk resistivity is still below 250 Ωcm. However, most often porous new bone deposits are filled with soft tissue, forming a fibro-osseous deposit.

The influence of this fibro-osseous tissue on the prediction of J_{rc} for monopolar stimulation in the Ineraid is shown in panels A-E of Figure 4-11. In panel A the distribution of intracochlear bone and fibrous tissue is replotted from Chapter 2, showing the typical fibro-osseous tissue occlusion found at the base. In panels B and C comparisons of J_{rc} for the bEAM and Ineraid psEAM show the impact of including intracochlear tissues on the prediction of current entering Rosenthal's canal. For monopolar stimulation of EL2 and EL6, J_{rc} for the bEAM (black line) and psEAM

[10]This includes a series of events, including protein adsorption onto the implant surface, monocyte migration, and macrophage attachment. Cytokine signalling elicits fibroblast migration and attachment, eventually leading to the collagen secretions that form the extracellular matrix of the dense fibrous tissue around the implant [153, 205].

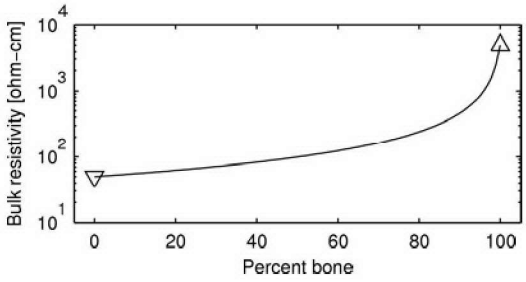

Figure 4-10: Bulk resistivity of a composite bone/fluid material where the percentage of fluid occupied by bone varies between 0 ($\bigtriangledown$) and 100 ($\bigtriangleup$) percent. In this simple calculation, the bone and fluid form parallel conductive paths, while in reality the topology and connectedness of the pores will determine the dielectric properties.

(gray line) are plotted on the same axis with areas where incorporating the fibro-osseous tissues increased the predicted J_{rc} shaded red and areas where the tissues tended to decease J_{rc} shaded gray. The impact is most significant for basal stimulation (panel B) where the fibro-osseous tissue deposit tends to force more current into the modiolus in areas apical to the stimulating electrode while decreasing J_{rc} in areas basal to it. Conversely, the model predicts the fibro-osseous tissue to have little impact on J_{rc} for apical stimulation in panel C.

Since the predictions in panels B and C assume an IAM exit pathway for monopolar current, is it interesting to investigate how these predictions change under the assumption that the primary exit pathway is, for instance, the round window.[11] Plotted in panels D and E are predictions of J_{rc} using a basal ground in the psEAM and EAM, with red and gray shading denoting a respective increase and decrease in J_{rc}. For both basal (panel D) and apical (panel E) stimulation, the large negative J_{rc} current at the base reflects current exiting the modiolus at the base en route to the cochlear window return. The effect of the fibro-osseous mass is most dramatic for basal stimulation in panel D. This is interpreted as current taking a circuitous route to exit the cochlea by first entering the modiolus, flowing around the fibro-osseous tissue occlusion at the base, and finally exiting at the base. Accordingly, model fibers near the stimulating electrode experience current *entering* Rosenthal's canal while the basal-most fibers experience current *exiting* the canal. If the neural activation pattern and J_{rc} are related as a function of cochlear length, this current pathway would indeed be expected to provide an ectopic, possibly confusing, excitation pattern.

In the Nucleus model the fibro-osseous tissue deposits are spread over a greater length of the bony duct (panel F). Comparisons of J_{rc} for bipolar stimulation of the Nucleus psEAM with and without new bone and fibrous tissues are given in panels G and H. The impact of the fibro-osseous deposits is similar to the monopolar case

[11] The results of Chapter 3 show a tight fit between model-predicted intracochlear potentials (IP_p) to measured data (IP_d) suggesting that, at least for apical stimulation, the IAM is the primary exit pathway. For basal monopolar stimulation the basal return may be a more likely exit pathway.

in that it tends to increase current flow into the modiolus, magnifying the biphasic J_{rc} pattern near each stimulating contact. This increase in J_{rc} can be explained by the segment of tissue between the stimulating electrode pair acting as an insulator to the longitudinal (shunting) current that would otherwise flow in the fluid parallel to the array.

For the example of apical bipolar stimulation (EP18, panel H) the influence of the tissue deposit is clearly asymmetric, tending to only increase J_{rc} apical to the stimulation pair. This type of asymmetry can vary across electrodes, preferentially increasing either the apical or basal lobe of J_{rc}, suggesting idiosyncratic patterns of tissue nearly filling the bony duct could shift the activation pattern to be maximal near either contact of the pair.[12] While the influence reported here is for tissue deposits to increase the current entering the modiolus, this is not exclusively the case (see discussion section).

[12]One might speculate this would lead to pitch reversals on a pitch-ranking task were electrodes along the array are sequentially stimulated and a subjective pitch judgement given.

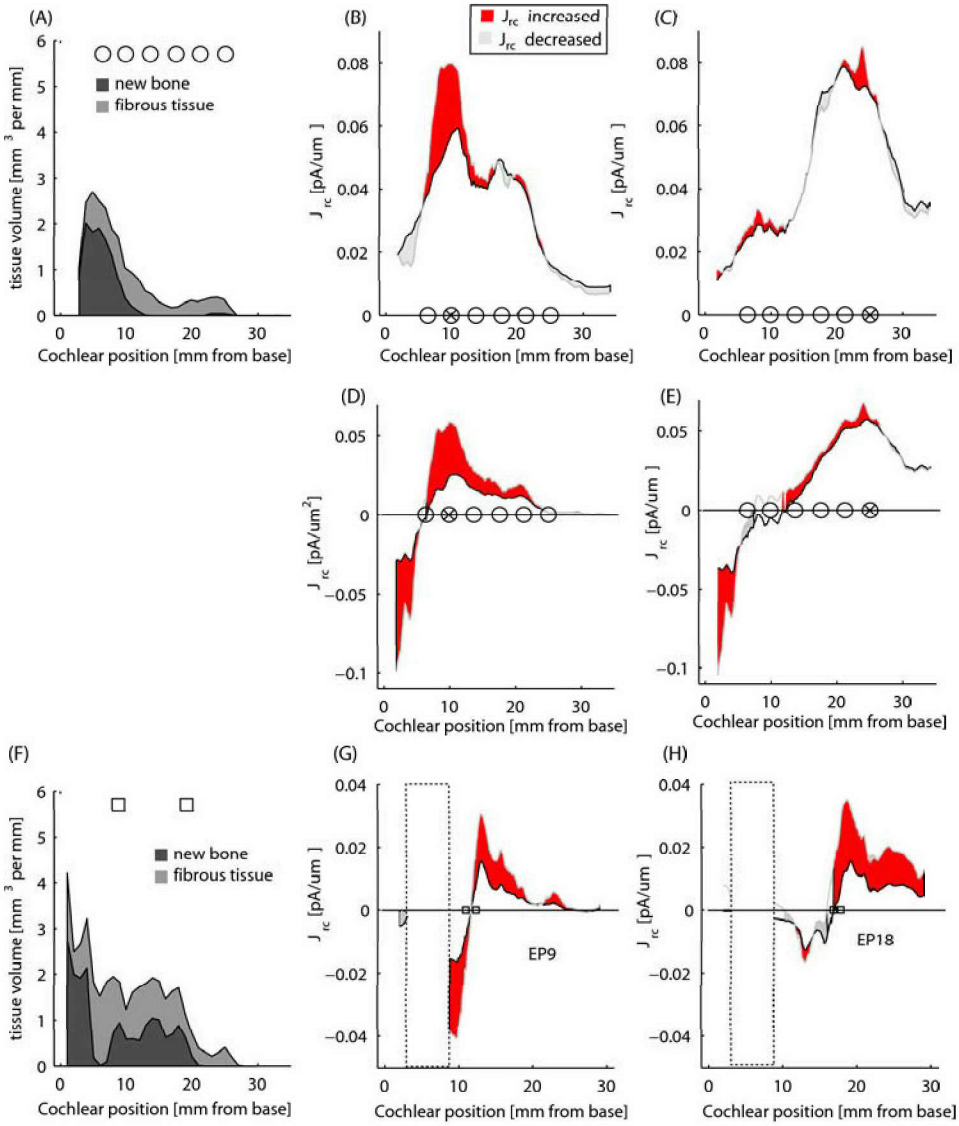

Figure 4-11: (A) Distribution of new bone and fibrous tissue in the Ineraid psEAM as a function of cochlear position. (B) J_{rc} versus cochlear position in the psEAM (gray line) and bEAM (black line) in response to stimulation of EL5 (⊗). Areas where J_{rc} in the psEAM (gray line) is greater than in the bEAM (black line) are shaded red, indicating the inclusion of intracochlear fibro-osseous tissues *increased* the amount of current entering the modiolus. Areas where J_{rc} in the psEAM is less than the bEAM are shaded light gray, indicated the intracochlear tissues *decreased* the amount of current entering the modiolus. (C) As in panel B for stimulation of EL1. (D-E) As in panel B, for stimulation of EL5 and EL1 using a basal ground at the round window. (F) Distribution of new bone and fibrous tissue in the Nucleus psEAM as a function of cochlear position. (G-H) As in panel B for bipolar stimulation of EP9 and EP18 in the Nucleus model with (gray line) and without (black line) new bone and fibrous tissue. Dotted line denotes atrophic region where neurons were absent.

4.2.7 Influence of the facial nerve canal and vestibular system

To investigate the influence of adjacent structures on the pattern of predicted intracochlear current flow, both the facial nerve canal and vestibular labyrinth were individually ossified in the bEAM. These modifications resulted in only small changes to J_{rc}, as shown in panels A and B of Figure 4-12 for basal and apical stimulation. Note the non-monotonicity discussed in section 4.2.3 is present for both modifications.

Panels C and D plot the *change* in J_{rc} after ossifying either the facial nerve canal or vestibular labyrinth, with positive values indicating an increase in current density. While small on a percentage basis, the changes in J_{rc} fit with intuition. In panels C and D, the maximum increase in J_{rc} for both apical and basal stimulation after facial canal ossification (dotted line) occurs near 300 degrees (marked by the $\diamondsuit$), adjacent to the cochlear position where the facial nerve canal courses superiorly over the cochlear labyrinth. The change in J_{rc} for vestibular ossification (gray line) is greatest toward the base for both apical and basal stimulation.

In the Nucleus psEAM, the influence of the facial nerve canal also appears to be relatively small. The small elevation of T_p^* for EP5 (Figure 4-8A) appears to be due to the proximity of the facial nerve canal. The two ring electrodes forming the EP5 pair rest against the lateral bony wall immediacy adjacent to the facial nerve canal, suggesting the facial canal may slightly shunt current delivered to EP5, increasing the predicted behavioral threshold estimate T_p^*.

In Chapter 2 the total longitudinal current exiting the bony duct of the cochlea into the vestibular system was measured (see Figure 2-17 p.53) to investigate the amount of the stimulus current entering the vestibular labyrinth. The magnitude of the vestibular current is impacted by the various anatomical manipulations discussed thus far. Plotted in panel A of Figure 4-13 is the vestibular current exiting the cochlea for stimulation of each electrode under different anatomical modifications.

Ossifying the vestibular system nearly eliminates the vestibular current, while ossifying the facial canal has only a small impact. An impacted section such as the one described in section 4.2.5 increases the current exiting the cochlea into the vestibular labyrinth when stimulating basal to the occlusion while decreasing it when stimulating apical to the occlusion (panel B). Finally, the fibro-osseous deposit in the basal turn of the Ineraid psEAM tends to lower the vestibular current, forcing current to remain in the cochlear spiral and exit through the modiolus into the IAM (panel C).

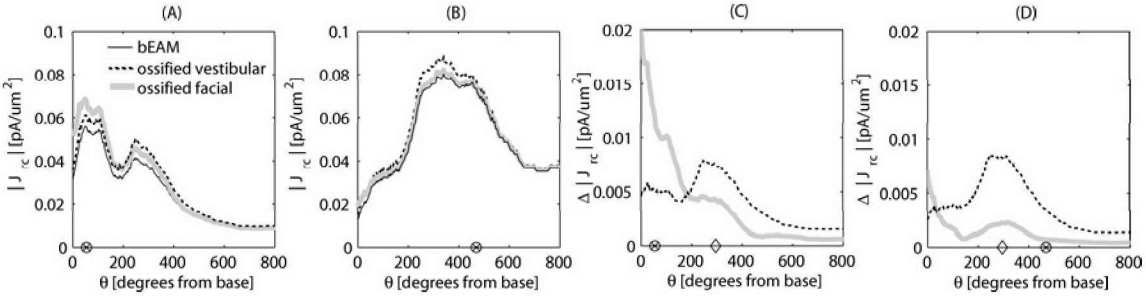

Figure 4-12: (A-B) $|J_{rc}|$ versus θ for basal (panel A) and apical (panel B) stimulation in the bEAM and bEAM version with the facial nerve canal (dotted line) or vestibular labyrinth (gray line) ossified. (C-D) As in panels A and B with the change in $|J_{rc}|$ plotted where positive values denote an increase in current with the ossified bEAM. The position in θ of the facial nerve is denoted by $\diamondsuit$.

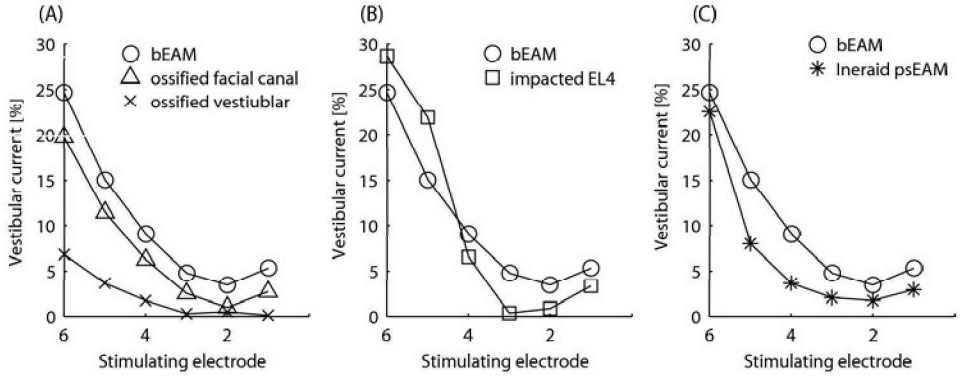

Figure 4-13: Vestibular current versus stimulating electrode comparing the bEAM to (A) bEAM versions with the facial nerve canal or vestibular labyrinth ossified, (B) the bEAM with a 5 kΩcm impacting tissue surrounding EL4, and (C) the Ineraid psEAM. The vestibular current refers to longitudinal current exiting the cochlear duct into the vestibular labyrinth. This current (expressed as a percentage of the stimulus current) is measured by integrating the current density on a plane as shown in Figure 2-17 (p.53).

4.2.8 Increasing spatial selectivity

Increasing the spatial selectivity of each intracochlear electrode has typically been considered advantageous. To this end, more recent electrode arrays have incorporated a positioning system designed to shift the electrode so it hugs the modiolar wall. Shifting the stimulating electrode medially from the lateral wall toward the modiolus in the bEAM did not have any remarkable effect on either the model's prediction of current entering Rosenthal's canal, J_{rc}, or on its prediction of single-fiber threshold. For example, shown in Figure 4-14 are predictions for J_{rc} (panel A) and SFT (panel B) as the EL3 electrode is moved from its position near the lateral wall, to a position in the center of the scala tympani, to a medial position near the modiolus. The peak J_{rc} for the medial electrode position is slightly higher (+2.1 dB) than the lateral position. Likewise, in panel B the minimum-threshold fiber is sightly lower (-2 dB) for the modiolar electrode position.

While moving the electrode medially does tend to slightly increase the spatial selectivity, this effect does not seem to be appreciable, likely because the bone-to-fluid resistivity leads to substantial longitudinal current spread regardless of whether the electrodes lies at the medial or lateral wall. Accordingly, the model predictions suggest a modiolus-hugging electrode will marginally lower thresholds and increase spatial selectivity, but the effect is predicted to be small (see discussion section). In the following sections, alternative manipulations are made to test their influence on spatial selectivity.

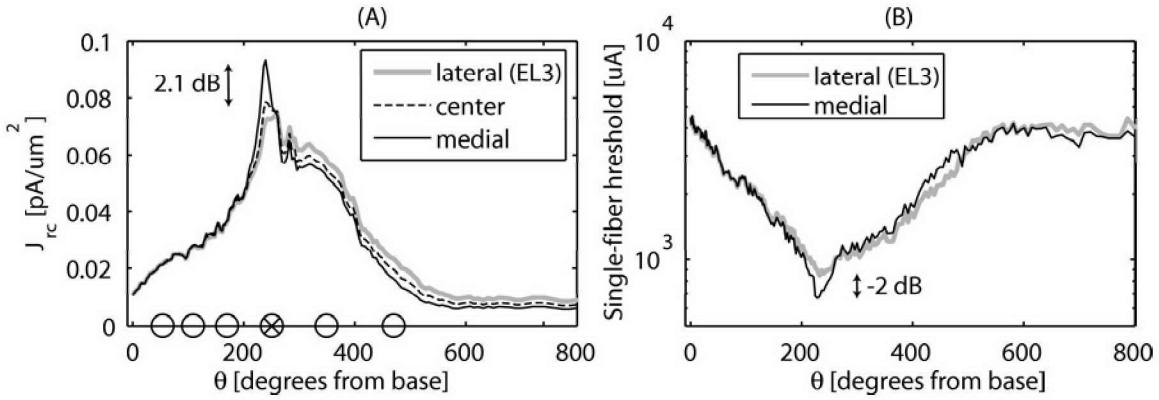

Figure 4-14: (A) J_{rc} versus θ in the bEAM for monopolar stimulation of EL3 positioned at the lateral wall (gray), at the center of the scala tympani (broken), and medially near the modiolar wall (black). All electrodes are at the same θ. The peak J_{rc} for the medial electrode position is slightly higher (+2.1 dB) than for the lateral position as shown by ↕. (B) Single-fiber threshold versus θ predicted for stimulation of EL3 positioned near the lateral wall (gray) and positioned medially near the modiolar wall (black). The minimum-threshold fiber is sightly lower (-2 dB) for the modiolar electrode position as shown by ↕.

Current flow in a periodically-obstructed cochlea

To test the extent to which periodically-spaced tissue deposits (or material) could be used to sharpen spatial selectivity by increasing the longitudinal impedance and guiding current into the modiolus, the bEAM was modified to include periodic segments of 5-kΩcm or 300-Ωcm tissue as illustrated in Figure 4-15A. Three tissue segments were tested with each separated by 1-mm fluid gaps containing an electrode: 3-mm segments of 300-Ωcm tissue, 3-mm segments of 5-kΩcm tissue, and 1-mm segments of 5-kΩcm tissue. Shown in panels B and C are predictions of $|J_{rc}|$ and single-fiber thresholds, respectively, for the bEAM and the periodically-obstructed bEAM. With only a millimeter of 5-kΩcm tissue separating adjacent compartments, the model predicts a focused $|J_{rc}|$ and a corresponding decrease in threshold at the position of the stimulating electrode. The 6-dB width used to characterize the spatial selectivity of SFTs (see Chapter 2) is reduced from 11.1 mm to 1.25 mm (29.5 deg, 0.28 octaves).

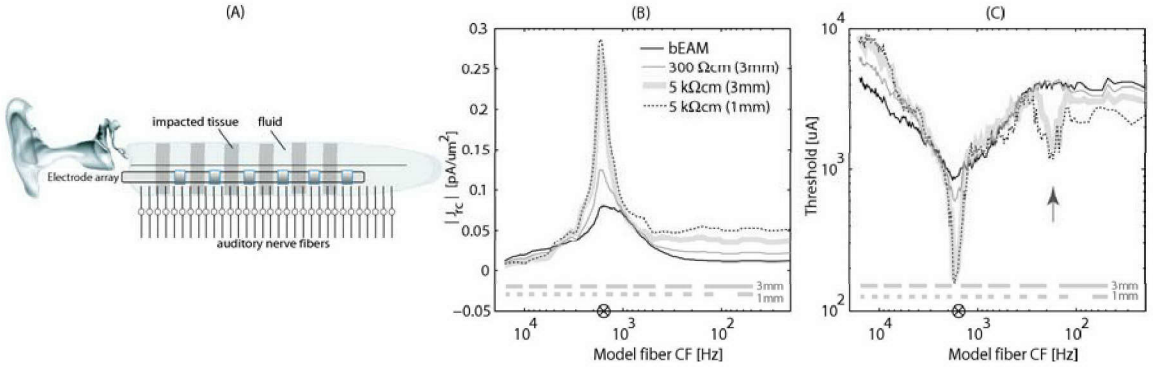

Figure 4-15: (A) Schematic of the periodically-obstructed cochlea. Regions of tissue are separated by 1-mm gaps each containing an electrode. Three tissue segments were tested: 3-mm segments of 300-Ωcm tissue, 3-mm segments of 5-kΩcm tissue, and 1-mm segments of 5-kΩcm tissue. (B) $|J_{rc}|$ versus model fiber CF for three periodically-obstructed EAMs. Spacing of 1- and 3-mm tissue segments is shown just above the x-axis with the gray bars denoting tissue. The stimulus level is 1 μA in each case. (C) Single-fiber threshold versus θ. A region where cross-turn coupling occurs is marked by ↑.

Replacement of cochlear fluids with adipose tissue

While the periodic tissue obstructions illustrated in Figure 4-15A tend to increase the predicted spatial selectivity of a monopolar electrode, delivering material or initiating tissue growth to create these insulated compartments would be difficult. An alternative is to completely replace the perilymphatic fluid of the inner ear with a tissue having a resistivity closer to that of the bone lining the otic capsule. For instance, an autologous suspension of mature adipose cells (in artificial perilymph) could be infused with a micro-pump to replace the cochlear fluid with cells harvested from a fat autograft. The graft would likely need to be partially digested (collagenase treated)

and processed to yield a suspension fluid enough to inject.[13] This suspension would contain adipose tissue constituents, including fibrocytes, that, after transplantation, would be expected to reestablish the collagen extra-cellular matrix (fibrogenesis), eventually replacing the fluid suspension with loose connective tissue similar to that of native subcutaneous fat.

Shown in panels A and B of Figure 4-16 are predictions of $|J_{rc}|$ and SFTs for the bEAM (gray) and adipose-infused bEAM (black). Both the current flow and SFTs show a substantial increase in spatial selectivity for monopolar stimulation. In the adipose-filled cochlea, the 6-dB width is reduced from 11.1 mm to approximately 0.84 mm (0.18 octaves, 20.1 degrees).

A bulk resistivity of 2,500 Ωcm has been assigned to the adipose tissue in these simulations [174, 25], although this value is likely to be sensitive to: (1) the volumetric ratio (volume fraction) of adipose cells to the fluid phase of the injected suspension [194], (2) the degree to which the entire cochlear fluid space is replaced with the adipose-type tissue, and (3) the extent of adipose cell adherence to adjacent structures. For example if the volume ratio of injected suspension were only 50 percent cellular, the resistivity of the perilymphatic suspension would only be expected to increase from 50 to roughly 140 Ωcm.[14] Our simulations suggest significant gains in spatial selectivity begin to occur using an adipose suspension with a resistivity as low as 300-600 Ωcm . Ideally one would achieve a high volume ratio of adipose cells in a reconstituted extracellular matrix, completely filling the cochlear spiral with fat cells without initiating an inflammatory reaction in the native cochlear tissues for the transplanted adipose cells.[15]

There are two primary mechanisms by which replacement of the cochlear fluid with a tissue or material of higher resistivity may lead to a more localized neural response. First, the increased resistivity will lead to increased potential gradients

[13]Since fat autographs have been successfully used in otologic surgery (e.g., acoustic neuroma) where the fat is in direct contact with cerebrospinal fluid (CSF), it is unlikely the perilymphatic environment would cause adipocyte degeneration. Many other safety issues would need to be verified in an animal model, for example whether the adipose cells interfere with cochlear homoeostasis, the frequency of microemboli [171], and the migration of fat into the subarachnoid CSF space [173]. Additionally, evidence has been reported (for example, Guilak et al. [68]) that human adipose-derived adult stem cells can be induced to differentiate into adipogenic, osteogenic, chondrogenic, neurogenic cell lineages. This expands the possibilities of what tissues the injected cells might eventually establish (e.g., bone or cartilage), as well as a variety of bioengineering therapeutics. For instance, transfection of the infused cells with viral vectors could be used to continuously deliver an *in vivo* cocktail of trophic factors that might either promote or discourage a target response (e.g., bone remodeling).

[14]Smye [194] applied the techniques of Hanai [71] to biologic tissues to describe the dielectric properties of a suspension of weakly conducting spherical cells in a conducting medium as a function of frequency, the volume fraction of the cells, and the cell conductivity. Using equation 28 of Smye [194] one can estimate that for a very weakly conductive cell in a 50-Ωcm solution, a 50% volume fraction of the cells will increase the resistivity to approximately 140 Ωcm .

[15]For example, in the mouse the typical method for isolating adipose cells by collagenase digestion has been shown to initiate inflammatory mediators [176].

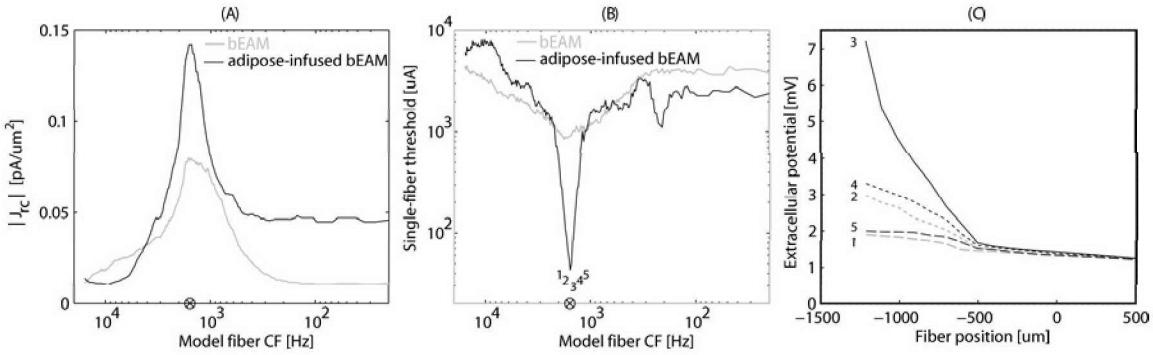

Figure 4-16: (A) Predictions of $|J_{rc}|$ versus model fiber CF for the bEAM (gray) and adipose-infused bEAM (black) in response to 1 μA of stimulation. (B) Predictions of single-fiber threshold, with the infused bEAM showing a 6 dB-width of ≈0.84 mm (0.18 octaves, 20.1 degrees). (C) Extracellular potential along model fibers labeled 1-5 in panel B, corresponding to -45, -25, 0, +25, and +45 degrees relative to the stimulating electrode. The potential gradient along fiber 3 (nearest to the electrode) changes abruptly as the fiber courses from the osseous spiral lamina into the spongy modiolus where the tissue resistivity, and thus the potential gradients, are lower.

in the interstitial fluids outside the nerve-fiber's peripheral process, tending to drive current across the cellular membrane and lowering thresholds. Shown in panel C of Figure 4-16 are the extracellular potentials along five model fibers (labeled 1-5 in panel B), representing the model fiber immediately adjacent to the stimulating electrode (marked 3) along with model fibers at ± 25 and ± 45 degrees to the electrode. The steep potential gradient on the peripheral process of the model fiber at the electrode is similar to those predicted in the homogenous model (see Figure 2-24, p.67), substantially decreasing threshold while increasing the spatial selectivity. Note the potential gradient along this fiber changes abruptly as the fiber courses from the osseous spiral lamina into the spongy modiolus where the tissue resistivity, and thus the potential gradients, are lower.

Second, the increased resistivity tends to decrease the longitudinal spread of current by counterbalancing the conductively mismatch between bone and cochlear fluid that, in previous chapters, has been shown to be responsible for the extensive spread of current across large spans of cochlear length. This alone is the operative method for increasing selectivity in the periodically-obstructed bEAM described in Figure 4-15.

Focused stimulating configurations

Modifications to the anatomy could be combined with modifications to the stimulating electrode configuration to further heighten the increase in spatial selectivity observed in the adipose-infused bEAM. One configuration that has been used is quadrupolar stimulation (also called tripolar) where current is delivered between intracochlear electrode e ($EL_{(e)}$) and its flanking neighbors ($EL_{(e-1)}$ and $EL_{(e+1)}$). This

is called quadrupolar because it resembles the superposition of two bipolar stimuli applied to three neighboring electrodes. Alternatively, a combination of monopolar and quadrupolar can be created (e.g., [228, 126]), by the superposition two stimuli applied to $EL_{(e)}$: a monopolar current returning to extracochlear return (E_R), and a quadrupolar current returning to the neighboring intracochlear $EL_{(e-1)}$ and $EL_{(e+1)}$ electrodes. The proportion of quadrupolar current (p_q) can be adjusted, changing this stimulus along a continuum between monopolar ($p_q = 0$) and quadrupolar stimulation ($p_q = 1$).[16] For convenience we refer this as hybrid-quadrupolar (HQ, after [126]), where the $HQ_{75\%}$ case denotes 75% of the current delivered to the center electrode returns to the flanking electrodes while 25% returns the extracochlear return (E_R).

Shown in panel A of Figure 4-17 are predictions of J_{rc} made using the bEAM where in each trace the percentage of quadrupolar current (p_q) varies from 0 (monopolar) to 100% (quadrupolar). In panel B one notices the quadrupolar case ($HQ_{100\%}$) J_{rc} has a more focused central peak located at the stimulating electrode ($\otimes$), along with alternate-polarity side-lobes near each of the flanking electrodes ($\oslash$). The $HQ_{75\%}$ case (highlighted) gives the most focused prediction of J_{rc} without alternate-phase side-lobes for the values of p_q tested. Here we choose the criteria for "most-focused" as the maximum value of p_q having a J_{rc} trace without negative side-lobes.

For the adipose-infused bEAM, variation in J_{rc} as the stimulus transitions from monopolar to quadrupolar (panel C) shows $HQ_{50\%}$ (highlighted) to have the most focused J_{rc} without negative side-lobes. In panel D, the $HQ_{50\%}$ case in the adipose-infused bEAM is compared to the $HQ_{75\%}$ case in the bEAM, showing (1) an increased amount of current entering Rosenthal's canal, and (2) a moderately more focused pattern.

These results suggest an optimum hybrid-quadrupolar stimulus can be designed for both the implanted ear without any intracochlear tissue deposits and for the adipose-infused cochlea. Here the optimum J_{rc} in the adipose-infused model could lead to substantially more focused stimulation of the spiral ganglion.

---

[16] More precisely, the unit current distribution across electrodes $EL_{(e-1)}$,$EL_{(e)}$, $EL_{(e+1)}$, and EL_R is $-\frac{(p_q)}{2}$, $+1$, $-\frac{(p_q)}{2}$, and $-(1-p_q)$ with $0 \leqslant p_q \leqslant 1$. Here p_q is the proportion of quadrupolar current such that $p = 0$ is equivalent to monopolar stimulation of EL_e, while $p = 1$ represents a tripolar stimulus with half the current return on each of the two flanking electrodes (EL_{e-1} and EL_{e+1}).

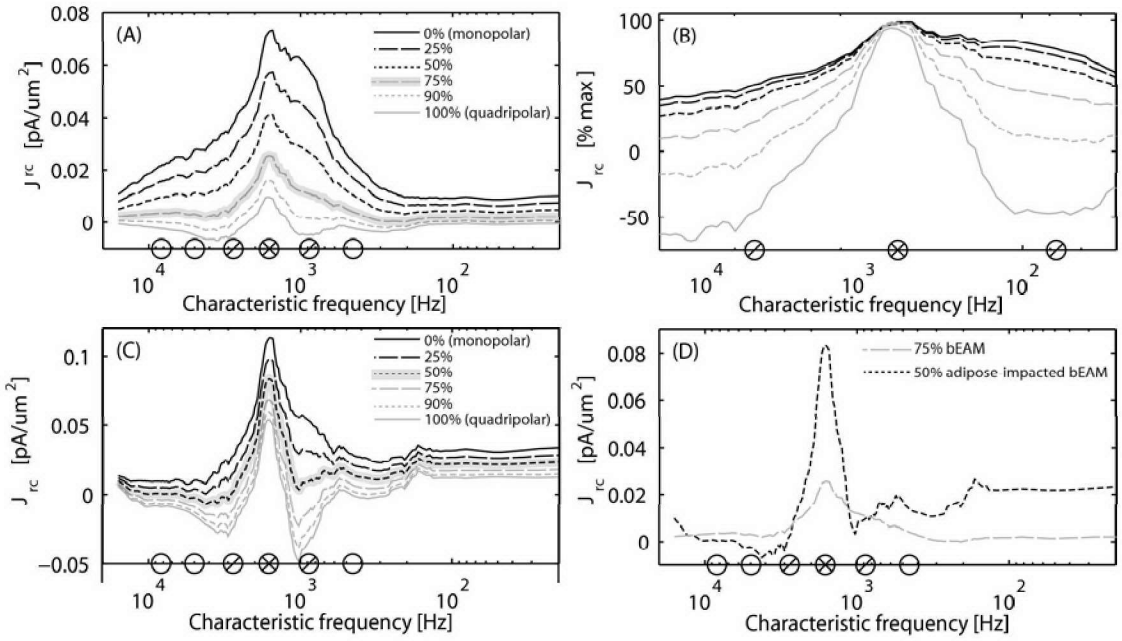

Figure 4-17: (A) J_{rc} versus model fiber CF predicted by the bEAM for values of p_q (the proportion of quadrupolar current) between 0 (monopolar) and 1 (quadrupolar). Quadrupolar current is delivered between the stimulating electrode ($\otimes$) and its flanking neighbors ($\oslash$). (B) As in panel A, with each trace normalized as a percent maximum. (C) J_{rc} in the adipose-infused bEAM for the same values of p_q between 0 and 1. (D) Comparison of the $HQ_{75\%}$ case in the bEAM with the $HQ_{50\%}$ case in the adipose-infused bEAM.

4.3 Discussion

The unmyelinated human spiral ganglion cell

The observation that spiral ganglion perikarya are generally unmyelinated [157] may have a large impact on the manner in which they are electrically excited. In animal models used to study electric stimulation, the polarization of the cell body membrane (seen in Figure 4-1) is not be expected to be significant because (1) voltage-gated channels are unlikely to be located at myelinated segments of the cell membrane, and (2) due to the many layers of myelin, the voltage drop across the neural membrane would only be a fraction of the voltage drop between the cell interior and the extracellular space.

However, the polarization of unmyelinated spherical cells is well described and has been observed experimentally using fluorescence imaging of cell preparations loaded with a voltage-sensitive dye (e.g., [79, 107]). If unmyelinated human SGCs have voltage-gated channels on or near the cell body, it is conceivable this type of depolarization could influence the initiation of an action potential.

Clusters of neighboring cells also might have an impact. For example, Ota and Kimura [157] report several human SGC perikarya to be surrounded by a single sheath of satellite cells, with neighboring cell bodies in close apposition and often contacting each other (also reported by [45, 210]). While non-synaptic specializations have been reported in the apposed cellular membranes between neighboring human SGC perikarya [211], the functional significance of these and whether they allow ion exchange (via gap junctions) or play a role in ephaptic transmission remains unknown. If an electrical connection were to exist between two or more apposed SGC perikarya, for example via gap junctions, it is conceivable these cells could form a multi-cell complex where the intracellular space essentially forms an axioplasmic isopotential, with increased polarization occurring at the poles of the multi-cell complex (e.g., [34, 33, 44]).

To account for these influences (not represented in a cable model), a 3D model of a cluster of SGCs might be created using transport lattice methods such as those described by Gowrishankar et al. [63]. These methods allow multicellular systems with irregular shapes to be represented on a regular meshwork. Each element of the lattice can include passive resistive and capacitive components, with elements representing nodal patches of cellular membrane also including nonlinear sources, allowing a spatio-temporal solution of the system that includes the prediction of propagating action potentials (see [201]).

In summary, two serious concerns can be identified with the one-dimensional single-fiber models such as the McNeal-type [125] used here. First is the failure of a peripherally-initiated action potential to reliably propagate past the unmyelinated cell body when a realistic morphology is used to derive the compartmental model (see discussion on p.60). This failure of trans-perikaryal conduction may be a result of one

or more inappropriate assumptions of applying the McNeal model to a spiral ganglion cell. Second is the possibility of a non-negligible transmembrane voltage elicited along patches of the cell body orthogonal to an applied electric field, due to cell polarization.

The influence of peripheral dendrites on ECAP recordings

If in implanted humans the action potential does tend to initiate on the cell body, the model predicts that the influence of the peripheral dendrites on the ECAP will be dependant on the spatial relationship between the activated fibers and the recording electrode. The model predicts this is because the antidromic AP recorded on nearby electrodes will often have a positive-to-negative morphology opposite in phase to the morphology of the orthodromic AP.[17] The model predicts that the orthodromic AP will dominate the recorded response, giving rise to a similar N1P1 morphology regardless of the recording electrode position, as is seen experimentally.

The asymmetric relationship between the cochlea and internal auditory meatus

The model's prediction that a local minimum in impedance can exist between the fluid of the bony duct and the internal auditory meatus is one example of how the detailed anatomy can influence the pattern of intracochlear current flow and neural activation. This suggests that with monopolar stimulation, the intricate 3D anatomy of the cochlea dictates a pattern of current flow much different than that predicted by a transmission line model. For example, taking $[J_{rc}(\theta)]^{-1}$ as the most rudimentary estimate of the pattern of neural activation (i.e., increased J_{rc} leads to lower thresholds), one can see the influence of this asymmetry. In Figure 4-18 the inverse of (J_{rc}) is plotted versus θ for basal and apical stimulation. In both, a significant amount of ectopic excitation is expected for areas of Rosenthal's canal between 250 and 400 degrees that are relatively remote from the electrode, a prediction that is due in large part to the asymmetry discussed in section 4.2.3. Further credibility to this prediction is given by the especially tight fit between the archival IP_d data and the intracochlear potential predictions (IP_p) for apical stimulation made using the Ineraid psEAM (see Chapter 3). In future EAMs of patients who in life used monopolar stimulation strategies, the detailed anatomy of the relationship between the internal auditory meatus and the modiolus will be an important consideration.

Distribution of surviving spiral ganglion cells

Kawano el al. [95] attempted to predict behavioral thresholds (T_d) for five subjects using 3D reconstructions of implanted temporal bones. In only two of five subjects was a significant relationship between SGC density and behavioral threshold level

[17]It is interesting to note that Miller et al. [133] recorded a positive-to-negative morphology with anodic monophasic stimuli in the cat which they attributed to antidromic action potentials initiated at a central site.

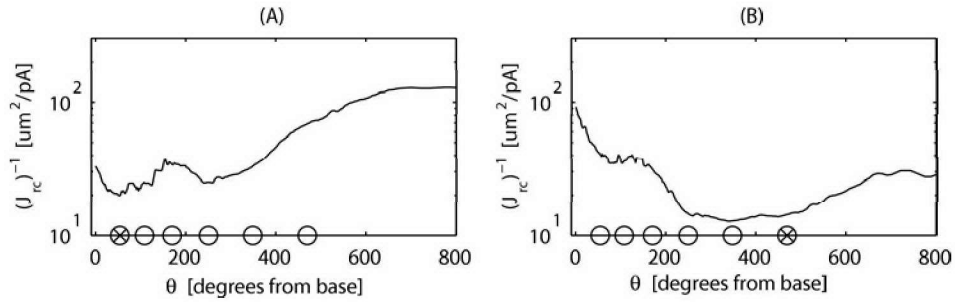

Figure 4-18: $[J_{rc}(\theta)]^{-}1$ versus θ for basal (panel A) and apical (panel B) stimulation using the bEAM.

found; in one subject the expected inverse correlation was found ($r^2 = 0.28$, subject VD) while in the other a counter-intuitive positive correlation was found ($r^2 = 0.24$, subject NM). Likewise, in earlier investigations comparing segmental SGC counts to behavioral thresholds across stimulating electrodes at our institution (Khan el al. [99]), in only one of five temporal bones studied was a significant negative correlation ($r^2 = 0.39$, subject N2) between SGC count and threshold found. This same subject was used to derive the Nucleus psEAM, which in the last chapter was shown to predict up to 84% of the variance in behaviorial threshold (see Figure 3-5).

Surprisingly, our simulations suggest that, as represented by the model, the detailed pattern of residual spiral ganglion survival may have little to do with psychophysical threshold. Only when there was a substantial region of cochlear length devoid of any SGCs did the SGC pattern ($N_{f(i)}$) tend to impact the threshold prediction. If behavioral threshold is determined by the excitation of only a few neurons, this is consistent with the idea that a small number of SGCs evenly spread across the cochlear length could lead to relatively low behavioral thresholds. This may also explain the inability of the Kawano and Kahn studies to find a consistent relationship between segmental SGC count and behavioral threshold.

It is encouraging that the most salient feature of the Nucleus behavioral T_d pattern, specifically the elevated EP19 measure that is nearly double its neighbors (see Figure 4-8), was captured by the Nucleus psEAM. According to the model, this elevated threshold is due primarily to its orientation in the coiled region of the array as opposed to the lack of SGCs, demonstrating that other factors of the peripheral anatomy besides SGC survival can determine the pattern of behavioral thresholds across the array. This suggests that even a very detailed representation of the surviving SGCs (e.g., a 3D representation of every single cell counted from every single histologically-prepared section) may not provide better predictions of behavioral threshold data. In other words, what may be important to identify and encode in a model are regions of cochlear length completely devoid of spiral ganglion cells.

Influence of longitudinal impedance

Another counter-intuitive prediction is the influence of a localized increase in impedance along the cochlear duct. For a monopolar stimulating electrode imbedded in a complete tissue occlusion, the increased longitudinal resistance-per-millimeter along the bony duct rises above the impedance along a path into the neural tissues of the modiolus, tending to prevent longitudinal current spread and focus current into the modiolus. We used this observation to suggest infusing the entire cochlea with a higher resistivity material to improve spatial selectivity. It should be emphasized here that this assumes a nearly complete occlusion of the bony canal for several millimeters, as opposed to a deposit that fills only a small fraction of the cross-sectional area, allowing an appreciable fluid communication across the tissue deposit.

Influence of new bone and fibrous tissue: Ineraid psEAM

Since the impact of new bone and fibrous tissues is likely different in the Ineraid and Nucleus bones (because of monopolar versus bipolar stimulation), we discuss them separately beginning with the Ineraid case. As mentioned in section 4.2.7, one predicted influence of the fibro-osseous deposit at the base is to impede current flow into the vestibular system, increasing the current exiting the cochlea via the modiolus.

For the Ineraid psEAM with a single IAM return, another predicted influence of the fibro-osseous deposit is to focus the stimulus currents from the basal electrodes into the modiolus, increasing J_{rc} (panel B, Figure 4-11) while decreasing the predicted behavioral thresholds, T_p (Figure 3-5A) and T_p^*(Figure 4-8C).

In the last chapter, we concluded that the disagreement between the archival data and the IP_p, T_p, and $ECAP_p$ predictions for basal stimulation may reflect (1) grounding pathways which need to include a secondary basal ground, or (2) a misrepresentation of the fibro-osseous deposit found in the basal turn near the cochleostomy site. There are at least two observations that suggest at least some current may exit via an alternative basal ground when stimulating basal electrodes.

First, including a basal ground improved the fit of the predicted intracochlear potentials, IP_p, to the measured IP_d . Replicated in panels A and B of Figure 4-19 are IP_p predictions using the psEAM with a single IAM ground and the dual-ground case with a secondary round window ground. The dual-ground case slightly improves the fit by lowering the IP_p potential gradients. In Panel C the dual ground case is shown for the bEAM without any fibro-osseous deposits. Collectively, panels A-C suggest a best fit to the IP_d data might be obtained by both adding the basal ground and lowering the resistivity assigned to new bone and/or fibrous tissue, predicting an IP_p pattern somewhere between that displayed in panels B and C.

Second, the basal ground tends to lower the current entering the modiolus for basal stimulating electrodes, consistent with the increasing behavioral thresholds (T_d) toward the base. With a single IAM ground, the psEAM predictions using either T_p from the last chapter, or the simplified T_p^* used here, both predict suspiciously low

thresholds for the two basal electrodes encapsulated in the fibro-osseous mass of the basal turn (e.g., EL6 and EL5 of T_p^* in panel D). Adding the basal ground (panel E) lowers the predicted J_{rc} for these two basal electrodes, returning T_p^* estimates that predict the T_d data better than any other model, accounting for 91% of the variance in the Ineraid behavioral thresholds.

A final alternative, is that an appreciable current exits via the basal ground only for stimulation of basal electrodes impacted in new bone and fibrous tissue, while current delivered to apical electrodes exits exclusively via the IAM pathway. The IP_p predictions for apical stimulation in the last chapter show a tight fit between predicted IP_p and measured IP_d (Figure 3-2C p.129) consistent with the idea that, for apical stimulation, current exits exclusively via the IAM.

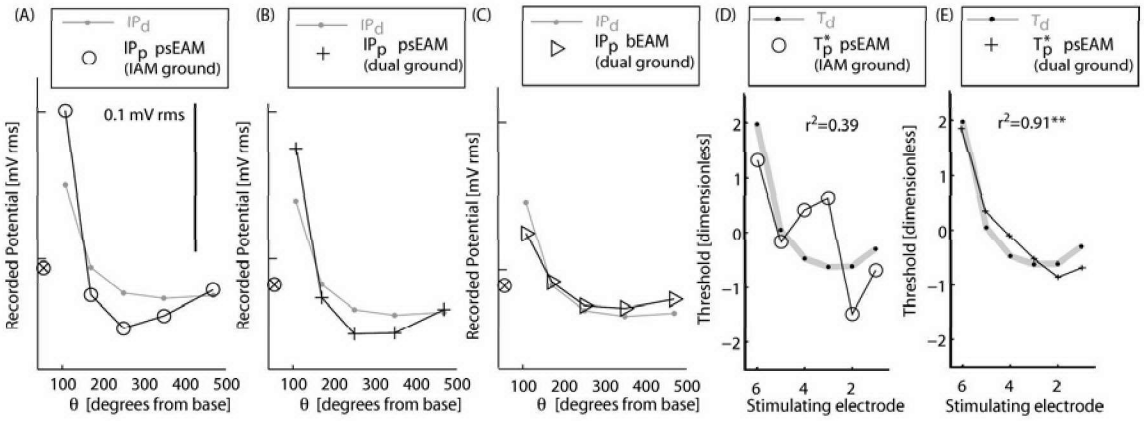

Figure 4-19: (A-C) Model-predicted (IP_p, black) and measured (IP_d, gray) intracochlear potentials versus θ for basal stimulation (EL6). Shown are predictions using the psEAM with an IAM ground (panel A), the psEAM with a dual ground (panel B), and the bEAM with a dual ground (panel C). (D-E) Model-predicted T_p^* (black) and measured T_d (gray) versus stimulating electrode for the psEAM with an IAM ground (panel D) and the dual-ground case (panel E). Statistical significance is given by asterisks: $^*(p < 0.05)$, $^{**}(p < 0.01)$. Note with only 6 points, statistical significance can depend on the test used, as is the case here. The Pearson product-moment correlation coefficient shows $r^2 = 0.91^{**}$ while the Spearman correlation coefficient gives $r^2 = 0.51$, insignificant at the 0.05 level.

Influence of new bone and fibrous tissue: Nucleus psEAM

In their 3D reconstructions of temporal bones implanted with the Nucleus device, Kawano et al. [95] reported a significant correlation between behavioral threshold and new bone (or fibrous tissue) in three of five bones studied. Two showed a positive correlation (subjects VD and WE) while one showed a negative correlation (subject OH). Kawano's results suggest either the influence of new bone and soft tissue was not captured by their reconstruction, or the influence is not consistent across implanted subjects.

In the Nucleus psEAM the impact of new bone and soft tissues appears to increase the current entering the modiolus as a result of the fibro-osseous tissues behaving as an insulator, resisting longitudinal current flow in the fluid between the contacts of the bipolar pair that otherwise occurs. Note this is only predicted to occur when a significant amount of tissue fills the cross-sectional area of the bony labyrinth between electrode pairs. In contrast, the thin layer of fibrous tissue found in the apical half of the Ineraid device was predicted to have almost no impact on current flow.

Other simulations using the bEAM suggest that it is possible for the fibro-osseous mass to either *increase or decrease* the current entering the modiolus. For example, in Figure 4-20 are four examples depicting the change in J_{rc} after including a tissue deposit around a bipolar pair. In each panel, the bipolar pattern of J_{rc} in the bEAM is shown with (black) and without (gray) the tissue deposit illustrated at the upper right. In panel A the entire cochlear duct around the electrode pair is filled by a 5-kΩcm tissue deposit, leading to an increase in J_{rc}. In panel B, approximately 50% of the cross-sectional area of the duct is filled by a deposit encapsulating the electrode pair, increasing J_{rc} to a lesser extent. In panel C, a deposit completely encapsulates the electrode pair, with an internal fluid pocket such that the electrode pair is surrounded by fluid. Here J_{rc} decreases significantly. In panel D, an open-ended, cylindrical deposit surrounds the electrode pair, allowing current to exit at both ends. In this case, J_{rc} is once again predicted to *increase*. Careful comparison of panels B and D will show that the peaks in the J_{rc} pattern in D are further separated than in B (because current tends to exit the cylindrical deposit before flowing through modiolar tissues).

On a qualitative level, the inclusion of the fibro-osseous tissues tended to better represent variation in T_d across the array, for example the increase in T_d near EP11 (compare T_p^* in panels A and B of Figure 4-8). One difficulty yet to be solved is how to assign a bulk resistivity value to a fibro-osseous mass consisting of an intricate architecture of calcified new bone and the fibrous tissue surrounding it that contains pockets of perilymphatic fluid. In formulating the Nucleus psEAM this was a difficult task, since it is impractical to separate on a voxel-by-voxel basis calcified voxels from the pockets of tissue that separate them.

It is possible the detailed architecture of the new bone, which we have not repre-

sented, forms an anisotropic capsule around the electrode array leaving a thin fluid layer on the interior in which an appreciable current flows. In this case we would expect that the fibro-osseous mass might tend to act as a tubular insulator, shielding the modiolus, decreasing J_{rc}, and increasing behaviorial threshold estimates.

In summary, our preliminary modeling suggests a significant amount of fibro-osseous tissue may force more current into the modiolus (increasing J_{rc} and decreasing behavioral thresholds), however this prediction is based on several assumptions about the detailed architecture of the calcification in the fibro-osseous mass. Alternatively in areas where only a small fraction of the cross sectional area is occupied by a fibro-osseous tissue, the models predict a negligible effect.

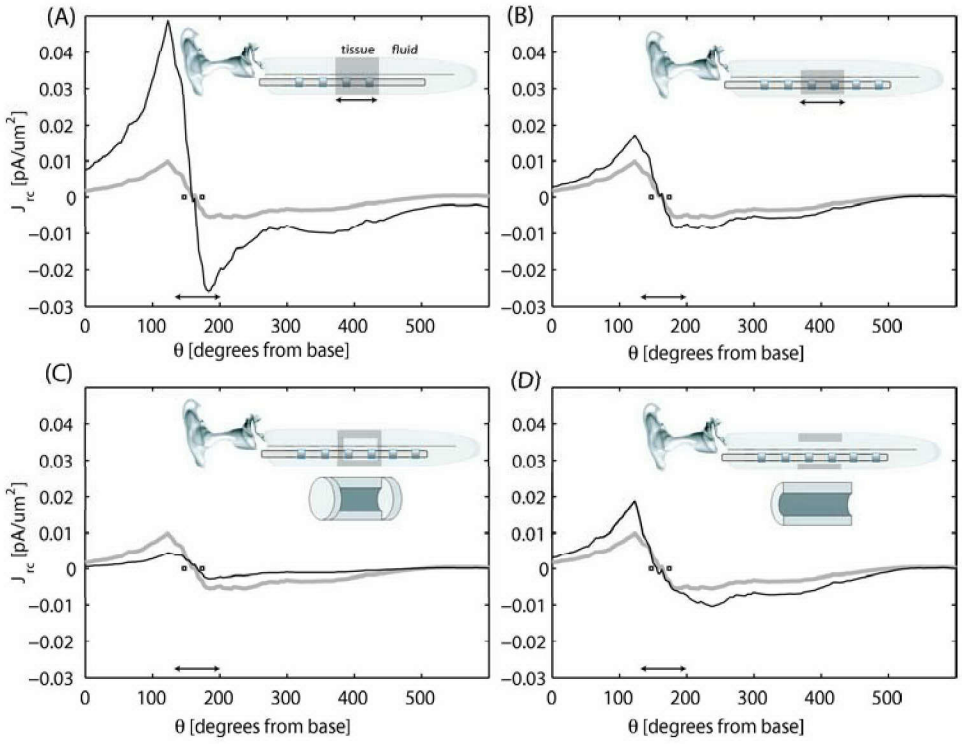

Figure 4-20: J_{rc} versus θ in the bEAM in response to bipolar stimulation with (black) and without (gray) tissue deposits of various constructions. In each panel the region spanned by the 5-kΩcm deposit is given above the x-axis by $\longleftrightarrow$, while the electrode contacts are marked by □s. The arrangement of the tissue deposit is schematized in the upper-right corner, showing a complete occlusion (panel A), a partial occlusion centered on the electrode pair (panel B), a fluid-filled cylindrical deposit closed at both ends (panel C), and a cylindrical deposit open at both ends (panel D).

Increasing spatial selectivity

Moving the position of a monopolar electrode (EL3) from the lateral to medial wall is predicted to have little influence, producing only a slightly more focused activation pattern, and slightly lower thresholds. This agrees with clinical investigations of modiolus-hugging arrays. For example, Hay-McCutcheon [76] did not find a reduction

in the threshold of either evoked potentials (ECAPs and EABR) or behavioral thresholds in a group of 10 patients implanted with a modiolus-hugging electrode (Nucleus CI24R device). Studies by Pfingst el al. [161] and ver Weert el al. [214] also found little difference in behavioral threshold between patients implanted with traditional and modiolus-hugging electrodes. Other authors have reported a small decrease in thresholds (e.g., -13.8 clinical units [182] or -2.3 dB) with modiolus-hugging arrays. This -2.3 dB decrease agrees with $\approx$2 dB effect size predicted by the model in Figure 4-14, and is close to the data reported in animal preparations. For example, using implanted cats Shepherd et al. [187] (table III) reported an average EABR threshold decrease of -4.27 dB after moving a bipolar pair medially from the outer wall. Considering these results it is not surprising that modiolus-hugging electrode arrays have not been reported to consistently improve performance.

Our modeling predicts the medial-lateral position of the electrode imparts a near-negligible change in spatial selectivity (as measured by J_{rc}) because the ratio of bone-to-fluid resistivity continues to cause undesired longitudinal current spread regardless of the electrode's position. Accordingly, we tested two methods for addressing longitudinal current spread by (1) placing periodic segments of tissue or material between electrodes or (2) replacing the cochlear fluid in its entirety with a higher resistivity material.

As one would expect, placing periodic segments of tissue between electrodes is predicted to focus the current into the modiolus, enhancing the spatial selectivity of each stimulating electrode as in Figure 4-15. These periodically-placed segments could be composed of inert materials (e.g., silicone), bio-derived macromolecules (e.g., bovine-purified collagen), biodegradable thermoplastics (e.g., polylactic acid), transplanted tissues or cell (e.g., adipocytes isolated from a subcutaneous, autologous fat graft), or a combination of these. The design goal being to replace the perilymphatic fluid space between neighboring electrodes with a material, tissue, or tissue-seeded scaffold that would eventually lead to a high impedance seal between neighboring contacts. However delivering these segments remains a challenging task. Replacing the entire cochlear fluid supply with a material or tissue of higher resistivity, such as adipose tissue, may be more feasible.

In the adipose-infused case, the potential gradients along fibers inside the osseous spiral lamina (which now protrudes into the infused adipose tissue) should increase substantially as shown in Figure 4-16C. Accordingly, an abrupt change in the gradient occurs between the osseous spiral lamina and the modiolar tissue (which has been modeled as 300 Ωcm). This type of effect has been documented elsewhere. For example, Grill [66] (figure 10) modeled how a nerve fiber crossing an interface between media of different conductivities can influence transmembrane potentials and lower excitation thresholds.

4.4 Chapter synopsis

In this chapter a collection of investigations are made regarding how individual attributes of the human peripheral anatomy can impact intracochlear current flow and the elicited neural activation pattern. The ultimate motivation is to identify those attributes that impose a relatively large impact and consequently need to be accounted for in order to predict differences that occur across patients. Once these are identified, we can use them to interpret histopathological variations found in the growing collection of implanted temporal bones available for study, hopefully refining our approach to eventually learn how the aspects of the peripheral anatomy can impact patient benefit.

We make several predictions regarding the impact of the anatomy found in implanted human ears. First, given the appreciable current flow predicted to be nearly parallel to the path of the auditory nerve fibers in Rosenthal's canal, the unmyelinated human SGCs require special attention. Appreciable membrane voltages may develop due to the transient polarization of the unmyelinated cell body by the exogenous electric field created by the stimulating electrodes. Because these membrane voltages (opposite in sign and located at the cell's poles) are predicted to be on the order of a few millivolts, and occur rapidly on a sub-microsecond time scale, it is conceivable they can influence the initiation of action potentials (e.g., [107]). This effect, unique to species such as man where ganglion cells tend to be unmyelinated, may influence excitation and has not been accounted for in previous cable models of the auditory nerve fiber.

Second, the rotationally-asymmetric 3D shape of the cochlea and adjacent structures of the temporal bone can lead to counter-intuitive patterns of current flow. For example, in the Ineraid-derived bEAM, a monopolar current preferentially enters the modiolus midway through the ascending basal turn ($\theta \approx 240$) regardless of the stimulating electrode position. This emphasizes both (1) the need to represent a detailed, anatomically-realistic cochlea in an EAM and (2) the ability of the model to make predictions that, because of their geometrical complexity, will not likely be made otherwise.

Third, the detailed distribution of spiral ganglion cells (especially for monopolar stimulation) may have little impact on variations in behavioral threshold across electrodes once a minimal constituency of cells populate all cochlear positions. In other words, our results imply what is important to identify and encode in a model are regions of cochlear length completely devoid of spiral ganglion cells.

Fourth, the influence of the facial nerve canal and vestibular system is predicted to be minimal, especially since the fibro-osseous mass typically found near the cochleostomy site is predicted to electrically isolate the fluids of the vestibular system from those of the implanted cochlear labyrinth, diminishing the stimulus current that enters the vestibular system.

Fifth, the influence of new bone and fibrous tissues, typically combining to form a fibro-osseous mass, can appreciably increase *or* decrease the predicted current flow entering the modiolus depending on the stimulus configuration (i.e., monopolar or bipolar) and the tissue's arrangement with respect to the electrode contacts. This suggests that measuring the volume of the fibro-osseous deposit associated with each stimulating electrode as a function of cochlear length will not allow one to correlate the tissue volume with either an increase or decrease in behavioral threshold because the tissue's architecture needs to be accounted for in making this prediction. In most cases, the model predicts an increase in current density entering the modiolus when the stimulating electrode is encased in a substantial fibro-osseous deposit. However, there are other arrangements of the tissue deposit that are predicted to decrease the current entering the modiolus, meaning an idiosyncratic patterns of tissue along the cochlear length could lead to unexpected current flow that could theoretically influence behavioral performance.

Sixth, the appreciable spread of longitudinal current, predicted by the model to be a consequence of the ratio of bone-to-fluid resistivity, will be relatively insensitive to manipulations such as moving an electrode from the lateral to the medial wall. In the latter case, thresholds are predicted to be slightly lower ($\approx$-2 dB), but the gains in spatial selectivity are predicted to be minimal. Accordingly, if current spread is a factor limiting CI user performance, the use of modiolus-hugging electrodes is unlikely to ameliorate this problem. Alternatively, replacing the perilymphatic fluid between neighboring electrodes (or the fluids of the entire entire bony duct) with a tissue or material of higher resistivity is predicted to increase the spatial selectivity of monopolar stimulation. This technique may be combined with hybrid-quadrupolar stimulation to develop a tissue environment matched with an electrode configuration that provides more focal stimulation of the spiral ganglion.

4.5 Future directions

The most important of our modeling predictions are those that are entirely counter-intuitive. For example, intuition suggests that a modiolus-hugging electrode ought to have a large impact on thresholds and spatial selectivity. Modeling suggests otherwise. Given the results reported in this thesis, there are several issues that can be suggested to focus future efforts on.

First, a new model of the unmyelinated human SGC seems necessary. The behavior of the SGC should be investigated using an approach that accounts for polarization of the cell body to determine if this has any impact on the initiation of an action potential. The dimensional characteristics of the SGC cell, and its relationship to the schwann cells that enclose one or more perikarya, might be described using serial electron-microscopy images. Further compartmental neural modeling may eventually yield a model of the unmyelinated SGC that reliably conducts an action potential past the cell body, without operating in a region of the model's parameter space that boarders on conduction failure. Ultimately, these models may challenge the predictions of the simplified model used here.

Further electrical characteristics of the inner ear might be investigated using scanning electron microscopy, such as the image in Figure 4-21. Since these show the detailed ultrastructure of the human temporal bone, they might be used to formulate more elaborate hypotheses about how currents flow in the anisotropic structures of the implanted ear. For example, the lattice methods such as those described by Gowrishankar et al. [63] can be used to derive an electrical model of the ultra-structure, modeling current flow, for instance, into the osseous spiral lamina through realistically sized perforations (caniculi perforates [184]).

Since some measures of bone resistivity seem to be at odds with our modeling results, a logical next step is to carefully measure the dielectric properties of the human temporal bone. Measures of cadaveric or surgically-obtained temporal bone might help address the disagreement between the value for bone resistivity used in this and other studies.[18] This parameter is shown to be an important one for determining current flow, leaving the 5-kΩcm value used in this study open to scrutiny. Here we note using a value significantly lower than 5 kΩcm does not allow our model to predict the empirical data. Alternatively, it is conceivable that the cellular membranes lining the cochlear duct act as an insulator, giving the structure electrical properties that mimic a structure with a higher bone-to-fluid resistivity ratio.

While our initial methodology was to construct a collection of psEAMs each ca-

[18]Recently, Micco [131] used the four-electrode reflection-coefficient method described by Suesserman [203] to report that the resistivity of the modiolus was lowered from 427 Ωcm in the normal gerbil cochlea to 288 Ωcm after substantial neural degeneration had occurred. Micco also reported the lateral bony wall to have a resistivity of 534 Ωcm, although this value may represent strial tissues or the endosteal layers of the lateral bony wall (see Figure 4-21). Both our modeling studies as well as other measures of bone resistivity suggest this value is surprisingly low.

pable of predicting behavioral threshold patterns, in light of the difficulties and assumptions needed to predict psychophysical measures, it seems more useful to focus attention on the Ineraid psEAM in the short term, since the collection of archival data is so extensive and includes many direct measures of the periphery that do not rely on any psychophysical measures.

Lastly, in previous chapters we notice the fit to the empirically recorded IP and ECAP data improved for basal stimulation when a secondary basal ground was added at the round window. To explore this a spatially expanded version of the bEAM could be used to further investigate grounding pathways. For example, using a volume conduction model of the human head (Figure 4-22A) constructed on a nonuniform grid (Figure 4-22B), grounding pathways between the intracochlear electrodes and the return on the device body might be modeled.

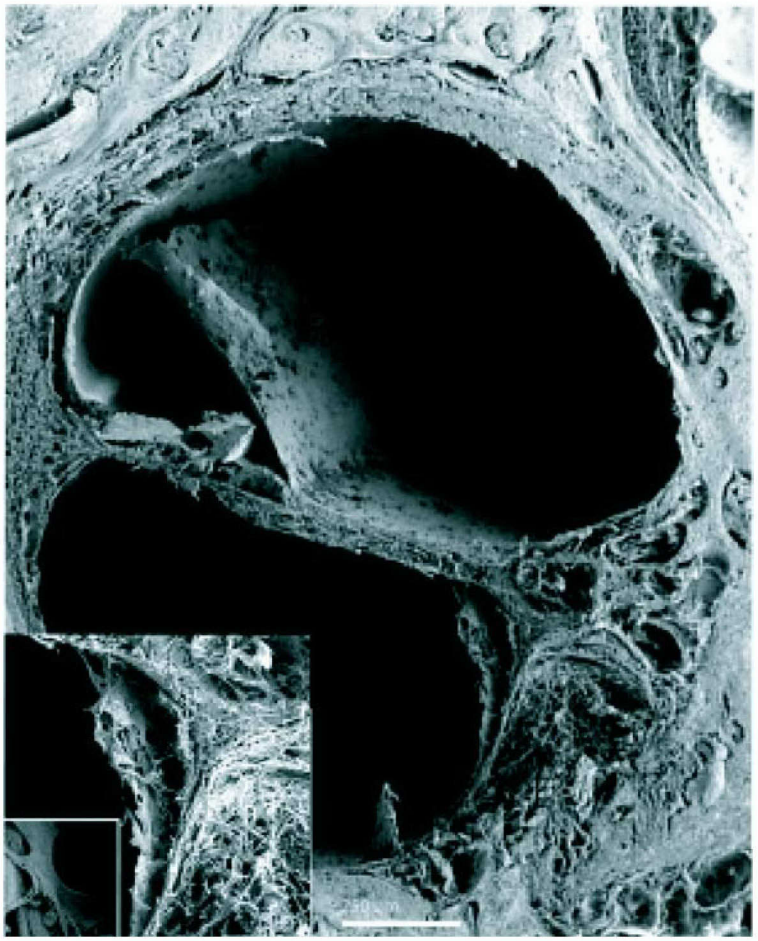

Figure 4-21: Scanning electron micrograph of a surgically-excised, freshly-processed human cochlea (from Glueckert et al. [61] figure 1A and 1B, permission granted, S. Karger AG). Inset shows magnified image of boundary between Rosenthal's canal and the scala tympani.

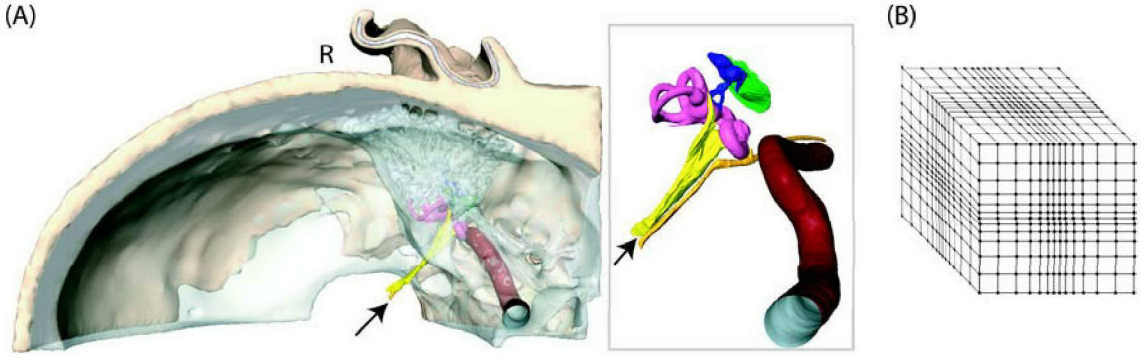

Figure 4-22: (A) 3D model of the temporal bone and surrounding structures (courtesy Wang et al [222], with model images provided by Sørensen et al. [197]). The entrance of the eighth nerve into the internal auditory canal is marked by the arrowhead. This model includes the major structures of the vasculature as well as areas of the temporal bone where the monopolar return (marked R) is located. (B) 3D nonuniform grid that can be used to extend the EAM methods to include a larger volume of the head (including the implant return in the temporalis muscle) while maintaining a high resolution centered on the implanted cochlea.

Chapter 5

Summary and Conclusions

A detailed modeling process has been described that captures the pathology of implant recipients on a patient-specific level of detail, capable of predicting current flow, neural activation, and evoked potentials. Current flow in these models is shown to be both complex and intricately tied to the disparate conductivities of the tissues present in the inner ear. Specifically, the predicted current flow is dictated by the 3D geometry and the ratio of resistivity between the bone of the otic capsule and the perilymphatic fluid.

At a bone-to-fluid ratio near 10, current flow delivered by a monopolar electrode resembles the diffuse pattern seen with a homogenous model, showing substantial current flow in all directions through the bone. This leads to predictions of activation that, in certain aspects, resemble those obtained with a homogenous model. For example, monopolar stimulation is paradoxically predicted to be more focused than bipolar, disagreeing with overwhelming physiological data to the contrary found in the literature. At a ratio of 1,000 an entirely different behavior is predicted, with the fluid spiral acting as an electrode contact, spreading current along the entire cochlear length to stimulate the entire ganglion with little or no spatial selectivity.

At a ratio of 100 (the value used in our modeling), current spreads longitudinally through the relatively conductive perilymphatic fluids entering the modiolus over several cochlear turns. This leads to predictions of extensive spread of activation across several millimeters of cochlear length, corresponding to nerve fibers that in the healthy ear code multiple octaves in frequency. For both monopolar and bipolar stimuli, the predictions of activation spread are significantly greater than previous models of the implanted ear, respectively spanning 11.1 and 4.4 millimeters in cochlear length at 6 dB above threshold. The predicted ratio of 2.5 describing monopolar-to-bipolar activation spread also appears to be more in line with physiological measures in the literature (see Chapter 2). This extensive longitudinal current spread suggests the familiar assumption that an implanted electrode can be treated as a point source in a homogenous medium is an especially misleading departure from the physical

situation. In other words, the simple Euclidian distance of any structure (especially a neuron) from the stimulating electrode is not a valid predictor of either current flow or the likelihood of neural activation.

Finally, the evoked potential predictions suggest that the inhomogeneous conductivities of the implanted ear also need to be appropriately represented in order to predict realistic ECAP waveforms. Model ECAP predictions are well fit by a phenomenological model where the growth in N1P1 amplitude is proportional to the product of (1) the excitation spread across cochlear length per dB increase in the stimulus level, (2) the number of neurons per unit cochlear length, and (3) the unitary N1P1 amplitude per neuron. This suggests that the ECAP amplitude is, to a first approximation, a near linear function of the number of neurons stimulated. This suggests the functions describing ECAP amplitude growth with level and neural recruitment with level are similarly shaped.

Testing model predictions

Virtually none of these modeling predictions are credible unless they can be validated against empirical data. We intentionally derived models from implanted temporal bones for which an extensive set of archival data existed, including intracochlear potential data (IP_d), behavioral threshold data (T_d), and evoked potentials recorded from intracochlear electrodes ($ECAP_d$). Since the ratio of bone-to-fluid resistivity was found to be a crucial determinant of the model behavior, and widely disparate values for this ratio have been reported and used in other modeling studies, we varied this parameters extensively during our validation testing.

At a ratio of 12 (i.e., 600-Ωcm bone paired with 50-Ωcm fluid) similar to that used in other models (e.g., Finley [47], Frijns et al. [56, 15], and Hanekom [73]), we found (1) monopolar stimulation was more focused than bipolar, (2) IP_p data could not be predicted accurately, and (3) the growth of the ECAP N1P1 amplitude with level was too shallow, only a fraction of that measured empirically.

At a ratio of 100 (i.e., 5-kΩcm bone paired with 50-Ωcm fluid) our patient-specific models were capable of accurately predicting both IP_d and $ECAP_d$ data, especially for apical stimulation. The archival IP_d and $ECAP_d$ data sets are the most meaningful comparisons from a validation standpoint because they directly reflect the behavior of current flow and neural activation, respectively, in the periphery without any of the hierarchal processes that make psychophysical types of data difficult to interpret.

The model's successful prediction of IP_p for apical stimulation is significant for several reasons. First, it suggests a bone-to-fluid ratio near 100 is an appropriate choice. Second, it strengthens the argument that monopolar-driven current primarily exits the cochlear labyrinth through the internal auditory meatus via the modiolus. Recent electron microscopy studies of the inner ear ultra-structure (e.g., [61, 166]) that detail the communication of perilymph between the scala tympani, scala vestibuli

and the modiolus may allow these electrical pathways to be better understood. For stimulation of basal electrodes, which are usually impacted in the fibro-osseous mass found near the cochleostomy site of the basal turn, it is likely current also exits via a basal pathway that we hypothesized to reside near the round window membrane.

The model's successful prediction of $ECAP_d$ data is also significant for several reasons. First, the model predicts the counter-intuitive similarity of ECAP waveforms experimentally recorded from different electrodes, showing a common N1P1 morphology regardless of the position of the recoding electrode relative to the stimulating electrode. Second, for half the electrodes tested, the model predicts variation in the N1P1 amplitude as the recording electrode position is varied. Third, the Ineraid psEAM predicts a growth of the N1P1 amplitude on the order of 50 $\left[\frac{\mu V}{dB}\right]$, consistent with measures made from the archival $ECAP_d$ showing a mean growth of 52 $\left[\frac{\mu V}{dB}\right]$. If ECAP amplitude growth is indeed roughly proportional to longitudinal activation spread, as in our phenomenological model, then the ECAP data are consistent with the model's prediction of very extensive activation spread with level.

While behavioral thresholds are a less direct measure of the periphery than IP_d or $ECAP_d$, even using rudimentary assumptions to link the predictions of current flow to a psychophysical percept (e.g., T_p^*), the models were able to predict a significant amount of variation in T_d for both the Ineraid and Nucleus subjects whose temporal bones were encoded into electro-anatomical models. To some extent this is surprising, since if behavioral threshold is dictated by the activity of only a few neurons at low levels where stochastic influences may dominate, we would not expect a deterministic model to perform well at all when predicting behavioral thresholds.

While there are many aspects of the model predictions that do not fit all the details of the available data (especially the psychophysical data), overall the results suggest an important step forward in representing and understanding the peripheral anatomy's influence on intracochlear stimulation. The predictions have certainly exceeded the minimum level of validation testing needed to inspire credibility, especially considering the paucity of testing that has been done with previous electro-anatomical models of both the cochlear implant and other systems where peripheral nerves are electrically excited. Therein lies the significance of this work and the potential for it to be a useful research tool. Future efforts will focus effort on tuning the Ineraid psEAM to predict as much of the archival IP_d and $ECAP_d$ data as possible before moving on to predict other forms of data that exist for the Ineraid subject.

The influence of the peripheral anatomy

Finally, using this tested model, we make several predictions regarding the impact of the anatomy found in implanted cochleae. First, the paradoxically unmyelinated human SGC requires special attention because of the possibility that an exogenous electric field may polarize the cell body enough to influence excitation.

Second, the rotationally-asymmetric 3D shape of the cochlea and adjacent structures of the temporal bone can lead to counter-intuitive patterns of current flow. For example, in the Ineraid-derived bEAM a monopolar current preferentially enters the modiolus midway through the ascending basal turn ($\theta \approx$ 240) regardless of the stimulating electrode position.

Third, the detailed distribution of spiral ganglion cell survival may have little impact on variations in behavioral threshold across electrodes (especially for monopolar stimulation) once a minimal constituency of cells populate all cochlear positions.

Fourth, in the Ineraid subject the influence of the facial nerve canal and vestibular system is predicted to be minimal, especially since the fibro-osseous mass typically found near the cochleostomy is predicted to electrically isolate the fluids of the vestibular system from those of the implanted cochlear labyrinth, diminishing the stimulus current that enters the vestibular system.

Fifth, the influence of new bone and fibrous tissues, typically combining to form a fibro-osseous mass, can appreciably increase *or* decrease the predicted current flow entering the modiolus depending on the tissue's arrangement with respect to the electrode contacts and the stimulus configuration (i.e., monopolar or bipolar). In most cases, the model predicts an increase in current density entering the modiolus when the stimulating electrode is encased in a substantial fibro-osseous deposit. However, other arrangements of the tissue deposit are predicted to decrease the current entering the modiolus. As a result, idiosyncratic patterns along the cochlear length can theoretically lead to unexpected current flow patterns that may influence behavioral performance.

Sixth, the appreciable spread of longitudinal current, predicted by the model to be a consequence of the ratio of bone-to-fluid resistivity, will be insensitive to manipulations such as moving the electrode from the lateral to medial wall. In the latter case, thresholds are predicted to be slightly lower ($\approx$-2 dB), but the gains in spatial selectivity are predicted to be minimal. Accordingly, if current spread is a factor limiting CI user performance, the use of modiolus-hugging electrodes is unlikely to ameliorate this problem. Alternatively, replacing the perilymphatic fluid between neighboring electrodes (or the fluid of the entire bony duct) with a tissue or material of higher resistivity is predicted to increase the spatial selectivity of monopolar stimulation. This technique may be combined with hybrid-quadrupolar stimulation to develop a tissue environment matched with an electrode configuration that provides more focal stimulation of the spiral ganglion.

Bibliography

[1] P. J. Abbas and C. J. Brown. Electrically evoked auditory brainstem response: growth of response with current level. *Hear Res*, 51(1):123–37, 1991.

[2] K. W. Altman and R. Plonsey. Point source nerve bundle stimulation: effects of fiber diameter and depth on simulated excitation. *IEEE Trans Biomed Eng*, 37(7):688–98, 1990.

[3] F. Andrietti and G. Bernardini. Segmented and "equivalent" representation of the cable equation. *Biophys J*, 46(5):615–23, 1984.

[4] R. C. Barr and R. Plonsey. Propagation under the influence of interstitial potentials. volume 2, page 598, 1992.

[5] R. C. Barr, R. Plonsey, and C. R. Johnson. Membrane current from transmembrane potentials in complex core-conductor models. *IEEE Trans Biomed Eng*, 50(4):405–11, 2003.

[6] P. J. Basser. Scaling laws for myelinated axons derived from an electrotonic core-conductor model. *J Integr Neurosci*, 3(2):227–44, 2004.

[7] R. D. Battmer, D. Gnadeberg, E. von Wallenberg, E. Lehnhardt, and D. J. Allum. A study of monopolar and bipolar stimulation modes with a modified nucleus mini-22 cochlear implant. *Adv Otorhinolaryngol*, 48:9–16, 1993.

[8] R.C. Black and G.M. Clark. Differential electrical excitation of the auditory nerve. *J Acoust Soc Am*, 67(3):868–74, 1980.

[9] P. Blamey. Are spiral ganglion cell numbers important for speech perception with a cochlear implant? *Am J Otol*, 18(6 Suppl):S11–2, 1997.

[10] P. Blamey, B.C. Pyman, G.M. Clark, R.C. Dowell, M. Gordon, A.M. Brown, and R.D. Hollow. Factors predicting postoperative sentence scores in postlinguistically deaf adult cochlear implant patients. *Ann Otol Rhinol Laryngol*, 101:342–348, 1992.

[11] Peter J. Blamey, Patti Arndt, F. Bergeron, G. Bredberg, J. Brimacombe, G. Facer, J. Larky, B. Lindstrom, J. Nedzelski, A. Peterson, D. Shipp, S. Staller, and L. Whitford. Factors affecting auditory performace of postlinguistically deaf adults using cochlear implants. *Audiology Neurootology*, 1(5):293–306, 1996.

[12] J. J. Briaire and J. H. Frijns. Field patterns in a 3d tapered spiral model of the electrically stimulated cochlea. *Hear Res*, 148(1-2):18–30, 2000.

[13] J. J. Briaire and J. H. Frijns. Unraveling the electrically evoked compound action potential. *Hear Res*, 205(1-2):143–56, 2005.

[14] J. J. Briaire and J. H. Frijns. The consequences of neural degeneration regarding optimal cochlear implant position in scala tympani: A model approach. *Hear Res*, 2006.

[15] J. J. Briaire and J. H. M. Frijns. Field patterns in a 3d tapered spiral model of the electrically stimulated cochlea. *Hearing Research*, 148(1-2):18–30, 2000.

[16] C. J. Brown, P. J. Abbas, J. Borland, and M. R. Bertschy. Electrically evoked whole nerve action potentials in ineraid cochlear implant users: responses to different stimulating electrode configurations and comparison to psychophysical responses. *J Speech Hear Res*, 39(3):453–67, 1996.

[17] C. J. Brown, P. J. Abbas, and B. Gantz. Electrically evoked whole-nerve action potentials: data from human cochlear implant users. *J Acoust Soc Am*, 88(3):1385–91, 1990.

[18] C. J. Brown, P. J. Abbas, and B. J. Gantz. Preliminary experience with neural response telemetry in the nucleus ci24m cochlear implant. *Am J Otol*, 19(3):320–7, 1998.

[19] C. J. Brown, M. L. Hughes, B. Luk, P. J. Abbas, A. Wolaver, and J. Gervais. The relationship between eap and eabr thresholds and levels used to program the nucleus 24 speech processor: data from adults. *Ear Hear*, 21(2):151–63., 2000.

[20] M. C. Brown. Morphology of labeled efferent fibers in the guinea pig cochlea. *J Comp Neurol*, 260(4):605–18, 1987.

[21] I. C. Bruce, L. S. Irlicht, M. W. White, S. J. O'Leary, S. Dynes, E. Javel, and G. M. Clark. A stochastic model of the electrically stimulated auditory nerve: pulse- train response. *IEEE Trans Biomed Eng*, 46(6):630–7, 1999.

[22] I. C. Bruce, M. W. White, L. S. Irlicht, S. J. O'Leary, and G. M. Clark. The effects of stochastic neural activity in a model predicting intensity perception with cochlear implants: low-rate stimulation [in process citation]. *IEEE Trans Biomed Eng*, 46(12):1393–404, 1999.

[23] I. C. Bruce, M. W. White, L. S. Irlicht, S. J. O'Leary, S. Dynes, E. Javel, and G. M. Clark. A stochastic model of the electrically stimulated auditory nerve: single-pulse response. *IEEE Trans Biomed Eng*, 46(6):617–29, 1999.

[24] D. Cafarelli Dees, N. Dillier, W. K. Lai, E. von Wallenberg, B. van Dijk, F. Akdas, M. Aksit, C. Batman, A. Beynon, S. Burdo, J. M. Chanal, L. Collet, M. Conway, C. Coudert, L. Craddock, H. Cullington, N. Deggouj, B. Fraysse, S. Grabel, J. Kiefer, J. G. Kiss, T. Lenarz, A. Mair, S. Maune, J. Muller-Deile, J. P. Piron, S. Razza, C. Tasche, H. Thai-Van, F. Toth, E. Truy, A. Uziel, and G. F. Smoorenburg. Normative findings of electrically evoked compound action potential measurements using the neural response telemetry of the nucleus ci24m cochlear implant system. *Audiol Neurootol*, 10(2):105–16, 2005.

[25] A. M. Campbell and D. V. Land. Dielectric properties of female human breast tissue measured in vitro at 3.2 ghz. *Phys Med Biol*, 37(1):193–210, 1992.

[26] L. A. Cartee and R. Plonsey. The transient subthreshold response of spherical and cylindrical cell models to extracellular stimulation. *IEEE Trans Biomed Eng*, 39(1):76–85, 1992.

[27] Y. Cazals, M. Pelizzone, O. Saudan, and C. Boex. Low-pass filtering in amplitude modulation detection associated with vowel and consonant identification in subjects with cochlear implants. *J Acoust Soc Am*, 96(4):2048–54, 1994.

[28] G. M. Clark, R. K. Shepherd, B. K. Franz, R. C. Dowell, Y. C. Tong, P. J. Blamey, R. L. Webb, B. C. Pyman, J. McNaughtan, D. M. Bloom, and et al. The histopathology of the human temporal bone and auditory central nervous system following cochlear implantation in a patient. correlation with psychophysics and speech perception results. *Acta Otolaryngol Suppl*, 448:1–65, 1988.

[29] J. R. Clay and L. J. DeFelice. Relationship between membrane excitability and single channel open-close kinetics. *Biophys J*, 42(2):151–7, 1983.

[30] L. M. Collins, G. H. Wakefield, and G. R. Feinman. Temporal pattern discrimination and speech recognition under electrical stimulation. *J Acoust Soc Am*, 96(5 Pt 1):2731–7, 1994.

[31] L. M. Collins, T. A. Zwolan, and G. H. Wakefield. Comparison of electrode discrimination, pitch ranking, and pitch scaling data in postlingually deafened adult cochlear implant subjects. *J Acoust Soc Am*, 101(1):440–55, 1997.

[32] E. A. Collison, B. Munson, and A. E. Carney. Relations among linguistic and cognitive skills and spoken word recognition in adults with cochlear implants. *J Speech Lang Hear Res*, 47(3):496–508, 2004.

[33] M. S. Cooper. Gap junctions increase the sensitivity of tissue cells to exogenous electric fields. *J Theor Biol*, 111(1):123–30, 1984.

[34] M. S. Cooper. Membrane potential perturbations induced in tissue cells by pulsed electric fields. *Bioelectromagnetics*, 16(4):255–62, 1995.

[35] P.W. Dawson, C.M. McKay, P. A. Busby, D.B. Grayden, and G. M. Clark. Electrode discrimination and speech perception in young children using cochlear implants. *Ear Hear*, 21(6):597–607, 2000.

[36] R. C. de Sauvage, Y. Cazals, J. P. Erre, and J. M. Aran. Acoustically derived auditory nerve action potential evoked by electrical stimulation: an estimation of the waveform of single unit contribution. *J Acoust Soc Am*, 73(2):616–27, 1983.

[37] Morris H. DeGroot and Mark J. Schervish. *Probability and statistics*. Addison-Wesley, Boston, 3rd edition, 2002.

[38] G. Donaldson and D. Nelson. Place-pitch sensitivity and its relation to consonant recognition by cochlear implant listeners using the mpeak and speak speech processing strategies. *J Acoust Soc Am*, 107(3):1645–1658, 2000.

[39] M.F. Dorman, K. Dankowski, G. McCandless, and L.M. Smith. Consonant recognition as a function of the number of channels of stimulation by patients who use the symbion cochlear implant. *Ear Hear*, 10(5):288–91, 1989.

[40] Richard O. Duda, Peter E. Hart, and David G. Stork. *Pattern classification*. Wiley, New York, 2nd edition, 2001.

[41] Scott Budd Chapman Dynes. *Discharge characteristics of auditory nerve fibers for pulsatile electrical stimuli*. Ph.d., MIT, 1996.

[42] D.K. Eddington, W.H. Dobelle, D.E. Brackmann, M.G. Mladevosky, and J.L. Parkin. Auditory prosthesis research with multiple channel intracochlear stimulation in man. *Ann Otol Rhinol Laryngol Suppl*, 87(6 Pt 2):1–39, 1978.

[43] J. Fayad, Jr. Linthicum, F. H., S. R. Otto, F. R. Galey, and W. F. House. Cochlear implants: histopathologic findings related to performance in 16 human temporal bones. *Ann Otol Rhinol Laryngol*, 100(10):807–11, 1991.

[44] E. C. Fear and M. A. Stuchly. Modeling assemblies of biological cells exposed to electric fields. *IEEE Trans Biomed Eng*, 45(10):1259–71, 1998.

[45] E. Felder, G. Kanonier, A. Scholtz, H. Rask-Andersen, and A. Schrott-Fischer. Quantitative evaluation of cochlear neurons and computer-aided three-dimensional reconstruction of spiral ganglion cells in humans with a peripheral loss of nerve fibres. *Hear Res*, 105(1-2):183–90, 1997.

[46] H. Felix. Anatomical differences in the peripheral auditory system of mammals and man. a mini review. *Adv Otorhinolaryngol*, 59:1–10, 2002.

[47] C.C. Finley, B.S. Wilson, and M.W. White. Models of neural responsiveness to electrical stimulation. In J.M. Miller and F.A. Spelman, editors, *Cochlear Implants: Models of the Electrically Stimulated Ear*, pages 55–93. Springer-Verlag, New York, 1990.

[48] Charles C Finley, C. Van den Honert, and B.S. Wilson. Speech processors for auditory prostheses: ninth quarterly progress report (nih n01-dc-5-2103), October 31 1997.

[49] K. E. Fishman, R. V. Shannon, and W. H. Slattery. Speech recognition as a function of the number of electrodes used in the speak cochlear implant speech processor. *J Speech Hear Res*, 40(5):1201–15, 1997.

[50] R. FitzHugh. Dimensional analysis of nerve models. *J Theor Biol*, 40(3):517–41, 1973.

[51] L. M. Friesen, R. V. Shannon, D. Baskent, and X. Wang. Speech recognition in noise as a function of the number of spectral channels: comparison of acoustic hearing and cochlear implants. *J Acoust Soc Am*, 110(2):1150–63, 2001.

[52] J. H. Frijns, S. L. de Snoo, and R. Schoonhoven. Potential distributions and neural excitation patterns in a rotationally symmetric model of the electrically stimulated cochlea. *Hear Res*, 87(1-2):170–86, 1995.

[53] J. H. Frijns, S. L. de Snoo, and J. H. ten Kate. Spatial selectivity in a rotationally symmetric model of the electrically stimulated cochlea. *Hear Res*, 95(1-2):33–48, 1996.

[54] Johannes Hubertus Maria Frijns. *Cochlear implants: a modelling approach.* PhD thesis, Rijksuniversiteit te Leiden, 1995.

[55] Johannes Hubertus Maria Frijns, J. J. Briaire, and J. J. Grote. The importance of human cochlear anatomy for the results of modiolus-hugging multichannel cochlear implants. *Otol Neurotol*, 22(3):340–9, 2001.

[56] Johannes Hubertus Maria Frijns, S. L. de Snoo, and R. Schoonhoven. Potential distributions and neural excitation patterns in a rotationally symmetric model of the electrically stimulated cochlea. *Hear Res*, 87(1-2):170–86, 1995.

[57] Q.J. Fu. Temporal processing and speech recognition in cochlear implant users. *NeuroReport*, 13:1635–1639, 2002.

[58] von G. Gassler. Uber die horschwelle fur schalleriegnisse mit verscheiden breitm frequenzspectrum. *Acustica*, 4:408–414, 1954.

[59] L. A. Geddes and L. E. Baker. The specific resistance of biological material–a compendium of data for the biomedical engineer and physiologist. *Med Biol Eng*, 5(3):271–93, 1967.

[60] G. Girzon. *Investigation of Current Flow in the Inner Ear During Electrical Stimulation of Intracochlear Electrodes.* S.m., M.I.T., 1987.

[61] R. Glueckert, K. Pfaller, A. Kinnefors, H. Rask-Andersen, and A. Schrott-Fischer. The human spiral ganglion: new insights into ultrastructure, survival rate and implications for cochlear implants. *Audiol Neurootol*, 10(5):258–73, 2005.

[62] P. R. Goldstein and Kiang N. Y. S. Synchrony of neural activity in electric responses evoked by transient acoustic stimuli. *J Acoust Soc Am*, 30:107–114, 1958.

[63] T. R. Gowrishankar and J. C. Weaver. An approach to electrical modeling of single and multiple cells. *Proc Natl Acad Sci U S A*, 100(6):3203–8, 2003.

[64] A. B. Grayeli, C. S. Yrieix, Y. Imauchi, F. Cyna-Gorse, E. Ferrary, and O. Sterkers. Temporal bone density measurements using ct in otosclerosis. *Acta Otolaryngol*, 124(10):1136–40, 2004.

[65] D D Greenwood. A cochlear frequency-position function for several species-29 years later. *J Acoust Soc Am*, 87(6):2592–605, 1990.

[66] Jr. Grill, W. M. Modeling the effects of electric fields on nerve fibers: influence of tissue electrical properties [in process citation]. *IEEE Trans Biomed Eng*, 46(8):918–28, 1999.

[67] W. M. Grill and J. T. Mortimer. Electrical properties of implant encapsulation tissue. *Ann Biomed Eng*, 22(1):23–33, 1994.

[68] F. Guilak, K. E. Lott, H. A. Awad, Q. Cao, K. C. Hicok, B. Fermor, and J. M. Gimble. Clonal analysis of the differentiation potential of human adipose-derived adult stem cells. *J Cell Physiol*, 206(1):229–37, 2006.

[69] R.D. Hall. Estimation of surviving spiral ganglion cells in the deaf rat using the electrically evoked auditory brainstem response. *Hear Res*, 45(1-2):123–36, 1990.

[70] C. Halpin. Personal communication, 2006.

[71] T Hanai. Electrical properites of emulsions. In Philip Sherman, editor, *Emulsion science*, pages x, 496 p. Academic Press, London, New York,, 1968.

[72] J. J. Hanekom and R. V. Shannon. Gap detection as a measure of electrode interaction in cochlear implants. *J Acoust Soc Am*, 104(4):2372–84, 1998.

[73] T. Hanekom. Three-dimensional spiraling finite element model of the electrically stimulated cochlea. *Ear Hear*, 22(4):300–15., 2001.

[74] T. Hanekom. Modelling encapsulation tissue around cochlear implant electrodes. *Med Biol Eng Comput*, 43(1):47–55, 2005.

[75] R. Hartmann and R. Klinke. Impulse patterns of auditory nerve fibres to extra- and intracochlear electrical stimulation. *Acta Otolaryngol Suppl*, 469(128-34), 1990.

[76] M. J. Hay-McCutcheon, C. J. Brown, K. S. Clay, and K. Seyle. Comparison of electrically evoked whole-nerve action potential and electrically evoked auditory brainstem response thresholds in nucleus ci24r cochlear implant recipients. *J Am Acad Audiol*, 13(8):416–27, 2002.

[77] B.A. Henry, C.M. McKay, H.J. McDermott, and G. M. Clark. The relationship between speech perception and electrode discrimination in cochlear implantees. *J Acoust Soc Am*, 108(3 Pt 1):1269–1280, 2000.

[78] B.A. Henry and C.W. Turner. The resolution of complex spectral patterns by cochlear implant and normal-hearing listeners. *J Acoust Soc Am*, 113(5):2861–2873, 2003.

[79] M. Hibino, H. Itoh, and Jr. Kinosita, K. Time courses of cell electroporation as revealed by submicrosecond imaging of transmembrane potential. *Biophys J*, 64(6):1789–800, 1993.

[80] M. B. Higgins and C. W. Turner. Summation bandwidths at threshold in normal and hearing-impaired listeners. *J Acoust Soc Am*, 88(6):2625–30, 1990.

[81] Marion M Hinojosa R. Histopathology of profound sensorineural deafness. *Ann N Y Acad Sci*, 405:459–484, 1983.

[82] A. L. Hodgkin and A. F. Huxley. A quantitative description of membrane current and its application to conduction and excitation in nerve. *J Physiol*, 117(4):500–44, 1952.

[83] A. E. Holmes, F.J. Kemker, and G. E. Merwin. The effects of varying the number of cochlear implant electrodes on speech perception. *Am J Otol*, 8(3):240–6, 1987.

[84] Strelioff D. Honrubia, V. and S. Sitko. Electroanatomy of the cochlea: Its role in cochlear potential measurements. In C. Elberling R.J. Ruben, G., and Salomon, editors, *Electrocochleography*, pages 23–39. University Park Press, Baltimore, 1976.

[85] W. A. Hossain, S. D. Antic, Y. Yang, M. N. Rasband. and D. K. Morest. Where is the spike generator of the cochlear nerve? voltage-gated sodium channels in the mouse cochlea. *J Neurosci*, 25(29):6857–68, 2005.

[86] [http://www.nidcd.nih.gov/health/hearing/coch.asp], Food and Drug Administration (FDA) 2005.

[87] T. Ifukube and R. L. White. Current distributions produced inside and outside the cochlea from a scala tympani electrode array. *IEEE Trans Biomed Eng*, 34(11):883–90, 1987.

[88] A. Incesulu and Jr. Nadol, J. B. Correlation of acoustic threshold measures and spiral ganglion cell survival in severe to profound sensorineural hearing loss: implications for cochlear implantation. *Ann Otol Rhinol Laryngol*, 107(11 Pt 1):906–11, 1998.

[89] E Javel, Y C Tong, R K Shepherd, and G M Clark. Responses of cat auditory nerve fibers to biphasic electrical current pulses. *Ann Otol Rhinol and Laryngol*, 96 Suppl. 128:26–30, 1987.

[90] W. Jesteadt. An adaptive procedure for subjective judgments. *Percept Psychophys*, 28(1):85–8., 1980.

[91] L. G. Johnsson, W. F. House, and F. H. Linthicum. Bilateral cochlear implants: histological findings in a pair of temporal bones. *Laryngoscope*, 89(5 Pt 1):759–62, 1979.

[92] L. G. Johnsson, W. F. House, and F. H. Linthicum. Otopathological findings in a patient with bilateral cochlear implants. *Ann Otol Rhinol and Laryngol*, 91(Suppl 91):74–89, 1982.

[93] B. M. Johnstone, J. R. Johnstone, and I. D. Pugsley. Membrane resistance in endolymphatic walls of the first turn of the guinea-pig cochlea. *J Acoust Soc Am*, 40(6):1398–404, 1966.

[94] A. Kasper, M. Pelizzone, and P. Montandon. Intracochlear potential distribution with intracochlear and extracochlear electrical stimulation in humans. *Ann Otol Rhinol Laryngol*, 100(10):812–6, 1991.

[95] A. Kawano, H. L. Seldon, G. M. Clark, R. T. Ramsden, and C. H. Raine. Intracochlear factors contributing to psychophysical percepts following cochlear implantation. *Acta Otolaryngol (Stockh)*, 118(3):313–26, 1998.

[96] D. R. Ketten, M. W. Skinner, G. Wang, M. W. Vannier, G. A. Gates, and J. G. Neely. In vivo measures of cochlear length and insertion depth of nucleus cochlear implant electrode arrays. *Ann Otol Rhinol Laryngol Suppl*, 175:1–16, 1998.

[97] A. M. Khan, O. Handzel, B. J. Burgess, D. Damian, D. K. Eddington, and Jr. Nadol, J. B. Is word recognition correlated with the number of surviving spiral ganglion cells and electrode insertion depth in human subjects with cochlear implants? *Laryngoscope*, 115(4):672–7, 2005.

[98] A. M. Khan. O. Handzel, D. Damian, D. K. Eddington, and Jr. Nadol, J. B. Effect of cochlear implantation on residual spiral ganglion cell count as determined by comparison with the contralateral nonimplanted inner ear in humans. *Ann Otol Rhinol Laryngol*, 114(5):381–5, 2005.

[99] A. M. Khan, D. M. Whiten, Jr. Nadol, J. B., and D. K. Eddington. Histopathology of human cochlear implants: correlation of psychophysical and anatomical measures. *Hear Res*, 205(1-2):83–93, 2005.

[100] Moxon E.C. Kiang, N.Y.S. and A.R. Kahn. The relationship of gross potentials recorded from the cochlea to single unit activity in the auditory nerve. In C. Elberling R.J. Ruben, G., and Salomon, editors, *Electrocochleography*, pages 95–115. University Park Press, Baltimore, 1976.

[101] J.F. Knutson, J.V. Hinrichs, R.S. Tyler, B.J. Gantz, H.A. Schartz, and G. Woodworth. Psychological predictors of audiological outcomes of multichannel cochlear implants: preliminary findings. *Ann Otol Rhinol Laryngol*, 100(10):817–22, 1991.

[102] Christof Koch and Idan Segev. *Methods in neuronal modeling: from ions to networks*. Computational neuroscience. MIT Press, Cambridge, 2nd edition, 1998.

[103] J. D. Kosterich, K. R. Foster, and S. R. Pollack. Dielectric properties of fluid-saturated bone–the effect of variation in conductivity of immersion fluid. *IEEE Trans Biomed Eng*, 31(4):369–74, 1984.

[104] A. Kral, R. Hartmann, D. Mortazavi, and R. Klinke. Spatial resolution of cochlear implants: the electrical field and excitation of auditory afferents. *Hear Res*, 121(1-2):11–28, 1998.

[105] P. A. Leake and G. T. Hradek. Cochlear pathology of long term neomycin induced deafness in cats. *Hear Res*, 33(1):11–33, 1988.

[106] PA Leake, O Olga A. Stakhovskaya, and D Sridhar. Protective and plastic effects of patterned electrical on the deafened auditory system. *Neural Prosthesis Program Contract N01-DC-3-1006, 7th Quarterly Progress Report, April 1 through June 30, 2005.*, 2005.

[107] D. C. Lee and W. M. Grill. Polarization of a spherical cell in a nonuniform extracellular electric field. *Ann Biomed Eng*, 33(5):603–15, 2005.

[108] J. Leung, N. Y. Wang, J. D. Yeagle, J. Chinnici, S. Bowditch, H. W. Francis, and J. K. Niparko. Predictive models for cochlear implantation in elderly candidates. *Arch Otolaryngol Head Neck Surg*, 131(12):1049–54, 2005.

[109] D. H. Liang, H. S. Lusted, and R. L. White. The nerve-electrode interface of the cochlear implant: current spread [in process citation]. *IEEE Trans Biomed Eng*, 46(1):35–43, 1999.

[110] M. C. Liberman. The cochlear frequency map for the cat: labeling auditory-nerve fibers of known characteristic frequency. *J Acoust Soc Am*, 72(5):1441–9, 1982.

[111] M. C. Liberman and M. E. Oliver. Morphometry of intracellularly labeled neurons of the auditory nerve: correlations with functional properties. *J Comp Neurol*, 223(2):163–76, 1984.

[112] F. H. Linthicum, J. Fayad, S. R. Otto, F. R. Galey, and W. F. House. Cochlear implant histopathology. *Am J Otol*, 12:245–311, 1991.

[113] Jr. Linthicum, F. H. and F. R. Galey. Histologic evaluation of temporal bones with cochlear implants. *Ann Otol Rhinol Laryngol*, 92(6 Pt 1):610–3, 1983.

[114] Leonid Litvak. *Towards a better speech processor for cochlear implants: Auditory- nerve responses to high-rate electric pulse trains*. PhD thesis, MASSACHUSETTS INSTITUTE OF TECHNOLOGY, 2002.

[115] Leonid Litvak, Bertrand Delgutte, and Donald K Eddington. Responses of auditory-nerve fibers to sustained, high-frequency electric stimulation. i. unmodulated pulse trains. *J Ascoust Soc Am*, 2002 (Submitted).

[116] Leonid Litvak, Bertrand Delgutte, and Donald K Eddington. Responses of auditory-nerve fibers to sustained, high-frequency electric stimulation. ii. sinusoidal modulators. *J Ascoust Soc Am*, 2002 (submitted).

[117] Leonid Litvak, Bertrand Delgutte, and Donald K Eddington. Responses of auditory-nerve fibers to sustained, high-frequency electric stimulation. iii. vowel modulators. *J Ascoust Soc Am*, 2002 (submitted).

[118] P. C. Loizou. Introduction to cochlear implants. *Ieee Engineering in Medicine and Biology Magazine*, 18(1):32–42, 1999.

[119] O. Macherey, A. van Wieringen, R. P. Carlyon, J. M. Deeks, and J. Wouters. Asymmetric pulses in cochlear implants: Effects of pulse shape, polarity, and rate. *J Assoc Res Otolaryngol*, 2006.

[120] M. A. Marsh, J. Xu, P. J. Blamey, L. A. Whitford, S. A. Xu, J. M. Silverman, and G. M. Clark. Radiologic evaluation of multichannel intracochlear implant insertion depth. *Am J Otol*, 14(4):386–91., 1993.

[121] M.A. Marsh, N.J. Coker, and H.A. Jenkins. Temporal bone histopathology of a patient with a nucleus 22-channel cochlear implant. *Am J Otol*, 13(3):241–248, 1992.

[122] A. J. Matsuoka, J. T. Rubinstein, P. J. Abbas, and C. A. Miller. The effects of interpulse interval on stochastic properties of electrical stimulation: models and measurements. *IEEE Trans Biomed Eng*, 48(4):416–24., 2001.

[123] C.M. McKay, H.J. McDermott, and R.P. Carlyon. Place and temporal cues in pitch perception: are they truly independent? *Acoustics Research Letters Online*, 1(1):25–30, 2000.

[124] B. McNamara and K. Wiesenfeld. Theory of stochastic resonance. *Phys. Rev. A*, 39:4854–4869, 1989.

[125] D. R. McNeal. Analysis of a model for excitation of myelinated nerve. *IEEE Trans Biomed Eng*, 23(4):329–37, 1976.

[126] L. H. Mens and C. K. Berenstein. Speech perception with mono- and quadrupolar electrode configurations: a crossover study. *Otol Neurotol*, 26(5):957–64, 2005.

[127] L. H. Mens, G. Huiskamp, T. Oostendorp, and P. van den Broek. Modelling surface potentials from intracochlear electrical stimulation. *Scand Audiol*, 28(4):249–55, 1999.

[128] L. H. Mens, T. Oostendorp, and P. van den Broek. Cochlear implant generated surface potentials: current spread and side effects. *Ear Hear*, 15(4):339–45, 1994.

[129] L. H. Mens, T. Oostendorp, and P. van den Broek. Identifying electrode failures with cochlear implant generated surface potentials. *Ear Hear*, 15(4):330–8, 1994.

[130] M.M. Merzenich and M.W. White. Cochlear implant: The interface problem. In J. Resnick and T. Hambrecht, editors, *Functional Electrical Stimulation*, pages 321–340. Marcel Dekker, NY, 1977.

[131] A. G. Micco and C. P. Richter. Electrical resistivity measurements in the mammalian cochlea after neural degeneration. *Laryngoscope*, 116(8):1334–41, 2006.

[132] C. A. Miller, P. J. Abbas, M. J. Hay-McCutcheon, B. K. Robinson, K. V. Nourski, and F. C. Jeng. Intracochlear and extracochlear ecaps suggest antidromic action potentials. *Hear Res*, 198(1-2):75–86, 2004.

[133] C. A. Miller, P. J. Abbas, M. J. Hay-McCutcheon, B. K. Robinson, K. V. Nourski, and F. C. Jeng. Intracochlear and extracochlear ecaps suggest antidromic action potentials. *Hear Res*, 198(1-2):75–86, 2004.

[134] C. A. Miller, P. J. Abbas, and J. T. Rubinstein. An empirically based model of the electrically evoked compound action potential. *Hear Res*, 135(1-2):1–18, 1999.

[135] C. A. Miller, P. J. Abbas, J. T. Rubinstein, B. K. Robinson, A. J. Matsuoka, and G. Woodworth. Electrically evoked compound action potentials of guinea pig and cat: responses to monopolar, monophasic stimulation. *Hear Res*, 119(1-2):142–54, 1998.

[136] C. A. Miller, B. K. Robinson, J. T. Rubinstein, P. J. Abbas, and C. L. Runge-Samuelson. Auditory nerve responses to monophasic and biphasic electric stimuli. *Hearing Research*, 151(1-2):79–94, 2001.

[137] M. Mohr and B. Vanrumste. Comparing iterative solvers for linear systems associated with the finite difference discretisation of the forward problem in electro-encephalographic source analysis. *Med Biol Eng Comput*, 41(1):75–84, 2003.

[138] A. R. Moller, V. Colletti, and F. G. Fiorino. Neural conduction velocity of the human auditory nerve: bipolar recordings from the exposed intracranial portion of the eighth nerve during vestibular nerve section. *Electroencephalogr Clin Neurophysiol*, 92(4):316–20, 1994.

[139] E. M. Monsell, D. D. Cody, H. G. Bone, G. W. Divine, J. P. Windham, G. P. Jacobson, C. W. Newman, and S. C. Patel. Hearing loss in paget's disease of bone: the relationship between pure-tone thresholds and mineral density of the cochlear capsule. *Hear Res*, 83(1-2):114–20, 1995.

[140] Brian C. J. Moore. Frequency analysis and masking. In Brian C. J. Moore, editor, *Hearing*, Handbook of perception and cognition (2nd ed.), pages xxi, 468 p. Academic Press, San Diego, 1995.

[141] M. Muller. Frequency representation in the rat cochlea. *Hear Res*, 51(2):247–54, 1991.

[142] J. Nadol and D. Eddington. Treatment of sensorineural hearing loss by cochlear implantation. *Annu Rev Med*, 39:491–502, 1988.

[143] J B Nadol. Quantification of human spiral ganglion cells by serial section reconstruction and segmental density estimates. *Am J Otolaryngol*, 9(2):47–51, 1988.

[144] J B Nadol. Patterns of neural degeneration in the human cochlea and auditory nerve: Implications for cochlear implantation. *Otolaryngol Head Neck Surg*, 117(3, part 1):220–228, 1997.

[145] J. B. Nadol and D. K. Eddington. Histopathology of the inner ear relevant to cochlear implantation. *Adv Otorhinolaryngol*, 64:31–49, 2006.

[146] J B Nadol, J Y Shiao, B J Burgess, D R Ketten, D K Eddington, B J Gantz, I Kos, P Montandon, N J Coker, J T Roland, and Shallop J K. Histopathology of cochlear implants in humans. *Ann Otol Rhinol and Laryngol*, 110:883–891, 2001.

[147] Jr. Nadol, J. B. Degeneration of cochlear neurons as seen in the spiral ganglion of man. *Hear Res*, 49(1-3):141–54, 1990.

[148] Jr. Nadol, J. B., J. Y. Shiao, B. J. Burgess, D. R. Ketten, D. K. Eddington, B. J. Gantz, I. Kos, P. Montandon, N. J. Coker, Jr. Roland, J. T., and J. K. Shallop. Histopathology of cochlear implants in humans. *Ann Otol Rhinol Laryngol*, 110(9):883–91., 2001.

[149] Jr. Nadol, J.B., D.R. Ketten, and B.J. Burgess. Otopathology in a case of multichannel cochlear implantation. *Laryngoscope*, 104(3 Pt 1):299–303, 1994.

[150] Jr. Nadol, J.B., Y.S. Young, and R.J. Glynn. Survival of spiral ganglion cells in profound sensorineural hearing loss: implications for cochlear implantation. *Ann Otol Rhinol Laryngol*, 98(6):411–16, 1989.

[151] Jr. Nadol, J.B., Y.S. Young, and R.J. Glynn. Survival of spiral ganglion cells in profound sensorineural hearing loss: implications for cochlear implantation. *Ann Otol Rhinol Laryngol*, 98(6):411–16, 1989.

[152] D. A. Nelson, D. J. Van Tasell, A. C. Schroder, S. Soli, and S. Levine. Electrode ranking of "place pitch" and speech recognition in electrical hearing. *J Acoust Soc Am*, 98(4):1987–99., 1995.

[153] C. Newbold, R. Richardson, C. Q. Huang, D. Milojevic, R. Cowan, and R. Shepherd. An in vitro model for investigating impedance changes with cell growth and electrical stimulation: implications for cochlear implants. *J Neural Eng*, 1(4):218–27, 2004.

[154] M. E. Nimni. Collagen: structure, function, and metabolism in normal and fibrotic tissues. *Semin Arthritis Rheum*, 13(1):1–86, 1983.

[155] M. J. O'Leary, J. Fayad, W. F. House, and Jr. Linthicum, F. H. Electrode insertion trauma in cochlear implantation. *Ann Otol Rhinol Laryngol*, 100(9 Pt 1):695–9, 1991.

[156] S. J. O'Leary, R. C. Black, and G. M. Clark. Current distributions in the cat cochlea: a modelling and electrophysiological study. *Hear Res*, 18(3):273–81, 1985.

[157] C. Y. Ota and R. S. Kimura. Ultrastructural study of the human spiral ganglion. *Acta Otolaryngol*, 89(1-2):53–62, 1980.

[158] J Otte, H F Schuknecht, and A G Kerr. Ganglion cell populations in normal and pathological human cochleae: Implications for cochlear implantation. *Laryngoscope*, 88(8 Pt 1):1231–46, 1978.

[159] J. Otte, H. F. Schunknecht, and A. G. Kerr. Ganglion cell populations in normal and pathological human cochleae. implications for cochlear implantation. *Laryngoscope*, 88(8 Pt 1):1231–46, 1978.

[160] S.K. Peterson, L. S. Frishkopf, C. Lechene, C. M. Oman, and T. F. Weiss. Element composition of inner ear lymphs of cats lizards, and skates by electron probe microanalysis of liquid samples. *J. Comp. Physiol.*, 126:1–14, 1978.

[161] B. E. Pfingst and L. Xu. Across-site variation in detection thresholds and maximum comfortable loudness levels for cochlear implants. *J Assoc Res Otolaryngol*, 5(1):11–24, 2004.

[162] R. Plonsey. Action potential sources and their volume conductor fields. *Proceedings of the IEEE*, 65(5):601, 1977.

[163] R. Plonsey and K. W. Altman. Electrical stimulation of excitable cells-a model approach. *Proceedings of the IEEE*, 76(9):1122, 1988.

[164] Robert Plonsey and Roger C. Barr. *Bioelectricity: a quantitative approach*. Kluwer Academic/Plenum Publishers, New York, 2nd edition, 2000.

[165] P. V. Rao. *Statistical research methods in the life sciences*. Duxbury Press, Pacific Grove, CA, 1998.

[166] H. Rask-Andersen, A. Schrott-Fischer, K. Pfaller, and R. Glueckert. Perilymph/modiolar communication routes in the human cochlea. *Ear Hear*, 27(5):457–465, 2006.

[167] F. Rattay. Analysis of models for external stimulation of axons. *IEEE Trans Biomed Eng*, 33(10):974–7, 1986.

[168] F. Rattay, R. N. Leao, and H. Felix. A model of the electrically excited human cochlear neuron. ii. influence of the three-dimensional cochlear structure on neural excitability. *Hearing Research*, 153(1-2):64–79, 2001.

[169] F. Rattay, P. Lutter, and H. Felix. A model of the electrically excited human cochlear neuron. i. contribution of neural substructures to the generation and propagation of spikes. Technical report, Vienna University of Technology.

[170] F. Rattay, P. Lutter, and H. Felix. A model of the electrically excited human cochlear neuron i. contribution of neural substructures to the generation and propagation of spikes. *Hearing Research*, 153(1-2):43–63, 2001.

[171] J. Ray, A. R. D'Souza, S. V. Chavda, A. R. Walsh, and R. M. Irving. Dissemination of fat in csf: a common finding following translabyrinthine acoustic neuroma surgery*. *Clin Otolaryngol*, 30(5):405–8, 2005.

[172] S. J. Rebscher, R. L. Snyder, and P. A. Leake. The effect of electrode configuration and duration of deafness on threshold and selectivity of responses to intracochlear electrical stimulation. *J Acoust Soc Am*, 109(5 Pt 1):2035–48., 2001.

[173] A. T. Reece, B. O'Reilly, E. Teasdale, and N. V. Todd. Subarachnoid fat embolism complicating autologous fat grafting following translabyrinthine excision of acoustic neuroma. *J Laryngol Otol*, 103(9):870–1, 1989.

[174] J. Patrick Reilly and J. Patrick Reilly. *Applied bioelectricity: from electrical stimulations to electropathology*. Springer, New York, 1998.

[175] E. M. Relkin and J. R. Doucet. Is loudness simply proportional to the auditory nerve spike count? *J Acoust Soc Am*, 101(5 Pt 1):2735–40., 1997.

[176] H. Ruan, M. J. Zarnowski, S. W. Cushman, and H. F. Lodish. Standard isolation of primary adipose cells from mouse epididymal fat pads induces inflammatory mediators and downregulates adipocyte genes. *J Biol Chem*, 278(48):47585–93, 2003.

[177] J. T. Rubinstein. Analytical theory for extracellular electrical stimulation of nerve with focal electrodes. ii. passive myelinated axon. *Biophys J*, 60(3):538–55, 1991.

[178] J. T. Rubinstein. Threshold fluctuations in an n sodium channel model of the node of ranvier. *Biophys J*, 68(3):779–85, 1995.

[179] J. T. Rubinstein, C. A. Miller, H. Mino, and P. J. Abbas. Analysis of monophasic and biphasic electrical stimulation of nerve. *IEEE Trans Biomed Eng*, 48(10):1065–70., 2001.

[180] J. T. Rubinstein, B. S. Wilson, C. C. Finley, and P. J. Abbas. Pseudospontaneous activity: stochastic independence of auditory nerve fibers with electrical stimulation. *Hear Res*, 127(1-2):108–18, 1999.

[181] S. Saha and P. A. Williams. Comparison of the electrical and dielectric behavior of wet human cortical and cancellous bone tissue from the distal tibia. *J Orthop Res*, 13(4):524–32, 1995.

[182] E. Saunders, L. Cohen, A. Aschendorff, W. Shapiro, M. Knight, M. Stecker, B. Richter, S. Waltzman, M. Tykocinski, T. Roland, R. Laszig, and R. Cowan. Threshold, comfortable level and impedance changes as a function of electrode-modiolar distance. *Ear Hear*, 23(1 Suppl):28S–40S, 2002.

[183] H. F. Schuknecht and A. E. Seifi. Experimental observations on the fluid physiology of the inner ear. *Ann Otol Rhinol Laryngol*, 72:687–712, 1963.

[184] Harold F Schuknecht. *Pathology of the Ear*. Harvard University Press, Cambridge, 1974.

[185] J.R. Schwarz and G. Eikhof. Na currents and action potentials in rat myelinated nerve fibres at 20 and 37 degrees c. *European J Phys*, pages 569–77, 1987.

[186] R. V. Shannon. Threshold and loudness functions for pulsatile stimulation of cochlear implants. *Hear Res*, 18(2):135–43, 1985.

[187] R. K. Shepherd, S. Hatsushika, and G. M. Clark. Electrical stimulation of the auditory nerve: the effect of electrode position on neural excitation. *Hear Res*, 66(1):108–20, 1993.

[188] R. K. Shepherd and E. Javel. Electrical stimulation of the auditory nerve: Ii. effect of stimulus waveshape on single fibre response properties. *Hear Res*, 130(1-2):171–88, 1999.

[189] David Sheskin. *Handbook of parametric and nonparametric statistical procedures*. Chapman and Hall/CRC, Boca Raton, 2nd edition, 2000.

[190] T. Shinohara, G. Bredberg, M. Ulfendahl, I. Pyykko, N. P. Olivius, R. Kaksonen, B. Lindstrom, R. Altschuler, and J. M. Miller. Neurotrophic factor intervention restores auditory function in deafened animals. *Proc Natl Acad Sci U S A*, 99(3):1657–60., 2002.

[191] M. W. Skinner, D. R. Ketten, L. K. Holden, G. W. Harding, P. G. Smith, G. A. Gates, J. G. Neely, G. R. Kletzker, B. Brunsden, and B. Blocker. Ct-derived estimation of cochlear morphology and electrode array position in relation to word recognition in nucleus-22 recipients. *J Assoc Res Otolaryngol*, 3(3):332–50., 2002.

[192] L. Smith and F. B. Simmons. Estimating eighth nerve survival by electrical stimulation. *Ann Otol Rhinol Laryngol*, 92(1 Pt 1):19–23, 1983.

[193] Zachery M. Smith. *Binaural interactions in the auditory midbrain with bilateral electric stimulation of the cochlea*. Doctor of philosophy, Massachusetts Institute of Technology, 2006.

[194] S. W. Smye. A mathematical comparison of two models of the electrical properties of biological tissues. *Phys Med Biol*, 46(3):867–77, 2001.

[195] R. L. Snyder, J. A. Bierer, and J. C. Middlebrooks. Topographic spread of inferior colliculus activation in response to acoustic and intracochlear electric stimulation. *J Assoc Res Otolaryngol*, 5(3):305–22, 2004.

[196] R.L. Snyder, S.J. Rebscher, K.L. Cao, P.A. Leake, and K. Kelly. Chronic intracochlear electrical stimulation in the neonatally deafened cat. i: Expansion of central representation. *Hear Res*, 50(1-2):7–33, 1990.

[197] M. S. Sorensen, A. B. Dobrzeniecki, P. Larsen, T. Frisch, J. Sporring, and T. A. Darvann. The visible ear: a digital image library of the temporal bone. *ORL J Otorhinolaryngol Relat Spec*, 64(6):378–81, 2002.

[198] F.A. Spelman, B.M. Clopton, and B.E. Pfingst. Tissue impedance and current flow in the implanted ear. implications for the cochlear prosthesis. *Ann Otol Rhinol Laryngol Suppl*, 98:3–8, 1982.

[199] H. Spoendlin and A. Schrott. Analysis of the human auditory nerve. *Hear Res*, 43(1):25–38, 1989.

[200] H. Staecker, R. Kopke, B. Malgrange, P. Lefebvre, and T. R. Van de Water. Nt-3 and/or bdnf therapy prevents loss of auditory neurons following loss of hair cells. *Neuroreport*, 7(4):889–94., 1996.

[201] D. A. Stewart, T. R. Gowrishankar, and J. C. Weaver. Three dimensional transport lattice model for describing action potentials in axons stimulated by external electrodes. *Bioelectrochemistry*, 69(1):88–93, 2006.

[202] M. F. Suesserman and F. A. Spelman. Lumped-parameter model for in vivo cochlear stimulation. *IEEE Trans Biomed Eng*, 40(3):237–45, 1993.

[203] M. F. Suesserman and F. A. Spelman. Quantitative in vivo measurements of inner ear tissue resistivities: I. in vitro characterization. *IEEE Trans Biomed Eng*, 40(10):1032–47, 1993.

[204] M.F. Suesserman. *Noninvasive microelectrode measurement technique for performing quantitative, in vivo measurements of the inner ear tissue impedances,*. Ph.d., University of Washington, 1992.

[205] L. Tang and J. W. Eaton. Natural responses to unnatural materials: A molecular mechanism for foreign body reactions. *Mol Med*, 5(6):351–8, 1999.

[206] Leonid I. Terr, Guiseppe A. Sfogliano, and Solomon L. Riley. Effects of stimulation by cochlear implant on the cochlear nerve. *Laryngoscope*, 99:1171–1174, 1989.

[207] C.S. Throckmorton and L.M. Collins. Investigation of the effects of temporal and spatial interactions on speech-recognition skills in cochlear-implant subjects. *J Acoust Soc Am*, 105(2, Pt. 1):861–873, 1999.

[208] N. Trayanova, C. S. Henriquez, and R. Plonsey. Extracellular potentials and currents of a single active fiber in a restricted volume conductor. *Ann Biomed Eng*, 18(3):219–38, 1990.

[209] N. A. Trayanova, C. S. Henriquez, and R. Plonsey. Limitations of approximate solutions for computing the extracellular potential of single fibers and bundle equivalents. *IEEE Trans Biomed Eng*, 37(1):22–35, 1990.

[210] S. Tylstedt, A. Kinnefors, and H. Rask-Andersen. Neural interaction in the human spiral ganglion: a tem study. *Acta Otolaryngol*, 117(4):505–12, 1997.

[211] S. Tylstedt and H. Rask-Andersen. A 3-d model of membrane specializations between human auditory spiral ganglion cells. *J Neurocytol*, 30(6):465–73, 2001.

[212] A. B. Vallbo, K. A. Olsson, K. G. Westberg, and F. J. Clark. Microstimulation of single tactile afferents from the human hand. sensory attributes related to unit type and properties of receptive fields. *Brain*, 107(Pt 3):727–49., 1984.

[213] C. van den Honert and P.H. Stypulkowski. Single fiber mapping of spatial excitation patterns in the electrically stimulated auditory nerve. *Hear Res*, 29(2-3):195–206, 1987.

[214] S. van Weert, R. J. Stokroos, M. M. Rikers, and P. van Dijk. Effect of peri-modiolar cochlear implant positioning on auditory nerve responses: a neural response telemetry study. *Acta Otolaryngol*, 125(7):725–31, 2005.

[215] F. Vanpouchk, A. Zarowski, J. Casselman, J. Frijns, and S. Peeters. Facial nerve canal and efi. *J Otol and Neurotol*, 2002.

[216] F. J. Vanpoucke, A. J. Zarowski, and S. A. Peeters. Identification of the impedance model of an implanted cochlear prosthesis from intracochlear potential measurements. *IEEE Trans Biomed Eng*, 51(12):2174–83, 2004.

[217] H. Versnel, V. F. Prijs, and R. Schoonhoven. Round-window recorded potential of single-fibre discharge (unit response) in normal and noise-damaged cochleas. *Hear Res*, 59(2):157–70, 1992.

[218] A. A. Verveen. On the fluctuation of threshold of the nerve fibre. In *Structure and function of the cerebral cortex. Proceedings of the second International Meeting of Neurobiologists, Amsterdam, 1959*, pages xi, 448 p. Elsevier, Amsterdam,, 1960.

[219] A. A. Verveen. *Fluctuation in Excitability*. PhD thesis, University of Amsterdam, 1961.

[220] A. A. Verveen. Axon diameter and fluctuation in excitability. *Acta Morphol Neerl Scand*, 5:79–85, 1962.

[221] Binseng Wang. *The relation between the compound action potential and unit discharges of the auditory nerve*. Ph.d., MIT, 1979.

[222] Sorensen M. S. Wang H., Merchant S. N. A downloadable 3-d virtual model of the visible ear. *ORL Journal for Oto-Rhino-Laryngology and Its Related Specialties*, in press, 2006.

[223] E. N. Warman, W. M. Grill, and D. Durand. Modeling the effects of electric fields on nerve fibers: determination of excitation thresholds. *IEEE Trans Biomed Eng*, 39(12):1244–54, 1992.

[224] Thomas Fischer Weiss. *Cellular biophysics*. MIT Press, Cambridge, 1996.

[225] Darren M. Whiten. *Threshold Predictions Based on an Electro-anatomical Model of the Cochlear Implant*. Master of science, Massachusetts Institute of Technology, 2003.

[226] F. A. Wichmann and N. J. Hill. The psychometric function: I. fitting, sampling, and goodness of fit. *Percept Psychophys*, 63(8):1293–313, 2001.

[227] F. A. Wichmann and N. J. Hill. The psychometric function: Ii. bootstrap-based confidence intervals and sampling. *Percept Psychophys*, 63(8):1314–29, 2001.

[228] Blake S. Wilson, Dewey T. Lawson, Mariangeli Zerbi, and Charles C. Finley. Speech processors for auditory prostheses, final report. Technical Report Contract NO1-DC-2-2401, National Institutes of Health, 1995.

[229] T. Yamagata, J. M. Miller, M. Ulfendahl, N. P. Olivius, R. A. Altschuler, I. Pyykko, and G. Bredberg. Delayed neurotrophic treatment preserves nerve survival and electrophysiological responsiveness in neomycin-deafened guinea pigs. *J Neurosci Res*, 78(1):75–86, 2004.

[230] J. J. Zappia, J. K. Niparko, Dana L. Oviatt, John L. Kemink, and Richard A. Altschuler. Evaluation of the temporal bones of a multichannel cochlear implant patient. *Ann Otol Rhinol and Laryngol*, 100:914–921, 1991.

[231] A. F. Zehnder, A. G. Kristiansen, J. C. Adams, S. N. Merchant, and M. J. McKenna. Osteoprotegerin in the inner ear may inhibit bone remodeling in the otic capsule. *Laryngoscope*, 115(1):172–7, 2005.

[232] J. L. Zheng and W. Q. Gao. Differential damage to auditory neurons and hair cells by ototoxins and neuroprotection by specific neurotrophins in rat cochlear organotypic cultures. *Eur J Neurosci*, 8(9):1897–905., 1996.

[233] C. E. Zimmermann, B. J. Burgess, and Jr. Nadol, J. B. Patterns of degeneration in the human cochlear nerve. *Hear Res*, 90(1-2):192–201., 1995.

[234] T. A. Zwolan, L. M. Collins, and G. H. Wakefield. Electrode discrimination and speech recognition in postlingually deafened adult cochlear implant subjects. *J Acoust Soc Am*, 102(6):3673–85, 1997.